THE UNIVERSITY OF CHICAGO

SPIN-PHONON INTERACTIONS WITH DEFECTS IN SILICON CARBIDE

A DISSERTATION SUBMITTED TO
THE FACULTY OF THE DIVISION OF THE PHYSICAL SCIENCES
IN CANDIDACY FOR THE DEGREE OF
DOCTOR OF PHILOSOPHY

DEPARTMENT OF PHYSICS

BY
SAMUEL JAMES WHITELEY

CHICAGO, ILLINOIS
JUNE 2019

Table of Contents

List of Figures

List of Tables

Acknowledgments

All of this work that I was so fortunate to have been a part of was made possible by the contributions of many individuals and collaboration at University of Chicago and Argonne National Laboratory. I thank my advisor David Awschalom his guidance and fostering an excellent collaborative environment. Additionally, I thank David Schuster for stimulating scientific discussions, various cryogenic experiments, and encouragement to work on hybrid quantum systems as well as Andrew Cleland for advice on characterization and fabrication. I would like to thank Gary Wolfowicz for being a good friend, coworker, and mentor throughout multiple years and scientific projects. I have Peter Duda to thank for consulting on fabrication processes and talking through the basics as well as Joe Heremans for materials science and general academic discussions. It was truly a pleasure helping bring the Pritzker Nanofabrication Facility online, and that process taught me so much about device engineering.

So many of my fellow students and friends in the Physics Department and Institute for Molecular Engineering have helped me get through graduate school. In particular, I acknowledge my friends Zoheyr Doctor, Akash Dixit, Aziza Suleymanzade, Andrew Ludwig, Ryan McGeehan, Alex Crook, and Jon Trisnadi. Moreover, I will never forget how Alex Crook and I spent so many all-nighters completing problem sets in addition to how he helped me at times with cleanroom processing. I am grateful to all of the Awschalom group members including but not limited to Chris Anderson, Alex Bourassa, Berk Diler, Kevin Miao, Peter Mintun, Paul Jerger, Erzsebet Vincent, Masaya Fukami, and it has also been

a pleasure to work with Agnetta Cleland, Marie Wesson, Elena Glen, and Joseph Blanton. I am very excited to see what everyone accomplishes! I am also thankful to Paul Klimov for providing some of the original ideas to experiment on spins with surface acoustic waves in silicon carbide. Many people from the Cleland lab including Greg Peairs, Ming-Han Chou, and Rhys Povey helped answer nanomechanics or other questions, and I'm happy to have overlapped with Kevin Satzinger who also worked on SAWs. From the Schuster lab, I especially thank Gerwin Koolstra for all of our conversations, on top of his effort on our projects ranging from SAWs to superconducting resonators. There are also individuals from the Schuster lab that I have to thank for their support and friendship including Ravi Naik, Srivatsan Chakram, Abigail Shearrow, Nate Earnest, and Sasha Anferov. From Argonne National Laboratory, I extend my gratitude to Martin Holt for helping to initiate our X-ray microscopy collaboration and teach me advanced X-ray diffraction techniques, and I also acknowledge Nazar Delegan who has helped take up the reins on materials science of aluminum nitride and point defects. Last but certainly not least, I thank my family and Deanna for supporting me along this entire journey.

Abstract

Optically addressable defect spins in semiconductors are promising candidates for quantum memories. Merging spins and mechanics into hybrid quantum systems provides a route to engineering quantum registers and transducers. However, precise control of such systems requires a comprehensive understanding of each component as well as their mutual interactions. In this thesis we explore the imaging of surface acoustic wave phonons and their coupling to electron spins. We then present an overview of spin-strain coupling in silicon carbide divacancies, followed by fabrication and microwave characterization of Gaussian surface acoustic wave resonators on commercial wafer-scale substrates with a piezoelectric aluminum nitride film. The resonator's mechanical modes are measured optically using the point defect charge states sensitivity to electric fields that are piezoelectrically induced. Additionally, local strain and dynamic lattice distortions from standing waves produced by interdigitated transducers are imaged with nanometer-scale resolution using X-ray diffraction microscopy. Finally, we demonstrate all-optical detection of acoustic paramagnetic resonance with spin ensembles. Furthermore, we show magnetically forbidden Rabi oscillations for full ground-state spin control and use these resonant, coherent interactions with phonons for quantum sensing.

Chapter 1

Introduction

1.1 Hybrid Quantum Systems with Point Defects and Mechanics

Quantum information systems in the solid-state come in a wide variety of forms, length scales, and energies. Many of these systems have been proposed for quantum computing or other applications, but usually each system is specialized and caries its own unique advantages. For example, optical photons travel long distances in fibers before experiencing significant attenuation, and weakly interacting electron-nuclear spins yield long coherence times for memories. One solution to broaden interdisciplinary scientific scope and work towards more complex technologies is the creation of hybrid quantum systems that leverage advantages of multiple components [1]. Physical quantum states are often difficult to control with more than one or two mechanisms because extraneous coupling to environmental noise leads to decoherence. By the same token, this makes it challenging to couple multiple disparate quantum states simultaneously. Therefore, a quantum transducer like the one depicted in Figure 1.1a may have to be implemented using several components and systems with pair-wise interactions.

Optically addressable point defects in silicon carbide (SiC) have garnered interested as

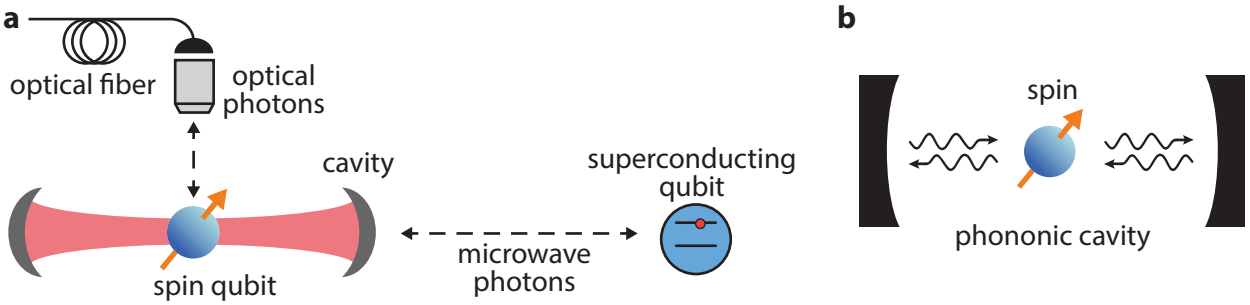

Figure 1.1: **A hybrid quantum system with optically addressable spins. a** A proposed quantum transduction platform for exchanging quantum information between optical photons, a solid-state spin, mechanical cavity that is piezoelectrically coupled to a superconducting microwave circuit, and qubit in order to illustrate connectivity across many systems. **b**. Spin ensembles collectively coupled to phonons in a cavity.

single photon sources in a crystalline semiconductor host that is amenable to device fabrication. Silicon carbide is attractive host material as it has versatile properties such as low mechanical losses [2], uses in optoelectronics [3], and contains deep defects with coherent defect spins analogous to the nitrogen-vacancy center in diamond [4, 5]. In the divacancy, any two spin sublevels within the electronic ground-state can in theory be used as a qubit, often controlled using radio frequency magnetic fields [6]. In combination with high photoluminescnence contrast of the spin state during optical readout and narrow band emission, point defects are powerful candidates for quantum sensing and spin-photon interfaces. The coherence time of these ground-state transitions can extend beyond one millisecond [7] in an isotopic naturally abundant material containing 1.1% carbon-13 and 4.7% silicon-29, which are both nuclear spin-1/2. Efforts have been made to couple electron spins in other materials such as diamond and silicon to superconducting resonators with magnetic field coupling, however, the coupling strength for single spin is very small and requires placing the spin less than 50 nanometers planar resonator's nanowire. In this scenario, the magnetic field mode hard to confine, and laser fields can easily inject quasiparticles into the resonator or make the superconductor go normal. Mechanical resontors (Fig. 1.1b) on the other hand are not so easily disturbed or made lossy by optics, although scattering of optical light can cause thermal fluctuations. Furthermore, there exist many types of mechanical resonators that

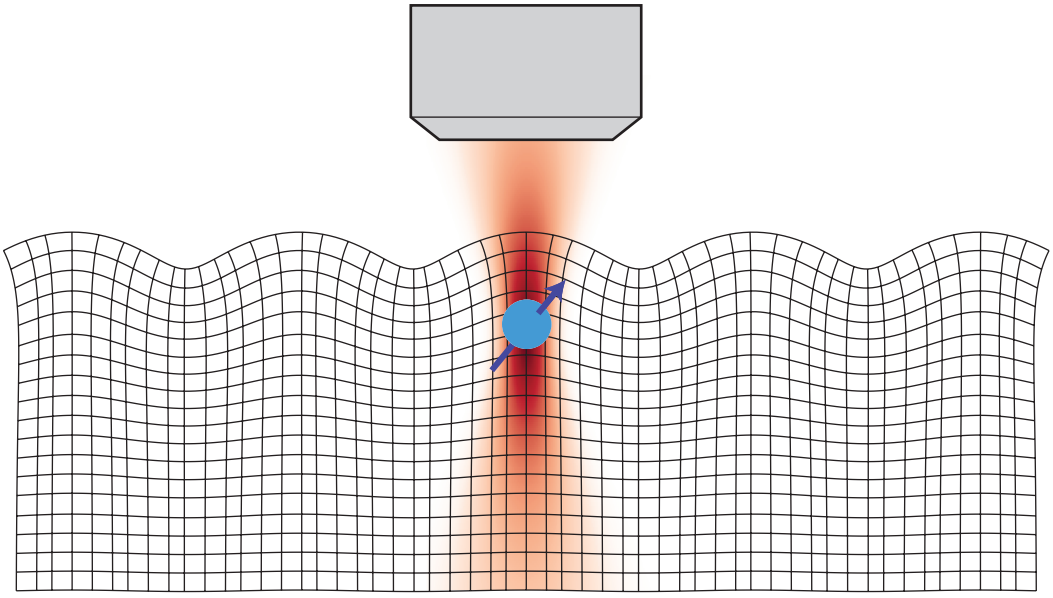

Figure 1.2: **Spin-mechanical platform with surface acoustic waves.** An objective (gray) focuses a near-infrared laser spot onto a spin (blue) being perturbed by the strain from a Rayleigh wave in the crystal. Emitted photoluminescence from the defect spin is also collected into the objective. The meshing shows the displacement field generated by a Rayleigh wave.

retain high quality factors up to room temperature.

Surface acoustic wave (SAW) devices on piezoelectric materials have been well developed for telecommunications and radio frequency filters. SAWs are of interest because there exist a number of methods for fabricating low loss resonators at gigahertz frequencies, and piezoelectric transducers give a natural way to eventually couple the mechanical cavity to a superconducting circuit [8]. The strain in a surface acoustic wave, specifically considering a Rayleigh wave mode, is located within one acoustic wavelength of the surface. This provides some confinement already for the mechanical mode as opposed to high-overtone bulk acoustic resonators. Spins in the SiC host can then be optically initialized and readout a as shown in Fig. 1.2 while other forms of radio frequency control can come from a device on either the front or backside of the sample. SAW resonator quality factors approach large values [9] at millikelvin temperatures that may rival superconducting cavities. In this thesis we will introduce key components of divacancy defects in SiC, spin resonance, and SAW

resonators fabricated for spin control. The SAW devices are studied by a variety of means, and importantly the dynamics are imaged using novel techniques with optical contrast from the point defects and X-ray Bragg diffraction with nanometer-scale spatial resolution. These methods allow us to precisely understand the mechanical mode and local dynamic strain directly to a high degree, in combination with both analytical and numerical models. Finally, the interaction strength between divacancy spin ensembles and phonons are probed in Gaussian SAW resonators and match well with first-principles calculations. We find that full ground-state spin control can be enabled with strain.

1.2 The Divacancy in Silicon Carbide

Silicon carbide is available commercially as single crystal wafers in a variety of polytypes [5]. Each polytype identifies a stacking order in the crystal lattice, and SiC has been identified in over 250 forms. Synthetically grown SiC by commercial manufacturers are 3C-SiC (cubic, diamond structure with two species), 4H-SiC (hexagonal), and 6H-SiC (hexagonal). Sometimes these can have specific uses such as nanophotonics [10, 11] because 3C-SiC can be grown epitaxially on silicon or 4H-SiC for doping [12, 13] and semiconductor devices [14]. Over the past decade, two popular defects that have been extensively studied for their optical and spin properties are the silicon vacancy (also referred to as V_{Si}) [15, 16] and the divacancy (sometimes referred to as VV) [6, 7]. From empirical evidence that will not be shown, 3C-SiC suffers from high film stress/strain when grown on silicon substrates whereas neutrally-charged divacancies in 4H-SiC are robust across various semi-insulating wafers, so we choose to focus on 4H-SiC in this thesis.

In 4H-SiC the lattice follows a four-fold stacking periodicity. Figure 1.3a shows a projection of the nearest neighbor lattice sites with some Si atoms colored red to highlight the stacking of hexagonal (h) and quasi-cubic (k) sites. Monovacancies in this lattice can exist at either a carbon or silicon site, and a divacancy defect is formed by two of these adjacent

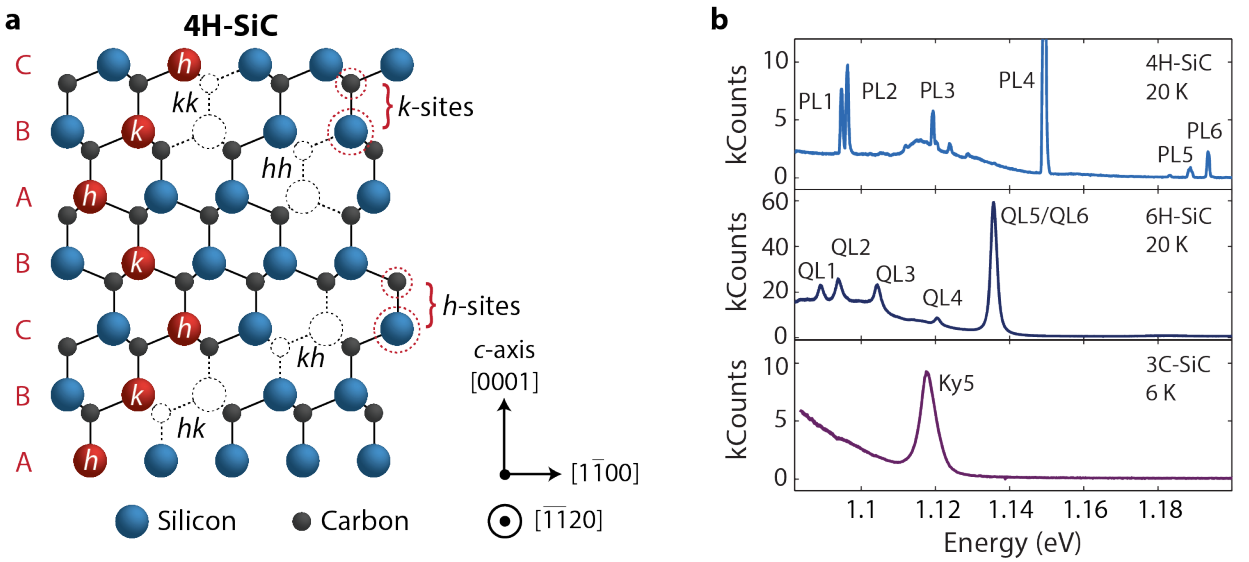

Figure 1.3: **Divacancy defects in silicon carbide. a**. Silicon carbide lattice (4H polytype) with the stacking order shown by the red atoms and each divacancy defect configuration illustrated. The convention for basally oriented divacancies shown here are the vacancies $V_C V_{Si}$ for consistency with experimental references such as [7, 17]. The crystal orientations are given in Miller-Bravais indexing for hexagonal systems. **b**. Photoluminescence emission spectra from divacancies in 4H-SiC (PL1-4) and unidentified similar defects (PL5-6), 6H-SiC (QL1-6), and 3C-SiC (Ky5) at a temperature of 20 K labeled by their zero-phonon line energy. PL1-4 are equivalent to *hh, kk, hk, kh* configurations. The spectra are extracted from Ref. [18].

vacancies. The configurations *hh* and *kk* result in divacancies that are oriented (dipole moment and crystal field splitting) along the crystal axis (*c*-axis). The configurations *hk* and *kh* using the notation $V_C V_{Si}$ are oriented approximately 109.5° relative to the *c*-axis, so these are occasionally referred to as basally oriented. These four defects we have discussed are also named PL1-4 for the order that they appear in optical spectroscopy (Fig. 1.3b) [6, 18]. When optically excited, less than 10% of the emitted photoluminescence (PL) spectrum is contained in a narrow *zero-phonon line* (approximately $5-7\%$ for divacancies, compared to $3-5\%$ for the nitrogen-vacancy center in diamond). The remainder of the emission is in a broad *phonon sideband* at lower energies due to phonon assisted, radiative decay.

The electronic orbitals of the divacancy are formed from dangling bonds by the nearby carbon and silicon atoms (Fig. 1.4a) [19, 21, 22]. These reduce to a ground-state (e^2) orbital singlet (A_2 symmetry) and an excited-state (ae) orbital doublet (E symmetry), that are spin

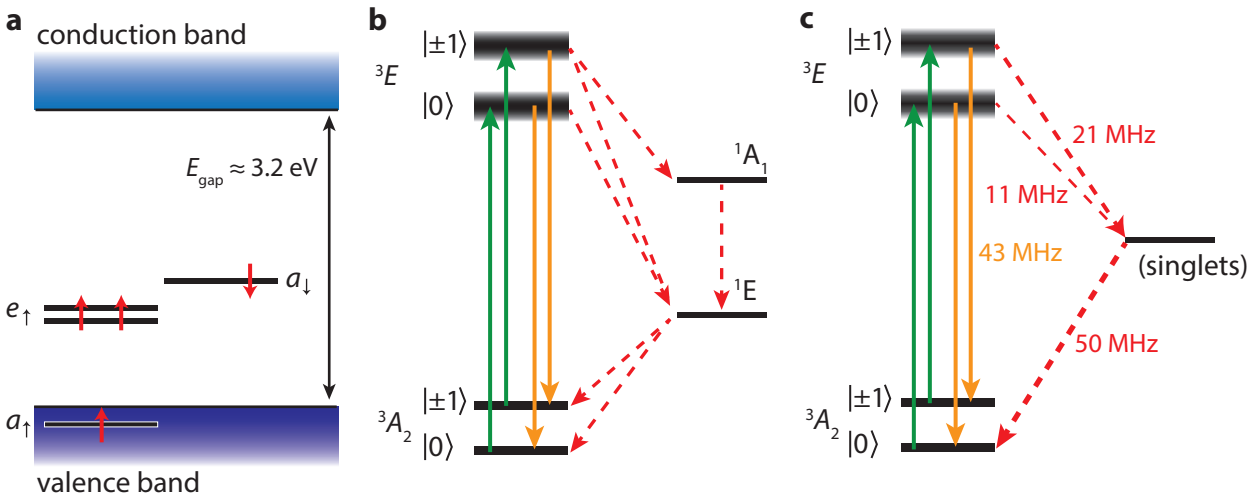

Figure 1.4: **The divacancy structure and intersystem crossing. a**. Electronic orbitals of the divacancy in 4H-SiC from dangling bonds. The two lines labeled $e_\uparrow$ represent the double degenerate $\{e_x, e_y\}$ orbitals. The ground-state and excited-state are within the 4H-SiC bandgap. **b**. General (simplified) model of the electronic ground-state, excited-state, and intersystem crossing of the divacancy that give rise to spin initialization and readout from optical absorption. The broadened excited-state levels represent the extra orbital states not shown. Solid lines are radiative and dashed red lines are non-radiative relaxation. **c**. Experimental decay rates in a simplified model for the divacancy in 3C-SiC. Both (**a**) and (**b**) are adapted from Ref. [19], and (**c**) is adapted from Ref. [20].

triplets ($s = 1$). Related theory for the nitrogen-vacancy center can be found in [23, 24]. Both orbital configurations are located within the 4H-SiC bandgap that is ≈ 3.2 eV, therefore, a near-infrared laser (e.g. 976 nm) can excite a divacancy without creating electron-hole pairs. A narrow line laser can optically excite the defect selectively (green arrows in Fig. 1.4b). Although, a more powerful off-resonant laser can also be used to excite all spin sublevels in a spin-conserving optical transition. From the excited state, the divacancy may take a few different paths of decay that will be simplified and summarized. Radiative decay (orange arrows in Fig. 1.4b) result in PL. The spin can also decay into lower-lying, metastable singlets (A_1 and E symmetry) due to spin-orbit and electron-phonon coupling, which then eventually decay into the ground-state $^3A_2$ (coupling rates shown as dashed red arrows in Fig. 1.4b). These are mostly non-radiative transitions, although it is known that the A_1 to E transition may emit optical photons like in the nitrogen-vacancy center in diamond. Each decay rate may be vary from one to another in this *intersystem crossing*, allowing for different relaxation

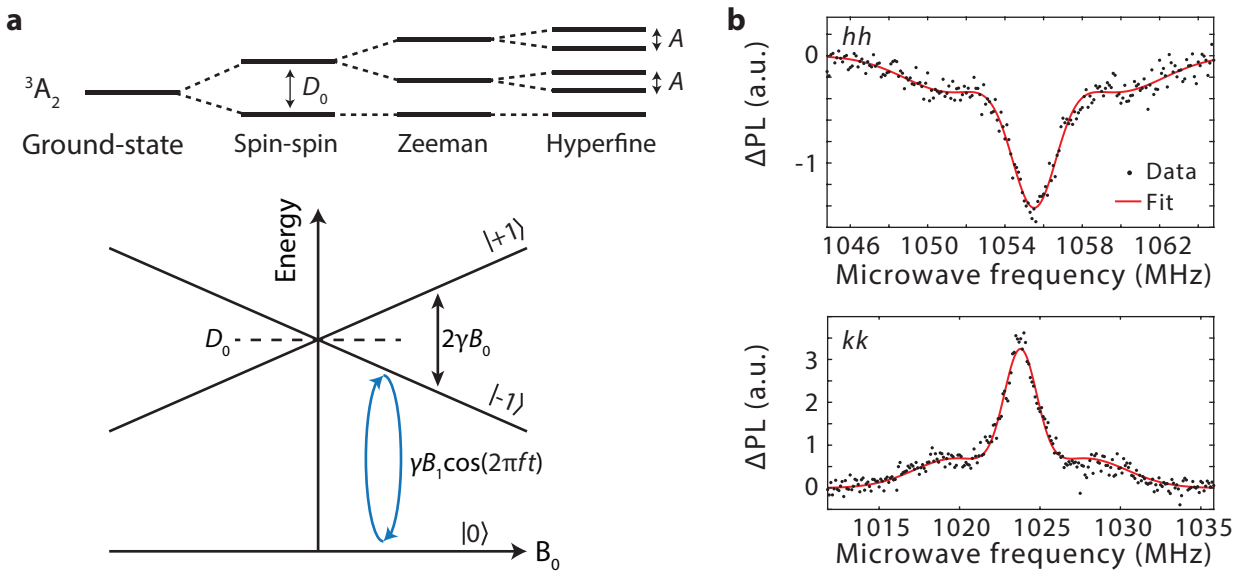

Figure 1.5: **The ground-state spin of *hh* and *kk* divacancies. a**. Level structure of the spin-1 ground-state for c-axis oriented divacancies. Spin-spin interactions are captured by the zero-field splitting parameter D_0. Electronic Zeeman interactions at low magnetic fields shift the electronic $|\pm 1\rangle$ states, nuclear Zeeman interactions can be ignored at low fields, and hyperfine interactions with nearby nuclear spins can further couple to each spin sublevel with the isotropic parameter A. The bottom plot illustrates the electronic Zeeman shift caused by a magnetic field without hyperfine interactions, where B_0 is the applied static magnetic field along the defect axis (SiC c-axis for hh and kk) and B_1 is perpendicular (in-plane). **b**. Optically detected magnetic resonance (ODMR) of hh and kk spin ensembles near 100 G and at a temperature of 30 K. Red lines are Gaussian fits, in which the side peaks are from electron spins more strongly coupled to neighboring nuclear spins.

rates from separate spin sublevels. For divacancies in 3C-SiC, the intersystem crossing rates have been measured on single defects[1] and are summarized in Fig. 1.4c. By applying only modest off-resonant laser power ($\sim$ mW), a divacancy spin will eventually get polarized into the ground-state $m_s = 0$ sublevel with over 90% spin polarization [20].

Spin initialization and readout are optically enabled by the defect's intersystem crossing. Just as using a near-infrared laser initializes the spin selectively into $m_s = 0$ after a few optical cycles, the defect will also emit different amounts of PL (optical contrast) depending on which spin state it is in before readout. The technique *optically detected magnetic resonance*

1. Similar rates are expected for single hh and kk divacancies in 4H-SiC due to having analogous host materials and the same point symmetry.

(ODMR) is when one probes electron spin resonance with radio frequncy magnetic fields while measuring optical contrast. Now, let us take a closer look at the ground-state spin level structure in the presence of a nearby nuclear spin such as ^{29}Si by writing out the Hamiltonian as,

$$H = D_0 S_z^2 + \gamma_{\mathrm{e}} \mathbf{B} \cdot \mathbf{S} + \gamma_{\mathrm{n}} \mathbf{B} \cdot \mathbf{I} + \mathbf{S} \cdot \mathbf{A} \cdot \mathbf{I}\,, \tag{1.1}$$

where D_0 is the axial zero-field splitting parameter (~ 1.3 GHz for divacancies in SiC), $\mathbf{S}$ is the vector of electron spin-1 matrices, $\mathbf{I}$ is the vector of nuclear spin-1/2 matrices, $\mathbf{B}$ is the magnetic field vector assumed to be homogeneous, $\mathbf{A}$ is the hyperfine coupling tensor. The first term is from spin-spin interactions and only contains one parameter for hh and kk that have $\mathrm{C_{3V}}$ symmetry from three mirror planes and tetrahedrally coordinated atoms, otherwise, there is an additional term $E_0(S_x^2 - S_y^2)$ for hk and kh that have $\mathrm{C_{1h}}$ symmetry. The zero-field splitting (D_0 and E_0 for simplicity) is sensitive to external perturbations such as electric fields, temperature, and strain [17]. Therefore, $\mathbf{D}$ provides a way for quantum sensing of external non-magnetic perturbations using the spin. The second and third terms are the electronic and nuclear Zeeman terms, respectively, where the gyromagnetic ratios are $\gamma_{\mathrm{e}} = 28$ GHz/T for the divacancy and $\gamma_{\mathrm{n}} = -8.5$ MHz/T for ^{29}Si [25].

In the case of small magnetic fields (much less than one Tesla) where the nuclear Zeeman effect is neglible compared to the electron spin linewidth, we obtain the level structure shown in Fig. 1.5a, in which an a.c. magnetic field (B_1) perpendicular to the defect axis is used for ODMR while a static magnetic field (B_0) controls the electron spin transition frequency. In spin ensembles, the dominant source of inhomogeneous broadening in an electron spin resonance spectrum is usually from nuclear spins. Each electron spin may experience a different relative distance to nuclear spins (e.g. ^{29}Si and ^{13}C), so strong hyperfine coupled electron spins appear as sidebands in an ODMR spectrum while a large population of weakly coupled spins appears as a broadening (Fig. 1.5). By pulsing the microwave and sweeping the pulse length between experiments, one can measure ground-state spin Rabi oscillations

of the defects and use this to calibrate pulse times for other experiments such as Ramsey interferometry, and dynamical decoupling sequences to improve coherence times.

1.3 Spin-Lattice Coupling

In 1944 Russian physicist Evgenii Konstantinovich Zavoisky discovered Electrom Paramagnetic Resonance (EPR), published in 1945 after World War II had ended [26]. After the fields of EPR and nuclear magnetic resonance had become well established, the phenomenon of Acoustic Paramagnetic Resonance (APR), absorption of sound waves resonantly by spins, was first theoretically predicted in 1952 by Russian physicist Semen Alexandrovich Al'tshuler[2] [27] and independently by French physicist Alfred Kastler [28]. It is well known that spins exhibit energy decay by emitting thermal phonons to the host crystal lattice, so naturally one would expect that the time-reversed can also occur where spins absorb phonons from the lattice.

Initially, APR was performed by observing changes in EPR spectra while applying acoustic power at the sample from a quartz transducer for bulk acoustic waves. The first experimental evidence of APR observations on nuclear quadrupolar interactions and relaxation times of ^{35}Cl nuclei were in 1955 [29, 30] and on electron spin interactions with phonons in 1959 [31]. In the following decades, APR was performed and mapped out for various high-spin systems such as chromium and vanadium impurities in Al_2O_3 [32], as well as iron-group centers and various other transition metal ions in quartz [33]. Interestingly, ions in MgO have shown some of the highest spin-lattice coupling constants ($1 - 5$ cm^{-1} per unit strain $\approx 30 - 150$ GHz per unit strain, some centers occasionally in excess of 1000 GHz per unit strain) [34, 35, 36, 37]. One of the applications proposed for APR was to use double spin resonance, for example utilizing combined magneto-acoustic resonance methods on three or more spin sublevels with direct (single phonon) process interactions, could be used to create

2. Zavoisky is credited by Semen Al'tshuler for the initiative and motivation to study the theory of paramagnetic resonance with sound waves.

"maser-effects" for phonons to construct amplifiers of coherent sound waves [38]. This proposal still motivates us today in some regards. Unfortunately, however, this is a difficult task because it is hard to come by highly coherent, controllable spin ($s > 1/2$) systems that both respond strongly to phonons and are in a material host well suited for device engineering.

Two common mechanisms that couple phonons to electron spins through lattice strain is internal spin-spin and spin-orbit coupling, which can both lead to secord-order spin interactions. Additionally, first-order spin interactions can be available where the electron g-factor is directly modified by strain, although those are more common in ions with large spin-orbit coupling parameters. With these interactions present, more thermal phonons in a system will cause faster spin relaxation while coherent local phonons could be used for spin state manipulation.

Numerous recent studies involving nitrogen-vacancy centers have investigated spin-strain coupling in nanomechanical systems with static strain and observing changes to the ground-state spin transition frequencies [39, 40] or with acoustic phonons to drive $\Delta m_{\mathrm{s}} = \pm 2$ spin transitions [41, 42, 43, 44]. In particular, the static strain measurements, or equivalently dynamical decoupling (i.e. stroboscopic) on low frequency oscillators, revealed spin-strain coupling constants with a magnitude of 5-20 GHz per unit strain depending on the reference. These studies described their systems with Hamiltonians that grouped the 'axial' contributions into $d_{\parallel}(E_z + \varepsilon_z)S_z^2$ and the 'transverse' contributions into $\Pi_x(S_x^2 + S_y^2) + \Pi_y(S_xS_y + S_yS_x)$, where the electric field and strain (others write effective stress) are grouped into $\Pi_{x,y} = d_{\perp}(E_{x,y} + \varepsilon_{x,y})$ [45, 46]. The dipole moments/coupling parameters are $d_{\parallel,\perp}$, which actually get independently evaluated for electric field and strain susceptibilities.

While the form shown above has some intuitive truth for the electric field coupling and draws on equivalences to crystal field splittings for strain, the approximation is incorrect. We know from solid mechanics that strains are not three component vectors, neither do they transform like electric fields, nor would these perturbations map onto the *zero-field splitting tensor* due to being a different rank. Furthermore, shears do not appear to be directly

represented in the above formalism. One may ask, if scientists such as Al'tshuler understood that spin-strain coupling was rooted in field theory and symmetry, why would the modern color center community have forgotten about shear or APR literature, and then made so many assumptions? Perhaps the reason lies in diagonalization and frame of reference.

Experimentally the only observable differences one can measure with EPR and ODMR are the two spin transition frequencies, which may be written in two parameters as modified axial and transverse zero-field splitting ΔD_0 and ΔE_0, respectively. These parameter ΔD_0 quantifies an energy shift of $m_s = \pm 1$ relative to $m_s = 0$ and ΔE_0 is the change in energy difference between the $m_s = \pm 1$ spin sublevels. Clearly, the splittings alone cannot account for all matrix elements allowed by the second rank tensor for spin-spin interactions. In the next chapter we explain a more complete picture of spin-strain coupling in defects with C_{3v} symmetry and then demonstrate all-optical detection of APR ($\Delta m_s = \pm 1$ and ± 2 spin transitions with phonons) using divacancy ensembles in Chapter 6. Electric field-spin coupling in matrix form is presented in Appendix B. The surface acoustic wave resonator experiments we conduct in tandem with density functional theory predictions indicate a spin-strain coupling around 1-5 GHz per unit strain, which is in agreement with recent theoretical work done independently [47, 48]. Our understanding and demonstrations lay the groundwork for performing arbitrary manipulations of defect ground-state spins with strain and building spin-mechanical hybrid systems in silicon carbide.

Chapter 2

Electron Spin Resonance with Photons and Phonons

2.1 Quantum Information

2.1.1 Time-Evolution

In a quantum information platform, the physical state can be described as a vector in a Hilbert space, containing as many orthogonal dimensions as is necessary to describe the problem or process [49]. The quantum state in Dirac notation can then be written as the sum of independent vectors with complex coefficients,

$$|\psi\rangle = \sum_{a'} c_{a'} \left|a'\right\rangle . \tag{2.1}$$

The complex numbers $c_{a'}$ are normalized such that $\sum_{a'} |c_{a'}|^2 = 1$. The probabilities of $|\psi\rangle$ in various states can be seen in the density matrix $\rho = |\psi\rangle \langle\psi|$, which must have a trace $\mathrm{tr}(\rho) = 1$. The quantum state $|\psi\rangle$ is considered to be in a pure state when $\mathrm{tr}\left(\rho^2\right) = 1$, otherwise it is considered to be a mixed state where $|\psi\rangle$ is then composed of multiple vectors.

The differential Schrödinger equation for time-evolution of the state $|\psi(t)\rangle = U(t, t_0) \, |\psi(t_0)\rangle$,

where $U(t, t_0)$ is the time-evolution operator (called the propagator), can be written as:

$$i\hbar\frac{\partial |\psi(t)\rangle}{\partial t} = H |\psi(t)\rangle . \tag{2.2}$$

The Hamiltonian H is a Hermitian operator that describes energies and interactions in a system. If one wants to compute the time-evolution after multiple operations on the state $|\psi(t_0)\rangle$, then it is straightforward to use the propagator however many times as is necessary, e.g. $|\psi(t_2)\rangle = U(t_2, t_1)U(t_1, t_0) |\psi(t_0)\rangle$.

To understand the time-evolution of an initial state $|\psi(t_0)\rangle$, a few scenarios can be considered. In the case that H is time-independent, propagator $U(t, t_0)$ as derived from 2.2 is simply given by

$$U(t, t_0) = \exp[\frac{-iH(t - t_0)}{\hbar}]. \tag{2.3}$$

From this relation, one can see that energy eigenstates $H \left|a'\right\rangle = E_{a'} \left|a'\right\rangle$ will evolve into $\left|a'\right\rangle \rightarrow e^{\frac{-iE_{a'}t}{\hbar}} \left|a'\right\rangle$, therefore picking up a relative phase over time in general on each non-degenerate state. In the case that H is time-dependent but commutes at different times t, the propagator is

$$U(t, t_0) = \exp[\frac{-i\int_{t_0}^{t} H(t')dt'}{\hbar}]. \tag{2.4}$$

Throughout this thesis we will only need to use U in the case of the time-independent Schrödinger equation by working in the rotating frame of spin systems, which will be introduced in the next section.

2.1.2 Two-Level Systems and Magnetic Resonance

In this section we will review the Hamiltonian for a two-level spin system using electron spin resonance with Zeeman interactions and microwave photons as an example. Following the discussion earlier, a single electron spin in a pure state will need only two complex scalars,

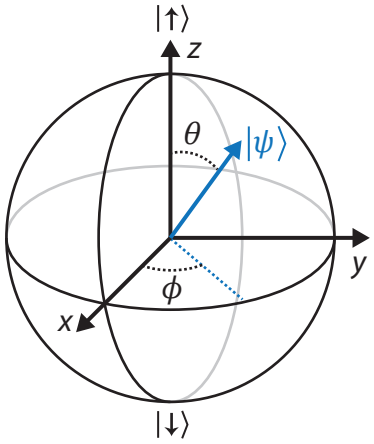

Figure 2.1: **Bloch sphere.** The quantum state $|\psi\rangle$ is represented as a vector on a sphere with a radius of 1 if normalized, polar angle θ, and azimuthal angle ϕ.

call them $c_\downarrow$ and $c_\uparrow$, to describe the superposition.

$$|\psi\rangle = c_\downarrow |\downarrow\rangle + c_\uparrow |\uparrow\rangle \tag{2.5}$$

These constants for the quantum state can also be expressed as a vector on the Bloch sphere using two constants, where θ and ϕ are the polar and azimuthal angles, respectively (Fig. 2.1). The pure state can then be written as,

$$|\psi\rangle = \cos(\theta/2)\,|\downarrow\rangle + \sin(\theta/2)e^{i\phi}\,|\uparrow\rangle \tag{2.6}$$

The complete set of Hermitian operators to describe a two-level system is the Pauli spin matrices,

$$\mathbb{1} = \begin{pmatrix} 1 & 0 \\ 0 & 1 \end{pmatrix}; S_x = \frac{\hbar}{2}\begin{pmatrix} 0 & 1 \\ 1 & 0 \end{pmatrix}; S_y = \frac{\hbar}{2}\begin{pmatrix} 0 & -i \\ i & 0 \end{pmatrix}; S_z = \frac{\hbar}{2}\begin{pmatrix} 1 & 0 \\ 0 & -1 \end{pmatrix}. \tag{2.7}$$

With these matrices we express any density matrix in terms of the Pauli matrices, and using these matrices as operators on $|\psi\rangle$ we can rotate a state arbitrarily around the Bloch sphere. Note that in other texts $\mathbb{1}$ can also be referred to as σ_0, and $\sigma_{1,2,3}$ are the standard Pauli matrices $\sigma_{x,y,z}$.

$$H = \hbar\gamma \mathbf{B} \cdot \mathbf{S} \tag{2.8}$$

where $\mathbf{B}$ is the magnetic field vector, $\mathbf{S} = \{S_x, S_y, S_z\}$ is the vector of Pauli spin matrices, $\gamma = g\mu_\mathrm{B}$ is the electron gyromagnetic ratio (g is the isotropic g-factor and μ_B is the Bohr magneton), which is approximately $2\pi \times 28$ GHz/T (the 2π is from using angular frequencies in this convention). Bold form will be used to represent vectors and tensors. The S_z projections $\left|m_\mathrm{s} = \pm\frac{1}{2}\right\rangle$ are synonymous with the $|\uparrow,\downarrow\rangle$ states. Let us suppose initially that the external magnetic field vector $B_0\hat{z}$ is applied along the z direction and is static, so $H_0 = \gamma B_0 S_z$. Note that it is possible to choose any other direction for B_0 on a spin-1/2 particle and this would only result in a basis change in the following work. Applying the propagator $U = e^{-i\gamma B_0 S_z/t}$ and rewriting the transition frequency $\omega_0 = \gamma B_0$ yields

$$U\left|\psi\right\rangle = c_\uparrow e^{-i\omega_0 t/2}\left|\uparrow\right\rangle + c_\downarrow e^{+i\omega_0 t/2}\left|\downarrow\right\rangle. \tag{2.9}$$

Here, we can see that there is a time-dependent relative phase $\phi = \omega_0 t$ between the two spin states. Any global phase factor $e^{i\Phi}\left|\psi\right\rangle$ is not important and can be neglected since it does not modify the magnitude of the vector $|\psi\rangle$. On the Bloch sphere the vector is rotating about the z-axis at an angular frequency ω_0, which is called the spin precession frequency or *Larmor frequency*.

Next, to coherently control the quantum state let us introduce an oscillating, transverse magnetic field $B_1\cos(\omega t + \varphi)\hat{x}$ with linear polarization as is common in experiments. It is important here that the field B_1 is perpendicular to the spin quantization axis. In the lab frame the total Hamiltonian ($H_\mathrm{lab} = H_0 + H_1(t)$) written in basis $\{\left|\uparrow\right\rangle, \left|\downarrow\right\rangle\}$ is,

$$H_\mathrm{lab}/\hbar = \begin{pmatrix} \omega_0/2 & \gamma B_1\cos(\omega t + \varphi) \\ \gamma B_1\cos(\omega t + \varphi) & -\omega_0/2 \end{pmatrix}. \tag{2.10}$$

The result of this Hamiltonian is easier to understand and calculate by removing the

time dependence and going into the interaction picture. In order to transform into the interaction picture using a reference rotating at a frequency ω, the same frequency as the transverse magnetic field, we need to apply a transformation matrix P. This matrix takes us into a rotating frame within the Hilbert space and cancels out either some or all of the time dependence caused by spin precession. For a spin-1/2 system, we can see that using $P = e^{-i\omega t H_0/\hbar}$ (sometimes with an identity term added to H_0 for convenience) and the transformation $|\psi(t)\rangle \rightarrow P^\dagger |\psi(t)\rangle$ the time-evolved state is

$$P^\dagger e^{-iH_0 t/\hbar} |\psi\rangle = |\psi(t)\rangle_{\mathrm{rf}} = c_\uparrow e^{-i(\omega_0-\omega)t/2} |\uparrow\rangle + c_\downarrow e^{+i(\omega_0-\omega)t/2} |\downarrow\rangle \tag{2.11}$$

The final state after time-evolution does not accumulate a relative phase when we are in a reference frame rotating at $\omega = \omega_0$. While it is convenient to remove the time-dependence from $|\psi\rangle$, our goal is remove the time-dependence from H_{lab}. The Hamiltonian in the rotating frame can be derived from transforming the Schrödinger equation,

$$\begin{aligned} i\hbar \frac{\partial (PP^\dagger |\psi(t)\rangle)}{\partial t} &= P(P^\dagger H P)(P^\dagger |\psi(t)\rangle) \\ i\hbar \frac{\partial |\psi(t)\rangle_{\mathrm{rf}}}{\partial t} &= (P^\dagger H P - i\hbar P^\dagger \frac{\partial P}{\partial t}) |\psi(t)\rangle_{\mathrm{rf}} . \end{aligned} \tag{2.12}$$

Therefore, the Hamiltonian in the rotating frame is $H_{\mathrm{rf}} = P^\dagger H P - i\hbar P^\dagger \frac{\partial P}{\partial t}$ and time-evolution follows as $|\psi(t)\rangle_{\mathrm{rf}} = e^{-iH_{\mathrm{rf}} t/\hbar} |\psi(t=0)\rangle_{\mathrm{rf}}$. The subscript 'rf' stands for 'rotating frame' and is not to be confused with 'radio-frequency' that will be used in later chapters. Using this information, the transformation for a spin in an oscillating magnetic field yields,

$$H_{\mathrm{rf}}/\hbar = \begin{pmatrix} (\omega_0-\omega)/2 & \frac{\gamma B_1}{2} e^{-i\varphi}(1 + e^{2i(\varphi+2\omega t)}) \\ \frac{\gamma B_1}{2} e^{i\varphi}(1 + e^{-2i(\varphi+2\omega t)}) & -(\omega_0-\omega)/2 \end{pmatrix} . \tag{2.13}$$

The co-rotating terms are preserved, whereas the counter-rotating terms are oscillating at twice the drive frequency. The counter-rotating terms 2ω get time-averaged and can

be canceled out: this is called the **rotating wave approximation** (RWA). The RWA is valid when $B_1 \ll B_0$. We define $\Delta = \omega_0 - \omega$ as the frequency detuning between our spin transition frequency and the a.c. drive, with a magnetic field drive strength $\Omega = \gamma B_1$, which will become apparent why when we review time-domain manipulation. It is possible to add an identity to H_{rf}, which will not affect the result for $|\psi(t)\rangle_{\mathrm{rf}}$ beyond a global phase factor, in order to group the diagonal terms for clarity. We find that

$$H_{\mathrm{rf}}/\hbar \approx \begin{pmatrix} \Delta/2 & \frac{\Omega}{2}e^{-i\varphi} \\ \frac{\Omega}{2}e^{i\varphi} & -\Delta/2 \end{pmatrix}. \tag{2.14}$$

The phase φ of the a.c. magnetic field offers access to both S_x and S_y for single-qubit gates rather than requiring independent, physical magnetic field control in both cartesian directions. This Hamiltonian is the case for *transverse driving* of a two-level system. It is worth noting that small oscillating magnetic fields along the spin quantization (z) axis can usually be neglected. Although, there is indeed interesting physics that arises from strong *longitudinal driving* using $H = H_0 + \Omega' \cos(\omega t) S_z$, such as sideband transitions and Landau-Zener-Stückelberg interferometry [50] which will not be discussed here.

2.1.3 Autler-Townes Effect

One result seen from the RWA applied to a driven two-level system is that the $|\uparrow\rangle$ and $|\downarrow\rangle$ get mixed, and in the rotating frame there is a new preferred basis. Diagonalizing 2.14 gives us the eigenvalues,

$$E_{\pm} = \pm\frac{\hbar}{2}\sqrt{\Delta^2 + \Omega^2}. \tag{2.15}$$

On resonance ($\Delta = 0$), there is an energy splitting of $E_+ - E_- = \hbar\Omega$ due to a.c. driving with a transverse field (Fig. 2.2), and the eigenstates are $|\pm\rangle = \frac{1}{2}(|\uparrow\rangle + |\downarrow\rangle)$. This splitting is called the Autler-Townes effect, also known as the AC Stark effect, and can be

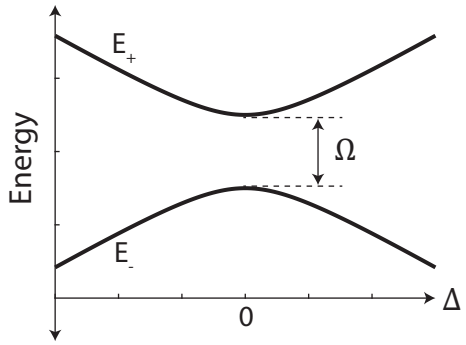

Figure 2.2: **Autler-Townes effect.** The eigenvalues of H_{rf} are plotted as a function of detuning (Δ) for a constant drive rate (Ω). An avoided level crossing with a gap size Ω is opened up at $\Delta = 0$.

directly observed during transition frequency spectroscopy of a two-level system mixed by a transverse field Ω. When Ω is driven by microwaves it is directly proportional to the drive field strength (e.g. B_1 for electron paramagnetic resonance), so one way to check this effect in experiments while driving at a constant power is to observe that the splitting is proportional to the square-root of the applied drive power.

2.1.4 Rabi Oscillations

We will now turn to investigating the result of H_{rf} for coherent control of the physical state as a function of time. Let us initialize the quantum state into spin-down, such that $|\psi(t=0)\rangle = |\downarrow\rangle$ where $|\downarrow\rangle \equiv \left(\begin{smallmatrix}0\\1\end{smallmatrix}\right)$ and $|\uparrow\rangle \equiv \left(\begin{smallmatrix}1\\0\end{smallmatrix}\right)$ in matrix form. We can find the state after time t, subject to the Hamiltonian H_{rf} from 2.14 and depicted in Fig. 2.3a. Solving $e^{-iH_{\mathrm{rf}}t/\hbar}|\downarrow\rangle$ for the coefficients $c_{\uparrow,\downarrow}$ yields exact solutions,

$$\begin{aligned} c_{\uparrow}(t) &= \frac{-i\Omega}{\sqrt{\Delta^2+\Omega^2}}\sin\left(\frac{t}{2}\sqrt{\Delta^2+\Omega^2}\right) \\ c_{\downarrow}(t) &= \cos\left(\frac{t}{2}\sqrt{\Delta^2+\Omega^2}\right) + \frac{i\Delta}{\sqrt{\Delta^2+\Omega^2}}\sin\left(\frac{t}{2}\sqrt{\Delta^2+\Omega^2}\right). \end{aligned} \tag{2.16}$$

Next, we can find the probabilities of measuring $|\psi(t)\rangle$ in each eigenstate by looking at the coefficients' norm given by

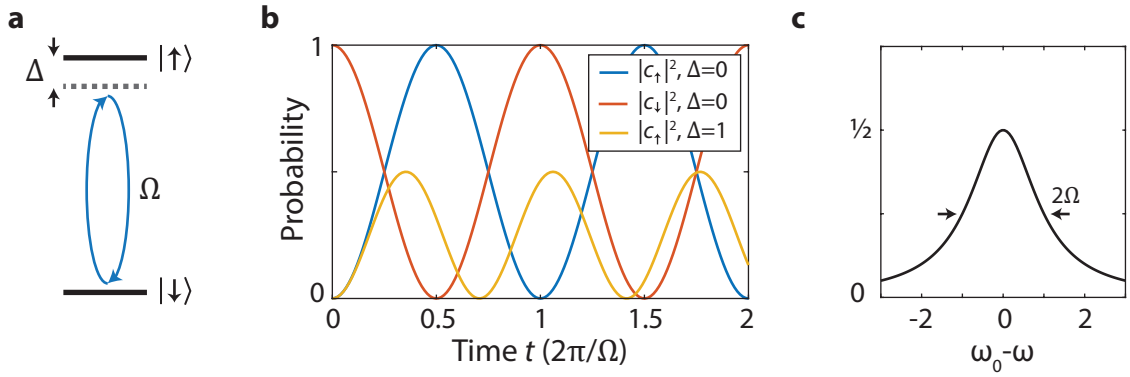

Figure 2.3: **Rabi oscillations in a two-level system. a**. Level structure of an electron spin being driven by $\Omega = \gamma B_1(t)$ with detuning Δ. **b**. Rabi oscillations between two spin states. **c**. Graph of $|c_\uparrow(t)|^2$ as a function of $\Delta = \omega_0 - \omega$, time-averaged over one period.

$$
\begin{aligned}
|\langle\uparrow|\psi(t)\rangle_{\mathrm{rf}}|^2 &= \frac{\Omega^2}{\Delta^2+\Omega^2}\sin^2\left(\frac{t}{2}\sqrt{\Delta^2+\Omega^2}\right) \\
|\langle\downarrow|\psi(t)\rangle_{\mathrm{rf}}|^2 &= 1 + \frac{\Omega^2}{2(\Delta^2+\Omega^2)}\left(\cos\left(t\sqrt{\Delta^2+\Omega^2}\right)-1\right).
\end{aligned}
\tag{2.17}
$$

On the Bloch sphere in the rotating frame and at zero detuning, the spin sees an effectively static magnetic B_x. The spin proceeds to precess about the x-axis leading to smooth spin rotations (oscillations) between $|\downarrow\rangle$ and $|\uparrow\rangle$. Equation 2.17 is also known as the Rabi formula. The presence of a non-zero detuning Δ increases the total Rabi rate $\Omega_{\mathrm{R}} = \sqrt{\Delta^2+\Omega^2}$ and lowers the Rabi contrast (Fig. 2.3b) because the effective magnetic field seen by the spin is no longer only along S_x. The time it takes to complete half an oscillation on resonance ($t = \pi/\Omega$) is called a 'π pulse' (σ_x gate) on the qubit because it corresponds to a change in the Bloch sphere polar angle of $\theta = \pi$.

Finally, it is also instructive to look at the transition probability as a function of drive frequency. While working at a fixed drive rate Ω, the time-averaged transition probability as a function of detuning $\Delta = \omega_0 - \omega$ is a Lorentzian centered on resonance $\Delta = 0$ with a full-width at half maximum of 2Ω. In general, driving a two-level system will broaden the measured resonance if Ω exceeds the natural line width (e.g. $\frac{1}{T_2^*}$) of the system.

2.1.5 Three-Level Systems: General Definitions

Multi-level systems offer more complexity for storing information and routes for quantum control. Three-level systems in particular can be used for probing interferences between the three eigenstates with applications to solid-state defect spins such as coherent population trapping [51], Berry phase manipulation [52], shortcuts to adiabaticity [53], and coherence protection from dephasing mechanisms [54]. In this section we will derive a Hamiltonian using the RWA on a general three-level system.

We begin by writing down the energies (eigenvalues) for our system in the $\{|1\rangle, |2\rangle, |3\rangle\}$ basis.

$$H_0 \equiv \begin{pmatrix} \hbar\omega_{01} & & \\ & \hbar\omega_{02} & \\ & & \hbar\omega_{03} \end{pmatrix} \tag{2.18}$$

In the laboratory frame, the three level system is subjected to transverse driving with linear polarization between any of the three sublevels with field strengths Ω_{jk} between states $|j\rangle$ and $|k\rangle$ (Fig. 2.4a). Each drive may have a phase ϕ_{jk}, which can be absorbed as a complex scalar into $\Omega_{jk} \to \Omega_{jk}e^{-i\phi_{jk}}$. We will ignore these relative phases for simplicity because they can be added back in at the end. Our Hamiltonian in the lab frame can be written as,

$$H_{\text{lab}}/\hbar = \begin{pmatrix} \omega_{01} & \Omega_{12}\cos(\omega_{12}t) & \Omega_{13}\cos(\omega_{13}t) \\ \Omega_{12}\cos(\omega_{12}t) & \omega_{02} & \Omega_{23}\cos(\omega_{23}t) \\ \Omega_{13}\cos(\omega_{13}t) & \Omega_{23}\cos(\omega_{23}t) & \omega_{03} \end{pmatrix} \tag{2.19}$$

For the transformation matrix P, we will use the convention a double-rotating frame relative to the ground state energy ($\hbar\omega_{01}$), so we can write $P \sim e^{-i(H_0 - \hbar\omega_{01}\mathbb{1})t/\hbar}$. However, the frequencies in P are ω_{12} for $|1\rangle \leftrightarrow |2\rangle$ and ω_{13} for $|1\rangle \leftrightarrow |3\rangle$ because it is convenient to work with our drive frequencies. The transformation matrix for the three-level system is,

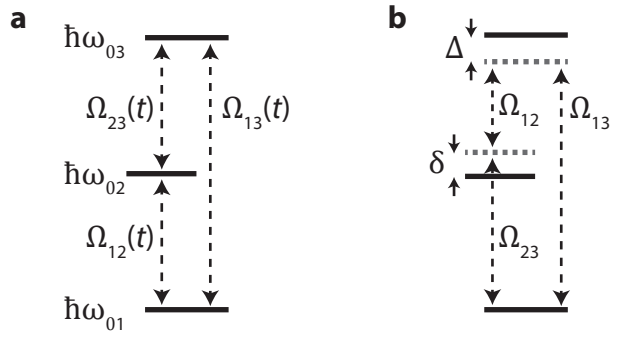

Figure 2.4: **Three-level system.** **a**. Laboratory frame view of the system with three transverse drives. **b**. Coupled system with one-photon and two-photon detunings portrayed.

$$P = \begin{pmatrix} 1 & & \\ & e^{-i\omega_{12}t} & \\ & & e^{-i\omega_{13}t} \end{pmatrix}. \tag{2.20}$$

After going into the rotating frame using $H_{\text{rf}} = P^\dagger H P - i\hbar P^\dagger \frac{\partial P}{\partial t}$, we find that

$$H_{\text{rf}}/\hbar = \begin{pmatrix} \omega_{01} & \frac{\Omega_{12}}{2}(1+e^{-2it\omega_{12}}) & \frac{\Omega_{13}}{2}(1+e^{-2it\omega_{12}}) \\ \frac{\Omega_{12}}{2}(1+e^{2it\omega_{12}}) & \omega_{02}-\omega_{12} & \frac{\Omega_{23}}{2}e^{-it\Delta'}(1+e^{-2it\omega_{23}}) \\ \frac{\Omega_{13}}{2}(1+e^{2it\omega_{13}}) & \frac{\Omega_{23}}{2}e^{it\Delta'}(1+e^{2it\omega_{23}}) & \omega_{03}-\omega_{13} \end{pmatrix}. \tag{2.21}$$

The parameter $\Delta' = \omega 12 + \omega_{23} - \omega 13$ yields a time-dependent phase unless $\Delta = 0$. In experiments one can carefully choose the drive frequencies $\omega_{12}, \omega_{23}, \omega_{13}$ and such that $\Delta = 0$, leading to a simpler final result. Making this assumption, adding an identity term so that energies are relative to the ground-state $|1\rangle$, and canceling out the fast oscillating counter-rotating terms with the RWA gives us the time-independent Hamiltonian

$$H_{\text{rf}}/\hbar \approx \begin{pmatrix} 0 & \Omega_{12}/2 & \Omega_{13}/2 \\ \Omega_{12}/2 & \delta & \Omega_{23}/2 \\ \Omega_{13}/2 & \Omega_{23}/2 & \Delta \end{pmatrix}, \tag{2.22}$$

where $\Delta = (\omega_{03} - \omega_{01}) - \omega_{13}$ is the one-photon detuning and $\delta = \Delta - (\omega_{03} - \omega_{02}) - \omega_{23}$ is the two-photon detuning. Relative phases between the various drive strengths ($\Omega_{jk} e^{-i\phi_{jk}}$) should be considered for many physical effects and experiments, especially those involving simultaneous, continuous driving with multiple fields.

2.1.6 Three-Level Systems: Divacancy Ground-State Spin

The divacancy electronic ground-state is a spin triplet state (s=1) with spin projections $m_\mathrm{s} = 0, \pm 1$. In this section we will be working in linear frequencies for consistency with defect spin literature as well as having simpler interpretations for experiments probing transitions with frequency spectroscopy. The Pauli matrices for a spin-1 system written in the $\{|+1\rangle, |0\rangle, |-1\rangle\}$ basis are,

$$S_x = \frac{1}{\sqrt{2}} \begin{pmatrix} 0 & 1 & 0 \\ 1 & 0 & 1 \\ 0 & 1 & 0 \end{pmatrix}; S_y = \frac{1}{\sqrt{2}} \begin{pmatrix} 0 & -i & 0 \\ i & 0 & -i \\ 0 & i & 0 \end{pmatrix}; S_z = \frac{1}{\sqrt{2}} \begin{pmatrix} 1 & 0 & 0 \\ 0 & 0 & 0 \\ 0 & 0 & -1 \end{pmatrix}. \tag{2.23}$$

The Planck constant does not appear in the Pauli matrices because we will add it back as a coefficient for all subsequent Hamiltonians. We can approximate the electronic ground-state as the sum of Zeeman interactions with external magnetic fields (H_Zeeman) and internal spin-spin interactions (H_ss). The total ground-state spin Hamiltonian can then be written as,

$$H = H_\mathrm{Zeeman} + H_\mathrm{ss} \tag{2.24a}$$

$$H_\mathrm{Zeeman}/h = \gamma \mathbf{B} \cdot \mathbf{S} \tag{2.24b}$$

$$H_\mathrm{ss}/h = \mathbf{S} \cdot \mathbf{D} \cdot \mathbf{S}, \tag{2.24c}$$

where $\mathbf{S} = \{S_x, S_y, S_z\}$ is the vector of Pauli matrices, $\mathbf{B} = \{B_x, B_y, B_z\}$ is the local magnetic field vector, $\gamma = 28$ GHz/T is the electron gyromagnetic ratio (notice our convention is linear frequency here), $\mathbf{D}$ is the zero-field splitting tensor. When no crystal or external perturbation is present (e.g. strain and electric fields), $H_{\rm ss}$ is reduced to two independent zero-field splitting parameters: $D_0 S_z^2$ and $E_0(S_x^2 - Sy^2)$ the axial and transverse crystal fields, respectively. D_0 (where $D_0 > E_0$ by choice of basis) creates a well defined defect-axis, which is the $\hat{z}$-axis. Since the divacancy configurations hh and kk investigated in later chapters are both oriented along the c-axis and C_{3v} symmetric, we will choose to set $E_0 = 0$. Strain and electric fields can modify $\mathbf{D}$, so all components of $H_{\rm ss}$ may have to be considered. A complete picture of spin-strain interactions from $H_{\rm ss}$ will be discussed in the next section. Let us suppose, as an example, that we can mechanically drive the spin with $|+1\rangle\langle -1| + \text{h.c.}$ mixing terms at a single frequency $\omega_{\rm m}$ close to the $|-1\rangle \rightarrow |+1\rangle$ resonance condition ($\omega_{\rm m}$ is very detuned from the other transitions). Additionally, we add a static magnetic field ($B_0\hat{z}$) to tune the spin transition frequencies and a.c. sinusoidal magnetic fields $B_{\pm 1}(t)\hat{x}$ at frequencies close to the $|0\rangle \rightarrow |\pm 1\rangle$ resonances, respectively. the Hamiltonian from 2.24 simplifies to,

$$H_{\rm lab}/h = D_0 S_z^2 + \gamma(B_0 S_z + B_{+1}(t) S_x + B_{-1}(t) S_x) + \Omega_{\rm m}(S_x^2 - S_y^2). \tag{2.25}$$

The spin transition (precession) frequencies are $H_0/h = D_0 S_z^2 + \gamma B_0 S_z$ while the magnetic drive strengths are $\Omega_{\rm B:\pm 1} = \gamma B_{\pm 1}$ at $B_0 \gg B_{\pm 1}$, as shown in Fig. 2.5a. Since we are working in the condition $B_0 \gg B_{\pm 1}$, the sinusoidal drives $\Omega_{\rm B:\pm 1}$ can only drive magnetically allowed $\Delta m_{\rm s} = \pm 1$ spin transitions near-zero detuned from $m_{\rm s} = 0$ to each of their respective spin sublevels. By working under the assumption that $\omega_{\rm B:-1} = \omega_{\rm B:-1} - \omega_{\rm m}$, transformation into the rotating frame is enabled by

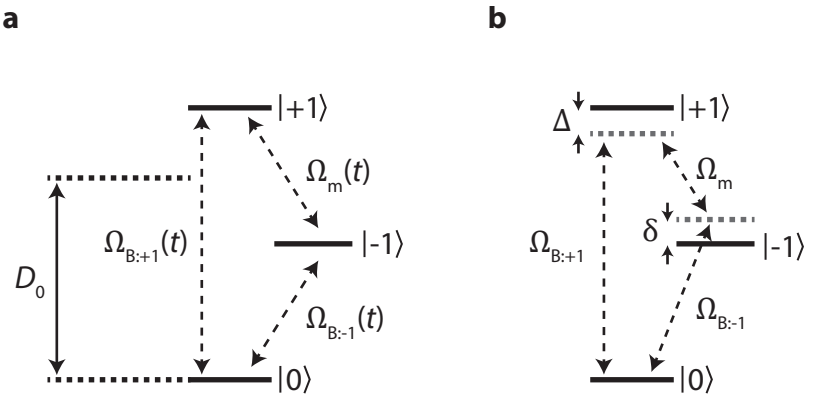

Figure 2.5: **Divacancy ground-state spin with three drives.** **a**. Laboratory frame Hamiltonian and setup for driving the ground-state spin with two a.c. magnetic fields $\Omega_{\rm B}$ and one a.c. mechanical (or electrical) drive $\Omega_{\rm m}$. **b**. Level structure with detunings Δ, δ illustrated.

$$P = \begin{pmatrix} e^{-i\omega_{\rm B:+1}t} & & \\ & 1 & \\ & & e^{-i(\omega_{\rm B:+1}-\omega_{\rm m})t} \end{pmatrix}, \tag{2.26}$$

which reads like the double-rotating frame for a Λ-system in the electron spin ground-state. After using the RWA and collecting the diagonal elements into two terms, the Hamiltonian can be written as,

$$H_{\rm rf}/h = \begin{pmatrix} \Delta & \Omega_{\rm B:+1}/2 & \Omega_{\rm m}/2 \\ \Omega_{\rm B:+1}/2 & 0 & \Omega_{\rm B:-1}/2 \\ \Omega_{\rm m}/2 & \Omega_{\rm B:-1}/2 & \delta \end{pmatrix}. \tag{2.27}$$

The parameter $\Delta = \langle +1|H_0|+1\rangle - \omega_{\rm B:+1}$ is the one-photon detuning from $|0\rangle$, and $\delta = \Delta - (\langle +1|H_0|+1\rangle - \langle -1|H_0|-1\rangle - \omega_m)$ is the two-photon detuning (Fig. 2.5b). In the case of mechanical driving, in fact, δ is actually a one-photon, one-phonon detuning, however, another interpretation one can see is that δ is the one-photon magnetic detuning from $|0\rangle$. Expressing the detunings in terms of our experimental parameters yields,

$$\begin{aligned}\Delta &= D_0 + \gamma B_0 - \omega_{\mathrm{B}:+1} \\ \delta &= D_0 - \gamma B_0 - (\omega_{\mathrm{B}:+1} - \omega_{\mathrm{m}}) = D_0 - \gamma B_0 - \omega_{\mathrm{B}:-1}.\end{aligned} \tag{2.28}$$

A mechanically induced Autler-Townes effect readily appears from this three-level when we consider a strong mechanical drive and weak magnetic driving. If we take $\Omega_{\mathrm{B}:\pm1} \to 0$, the eigenvalues of 2.28 are

$$\begin{aligned}E_0 &= 0 \\ E_\pm &= \frac{1}{2}(\Delta + \delta \pm \sqrt{(\Delta+\delta)^2 + \Omega_{\mathrm{m}}^2})\end{aligned} \tag{2.29}$$

Near resonance ($\Delta = \delta = 0$), the mechanics introduces a symmetric avoided level crossing. Since the first derivative of this avoided crossing on resonance is zero with respect to small magnetic field changes in B_0, like those caused by nuclear spin flips, the spin sublevels will encounter less dephasing.

2.2 Spin-Strain Coupling

2.2.1 Electronic Spin-Spin Interactions

We will now consider all general outcomes of spin-spin interactions and their relationship to perturbations by strain on defect spins with a symmetry point group $\mathrm{C}_{3\mathrm{v}}$. Spin-spin interactions (from dipole-dipole effects and the Pauli Exclusion Principle) and spin-orbit coupling lead to a second order spin interaction, depending greatly on the symmetries and geometry of the electronic wavefunction. The divacancy in silicon carbide has a relatively weak spin-orbit coefficient in the excited state, and furthermore spin-orbit coupling in the ground-state spin is a second order perturbation from the excited state orbital doublet so

we will ignore spin-orbit contributions. The spin-spin interactions may be expressed as a zero-field splitting Hamiltonian,

$$H_{\rm ss}/h = \mathbf{S}\cdot\mathbf{D}\cdot\mathbf{S}\,. \tag{2.30}$$

It can be helpful to see this in matrix form after contracting the Pauli Matrices and terms in the 3x3 matrix D_{ij} in $H_{\rm ss}/h = \sum_{ij} S_i D_{ij} S_j$. Considering all terms in the $\{|+1\rangle, |0\rangle, |-1\rangle\}$ basis, the Hamiltonian can be written as,

$$H_{\rm ss}/h = \begin{pmatrix} \frac{1}{2}(D_{xx}+D_{yy})+D_{zz} & \frac{1}{\sqrt{2}}(D_{xz}-iD_{yz}) & \frac{1}{2}(D_{xx}-D_{yy})-iD_{xy} \\ \frac{1}{\sqrt{2}}(D_{xz}+iD_{yz}) & D_{xx}+D_{yy} & \frac{1}{\sqrt{2}}(-D_{xz}+iD_{yz}) \\ \frac{1}{2}(D_{xx}-D_{yy})+iD_{xy} & \frac{1}{\sqrt{2}}(-D_{xz}-iD_{yz}) & \frac{1}{2}(D_{xx}+D_{yy})+D_{zz} \end{pmatrix}. \tag{2.31}$$

In our rest frame with no other zeroth-order contributions or perturbations, $H_{\rm s}$ reduces to $D_{xx}S_{xx} + D_{yy}S_{yy} + D_{zz}S_{zz}$. With our single defect at the origin in space, D_{xz}, D_{yz} are equivalent to a spatial rotation of our defect basis vectors, so these off-diagonals are set to zero. Each diagonal component D_{ii} correspond to compressions or elongations in those respective axes. Given that $H_{\rm rm}$ is traceless ($D_{xx} + D_{yy} = -D_{zz}$), we can rewrite the Hamiltonian and sum up the observables as

$$H_0/h = \begin{pmatrix} \frac{1}{3}D_0 & 0 & E_0 \\ 0 & -\frac{2}{3}D_0 & 0 \\ E_0 & 0 & \frac{1}{3}D_0 \end{pmatrix}, \tag{2.32}$$

where the independent component D_0 is defined in the conventional notation as $\frac{3}{2}D_{zz}$ [55], and $E_0 = (D_{xx} - D_{yy})/2$. D_0 is called the axial crystal field splitting and partially lifts the system's degeneracies by moving Kramers doublets away from other states (e.g. $m_{\rm s} = \pm 1$ from $m_{\rm s} = 0$) in energy, while E_0 is called the transverse crystal field splitting

and lifts Kramers degeneracy (e.g. splits $m_{\mathrm{s}} = 1$ and $m_{\mathrm{s}} = -1$). Since we are focusing on c-axis oriented divacancy defects with $\mathrm{C}_{3\mathrm{v}}$ symmetry, the $\mathbf{D}$ tensor has only one independent component (D_0) and the transverse crystal field splitting (E_0) is zero due to three-fold mirror symmetry. In addition, it is common to add an identity to make $\langle 0|H_0|0\rangle = 0$, that way $H_0 = D_0 S_z^2$ mimics the spin transition frequencies observed in experiments.

If a strain is then applied to the system, $\mathrm{C}_{3\mathrm{v}}$ symmetry may be broken, leading to additional diagonal and non-zero off-diagonal elements in the original basis. The relation between strain and $\mathbf{D}$ is characterized by how much energy the zero-field splitting components shift by when a small strain perturbation is present. Expanding the $\mathbf{D}$ tensor to leading order in strain yields,

$$D_{ij}(\varepsilon_{kl}) = D_0 S_z^2 + \frac{\partial D_{ij}}{\partial \varepsilon_{kl}} \varepsilon_{kl} + \mathcal{O}\Big(\varepsilon^2\Big). \tag{2.33}$$

We define $\mathbf{G}$ as the first-derivative of $\mathbf{D}$ with respect to the strain tensor ε_{ij} linear response regime (small ε). The coupling coefficients in $\mathbf{G}$ are a fourth rank tensor,

$$G_{ijkl} \equiv \frac{\partial D_{ij}}{\partial \varepsilon_{kl}} \tag{2.34}$$

where i, j, k, l are indices that represent the Cartesian coordinates $\{x, y, z\}$. The strain is defined as $\varepsilon_{kl} = \frac{1}{2}(\frac{u_k}{x_l} + \frac{u_l}{x_k})$, where $u_i = \{u_x, u_y, u_z\}$ is the material displacement vector while treating the crystal as a continuum. In this convention, compressive uniaxial strains are negative and tensile uniaxial strains are positive (uniaxial strains are the diagonal elements ε_{ii}).

In Voigt notation, in order to reduce the number of redundant components written down, both the symmetric tensors $\mathbf{D}$ and $\boldsymbol{\varepsilon}$ are written as 6-dimensional vectors in the order of (xx, yy, zz, yz, xz, xy), and $\mathbf{G}$ is represented by a 6×6 matrix. When performing computations in Voigt notations, particularly for solid mechanics, one should note that 'strain-like' tensors $\boldsymbol{\varepsilon} = \{\varepsilon_{xx}, \varepsilon_{yy}, \varepsilon_{zz}, 2\varepsilon_{yz}, 2\varepsilon_{xz}, 2\varepsilon_{xy}\}$ have extra factors in the off-diagonal elements

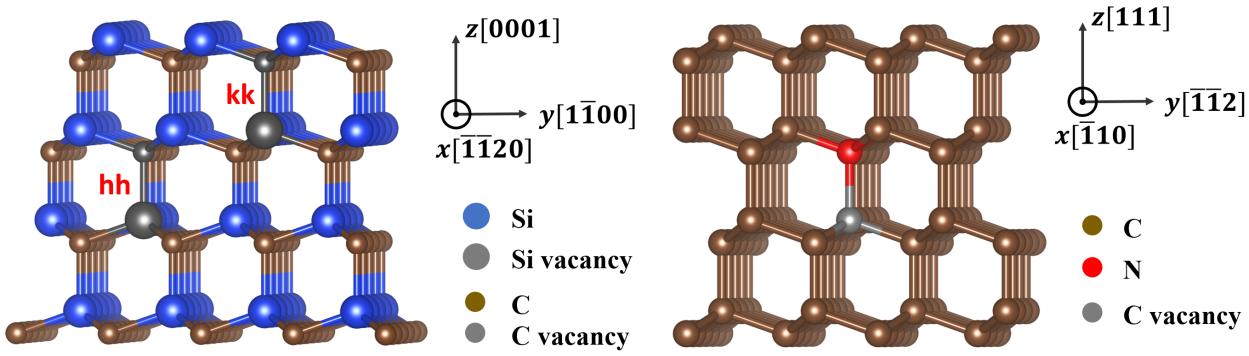

Figure 2.6: **Silicon carbide and diamond lattices containing color centers.** The structures of (hh, kk)-VV in 4H-SiC (left) and NV in diamond (right). The lattices are slightly rotated around z-axis to show more detail.

whereas 'stress-like' tensors $\boldsymbol{\sigma} = \{\sigma_{xx}, \sigma_{yy}, \sigma_{zz}, \sigma_{yz}, \sigma_{xz}, \sigma_{xy}\}$ do not. This happens so that the Voigt transformation preserves an invariance, such as energy ($\boldsymbol{\sigma} \cdot \boldsymbol{\varepsilon}$). **G** and **D** both transform stress-like, which is more convenient to work with.

In the following discussion we choose a spatial coordinate system by defining the Cartesian frame for 4H-SiC to be $\hat{x} \equiv [\bar{1}\bar{1}20]$, $\hat{y} \equiv [1\bar{1}00]$, and $\hat{z} \equiv [0001]$, consistent with surface acoustic wave experiments. Similarly, we define the Cartesian frame for diamond as $\hat{x} \equiv [\bar{1}10]$, $\hat{y} \equiv [\bar{1}\bar{1}2]$, $\hat{z} \equiv [111]$. Under this convention, there is a mirror plane perpendicular to the x-axis in both 4H-SiC and diamond. The structures of (hh, kk)-VV and NV in their respective frames are shown in Fig 2.6.

$$\begin{pmatrix} \Delta D_{xx} \\ \Delta D_{yy} \\ \Delta D_{zz} \\ \Delta D_{yz} \\ \Delta D_{xz} \\ \Delta D_{xy} \end{pmatrix} = \begin{pmatrix} G_{11} & G_{12} & G_{13} & G_{14} & G_{15} & G_{16} \\ G_{21} & G_{22} & G_{23} & G_{24} & G_{25} & G_{26} \\ G_{31} & G_{32} & G_{33} & G_{34} & G_{35} & G_{36} \\ G_{41} & G_{42} & G_{43} & G_{44} & G_{45} & G_{46} \\ G_{51} & G_{52} & G_{53} & G_{54} & G_{55} & G_{56} \\ G_{61} & G_{62} & G_{63} & G_{64} & G_{65} & G_{66} \end{pmatrix} \begin{pmatrix} \varepsilon_{xx} \\ \varepsilon_{yy} \\ \varepsilon_{zz} \\ 2\varepsilon_{yz} \\ 2\varepsilon_{xz} \\ 2\varepsilon_{xy} \end{pmatrix}. \tag{2.35}$$

Under C_{3v} point group symmetry, a fourth-rank tensor like **G** only has 6 independent components. Using the reference frame from earlier (shown in Fig 2.6), we find that **G** in

Voigt notation has the following form [56],

$$\mathbf{G} = \begin{pmatrix} G_{11} & G_{12} & G_{13} & G_{14} & & \\ G_{12} & G_{11} & G_{13} & -G_{14} & & \\ -G_{11}-G_{12} & -G_{11}-G_{12} & -2G_{13} & & & \\ G_{41} & -G_{41} & & G_{44} & & \\ & & & & G_{44} & G_{41} \\ & & & & G_{14} & (G_{11}-G_{12})/2 \end{pmatrix}, \tag{2.36}$$

where independent components are chosen to be G_{11}, G_{12}, G_{13}, G_{14}, G_{41} and G_{44} (see Ch. 6 for numerical values). Combining the above equation with (2.31b), one can see that d.c. arbitrary strains can generally be used to add any component to modify H_{ss} and shift spin sublevels. Moreover, applying a.c. strains at the appropriate frequencies can induce both $\Delta m_{\rm s} = \pm 1$ and $\Delta m_{\rm s} = \pm 2$ transitions, corresponding to phonon absorption and emission from the defect spin.

2.2.2 Acoustic Paramagnetic Resonance

Applying a.c. strain near resonance with the spin transition frequencies can lead to coherent spin transitions. We will now see how general lattice strains of classical waves, which are made up of phonons with creation and annihilation operators $a^\dagger, a$, couple to the system through a defect's internal spin-spin interactions. Let us suppose that we have a time-periodic wave with a mechanical mode described by a local strain tensor component $\varepsilon_{kl} = \varepsilon_{kl}(\boldsymbol{r}, t)$, and assume that the strain is approximately homogeneous over one unit cell located at Cartesian coordinate $\boldsymbol{r} = (x, y, z)$. This is true for coherently driven strain with acoustic phonons at GHz frequencies, where the acoustic wavelengths span on the order of a micrometer.

It is instructive to look at our Hamiltonian for spin-phonon coupling $H_{\rm ss} \to H_{\rm s-p}$ by grouping terms responsible for spin sublevel mixing and shifting. Any mechanical operations

that break the defect C_{3v} symmetry lead to off-diagonal terms in H_{s-p} while symmetry-preserving lead to modification of D_0. In the rotating frame of acoustic phonons with detuning neglected,

$$H_{\text{s-p}}/h = \frac{1}{2}\begin{pmatrix} \Delta D_0' & \Omega_1 & \Omega_2 \\ \Omega_1^\dagger & -2\Delta D_0' & \Omega_3 \\ \Omega_2^\dagger & \Omega_3^\dagger & \Delta D_0' \end{pmatrix}. \tag{2.37}$$

In this form all spin-strain coupling terms from $D_{xz}\{S_x, S_z\}$ and $D_{yz}\{S_y, S_z\}$ are contained in Ω_1, Ω_3, which lead to $\Delta m_s = \pm 1$ spin transitions. Terms from $\frac{D_{xx}-D_{yy}}{2}(S_x^2 - S_y^2) + D_{xy}\{Sx, Sy\}$ are grouped into Ω_2, which lead to $\Delta m_s = \pm 2$ spin transitions; these are magnetically forbidden in well-aligned system (B_0 is along the defect axis) because Zeeman interactions cannot produce this matrix element. The transition rates from phononic driving on a divacancy spin as well as shifts to the zero-field splitting are below.

$$\begin{aligned} \Omega_1 &= \frac{-i(G_{41} - G_{41})}{\sqrt{2}}(\varepsilon_{xx} - \varepsilon_{yy}) - i\sqrt{2}G_{14}\varepsilon_{yz} + \sqrt{2}G_{41}\varepsilon_{xy} + \sqrt{2}G_{44}\varepsilon_{xz} \\ \Omega_2 &= \frac{G_{11} - G_{12}}{2}(\varepsilon_{xx} - \varepsilon_{yy}) + 2G_{14}\varepsilon_{yz} - \frac{i(G_{11} - G_{12})}{2}\varepsilon_{xy} - 2iG_{14}\varepsilon_{xz} \\ \Omega_3 &= -\Omega_1 \\ \Delta D_0 = \frac{3}{2}\Delta D_0' &= -\frac{3(G_{11} + G_{12})}{2}(\varepsilon_{xx} + \varepsilon_{yy}) - 3G_{13}\varepsilon_{zz} \end{aligned} \tag{2.38}$$

These expressions offer direct insight into the Rabi rates of spin transitions driven by strain from mechanical waves. Clearly, shears and uniaxial transverse strains couple to all three types of spin transitions, however, careful attention should be given to the relative phase between various strain and shear contributions. Another observation that was not described well in past literature is the dependence of D_0 on strain. D_0 is sensitive to volumetric/hydrostatic strains, although there are different coupling constants for uniaxial strains along the defect axis (ε_{zz}) compared to uniaxial strains that are transverse ($\varepsilon_{xx}+\varepsilon_{yy}$).

In this convention, an increase in D_0 corresponds to compressive strain.

Chapter 3

Surface Acoustic Waves

3.1 Solid Mechanics

In an elastic continuous material, accelerations and stresses are related by an equation of motion. Although, before we get to this relation, a few variables need to be defined. Inside the material, displacement vectors $\mathbf{u}$ at any point in space $\mathbf{r} = (x, y, z)$ are assumed to be differentiable at all locations. Importantly, the absolute displacement is not so important for physical results because adding and a constant offset to $\mathbf{u}$ will not generate any forces on the system. The gradient of displacement is called *strain*, which is interpreted as a fractional change of length and is therefore a relative quantity. We can express any strain as a symmetric second-rank tensor (matrix), $\varepsilon_{kl} = \frac{1}{2}(\frac{\partial u_k}{\partial x_l} + \frac{\partial u_l}{\partial x_k})$ for each index spanning the three dimensional spatial coordinates (e.g. Cartesian coordinate system $1 = x, 2 = y, 3 = z$). We will sometimes refer to the diagonal elements of the strain tensor as *uniaxial strain*, in which we will use the convention of negative for compression and positive for tensile (expansion) changes, and the off-diagonal elements as *shear*. Forces and pressures are directly related to the strain by Hooke's law $\sigma_{ij} = c^{\mathrm{E}}_{ijkl}\varepsilon_{kl}$, where σ_{ij} is the stress and $\mathbf{c}^{\mathrm{E}}$ is a fourth-rank tensor called the *stiffness tensor* that contains all anisotropic material constants of elasticity. The general equation of motion for a material with constant density (ρ) can be written as,

$$\rho \frac{\partial^2 u_i}{\partial t^2} = \frac{\partial \sigma_{ij}}{\partial x_j} \,. \tag{3.1}$$

Solving this differential equation under specific conditions allows one to understand a wide variety of physical phenomena including elastic waves. In a material with isotropic elastic constants, the general equation of motion (3.1) becomes [57],

$$\frac{\partial^2 \mathbf{u}}{\partial t^2} = v_{\mathrm{t}}^2 \nabla^2 \mathbf{u} + (v_\ell^2 - v_{\mathrm{t}}^2) \boldsymbol{\nabla}(\boldsymbol{\nabla} \cdot \mathbf{u}) \,. \tag{3.2}$$

In an infinite elastic medium there are two separate solutions: *longitudinal waves* propagating with a velocity v_ℓ and *transverse waves* propagating with a velocity v_{t}, and they are constrained by $v_\ell > \sqrt{4/3} v_{\mathrm{t}}$. The total displacement for any wave satisfying the equation above can be decomposed $\mathbf{u} = \mathbf{u}_\ell + \mathbf{u}_{\mathrm{t}}$, where $\boldsymbol{\nabla} \cdot \mathbf{u}_{\mathrm{t}} = 0$ and $\boldsymbol{\nabla} \times \mathbf{u}_\ell = 0$. Using these representations of $\mathbf{u}$, we can rearrange the general equation of motion into two ordinary wave equations,

$$\begin{aligned} \nabla^2 \mathbf{u}_\ell - \frac{1}{v_\ell^2} \frac{\partial^2 \mathbf{u}_\ell}{\partial t^2} &= 0 \,, \\ \nabla^2 \mathbf{u}_{\mathrm{t}} - \frac{1}{v_{\mathrm{t}}^2} \frac{\partial^2 \mathbf{u}_{\mathrm{t}}}{\partial t^2} &= 0 \,. \end{aligned} \tag{3.3}$$

3.1.1 The Piezoelectric Effect

Lattices that lack inversion symmetry obtain a net electric polarization in response to applied strain, thus causing a coupling between electric fields and internal strain/stress. In an anisotropic material with elastic constants c_{ijkl}^{E}, the piezoelectric effect can be summed up in the coupled equations (*stress-charge form*),

$$\begin{aligned} \sigma_{ij} &= c^{\mathrm{E}}_{ijkl} S_{kl} - e_{kij} E_k \,, \\ D_i &= \epsilon_{ij} E_j + e_{ijk} S_{jk} \,, \end{aligned} \tag{3.4}$$

where σ_{ij} is the stress tensor, S_{kl} is the strain tensor (using S in this section to avoid confusion with the dielectric constant), E_i is the electric field vector, D_i is the electric displacement field vector, and ϵ_{ij} is the matrix of anisotropic dielectric constants. The *piezoelectric coupling tensor* e_{kij} is equal to the transpose of e_{ijk} in Voigt notation, where

$$\mathbf{e} = \begin{pmatrix} 0 & 0 & 0 & 0 & e_{15} & 0 \\ 0 & 0 & 0 & e_{15} & 0 & 0 \\ e_{31} & e_{31} & e_{33} & 0 & 0 & 0 \end{pmatrix}, \tag{3.5}$$

for crystal class 6mm including 4H silicon carbide (4H-SiC) and hexagonal (wurtzite) aluminum nitride (AlN). The tensor $\mathbf{e}$ transposed in Voigt form are ordered to converts from an electric field vector $\mathbf{E} = \{E_x, E_y, E_z\}$ to a stress tensor $\boldsymbol{\sigma} = \{\sigma_{xx}, \sigma_{yy}, \sigma_{zz}, \sigma_{yz}, \sigma_{xz}, \sigma_{xy}\}$. These piezoelectric constants are summarized in the table below.

Table 3.1: **Piezoelectric constants (e) of AlN and 4H-SiC.** All values are in [$\mathrm{C\,m^{-2}}$] from Ref. [58]. Other literature references [59] give different (often smaller) results for e in 4H-SiC while staying within the same order of magnitude.

	AlN	4H-SiC
e_{31}	-0.58	-0.197
e_{33}	1.55	0.341
e_{15}	-0.48	-0.198

Putting the piezoelectric equations back into the general equation of motion $\rho\frac{\partial^2 \mathbf{u}}{\partial t^2} = \frac{\partial \sigma}{\partial \mathbf{x}}$, one can arrive at the differential equations for elastic waves including piezoelectricity. Typically, piezoelectric waves are difficult to find analytical solutions to, so finite-element

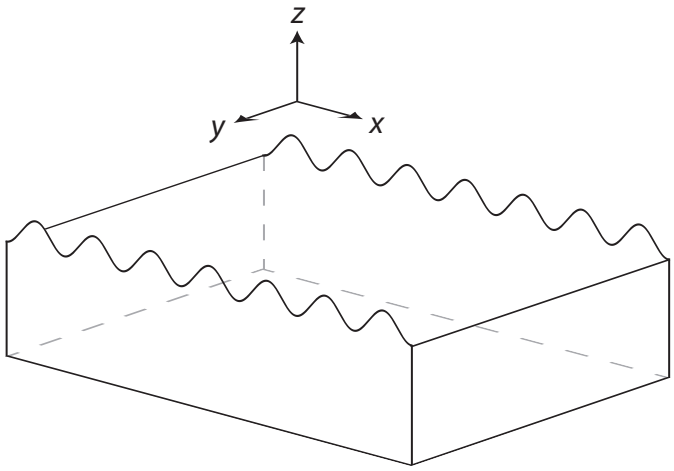

Figure 3.1: **Rayleigh waves in an isotropic medium.** The crystal surface is located at $z = 0$ and the wave is propagating in the $\hat{x}$ direction.

simulations are often used for a precise understanding. The piezoelectric coupling constant between a surface acoustic wave (SAW) and metal electrode array is summed up as $k^2_{\text{piezo}} = 2\Delta v_{\text{f}}/v_{\text{f}}$, in which $\Delta v_{\text{f}} = v_{\text{m}} - v_{\text{f}}$ is the difference between the SAW velocity on a metalized surface and free surface as caused by shorting at the metal interface. To summarize a few materials for reference, k^2_{piezo} of 4H-SiC is $\leq 10^{-4}$ (simulation), AlN $\approx 2.5 \times 10^{-3}$ [59], ST-X quartz $\approx 1.2 \times 10^{-3}$ [60], and *Y-Z* $LiNbO_3$ $\approx 4.8 \times 10^{-2}$ [60]. Indeed, the piezoelectric constant of 4H-SiC is so small that radio frequency electrical characterization of interdigitated transducers on SiC crystals is nearly impossible. Since the k^2_{piezo} of SiC is over an order of magnitude less than other 'weak' piezoelectric crystals like quartz, a thin film of AlN will be used for enhanced coupling.

3.1.2 Rayleigh Waves in a Non-Piezoelectric Substrate

As a model of acoustic waves propagating along the surface of a crystal, solutions to Rayleigh waves (named after John William Strutt, third Baron Rayleigh for his discovery in the nineteenth century [61]) in an isotropic, non-piezoelectric, semi-infinite medium will be summarized. Following the equation of motion for longitudinal and transverse waves 3.3, we are interested in solutions with displacement fields of the type $\mathbf{u} = \mathbf{u}_\ell + \mathbf{u}_{\text{t}}$ that have a total

dependence $\propto f(z)e^{i(kx-\omega t)}$ and surface wave velocity $v_{\mathrm{R}} = \omega/k$. Differentiation with Eq. 3.3 yields,

$$\frac{\partial^2 f(z)}{\partial z^2} = k^2 - \frac{\omega^2}{v^2}\,, \tag{3.6}$$

for v being either v_ℓ or v_{t}, and the function $f(z)$ is therefore proportional solved by $e^{\kappa z}$ with $\kappa = \sqrt{k^2 - \omega^2/v^2}$. If κ is imaginary then the wave oscillates throughout the bulk rather than decaying, so we must have $k > \omega/v_{\ell,}\omega/v_{\mathrm{t}}$ or in other words the *Rayleigh wave velocity* $v_{\mathrm{R}} = \omega/k < v_\ell, v_{\mathrm{t}}$. Given these relations, we can define new constants for effective decay lengths [62]

$$\begin{aligned} \kappa_\ell^2 &= k^2(1 - (\frac{v_{\mathrm{R}}}{v_\ell})^2)\,, \\ \kappa_{\mathrm{t}}^2 &= k^2(1 - (\frac{v_{\mathrm{R}}}{v_{\mathrm{t}}})^2)\,. \end{aligned} \tag{3.7}$$

The ratio between transverse and longitudinal wave velocities are related to *Poisson's ratio* (ν) by $v_{\mathrm{t}}/v_\ell = \sqrt{(1-2\nu)/(2-2\nu)}$. By solving for v_{R} in terms of v_{t}, v_ℓ from (3.7), it can be shown from the *Rayleigh-Lamb equation* [60, 62] that the condition for surface waves is satisfied whenever $0 < \nu < 1/2$. The spatial distributions of $\mathbf{u}$ can be found by imposing the surface boundary condition $\sigma_{xz} = \sigma_{yz} = \sigma_{zz} = 0$ at $z = 0$, and so $u_y = 0$. The displacement vector of a propagating Rayleigh wave in the x direction are,

$$\begin{aligned} u_x(x,z,t) &= ku_0(e^{\kappa_\ell z} - \frac{2\kappa_\ell\kappa_{\mathrm{t}}}{k^2+\kappa_{\mathrm{t}}^2}e^{\kappa_{\mathrm{t}} z})e^{i(kx-\omega t)}\,, \\ u_y(x,z,t) &= 0\,, \\ u_z(x,z,t) &= -i\kappa_\ell u_0(e^{\kappa_\ell z} - \frac{2k^2}{k^2+\kappa_{\mathrm{t}}^2}e^{\kappa_{\mathrm{t}} z})e^{i(kx-\omega t)}\,. \end{aligned} \tag{3.8}$$

We also include a constant coefficient u_0, which does not exactly correspond to the

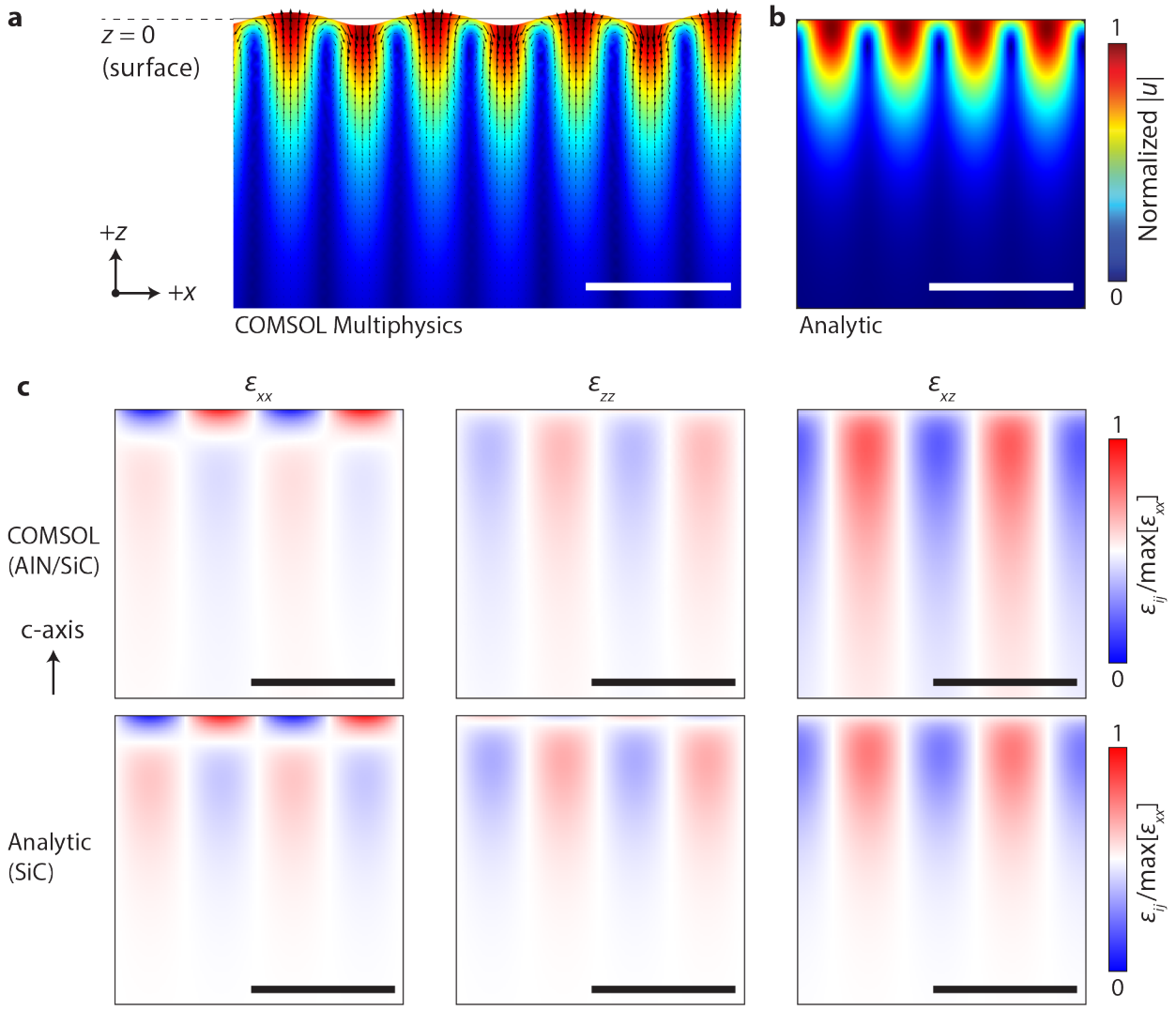

Figure 3.2: **Propagating Rayleigh wave equations compared to finite element analysis. a**. Finite element simulation (2D cross-section) showing the absolute crystal displacements ($|u| = \sqrt{u_x^2 + u_z^2}$) a propagating SAW in the $+\hat{x}$ as launched by an IDT, which is computed in frequency domain at 556 MHz and IDT electrode spacing with periodicity λ=12 μm. The arrows and deformation (not to scale) help show the displacement profile. **b**. Absolute displacement ($|u|$) from Eq. (Eq. 3.8). **c**. Finite element simulation (top row) and analytic solution from (Eq. 3.8) (bottom row) for uniaxial strains $\varepsilon_{xx}, \varepsilon_{zz}$ and shear ε_{xz}. All scalebars are one acoustic wavelength ($\lambda = 12$ μm). The coordinate system in (**a**) are consistent across all plots and the center of each square $2\lambda \times 2\lambda$ plot in (**b,c**) corresponds to $x = 0$.

oscillation amplitude because u_i in this form is not normalized. In order to assess the applicability of these solutions to a piezoelectric SAW on an AlN/SiC heterolayered substrate, the spatial distributions are compared to finite element simulations of a SAW in a realistic

Table 3.2: **Elastic constants and acoustic velocities of AlN and 4H-SiC.** Densities (ρ) are in units of kg m^{-3}, elastic constants of $\mathbf{c}^{\mathrm{E}}$ written as c_{ij} in Voigt notation are in units of GPa, and acoustic velocities are in units of m s^{-1}. The elastic constants are from Ref. [63] and the acoustic velocities are extracted from Ref. [59].

	ρ	c_{11}	c_{12}	c_{13}	c_{33}	c_{44}	v_{t1}	v_{t2}	v_{ℓ}	v_{R}
AlN	3.23	410	149	99	389	125	6095	6465	11267	5790
4H-SiC	3.211	501	111	52	553	163	7276	7882	12566	6832

substrate, shown in Fig. 3.2. The simulation is performed using the commercial software package COMSOL Multiphysics with solid mechanics and electrostatics in the frequency domain, coupled through the piezoelectric constants in Table 3.1. The AlN is 500 nm thick on the top surface of the 4H-SiC substrates, aluminum electrodes 100 nm thick are on top of the AlN surface, and more than 50 μm of air is above the electrodes to give space for electric field distributions. Additionally, there is a symmetry plane at $x = 0$ to reduce the model's complexity and a perfectly matched layer on the right boundary to provide a low-reflecting acoustic boundary condition. The metal electrodes are organized into a periodic array (interdigitated transducer) with a wavelength of 12 μm, which is found to have a peak admittance at 556 MHz (Fig. 3.2a) that closely matches devices in actual experiments discussed later in this chapter. The right-traveling SAW mode is then inspected and normalized by their respective amplitudes. This simulation is then visually contrasted to results from Eq. 3.8.

The AlN has a slower wavespeed than SiC and the film thickness is less than 10% of the acoustic wavelength we are interested in, so the Rayleigh wave will be non-leaky and penetrate into the SiC crystal. We can expect that the effective Rayleigh wave velocity in this heterolayer should be slower yet still similar to bare 4H-SiC. The results of our analytic solutions plotted in Fig. 3.2b,c only rely on the acoustic velocities from Table 3.2 and knowledge of the wave vector. Nearly full quantitative agreement is obtained for the mechanical mode summarized with absolute displacement $|u|$, uniaxial strain ε_{xx}, ε_{zz}, and the shear component ε_{xz} (Fig. 3.2b,c). The only striking differences are the decay coefficients

from COMSOL simulations appear to be smaller (slower fall off of the displacement into the bulk) and the near-surface sign switch in ε_{zz} is more pronounced in the analytic result. In summary, we found exact expressions for Rayleigh waves in an isotropic substrate and observed that they a good model for the mechanical nature of a SAW in AlN on 4H-SiC.

3.2 Surface Acoustic Wave Resonators

3.2.1 The Interdigitated Transducer

Inside a resonator we will need a method for coupling to the waves with a.c. electric fields. The simplest device for coupling electrical signals to SAW modes is an array of interleaved electrodes. This array, called an *interdigtated transducer* (IDT), uses thin metal on the piezoelectric crystal's surface with some periodicity λ and pitch[1] p. We will be using $p = \lambda/2$ (i.e. an even duty cycle of 1:2, or equal metal to gap widths) in this discussion to focus our investigations.

An IDT launches and receives SAWs when the acoustic dispersion is matched to the radio frequency (RF) signal causing a resonance at some center frequency ω_c. We can see that an IDT with periodicity λ must couple to waves with velocity v_f at $\omega_c = 2\pi v_\mathrm{f}/\lambda$ due to the linear dispersion relation and approximately constant velocity. The IDT functions near some frequency around ω_c given by,

$$\Theta = \pi N_\mathrm{p} \frac{\omega - \omega_c}{\omega_c}\,, \tag{3.9}$$

where N_p is the number of finger pairs in the IDT (Fig. 3.3a). This structure will launch and receive SAWs equally from both the left and right directions symmetrically. An equivalent circuit model of an IDT is depicted in Fig. 3.3b where the total admittance Y of this 1-port circuit is given by the acoustic conductance (real admittance) $G_a(\omega)$, acoustic

1. The pitch of grating strips and IDT fingers can also be varied for subtle effects on the reflectivity and capacitance, respectively.

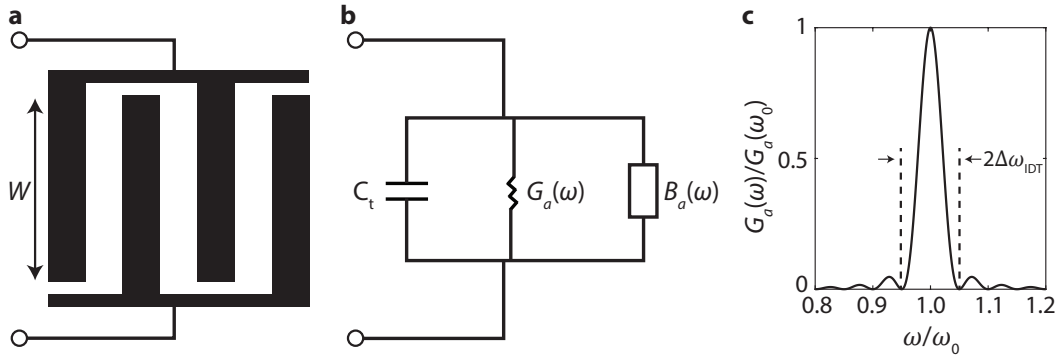

Figure 3.3: **Interdigitated transducer. a**. An IDT with N_p finger pairs ($N_\mathrm{p} = 2$ shown in cartoon) probed by RF signals externally. **b**. Equivalent circuit for the IDT with capacitance C_t from the geometry, acoustic conductance $G_a(\omega)$, and acoustic susceptance $B_a(\omega)$. **c**. Graph of the normalized real admittance of an IDT with $N_\mathrm{p} = 20$.

susceptance (imaginary admittance) $B_a(\omega)$, and geometric capacitance of the transducer C_t. The total admittance as a function of frequency is therefore $Y(\omega) = i\omega C_\mathrm{t} + G_a(\omega) + iB_a(\omega)$, and it is known that $B_a(\omega)$ can be related to the Hilbert transform of $G_a(\omega)$ [60]. Our geometric capacitance from the IDT structure with an aperature (electrode overlap W) that is typically much longer than λ, finger pairs N_p (total number of electrodes divided by two), and effective permittivity ϵ_∞ can be written as as,

$$C_\mathrm{t} \approx \epsilon_\infty W N_\mathrm{p}\,, \tag{3.10}$$

where ϵ_∞ can be found from *Ingebrigtsen's approximation* for a piezoelectric Rayleigh wave $\epsilon_\infty \approx \epsilon_0 + \sqrt{\epsilon_{11}\epsilon_{33} - \epsilon_{13}^2}$, which gives $\epsilon_\infty \approx 11\epsilon_0$ for 4H-SiC using textbook values [58]. Note that for double finger IDTs there is an extra factor of $\sqrt{2}$ in C_t. We can expect that the acoustic admittances G_a and B_a will scale linearly with the piezoelectric constant $\Delta v_\mathrm{f}/v_\mathrm{f}$. These are described by the expressions [60],

$$\begin{aligned} G_a(\omega) &\approx G_a(\omega_\mathrm{c})\left(\frac{\sin(\Theta)}{\Theta}\right)^2, \\ B_a(\omega) &\approx G_a(\omega_\mathrm{c})\frac{\sin(2\Theta) - 2\Theta}{2\Theta^2}\,, \end{aligned} \tag{3.11}$$

The value of G_a on resonance, is given by the real, positive number $G_a(\omega_c)$. The function $G_a(\omega)$ has nodes at $\omega = \omega_c \pm \omega_c/N_p$, so the IDT has a bandwidth of approximately $\Delta\omega_{IDT} = \omega_c/N_p$ (Fig. 3.3c). The coefficient on resonance can be written,

$$G_a(\omega_c) = \alpha C_t N_p \omega_c \frac{\Delta v_f}{v_f}\,, \tag{3.12}$$

where $\alpha = 2.871$ is a geometric factor for single finger electrodes in an IDT with an even duty cycle of 1:2 (equal metal to gap widths). Highly piezoelectric crystals enables substantially larger real admittance without the need for excessively long transducers arrays, which allows for wider IDT bandwidths. Weak piezoelectric materials (small $\Delta v_f/v_f$) require many finger pairs, so the IDT typically only works within a few percent of the center frequency. Internal reflections and mass loading, not considered here, lead to a skewing of the IDT admittance Sinc-squared behavior towards lower frequencies.

3.2.2 Acoustic Mirrors

The next ingredient we want to use for a SAW resonator is a mirror to reflect incoming acoustic waves. A common tool for building a SAW mirror are distributed Bragg reflectors in the form of gratings (Fig. 3.4a). Bragg gratings can be made out of thin metal strips or grooves. These features will change the acoustic wavespeed and reflect a small portion of the wave's amplitude. By analogy to optics, this is similar to a change in refraction index encountered by electromagnetic waves in optics. Although for thin strips or grooves with a metal height or depth $h \ll \lambda$ the reflection mechanism is either electrical from the piezoelectric effect or mechanical. We can express the total complex reflection coefficient per strip as $r_s = r_e + r_m$ for electrical and mechanical contributions r_e and r_m, respectively, and the reflected phase is always $\pm\pi/2$. The electrical part is $r_e \approx \pm\frac{\Delta v_f}{v_f} i$ depending on the material and whether the grating is shorted or open strips, and the mechanical part is $r_e \propto \pm\frac{h}{\lambda} i$. For grooves, the reflection coefficient is only mechanical, taking a value $r_s \sim +0.5\frac{h}{\lambda} i$.

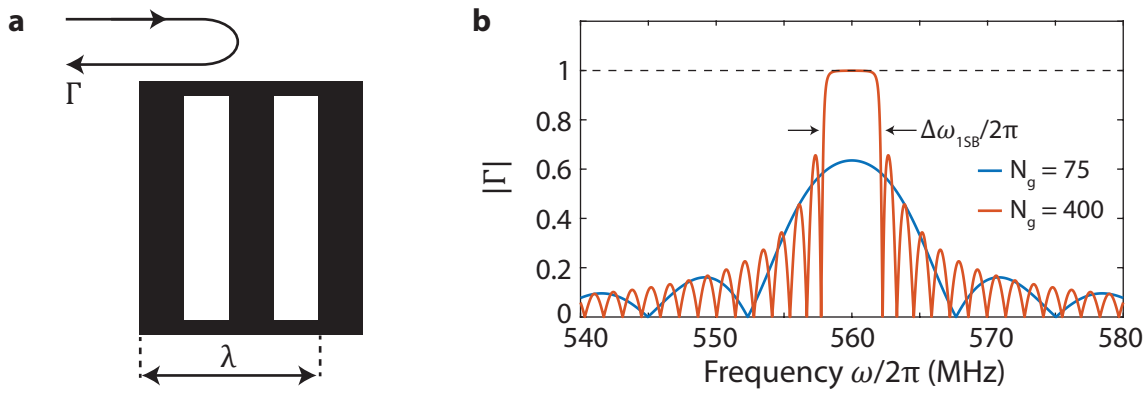

Figure 3.4: **Bragg grating frequency response. a**. Illustration of a distributed Bragg grating with pitch $p = \lambda/2$ that reflects a wave incoming from the left with a total reflection coefficient Γ. **b**. Graph of the reflection magnitude ($|\Gamma|$) as a function of frequency around the center frequency $f_0 = 560$ MHz for two different lengths of gratings. The reflection per strip ($|r_s|$) is $+0.01i$ and wavelength (λ) in the model is 12 μm.

A constructive interference condition for the reflected waves is set up when the total path length is an integer multiple of λ. Therefore the strips or grooves with a pitch $p = \lambda/2$ are placed at locations $x = n\lambda/2$ for integers n (Fig. 3.4). In the limit of a few reflector strips the grating will give some finite transmission and reflection. When many strips are placed, the total reflection magnitude by the Bragg grating will converge to unity over some frequency range that can be understood from the *coupling of modes* equations [60]. It can be shown that,

$$\Gamma = \left(\frac{r_s}{p}\right) \frac{\sin\left(sL_g\right)}{s\cos\left(sL_g\right) + i\delta\cos\left(sL_g\right)}, \tag{3.13}$$

where the grating length $L_g = pN_g$ for N_g grating strips, the detuning $\delta = (\omega - \omega_0)/v_f$, and the parameter s is defined as,

$$s^2 = \left(\frac{\omega - \omega_0}{v_f}\right)^2 - \left(\frac{r_s}{p}\right)^2. \tag{3.14}$$

Using a few similar parameters from SAW devices, Fig. 3.4b shows examples of the reflection magnitude as a function of frequency for short ($N_g = 75$) and long ($N_g = 400$) gratings with the same reflectivity per strip of $|r_s| = 1\%$. The longer grating clearly ex-

hibits a higher reflection magnitude close to $|\Gamma| \approx 1$ near ω_0. Additionally, there is a well defined bandwidth visible in the longer grating called the *first stop band*, which has a width $\Delta\omega_{1\mathrm{SB}}/2\pi = 2f_0|r_\mathrm{s}|/\pi$. In general, materials and gratings with a larger reflectivity per strip are beneficial for creating large stop band widths so long as other loss mechanisms are not introduced, such as bulk mode coupling from thick grating strips (or deep grooves) or surface propagation loss.

3.2.3 Fabry-Pérot SAW Cavities

Mechanical resonators including SAW cavities may store energy for large periods of time. For this reason they are used as narrow band filters in common technologies and telecommunications. Energy storage, in the form of classical waves bouncing between two mirrors, also means that in the steady state more power can be built up in the resonator therefore leading to greater field strengths for interactions with other systems. A SAW resonator can be constructed out of two Bragg gratings separated by some distance d. At least one transducer is needed for readout, either with two IDTs outside the cavity for transmission or by a single IDT inside the cavity for reflection measurements. In weak piezoelectric materials, smaller impedances can be obtained using one IDT inside the cavity as depicted in Fig. 3.5a. The SAW resonator can be understood using an equivalent circuit model called a *Butterworth-van Dyke* (BVD) circuit (Fig. 3.5b). The acoustic resonator is captured by a series RLC circuit with resistance R_m, capacitance C_m, and inductance L_m, while the parallel capacitance C_t is from the IDT geometry. The total admittance $(1/Z)$ of the BVD circuit is,

$$Y_\mathrm{BVD} = i\omega C_\mathrm{t} + (R_\mathrm{m} + i\omega L_\mathrm{m} + 1/(i\omega C_\mathrm{m}))^{-1}. \tag{3.15}$$

This circuit has an impedance minimum at the series resonance frequency $\omega_0 = 1/\sqrt{L_\mathrm{m}C_\mathrm{m}}$ and impedance maximum at the anti-resonance $\omega_a = \omega_0\sqrt{1 + \frac{C_\mathrm{m}}{C_\mathrm{t}}}$. The circuit elements can be written in terms of the SAW device parameters as [60],

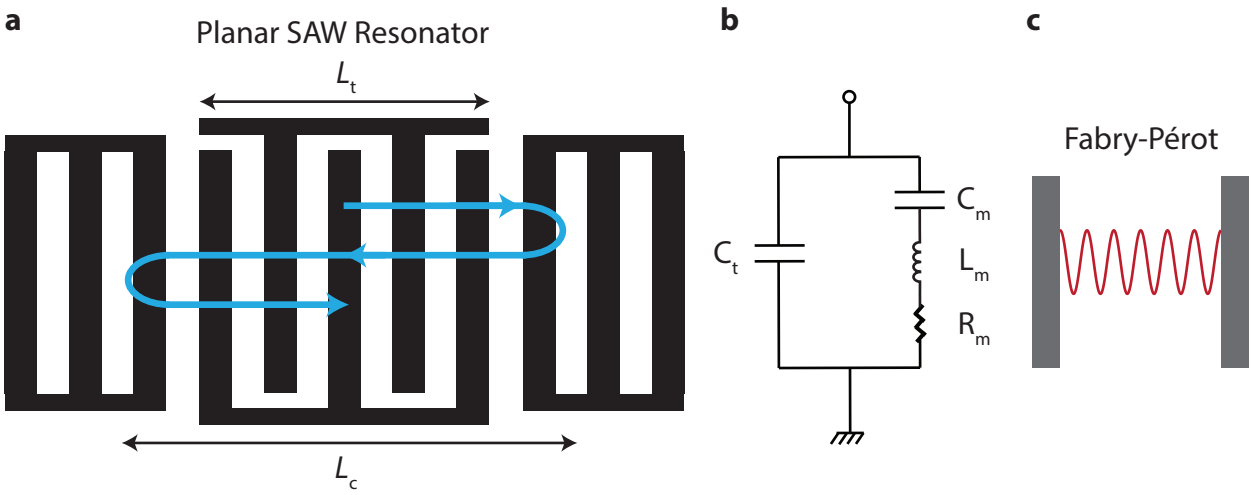

Figure 3.5: **Fabry-Pérot style SAW resonators. a**. Surface acoustic wave resonator with a transducer length L_t and total cavity length L_c. The blue line represents a wave bouncing between the mirrors. **b**. The Butterworth-van Dyke circuit. **c**. Planar optical resonator (analogy) that confines a mode shown in red, fitting many wavelengths inside the cavity.

$$\begin{aligned} R_m &\approx \frac{1-|\Gamma|}{2G_a(\omega_0)}\,, \\ L_m &\approx \frac{L_\mathrm{c}}{4v_\mathrm{f}G_a(\omega_0)}\,, \\ C_m &\approx 1.8C_\mathrm{t}\frac{L_\mathrm{t}}{L_\mathrm{c}}\frac{\Delta v_\mathrm{f}}{v_\mathrm{f}}\,, \end{aligned} \tag{3.16}$$

where $|\Gamma|$ is the reflection coefficient of each Bragg grating, $G_a(\omega_0)$ is the conductance of the IDT on resonance, $L_\mathrm{t} \approx N_\mathrm{p}\lambda$ is the length of IDT, and L_c is the total effective length of the cavity. We can see that $L_\mathrm{c} = d + 2L_\mathrm{p}$, where L_p is the effective penetration depth of the wave into each mirror grating and can be understood as $L_\mathrm{p} = \lambda/(4|r_\mathrm{s}|)$ for the $1/e$ decay into a grating of equally spaced strips. The effective piezoelectric coupling constant of any BVD circuit in the limit $C_\mathrm{m} \ll C_\mathrm{t}$ is $k^2_\mathrm{eff} = (\omega_a - \omega_0)/\omega_0 \approx (C_\mathrm{m}/C_\mathrm{t})/2$. Inserting the expressions for the capacitances, we can see that for our SAW circuit model the effective piezoelectric constant is,

$$k_{\text{eff}}^2 \approx \frac{L_{\text{t}} \Delta v_{\text{f}}}{L_{\text{c}} v_{\text{f}}} \,. \tag{3.17}$$

The potential coupling is maximized when the mirrors are placed next to the edge of the IDT, and the *internal quality factor* of this circuit is defined by the mechanical resonance due to mirror leakage $Q_{\text{r}} = \omega_0 L_{\text{m}} / R_{\text{m}}$. In reality, there will be other sources of loss in the resonator, and these can be modeled with resistors in parallel to R_{m}. Considering losses [64, 65] such as diffraction out of the mirror sides ($Q_{\text{d}} \propto W^2$), bulk mode scattering from grating strips (Q_{b}), material loss and surface damping (Q_{m}), the total internal quality factor can be written as,

$$Q_{\text{i}}^{-1} = Q_{\text{r}}^{-1} + Q_{\text{d}}^{-1} + Q_{\text{b}}^{-1} + Q_{\text{m}}^{-1} + ...\text{etc.} \tag{3.18}$$

Furthermore, the coupling rate of RF photons must be considered (see Section 3.4), which is commonly called the *external quality factor* (Q_{e}). The total (or *loaded*) quality factor is found by adding its reciprocol in the same way as before, $Q^{-1} = Q_{\text{i}}^{-1} + Q_{\text{e}}^{-1}$. The Q is relevant to measurements because for any resonator or Fabry-Pérot (Fig. 3.5c), the cavity spectral linewidth (FWHM = $\Delta\omega_0$) is related by,

$$Q \equiv \frac{\omega_0}{\Delta\omega_0} \,, \tag{3.19}$$

since in general the cavity Q-factor is the ratio between the total energy stored and the energy lost per round trip in the wave. One can see that the observed line width will take on a value determined predominantly by the smallest quality factor (biggest loss mechanism) in the system. This relation for the dimensionless value Q also measures the exponential ring-down time ($\tau = 2/\Delta\omega_0$) before a photon (or phonon) escapes the cavity, then $\tau = 2Q/\omega_0$.

Lastly, there are some important phenomenon not captured by the BVD circuit, like the aspect of using long cavities filled with many wavelengths and frequency errors caused by wavespeed differences over the grating, IDT, and free surfaces [66, 64]. An optimal SAW

cavity is formed out of having a resonance located in the center of both the IDT and Bragg grating frequency responses, however, all of these can actually exhibit slightly different center frequencies. From intuition, we can be sure that a resonance frequency near the Bragg stop bands will result in a low Q due to low grating reflectivity, and resonances detuned from the IDT center frequency will result in lower coupling (smaller C_{m}). It is useful to have a method for making small design modifications to shift ω_0 without needing to make small ($< 1\%$) changes to p and strip periodicities in the grating and IDT. One crude method is simply modifying the whole cavity length by some amount smaller than λ. We can understand this by going back to a typical optical cavity (Fig. 3.5c, the reflected phase $\Delta\phi = \pi$ from the mirrors is depicted), where the fundamental cavity frequency $\omega_0 = 2\pi f_0 = 2\pi v_{\mathrm{f}}/\lambda$ can be from fitting one half-wavelength into the cavity. For longer cavities, it is possible to fit many wavelengths and obtain higher-order axial modes at frequencies $n\omega_0$. The frequency difference between each mode is the *free spectral range* defined as,

$$\Delta\omega_{\mathrm{FSR}} = \pi v/L_{\mathrm{c}}\,. \tag{3.20}$$

This expresses the frequency difference between the next cavity mode that contains one more half-wavelength. When the device has a length d' added to the total cavity so $L_{\mathrm{c}} \to L_{\mathrm{c}} + d'$ where $d' < \lambda/2$, both ω_0 and $\Delta\omega_{\mathrm{FSR}}$ get modified (Fig. 3.6a). The new free spectral range can be found from the formula above, and we can find the new cavity frequency from $\omega_0' = v/\lambda'$. The adjusted wavelength supported by the cavity is $\lambda' = \lambda(1 + d'/L_{\mathrm{c}})$. In the limit $d' < \lambda/2 \ll L_{\mathrm{c}}$, otherwise it wraps around ($\omega_0 = \omega_0'$ if we add or subtract one half-wavelength), the new frequencies can be written as,

$$\begin{aligned} \omega_0' &= \frac{v_{\mathrm{f}}}{\lambda}(1 - \frac{d'}{\lambda})\,, \\ \Delta\omega_{\mathrm{FSR}}' &= \frac{v_{\mathrm{f}}}{2L_{\mathrm{c}}}(1 - \frac{d'}{\lambda})\,. \end{aligned} \tag{3.21}$$

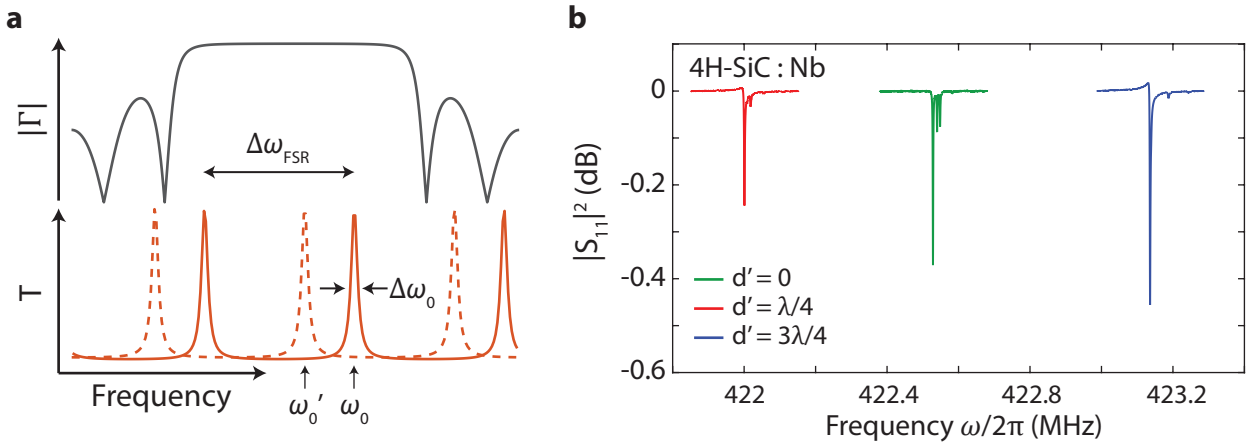

Figure 3.6: **Cavity length control of the SAW resonator frequency.** **a**. Reflection coefficient magnitude $|\Gamma|$ of the Bragg gratings (top) and transmission of resonators for two different cavities lengths: L_c with a frequency ω_0, and length $L_c + d'$ with a frequency ω_0' (bottom). **b**. Measurements of SAW resonators on 4H-SiC made from superconducting niobium ($N_p = 50$, $\lambda = 16$ μm, double finger, $W = 150\lambda$, $N_g = 1100$, 100 nm thick metal), and magnitude offsets are added to remove stray attenuation. The piezoelectricity of bare SiC is too small to see an IDT response, so it is hard to know the Bragg stop bands or grating strip reflectivity from RF measurements. All resonator experiments were performed at 1.8 K in a Quantum Design PPMS.

This is demonstrated on 4H-SiC from Cree Inc. with niobium (Nb) resonators patterned by optical lithography and lift-off. These devices showed SAW cavity resonances when the Nb went superconducting because at higher temperatures the normal metal was too resistive. Since the distance between both gratings is almost the same as the IDT length, only one resonance was observed and supported within the first stop band (Fig. 3.6). The extra peaks observed are likely from higher order transverse modes in the resonators. The control device (cavity length L_c) is in the center, while SAW cavities with total lengths $L_c + \lambda/4$ and $L_c + 3\lambda/4$ resonate at a lower and higher frequency, respectively. This is explained by the $+3\lambda/4$ device being equivalent to the scenario of $d' = -\lambda/4$. The technique for changing the cavity frequency, to move ω_0 away from either stop band, is employed in many of the later SAW devices through iterative rounds of fabrication. Niobium worked well on SiC for producing ultra-high Q resonators ($Q_i > 10^5$), however, the insertion loss and piezoelectric coupling are very poor, and the metal usually went normal above -20 dBm RF power, so

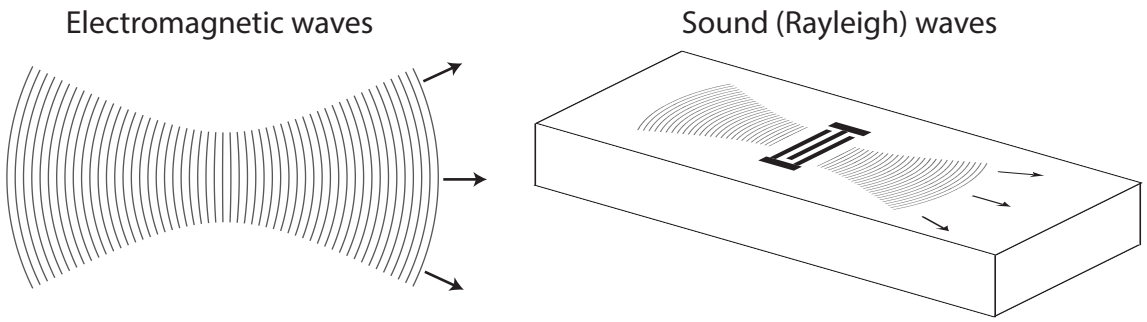

Figure 3.7: **Gaussian optics and acoustics.** Waves of light in an isotorpic medium (left) and surface acoustic waves on a piezoelectric crystal with isotropic in-plane velocities (right).

AlN is employed for enhanced piezoelectric coupling in experiments.

3.3 Gaussian Surface Acoustic Waves

When designing a Fabry-Pérot cavity to have a maximal wave amplitude interacting with a spin or atom, naturally it is helpful to make the cavity as small as possible in order to enhance the mode's energy density. Although, one of the issues with making small planar SAW resonators highly confined in the transverse direction is diffraction loss. If we want to confine plane waves and increase the energy density into a very small region, one might be inclined to try using spherical waves in the hopes of focusing the energy at the center. However, as we might know from the field of Gaussian optics this is difficult and in theory creating a perfectly concentric cavity requires careful control of all far-field plane wave angles ($-\pi$ to π). Gaussian optics on the other hand offers simple, analytical solutions for transverse modes, resonator profiles, diffraction, and focusing of electromagnetic waves (Fig. 3.7a) in materials or vacuum. Since Rayleigh wave velocities on piezoelectric AlN (wurtzite) and 4H-SiC are isotropic due to the symmetries of their crystal class 6mm [67], we can consider borrowing tools from Gaussian optics to use them as in-plane profiles for acoustic waves (Fig. 3.7b).

3.3.1 Gaussian Optics

We begin a review of Gaussian optics with the wave equation for the electric field (E) in an isotropic medium or dielectric,

$$(\nabla^2 - \frac{1}{c^2}\frac{\partial^2}{\partial t^2})E = 0\,. \tag{3.22}$$

Knowing that we are interested in a solution with $E = f(x,y,z)e^{\pm i\omega t}$ for some scalar function f, and substituting in $c = \omega/k$ using the speed of light in our medium, we find the *Helmholtz equation* for the electric field,

$$(\nabla^2 + k^2)E = 0\,. \tag{3.23}$$

Next, it is convenient to reduce the equation to only its spatial distribution. The formal definition of $E(t)$ for linearly polarized light is $\frac{1}{2}(\tilde{E}e^{i(\omega t+\varphi)} + \tilde{E}^\dagger e^{-i(\omega t+\varphi)})$, where the spatial dependence $\tilde{E}$ is a complex function called a *phasor* [68]. The real actual electric field in the system is simply the real part of this phasor, i.e. $E(t) = \mathrm{Re}[\tilde{E}e^{i(\omega t+\varphi)}]$. Using Euler's formula we see that the cosine dependence is recovered from the real part in $E(t) = |\tilde{E}|\cos(\omega t + \varphi)$. From here on, we will be working with $\tilde{E} = E_0\tilde{u}e^{-i(kz-\omega t)}$, where E_0 is the electric field amplitude, the function $\tilde{u} = \tilde{u}(x,y,z)$ contains the spatial dependence (mode profile). The cosinusoidal dependence on z and t (up to a phase factor) is shown for a right moving plane wave for completeness.

We will work with a beam propagating along the $\hat{z}$ direction, which is called the optical axis, with a wave number $k = 2\pi/\lambda$. Substituting in the expression for $\tilde{E}$ in terms of $\tilde{u}$ into (3.23) and factoring out the cosinusoidal dependences after differentiation yields,

$$\frac{\partial^2\tilde{u}}{\partial x^2} + \frac{\partial^2\tilde{u}}{\partial y^2} + \frac{\partial^2\tilde{u}}{\partial z^2} - 2ik\frac{\partial\tilde{u}}{\partial z} = 0\,. \tag{3.24}$$

The solution becomes much easier to analytically solve for when the profile varies much

slower than the wavelength. From here we can use the **paraxial approximation**,

$$\left|\frac{\partial^2 \tilde{u}}{\partial z^2}\right| \ll \left|\frac{\partial^2 \tilde{u}}{\partial x^2}\right|, \left|\frac{\partial^2 \tilde{u}}{\partial y^2}\right|, \left|2ik\frac{\partial \tilde{u}}{\partial z}\right| \tag{3.25}$$

which is when the mode profile $\tilde{u}$ varies slowly as a function of z compared to the transverse dimensions and λ. This results in the *paraxial equation*,

$$\frac{\partial^2 \tilde{u}}{\partial x^2} + \frac{\partial^2 \tilde{u}}{\partial y^2} - 2ik\frac{\partial \tilde{u}}{\partial z} = 0\,. \tag{3.26}$$

It can be shown from 3.26 that the paraxial approximation is valid when the divergence angle of the beam is sufficiently small such that $\Theta/4 \ll 1$, so Θ must be less than approximately $30°$. Let us suppose that we are working with a modes in Cartesian coordinate system that are separable for the two transverse dimensions x, y. We can then decompose $\tilde{u}$ into separable functions,

$$\tilde{u}_{n,m}(x, y, z) = \tilde{u}_n(x, z) \times \tilde{u}_m(y, z)\,, \tag{3.27}$$

for the Hermite-gaussian mode in each dimension. The form of $\tilde{u}_n$ for one transverse dimension is [68],

$$\tilde{u}_n(x, z) = \left(\frac{2}{\pi}\right)^{1/4} \left(\frac{\exp[i(2n+1)\Psi(z)]}{2^n\, n!\, w(z)}\right)^{1/2} \exp[(\frac{-y^2}{w^2(z)} - \frac{iky^2}{2R(z)})]\,, \tag{3.28}$$

where w is the beam width as a function of the optical axis coordinate z, R is the radius of curvature, and Ψ is the Guoy phase for an isophase line at z. These physical parameters are given by,

$$
\begin{aligned}
w(z) &= w_0\sqrt{1+\left(\frac{z}{z_{\mathrm{R}}}\right)^2}\,, \\
R(z) &= z+\frac{z_{\mathrm{R}}^2}{z}\,, \\
\Psi(z) &= \tan^{-1}\!\left(\frac{z}{z_{\mathrm{R}}}\right).
\end{aligned}
\tag{3.29}
$$

The beam waist at $z = 0$ is characterized by the constant w_0, so we can see that the $w_0 = 4\lambda/\pi$ is the smallest beam waist we can use before serious optical aberrations begin to occur. Furthermore, the beam is approximately collimated over a distance $z_R = \frac{\pi w_0^2}{\lambda}$, called the **Rayleigh range**. The field strength of a Gaussian optical mode near this limit is shown in Fig. 3.8a. From the transverse Gaussian distribution in (3.28), the Gaussian focal spot can be characterized by a standard deviation $\sigma = w/\sqrt{2}$ - this will be referred to for Gaussian acoustic designs later. Therefore, the full width at half maximum (FWHM) of the Gaussian profile is $2\sqrt{2\ln(2)}\sigma \approx 2.355\sigma$.

Power in the optical beam is defined as $P(z) = \iint \left|\tilde{E}\right|^2 dA$. One can show that the power at any distance z is conserved along the optical axis. The energy density and mode profile are $\propto |\tilde{u}|^2$ (saggital cross-section of $\tilde{u}^2$ shown in Fig. 3.8b), which are Gaussian distributed about the focus and therefore are increased by making the beam waist w_0 smaller. There are subtle effects caused by the Guoy phase $\Psi(z)$, which corresponds to an increase in the phase velocity near the beam waist (Fig. 3.8c). The Guoy effect adds a total phase of π as a wave passes from $z = -\infty$ to $+\infty$, although most of this phase accumulation ($\pi/2$) happens near the beam waist center as illustrated in Fig. 3.8d.

3.3.2 Gaussian Acoustics and Device Design

When discussing the plane wave solutions for Raleigh wave modes earlier, we had expressions for the general displacements $\mathbf{u} = \mathbf{u}_{\mathrm{t}} + \mathbf{u}_{\ell}$, where $\mathbf{u}_{\mathrm{R}} e^{i(kx-\omega t)}$ is the total displacement vector for a SAW propagating towards the $+\hat{x}$ direction. Planar surface acoustic

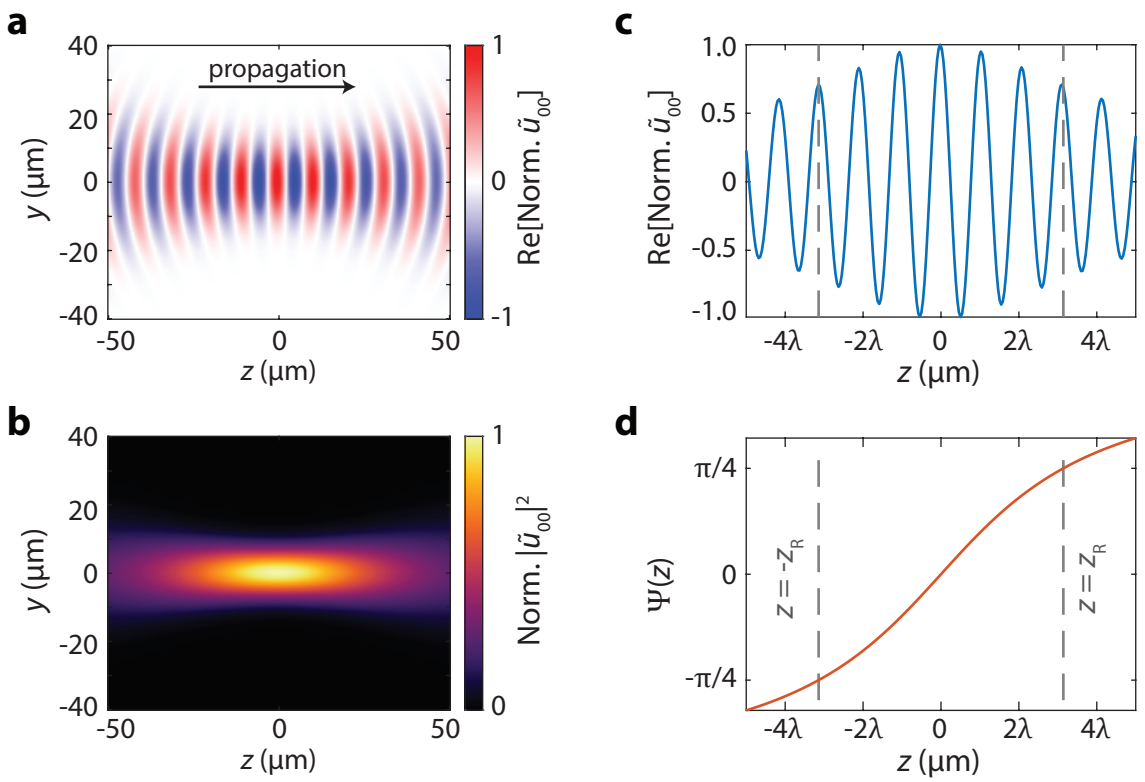

Figure 3.8: **Simulated lowest order Gaussian mode profile. a**. Real part of the fundamental Hermite-Gaussian mode profile with parameters $w_0 = \lambda$, $\lambda = 10$ μm, normalized to unity amplitude. **b**. Square of the profile, which shows the energy density. **c**. Line cut of the mode in (**a**) at $y = 0$. **d**. Guoy phase as a function of the optical axis coordinate. The dashed gray lines mark the Rayleigh range $\pm z_{\mathrm{R}}$.

waves on a semi-infinite material satisfied the equations of motion for longitudinal ($\mathbf{u}_\ell$) and transverse ($\mathbf{u}_{\mathrm{t}}$) components in Eq. (3.3) with a total wave vector $k = \omega/v_{\mathrm{R}}$, such that $u_i = f(x,y)g(z)e^{i(kx-\omega t)}$ for separable functions f and g. Since the general displacement vector $\mathbf{u}_{\mathrm{R}}$ is periodic in time, the equations of motion in an isotorpic material (substituting in $k_\ell = \omega/v_\ell$ and $k_{\mathrm{t}} = \omega/v_{\mathrm{t}}$) take a familiar form,

$$\begin{aligned}(\nabla^2 + k_\ell^2)\mathbf{u}_\ell &= 0 \\ (\nabla^2 + k_{\mathrm{t}}^2)\mathbf{u}_{\mathrm{t}} &= 0\,.\end{aligned} \tag{3.30}$$

Particularly in AlN and SiC, these wave equations are the same for a surface plane

wave propagating in the x and y crystal directions, so an *ansatz* could be made that the wave equations above should obey the paraxial approximation and the in-plane modes of Rayleigh waves should follow Hermite-Gaussian solutions. In analogy with Gaussian optics, let us decompose $\mathbf{u}$ into its complex acoustic plane wave profile ($\tilde{\mathbf{u}}_{\mathrm{R}}(z)$), complex spatial envelope ($\tilde{u}_n(x,y)$) and a scalar amplitude (u_0) that we will leave out for now. Note that while the phasor convention may use $+i(kx)$ or $-i(kx)$ does not matter after taking the real part. However, it is important that relative phase accumulation from the Guoy effect be $\propto kx - \Psi(x)$, so we will use the $-i(kx)$ convention for consistency with definitions used in Gaussian optics and Eq. 3.28. The total displacement can be written as,

$$\mathbf{u} = \tilde{u}_{n,m}\, \tilde{\mathbf{u}}_{\mathrm{R}} e^{-i(kx-\omega t)}. \tag{3.31}$$

Similar to before, combining the formalisms from Gaussian optics with Rayleigh waves propagating in the $\hat{x}$ direction we get,

$$\tilde{u}_n(y,x) = \tilde{u}_n(y,x) \times \tilde{u}_0(0,x) \tag{3.32}$$

where the $\tilde{u}_0$ is needed for normalization and completeness. From here, it is straightforward to build a device out of strips (electrodes and/or grooves) matched to the isophase lines predicted by $\tilde{u}_n$. An example of a 1-port Gaussian IDT near the beam waist is shown in Fig. 3.9a. The Guoy effect leads to a small spatial shift in the position of each electrode (Fig. 3.9b), which is submicron near the center but approaches $\pm\lambda/2$ far away. Since the electrodes will be excited with the same voltage along every finger (different from the Gaussian acoustic mode), it does not make sense to apodize the IDT over distances much greater than the focal spot width. The apodization is chosen to be $\pm 2\sigma = \sqrt{2}w_0$ using a 2 μm gap to the remainder of IDT geometry kept structurally intact. The entire Gaussian IDT geometry and any grooves for acoustic mirrors are typically designed for $\pm 3\sigma$, which should capture $\approx 99.73\%$ of the Gaussian mode's transverse profile, is only limited by the available space

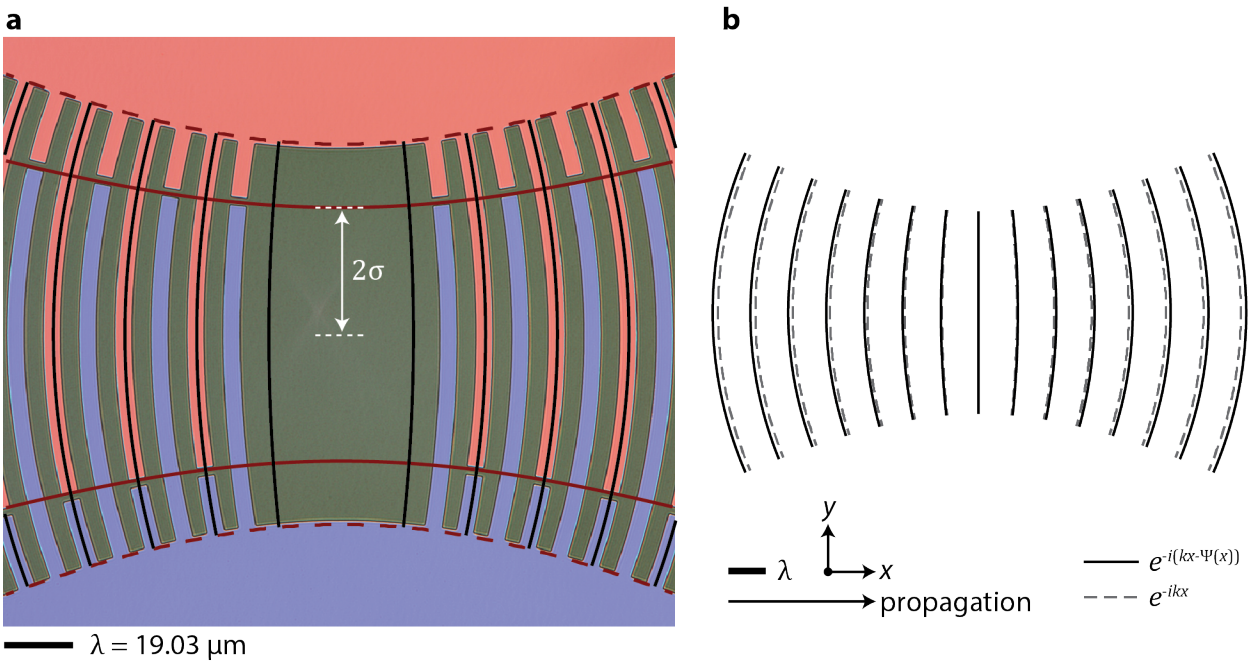

Figure 3.9: **Gaussian SAW interdigitated transducers.** **a**. Optical micrograph of a fabricated Gaussian IDT ($w_0 = 1.25\lambda$) with false-coloring on the aluminum electrodes. Dark red lines mark the 2σ apodization (solid) and 3σ extent (dashed) of the lowest-order Gaussian mode from analytical simulation, and solid black lines are simulated isophase lines of the wave with Guoy phase incorporated for $\tilde{u}_{00}$. **b**. Gaussian wave geometry illustrating isophase lines (3σ shown) with and without Guoy phase taken into account.

on the wafer for device fabrication since small beam waists lead to large opening angles.

3.4 Microwave Characterization

The characterization of resonators is an important process underscoring circuit quantum electrodynamics, radio frequency device engineering, and feedback on fabrication processes. Here we will focus on impedance descriptions for understanding and analyzing RF, microwave, and electromechanical resonators.

3.4.1 *RLC* Resonators

Bare resonators are often measured using a vector network analyzer (VNA) in reference to an external load Z_0 (see setup in Fig. 3.10a) and usually modeled as either a series or

parallel RLC depending on circumstances of the measurement and type of device. In the final fit equations for a 1-port reflection, it will not matter whether the resonator model uses a series or parallel configuration as it only changes the definitions of the internal and external quality factors. Although, either the series or parallel configuration may yield a more accurate physical description depending on whether one wants an impedance minimum or maximum on resonance.

Up to a global phase factor, the complex scattering parameter S_{11} can be written as

$$S_{11} = \frac{Z_r - Z_0}{Z_r + Z_0} = \frac{Y_0 - Y_r}{Y_r + Y_0} \tag{3.33}$$

This gives us the microwave reflection as a function of frequency. For details involving $ABCD$ matrix equations, derivations, and extensions to scattering parameters of multi-port circuits see [69]. The resonator (and external load) admittance Y_r (Y_0) is equal to $1/Z_r$ ($1/Z_0$). The magnitude and phase of (3.33) can be directly compared to device measurements taken with a VNA, and given a model of the resonator impedance we can extract device properties. Taking the series RLC circuit as an example (3.10b), the resonator impedance is $Z_r = R+i\omega L-i/(\omega C)$. Rearranging this equation, the impedance becomes $R+iL(\omega^2-\omega_0^2)/\omega$ where $\omega_0^2 = 1/(LC)$.

Since we are only interested in the microwave reflections near resonance ($\omega \approx \omega_0$), it is convenient to make the approximation

$$Z_r \approx R + 2iL(\omega - \omega_0) \tag{3.34}$$

Plugging this back into (3.33), the reflection as a function of frequency can be written as

$$S_{11} = \frac{1/Q_i - 1/Q_e + 2i(\omega - \omega_0)/\omega_0}{1/Q_i + 1/Q_e + 2i(\omega - \omega_0)/\omega_0} \tag{3.35}$$

where the internal quality factor is $Q_i = \omega_0 L/R = 1/(\omega_0 RC)$ and the external quality factor is $Q_e = \omega_0 L/Z_0$. Note that for a parallel RLC resonator, the relations are inverted:

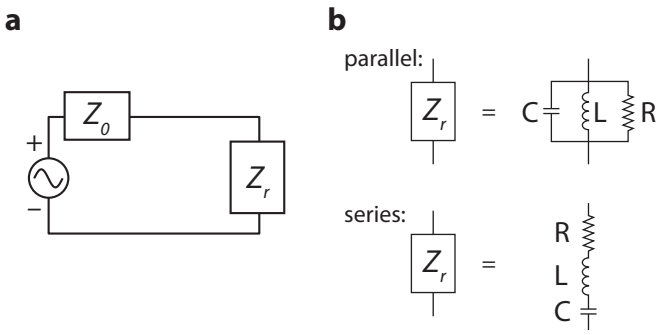

Figure 3.10: **Parallel and series RLC circuits.** **a**. Setup for driving and reflection measurements of a resonator with impedance Z_r and an external load Z_0, which is usually 50 Ω. **b**. RLC circuits for parallel and series resonator impedances.

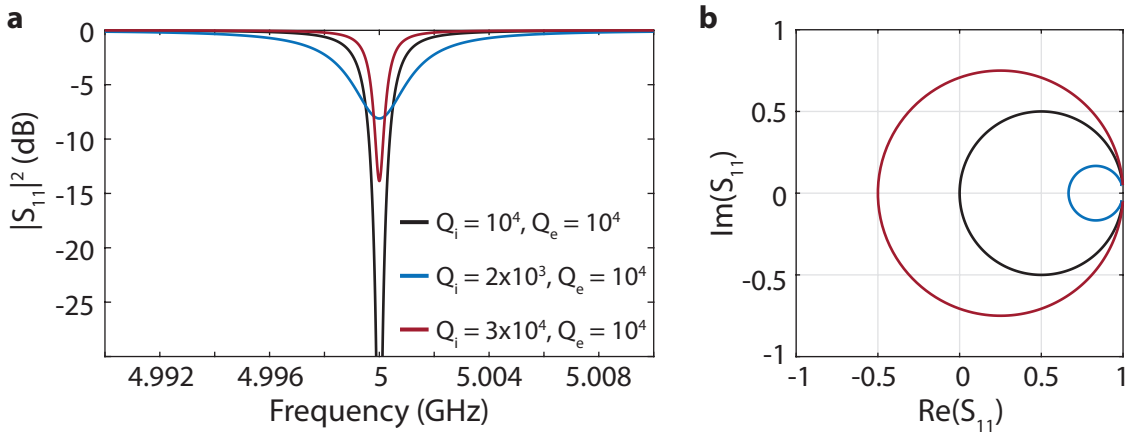

Figure 3.11: **Simulations of S_{11} for RLC resonances.** **a**. Log-scale plot of reflection magnitude as a function of frequency with $\omega_0 = 2\pi \times 5$ GHz using (3.35). **b**. Polar plot of S_{11} in the complex plane.

$Q_i = R/(\omega_0 L)$ and $Q_e = Z_0/(\omega_0 L)$.

The results of (3.35) are plotted in Fig. 3.11 for three different combinations of Q_i and Q_e at a constant resonance frequency. When the magnitude of S_{11} is plotted in log-scale as a function of frequency, the resonance is observed as a Lorentzian-type dip of reflected power (Fig. 3.11a). In the complex plane, S_{11} is a circle pointing towards the origin. *Undercoupled* ($Q_i < Q_e$) and *overcoupled* ($Q_i > Q_e$) resonators have a shallower dip (great reflection on resonance) since their circles in the complex plane undershoot and overshoot the origin, respectively (Fig. 3.11b). The greatest "visibility" of the resonance occurs when the system is *critically coupled* ($Q_i = Q_e$). In order to fit a measurement, it is common to add a

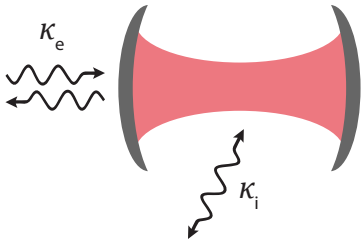

Figure 3.12: **One-port Fabry-Pérot cavity.** The internal loss rate is κ_i and the coupling rate to the left port is κ_e.

magnitude offset to account for external resistive loss or stray reflections and a phase offset. We call this form of S_{11} a "symmetric" fit function because the line shape even or symmetric about the resonance frequency ω_0. It is also useful to subtract out or experimentally remove any electrical delay before fitting.

The expression for a symmetric S_{11} as function of the resonator quality factors is equivalent to the result from input-output theory for a cavity with one semi-transparent mirror, depicted in Fig. 3.12. Hence, the resonator's quality factors and impedance elements, which may be useful for understanding how to modify or improve the device, can be easily mapped onto general input-output theory relations for calculating the average photon number.

Another way of writing (3.35) is to express it in terms of the internal cavity loss rate $\kappa_i = \omega_0/Q_i$ and the input coupling rate $\kappa_e = \omega_0/Q_e$ defined in angular frequency. Substituting in these relations, the microwave reflection coefficient can be written as

$$S_{11} = \frac{\kappa_i - \kappa_e + 2i(\omega - \omega_0)}{\kappa_i + \kappa_e + 2i(\omega - \omega_0)} \tag{3.36}$$

This is a compact form for S_{11} that applies to many resonators including optical, mechanical, and electromagnetic cavities with an isolated mode. The full width half maximum (FWHM) of the cavity resonance in linear-scale is equal to the sum of all loss rates. Therefore, in Fig. 3.12 the measured resonance FWHM is $\kappa = \kappa_i + \kappa_e$, which is equivalent to the statement $Q^{-1} = Q_i^{-1} + Q_e^{-1}$ where Q is the loaded quality factor.

3.4.2 The Asymmetric Resonance

When microwave resonators are measured in a lab, more often than not the resonance $S_{11}(\omega)$ will appear skewed. For example, the magnitude $|S_{11}|$ may show a peak approximately one linewidth off-center from the resonance frequency. These types of features, which we will call "asymmetric" resonances, many times arise from impedance mismatches such as reflections by connectors, coaxial cables, and stray inductance from wire bonds, outside the circuit of interest. One common solution is to add a complex number $\tilde{z}$ to the fit function so that $S_{11}(\omega) \rightarrow (S_{11}(\omega) + \tilde{z})Ae^{iB}$ with real numbers A, B modifying the magnitude and phase, respectively [70, 71]. While this approach usually yields a good fit, it does not give much insight into how stray impedances cause asymmetric line shapes. In this section we will show that a small impedance mismatch from a waveguide or coax cable can yield an elegant fit function, generally applicable to asymmetric resonances.

We begin by modeling the circuit with a length of lossless transmission line before the resonator (3.13). The $ABCD$ matrix for a lossless transmission with characteristic impedance Z_c, length l, and phase constant $\beta = 2\pi/\lambda$ is

$$\begin{pmatrix} A & B \\ C & D \end{pmatrix} = \begin{pmatrix} \cos(\beta l) & iZ_c \sin(\beta l) \\ i\sin(\beta l)/Z_c & \cos(\beta l) \end{pmatrix} \tag{3.37}$$

Then after carrying out the calculation for $S_{11}(\omega)$ using the new $ABCD$ parameters of the entire circuit, we find the general form of the microwave reflection can be written as

$$S_{11} = \frac{(iZ_c(Z_0 - Z_r)\cos(\beta l) + (Z_c^2 - Z_0 Z_r)\sin(\beta l)}{(-iZ_c(Z_0 + Z_r)\cos(\beta l) + (Z_c^2 + Z_0 Z_r)\sin(\beta l)} \tag{3.38}$$

We note that in the limit that $Z_c = Z_0$, this expression converges to (3.33) and results in a symmetric resonance with only an added electrical delay as expected. Next, we approximate the phase term $\psi = \beta l$ as a constant because β is relatively constant within one linewidth of the ω_0 in a high Q cavity, and we are mainly interested in the behavior at $\omega \sim \omega_0$. Since it

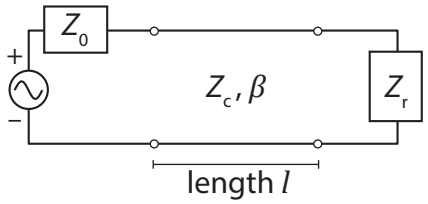

Figure 3.13: **Circuit model for a characteristic impedance (Z_c) mismatch.** A length of lossless transmission line is in series with the resonator impedance Z_r.

is more insightful to separate Z_r from the other constants, we reorganize the expression into

$$S_{11} = \frac{Z_r + \frac{iZ_0Z_c\cos(\psi)+Z_c^2\sin(\psi)}{-iZ_c\cos(\psi)-Z_0\sin(\psi)}}{Z_r + \frac{-iZ_0Z_c\cos(\psi)+Z_c^2\sin(\psi)}{-iZ_c\cos(\psi)+Z_0\sin(\psi)}} \tag{3.39}$$

Next, we model the length of impedance mismatched transmission line as being short ($l \ll \lambda$), so we can approximate ψ by taking its Taylor expansion about zero. To leading order in ψ, the numerator of (3.39) is

$$Z_r - Z_0 + (\frac{-Z_0^2}{Z_c} + Z_c)i\psi + \mathcal{O}(\psi^2) \tag{3.40}$$

So the presence of Z_c essentially adds a complex scalar to Z_0 since Z_c and ψ are constants. We note that in comparison to (3.33), Z_0 is now effectively multiplied by a complex number. Analyzing the denominator in the same manner yields a similar result.

By collecting Z_c and ψ into a new complex number, the external load seen by the resonator becomes $Z_0 \rightarrow Z_0^* e^{i\phi}$. The load magnitude Z_0^* is a real number which is similar to Z_0 if the impedance mismatch Z_c is reasonably small. Unfortunately, it is normally difficult to relate the magnitude Z_0^* and angle ϕ back to the physical impedance mismatch sources because these final parameters will also absorb a multitude of external resistors and reactances.

Using similar conventions to the previous section, the microwave reflection as a function of frequency can be written as

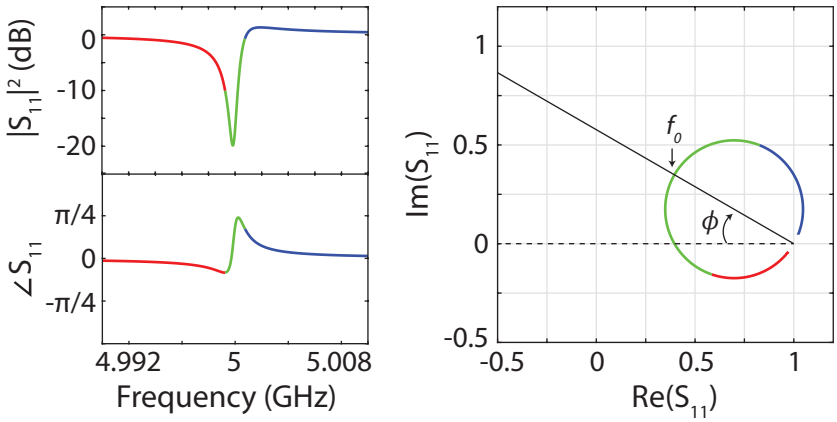

Figure 3.14: ***RLC* resonator with an external impedance mismatch**. The magnitude and phase of S_{11} as a function of linear frequency (left) and a polar representation in the complex plane (right), given by (3.41). The resonance parameters are $\omega_0 = 2\pi \times 5$ GHz, $Q_i = 5 \times 10^3$, $Q_e^* = 10^4$ and $\phi = 30°$. The green trace's frequency boundaries are the effective 3 dB points: $f_0 - \frac{f_0}{2Q}$ and $f_0 + \frac{f_0}{2Q}$, where $Q^{-1} = Q_i^{-1} + Q_e^{*-1}$.

$$S_{11} = \frac{1/Q_i - e^{-i\phi}/Q_e^* + 2i(\omega - \omega_0)/\omega_0}{1/Q_i + e^{-i\phi}/Q_e^* + 2i(\omega - \omega_0)/\omega_0} \tag{3.41}$$

In this form, it is simple to observe that the impedance mismatch modifies the external quality factor of this system. The impedance mismatch angle ϕ rotates the circle in a polar plot, depicted in Fig. 3.14. Note that this effect is similar to results for resonators capacitively and inductively coupled to a feedline [72]. In $|S_{11}(\omega)|^2$ there is a peak on one side of the resonance. Although the magnitude goes above 0 dB in the simulation, in a measurement this would normally be interpreted as less insertion into the resonator (not gain) at a particular frequency compared to the background that is often attenuated.

The fit equation can be further rearranged into the form

$$S_{11} = \frac{\kappa_i - \kappa_e^* e^{-i\phi} + 2i(\omega - \omega_0)}{\kappa_i + \kappa_e^* e^{-i\phi} + 2i(\omega - \omega_0)} A e^{iB} \tag{3.42}$$

where the internal loss rate is $\kappa_i = \omega_0/Q_i$, external loss rate is $\kappa_e = \omega_0/Q_e^*$, and the parameters A and B are real numbers to account for magnitude and phase offsets. In summary, this fit equation is widely applicable to cavities and resonators measured by microwave

reflection. We showed that mismatches of any transmission line or waveguide characteristic impedance outside the resonator ($Z_c \neq Z_0$) can cause a rotation of the S_{11} response, which manifests as an asymmetric line shape.

3.5 Aluminum Nitride/Silicon Carbide Resonators

3.5.1 Device Fabrication

Devices are fabricated directly on single crystal, hexagonal (4H) silicon carbide (SiC) wafers commercially sourced. These wafers are high purity semi-insulating (not vanadium doped) grown on-axis (no miscut) and bought from either Cree Inc. in the United States or Norstel AB in Sweden. Wafers from Cree Inc. were grown in ingots then sliced into individual wafers, containing $\approx 10^{14} - 10^{15}$ cm^{-3} concentration of native divacancies in the bulk material. This is in contrast to wafers from Norstel AB that were grown by high temperature chemical vapor deposition (HTCVD), containing $\approx 10^{12} - 10^{14}$ cm^{-3} concentration of native divacancies depending on the wafer. These concentrations are determined by our experimental measurements of confocal microscopy scans for divacancy photoluminescence and ODMR on samples that were implanted compared to samples that were not implanted for ensembles. A general overview of the essential fabrication layers and methods are listed below.

1. (Optional) Implantation with carbon-12 (^{12}C) ions to create a layer of vacancies. Follow with annealing to form divacancy complexes typically performed at 850 °C for 30 minutes in an argon atmosphere. Organic solvent clean (e.g. sonicate in acetone, sonicate in isopropanol, and then rinse with DI water and N_2 dry) the 4H-SiC substrate beforehand to ensure a residue-free surface.

2. **Clean samples.** Organic solvent clean, nanostrip, buffered hydrofluoric acid (HF) dip in order to remove all dust, residues, and native oxides (abridged RCA clean). This is intended to offer the best AlN growth possible on a crystalline SiC surface.

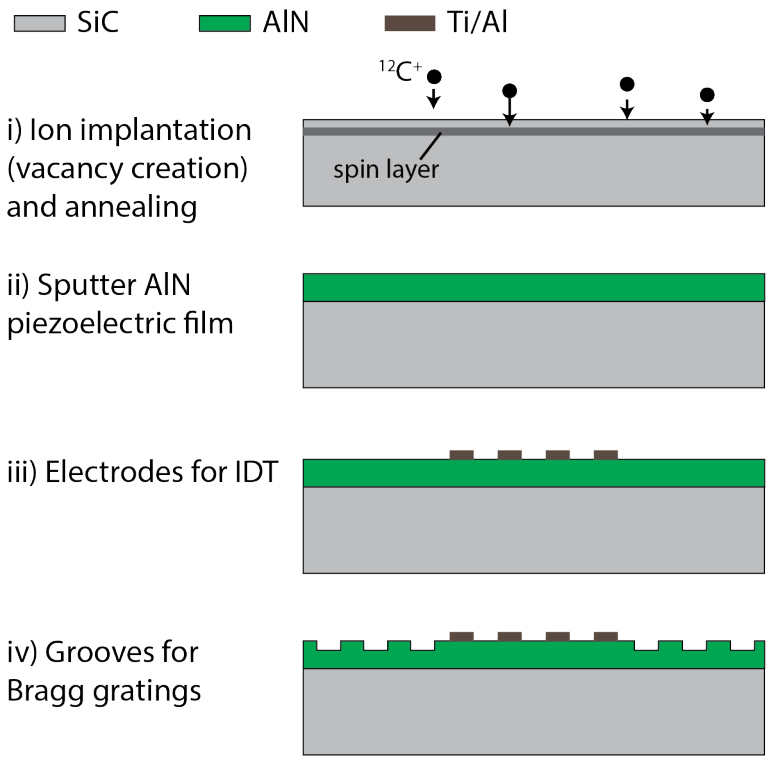

Figure 3.15: **Fabrication summary of SAW resonators with AlN on SiC.**

3. **Deposit AlN 500 nm thick by reactive sputtering on the Si-face of the 4H-SiC wafer.** AlN is chosen as the material for a piezoelectric film because it is has been well developed for the MEMS industry on Si, the hexagonal crystal form (2H) has the same symmetry groups (class 6mm) as 4H-SiC, and AlN lattice constants ($a = 3.11$ Å, $c/2 = 2.49$ Å) are nearly matched to 4H-SiC ($a = 3.073$ Å, $c/4 = 2.513$ Å).

4. **Dice into smaller chips for processing.** Cover with a photoresist cap before dicing and clean with *N*-methyl-2-pyrrolidone (NMP), isopropanol, DI water after dicing.

5. **Pattern and deposit metal IDT.** Usually by *lift-off* methods – lithography with a negative photoresist or bilayer containing an undercut followed by electron beam evaporation – are the preferred because the substrate surface is not roughened or damaged. *Etching* methods also work involving metal deposition first, followed by lithography and etching with an inductively coupled plasma (e.g. Ar, Cl_2, BCl_3 gas flow), and result in good metal quality, adhesion, and smooth sidewalls. Organic

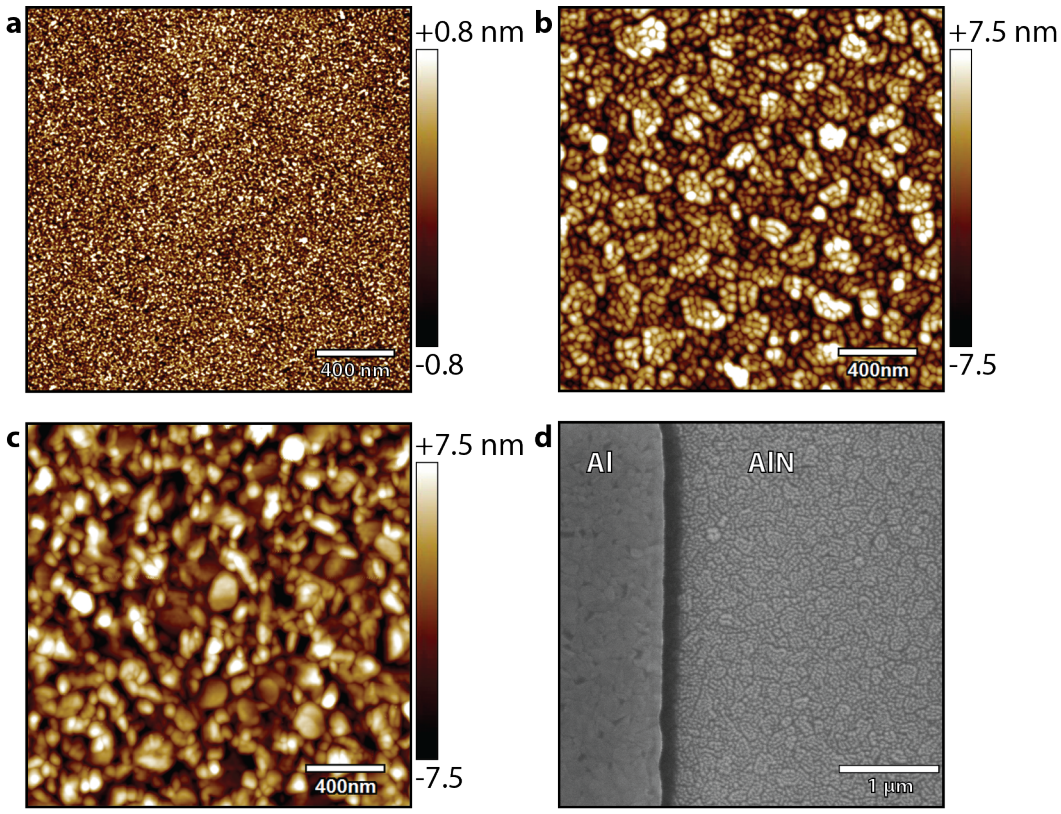

Figure 3.16: **Surface characterization of sputtered AlN on SiC.** Atomic force microscopy (AFM) of **a**. 4H-SiC from Cree Inc., **b**. Sputtered AlN on the 4H-SiC Si-face, and **c**. Aluminum after e-beam evaporation (20 nm Ti under-metal layer, 150 nm Al). All AFM measurements are $2 \times 2\mu\text{m}^2$ scans in taping mode taken with an Asylum Cypher. **d**. Scanning electron micrograph (SEM) at zero tilt and 10 kV of the ground plane electrode and AlN surface after etching the metal (Ti/Al) device layer. The AlN grains appear to grow in small columns ≤ 50 nm in diameter grouped and organized in macro-columns that are ≤ 200 nm diameter.

solvent clean before moving to the next step.

6. **Etch grooves in the AlN layer for Bragg gratings.** This was accomplished by patterning a positive photoresist (AZ 703 MiR) and ICP etching to a depth $h/\lambda < 2\%$ to not introduce bulk wave scattering losses by the acoustic Bragg grating strips [64]. The depth was calibrated to nominally yield $h/\lambda = 1.5\%$.

The wafer of devices were usually protected with a photoresist cap, diced into separate chips, and cleaned for individual characterization and analysis. Full recipes with more detailed steps and explanations can be found in Appendix A. The AlN film is polycrystalline,

oriented with the [0002] crystal direction parallel to the 4H-SiC c-axis [0001], which is normal to the wafer surface. AlN is always grown on the Si-face because often companies chemical-mechanical polish (CMP) the Si-face to be epi-ready (< 0.5 nm r.m.s. roughness), on the other hand, the C-face is typically mechanically polished (> 3 nm r.m.s.). On our samples, the measured surface roughness after sputtering AlN is ≈ 7 nm r.m.s. Our AlN grain size is about $30-50$ nm in-plane, which qualitatively also agrees with SEM of the grain boundaries (Fig. 3.16).

3.5.2 Planar SAW Resonators

Traditional SAW resonators are designed and fabricated in order to characterize the performance on the 4H-SiC substrates with sputtered AlN, usually 500 nm thick and $< 2°$ FWHM [0002] rocking curve. In the planar SAW resonator shown in Figs. 3.17 and 3.18 there are $N_p = 80$ finger pairs, the acoustic wavelength $\lambda = 16$ μm, the aperture $W = 150\lambda$, and there is a window of 3λ missing fingers in the center. The missing IDT strips in the center provide a region where the standing wave and divacancy defects can be imaged without interrupting the optical spot. From SAW fabrication iterations and COMSOL models, this region appears

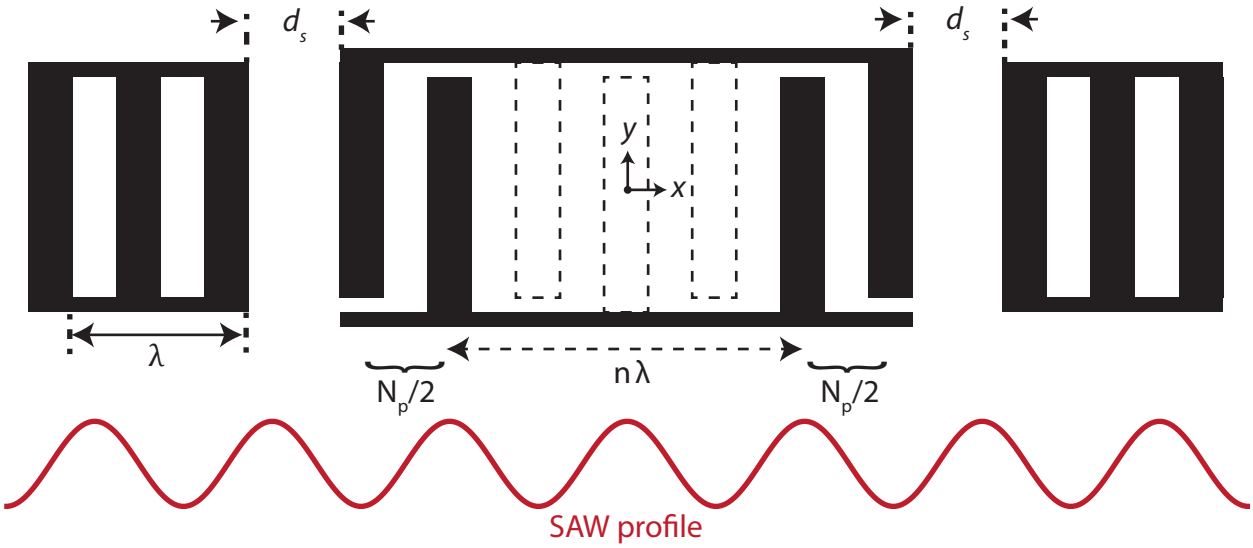

Figure 3.17: **Adapted planar SAW resonator layout.**

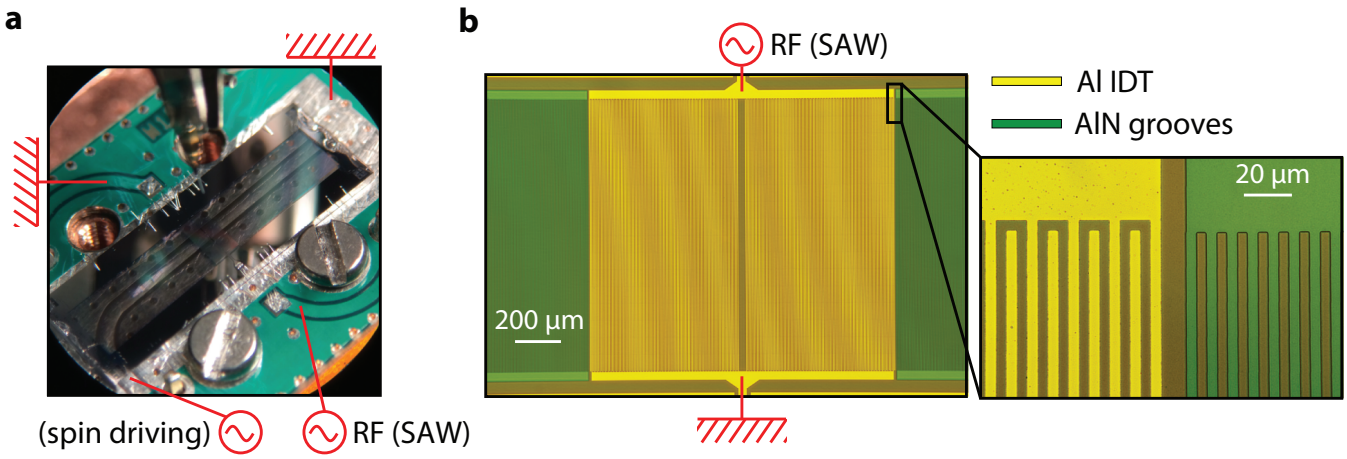

Figure 3.18: **Optical micrographs of the planar SAW resonator.** SAW resonator sample mounted on a printed circuit board with radio-frequency (RF) input for the acoustic drive. A shorted microwave coplanar stripline is directly beneath the sample to allow spin measurements for testing purposes (e.g. confirming the PL signal comes only from VV). The sample has an AlN layer on top of the 4H-SiC substrate with Al interdigitated transducers (yellow) deposited on top of the AlN for driving the SAW. Grooves (green) were etched in the AlN to create the reflectors of the cavity.

to have little to no effect on the mechanical mode, although it will narrow the IDT spectrum because the transducer size appears larger. The symmetry of the IDT is designed to place the SAW standing such that unaxial strain ϵ_{xx} is maximized at the center (it can be shown in simulations that ϵ_{xx} extrema occur underneath IDT electrodes).

Upon testing the device with a VNA, a wide frequency scan near the resonance shows one main resonance in a 'plateau region' (the stop band width Δf_{1SB}) towards higher frequencies (Fig. 3.19a). We can be sure that the broad, undercoupled dips are from the Bragg stopbands because they are not equally spaced away from the cavity resonance (deep dip), so they cannot be caused by the free spectral range. A zoom-in on the main resonance reveals a relatively well coupled, narrow feature with familiar kinds of magnitude and phase features (Fig. 3.19b). We can make a complete model using a modified Butterworth-van Dyke circuit (MBVD), in this case by adding a stray resistance in series with a normal BVD circuit in order to model attenuation caused by the cables, wirebonds, on-chip waveguide, and printed circuit board (Fig. 3.19c). The geometric capacitance is estimated from the fabricated

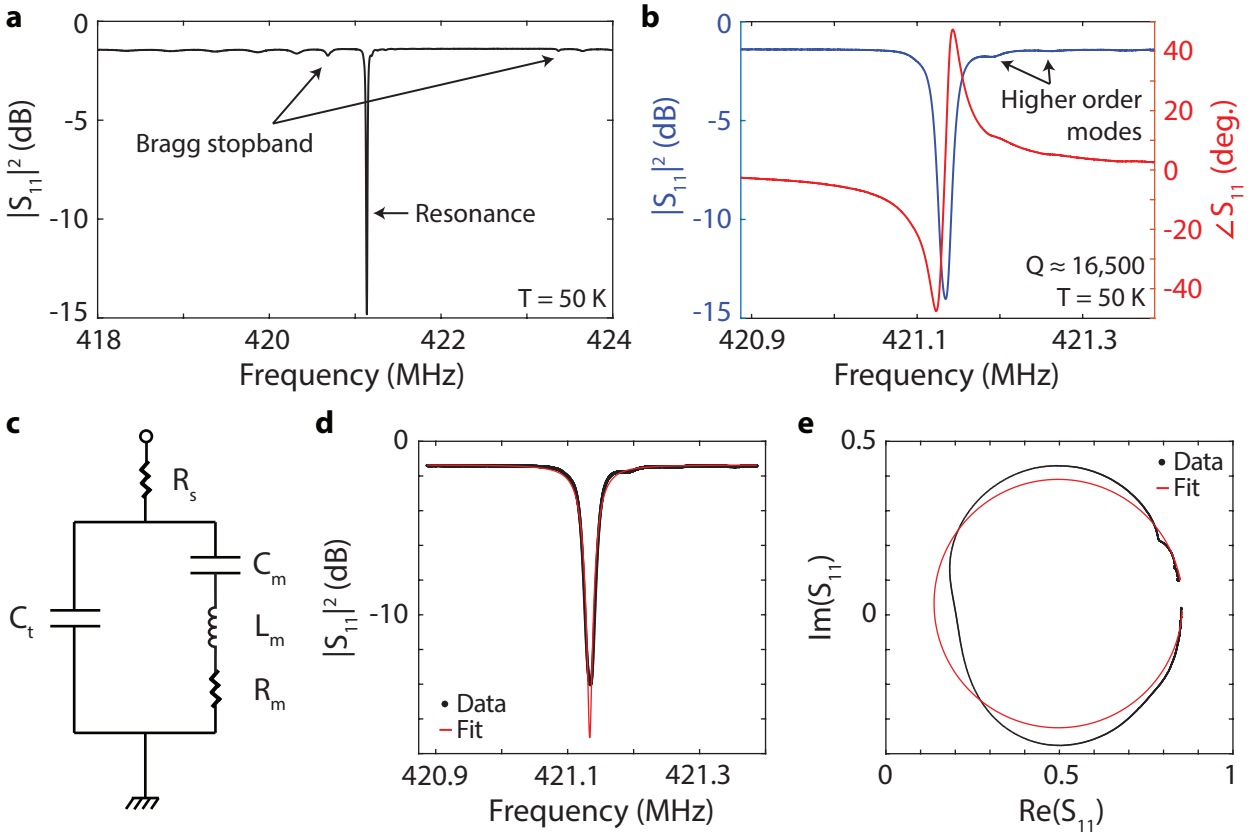

Figure 3.19: **Electrical characterization of the planar SAW resonator. a**. RF reflection measurement at 50 K using a vector network analyzer (VNA). The acoustic wavelength λ is 16 μm. **b**. Zoom in on the resonance in (**a**). The resonator's FWHM yields a loaded quality factor close to 16,500 by hand measurement. **c**. Equivalent circuit of the SAW resonator for fits is a modified Butterworth-Van Dyke (MBVD) filter. **d**. Magnitude plot of the S_{11} measurement and fit overlaid. **e**. Polar plot and fit. Numerical results are discussed in the text.

geometry $C_\mathrm{t} \approx N_\mathrm{p} W \epsilon_\infty = 18.70$ pF, with $N_\mathrm{p} = 80$ the number of electrode finger pairs, $W = 150\lambda$ the aperture or transverse length of capacitor overlap and $\epsilon_\infty \approx 11\epsilon_0$ the dielectric constant (adjusted for IDT calculations) of 4H-SiC. In other devices it was found that the experimental C_t is within $< 20\%$ of the predicted value. The fitted parameters in the model from the data at 50 K are: the resonator capacitance $C_\mathrm{m} = 1.69$ fF, the resonator inductance $L_\mathrm{m} = 84.6$ μH, the resonator resistance $R_\mathrm{m} = 10.3$ Ω and the external stray resistance $R_\mathrm{s} = 4.45$ Ω (Fig. 3.19d,e). This yields a resonator quality factor $Q_\mathrm{i} = \omega_0 L_\mathrm{m}/R_\mathrm{m} \approx 21,730$. Deviations from the model appear to be caused by extra undercoupled resonances, possibly by higher order transverse modes. These will be investigated and even imaged in the next

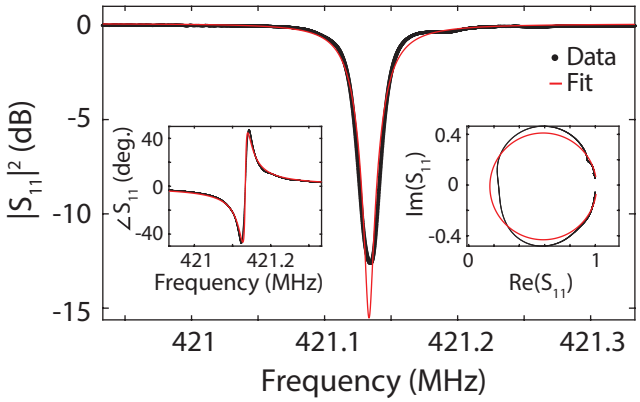

Figure 3.20: **Asymmetric fit to planar SAW resonator.** The measurement from Fig. 3.19b, taken at T = 50 K, fit to Eq. 3.42. The results from the fit are $Q_\mathrm{i} = 22,520 \pm 140$, $Q_\mathrm{e}^* = 31,500 \pm 100$, $\phi = -1.1^\circ \pm 0.2^\circ$.

chapter.

Next, it is helpful to see how our model of general cavity resonances from Eq. 3.42, which is simpler in some regards by assuming less knowledge, compared to the MBVD circuit. Total impedance from a regular BVD circuit is $(Z_\mathrm{t}^{-1} + Z_\mathrm{m}^{-1})^{-1}$ where $Z_\mathrm{t} = (i\omega Ct)^{-1}$ is the impedance of the transducer's geometric capacitance and Z_m is the series RLC impedance of the mechanical resonator. Inserting these into Eq. 3.33, the 1-port RF reflection coefficient as a function of frequency can be written as,

$$S_{11} = \frac{Z_\mathrm{m} - Z_0(1 + \frac{Z_\mathrm{m}}{Z_\mathrm{t}})}{Z_\mathrm{m} + Z_0(1 + \frac{Z_\mathrm{m}}{Z_\mathrm{t}})}\,. \tag{3.43}$$

We can see here that $Z_0 \to Z_0(1+\frac{Z_\mathrm{m}}{Z_\mathrm{t}})$, by approximation should modify Z_0 (and therefore Q_e) with a complex coefficient near resonance when $Z_\mathrm{t} \sim Z_\mathrm{m}$. A fit to the function for asymmetric cavity resonances (Fig. 3.20) results in $Q_\mathrm{i} = 22,520 \pm 140$, $Q_\mathrm{e}^* = 31,500 \pm 100$, $\phi = -1.1^\circ \pm 0.2^\circ$. This fit, corresponding to a loaded $Q \approx 13,100$, is in quantitative agreement with results from the MBVD circuit model and finds the same value for Q_i. We can say that Eq. (3.42) gives meaningful results on the mechanical resonator's internal properties and quality factors, complimentary to BVD analysis methods.

3.5.3 Gaussian SAW Resonators

Using the same fabrication protocols and analysis methods, we will now examine Gaussian SAW resonators. The IDT and gratings are both curved according to the isophase lines predicted earlier for the lowest-order Hermite-Gaussian mode including Guoy effects. Because of the wide curvatures and transverse lengths far away from the center, and also in the interest of making a smaller resonator mode volume, the SAW wavelength is 12 μm (corresponding to electrode and grating strip line widths 3 μm). The metal device layer is fabricated on the AlN by e-beam evaporating 20 nm of Ti and 150 nm of Al. Afterwards, the IDT and ground plane mask is defined with optical lithography and ICP etching (Cl_2, BCl_3, Ar gas chemistry). Lastly, the AlN grooves for Bragg gratings are aligned to markers from the previous layer and also patterned with optical lithography/ICP etching using the same recipe.

Cooling down the Gaussian SAW resonator with a beam waist $w_0 = 2\lambda$ (Fig. 3.21) to

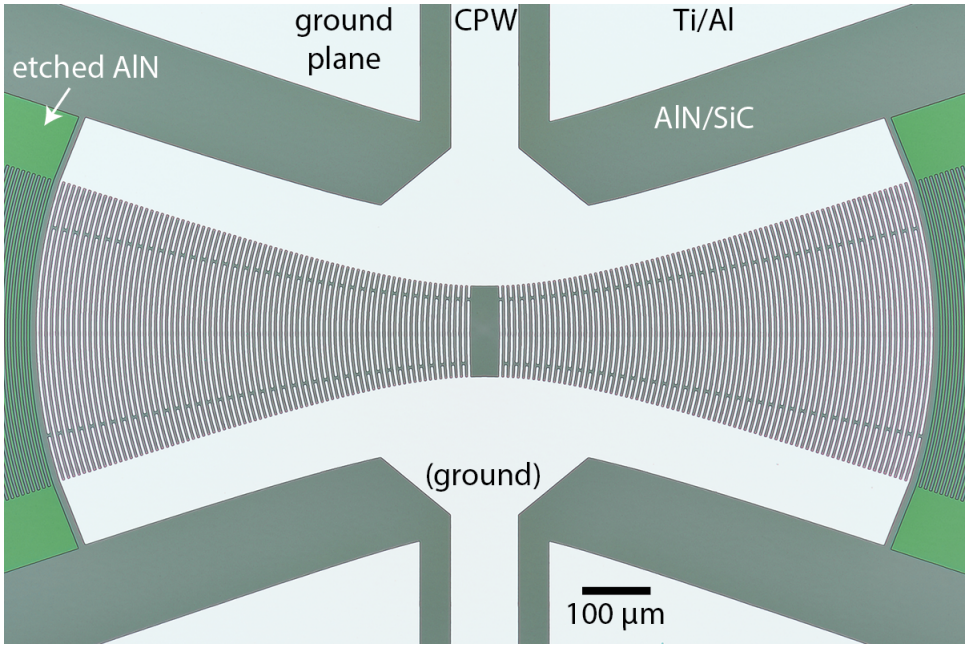

Figure 3.21: **Gaussian SAW resonator: optical micrograph.** The upper coplanar waveguide (CPW) is connected to an RF sources. The lower CPW is available for transmission measurements but is wirebonded to ground for 1-port reflection measurements. The device geometry parameters are $\lambda = 12$ μm, $w_0 = 2\lambda$, $N_p = 80$.

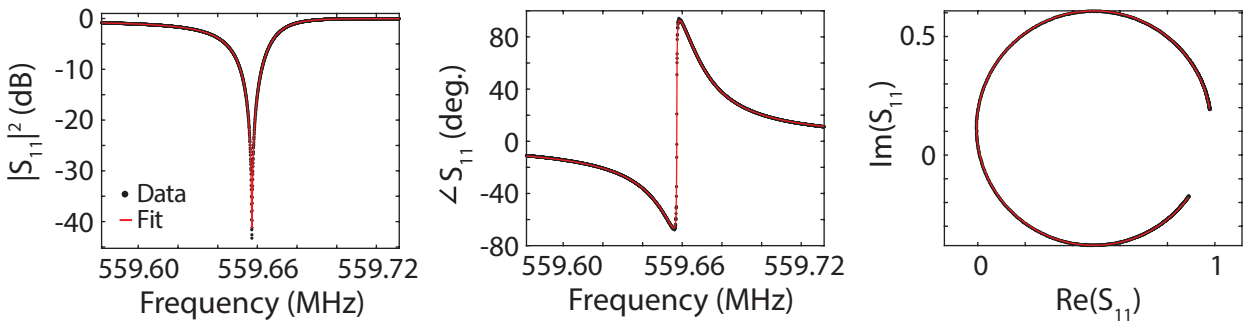

Figure 3.22: **Asymmetric fit to a Gaussian SAW resonator.** RF reflection measurement taken at T = 30 K device shown in Fig. 3.21. The experimental data is in black and the fits shown as red lines use Eq. 3.42.

cryogenic temperatures and performing RF measurements yield a nearly impedance matched cavity resonance (Fig. 3.22). The resonance is clearly well isolated from any spurious modes, such as transverse modes, due to the Gaussian geometry [68]. More measurements including higher temperatures are discussed in Ch. 6. Our results from fitting the data taken at 30 K to Eq. (3.42) are $\omega_0/2\pi = 559.6591$ MHz, $Q_\mathrm{i} = 36,650 \pm 10$, $Q_\mathrm{e}^* = 36,210 \pm 10$, and $\phi = 14.0 \pm 0.1$. The loaded quality factor of this device is $Q \approx 18,200$, and its normalized coupling strength to the CPW transmission line is $Q_\mathrm{i}/Q_\mathrm{e}^* \approx 1.01$, which means power can be transfered into the mechanical cavity very efficiently from a 50 Ω source at its resonance frequency.

Chapter 4

Optically Imaging Surface Acoustic Waves with Deep Defects

The following chapter is adapted from previously published work in reference [73].

4.1 Electrometry by Optical Charge Conversion

The detection of electric fields and charge is critical to a wide range of applications including device characterization [74], mapping electrical potential [75] and electrical quantum metrology [76, 77, 78]. Recently, electrometry was demonstrated using the spin state of optically-active point defects, specifically nitrogen-vacancy (NV) centers in diamond, enabling quantum-limited sensitivity with nanoscale spatial resolution [45]. Similar experiments were also reproduced in divacancies (VV) in silicon carbide [17]. Nevertheless, electric fields (and strain) only weakly interact with the spin state of typical qubit defects by altering the zero-field splitting [17, 79] or hyperfine interaction [80, 81]. In contrast, an impuritys charge state, though not coherently controllable, is directly sensitive to the electric and charge environment which perturb the electronic wavefunction, and is drastically modified by defect ionization and recombination [82]. The defect charge state provides a naturally occurring analog of quantum point contacts, single electron transistors or other charge-based

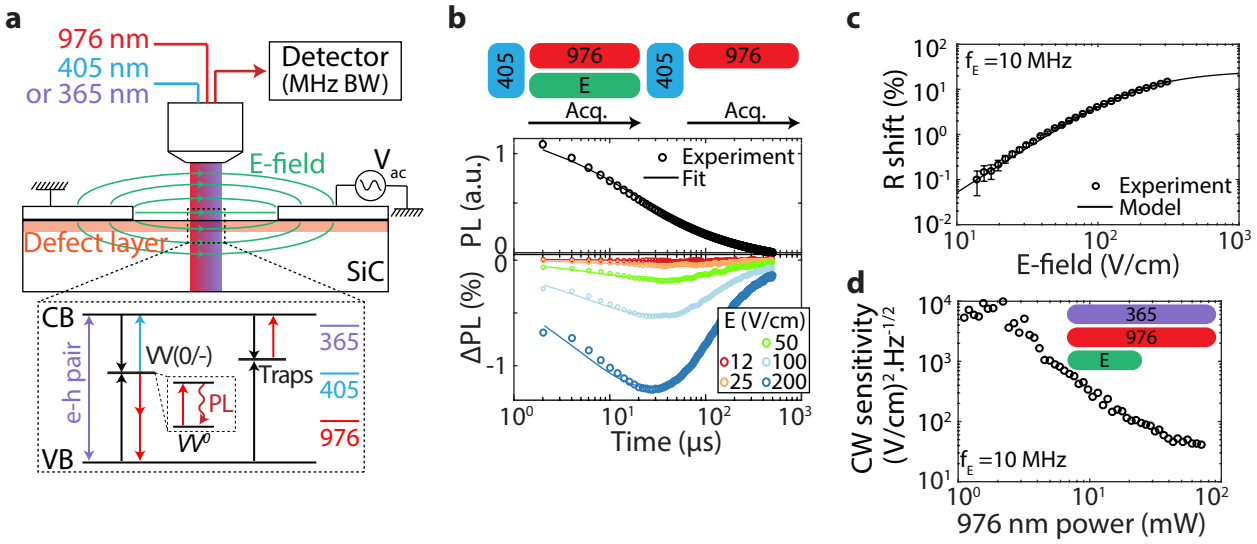

Figure 4.1: **Electrometry by optical charge conversion (EOCC). a**. Schematic of the optical setup with one reset color (365 nm or 405 nm) and one pump color (976 nm). Illumination at 365 nm generates electron-hole (e-h) pairs that reset VV to VV^0 (bright state) in the steady-state, at 405 nm directly ionizes VV^- (dark state) to VV^0, and at 976 nm excitation converts VV^0 to VV^- by direct two-photon ionization or indirectly by one-photon ionization of local traps [82, 83]. In addition, VV^0 photoluminescence is provided through excitation at 976 nm. VV(0/−) is the transition energy level between the neutral and negatively charged states. VB and CB are the valence and conduction bands, respectively. An RF electric field (r.m.s. amplitude E, frequency f_E) is applied across a coplanar capacitor with a 17 μm gap. Divacancies are created by carbon implantation immediately below the surface. A fast detector with 10 MHz bandwidth (BW) allows for direct detection of a full OCC transient signal in a single measurement. **b**. VV is first reset to its bright state (VV^0) by 405 nm illumination, followed by PL detection (top) of the charge conversion toward the VV dark state by 976 nm excitation. Below, the difference between conversion with and without applied electric field (10 MHz) is shown. Data is fit to a stretched exponential function with $R = 42$ kHz and $n = 0.54$ obtained using a global fit for all electric field values. **c**. Fitted decay rate shifts as a function of electric field. Error bars are 95% confidence intervals. **d**. EOCC sensitivity with continuous (CW) laser (365 nm and 976 nm) pumping as a function of 976 nm laser power. We estimate a 10% error in electric field estimation, corresponding to 20% error in sensitivity (not shown).

electrometry devices [76, 77].

Optical detection of charge states can be adapted depending on the defect: for the NV center in diamond, a change from the NV^- to the NV^0 provides different emission spectra [84], while in VV or silicon vacancies (V_{Si}) in 4H and 6H-SiC, only one charge state (VV^0, V_{Si}^-) has a known photoluminescence (PL) spectrum [6, 85]. Charge conversion be-

tween the various charge states can be efficiently realized by optical pumping at specific wavelengths [82, 86, 87]. Here we show that the optical charge conversion (OCC) rate between the bright and dark charge states of both VV and V_{Si} defects is strongly modulated by the presence of an applied radio-frequency (RF) or microwave (MHz to GHz) electric field, and therefore can be detected through changes in PL. The frequency range of this electrometry by optical charge conversion (EOCC) would be challenging using conventional spin sensing due to limitations in Rabi drive rates, though a method of circumventing this limit has recently been shown [88]. We further demonstrate spectroscopic techniques (frequency and phase resolution) using EOCC as well as its application to three-dimensional microelectromechanical system (MEMS) characterization.

In 4H-SiC, OCC of divacancy ensembles requires a near or above bandgap (3.2 eV) excitation to obtain VV^0 (bright), while illumination below 1.3 eV pumps the defect toward a dark charge state (likely VV^-) [82, 83]. We use either 365 nm (continuous) or 405 nm (pulsed) light as reset to VV^0 and 976 nm laser as dark state pump, with the 976 nm laser also exciting PL from VV^0. Fig. 4.1a shows all dominant capture and photoionization transitions in the system, as well as electron-hole pair generation by 365 nm illumination as described in ref. [82]. The experimental setup consists in two laser beams focused on divacancies localized near the surface, in between two metal contacts on top of the SiC substrate (see also Fig. 4.7). Applying a voltage across the contacts generates in-plane electric fields orthogonal to the c-axis.

We first characterize OCC transient decays by resetting the charge state with 405 nm illumination followed by a 976 nm pump laser. A fast detector is able to capture a complete transient signal from bright to dark in a single experiment (see Methods section for more details), as shown in Fig. 4.1b (top). The decay is well fitted by a simple stretched exponential decay $f(t) \propto \exp\{(-(Rt)^n)\}$, where R is the characteristic decay time and n the stretch factor, the latter describing the complexity of the charge conversion mechanism ($n = 1$ for simple photoionization and $n < 1$ for competition between ionization, carrier capture and

carrier diffusion) [89, 90]. We then apply simultaneously an RF electric field along with the 976 nm illumination, resulting in a time-dependent PL variation $\Delta PL(t, E) = PL(t, E) - PL(t, E = 0)$ as plotted in Fig. 4.1b (bottom), where E is the root mean square amplitude (r.m.s.) of the electric field with corresponding frequency $f_E = 10$ MHz. The fit function in this case becomes $f(t, E) \propto \exp\Big\{(-(R(1 + \Delta R(E))t^{n(1+\Delta n(E))})\Big\} - \exp\{(-(Rt)^n)\}$, with $\Delta R(E)$ and $\Delta n(E)$ the relative rate and stretch factor shifts under electric field.

While n remains nearly constant ($\Delta n < 1\%$ observed variations), the electric field changes R (see Fig. 4.1c) according to a phenomenological quadratic dependence with saturation:

$$\Delta R(E) = \Delta R_\infty \left\langle \frac{(E/E_{\text{sat}})^2}{1 + (E/E_{sat})^2} \right\rangle_t \tag{4.1}$$

where $\langle\ \rangle_t$ correspond to a time average over an oscillation of the RF electric field, E_{sat} is the saturation electric field and ΔR_∞ is the maximum R shift when $E \gg E_{\text{sat}}$. We find for VV in this sample $\Delta R_\infty = 27 \pm 1$ % and $E_{\text{sat}} = 158 \pm 20$ V/cm. It is unclear whether these values are specific to the sample or to the defect itself and additional studies are required. In the first case, EOCC would likely be due to variations in carrier recapture after ionization and would depend on parameters such as mobility or drift velocity. In the second and most likely case, E_{sat} may be directly related to the defect electronic wavefunction and changes in photoionization and capture cross-sections (see Fig. 4.1a). Finally, the EOCC effect was confirmed separately in multiple SiC wafers, in bulk and implanted ensembles, and using different device geometries (see Methods section). We also did not observe any magnetic field dependence of EOCC up to 400 G, precluding any spin contribution to the signal.

Due to the quadratic response given by (4.1), EOCC effectively measures the electric field energy density. We define the sensitivity S of this sensing technique for all values of electric fields below saturation as:

$$S = \frac{E^2 \sigma_{\Delta PL}(E) \sqrt{T_{\text{exp}}}}{\Delta PL(E)} \tag{4.2}$$

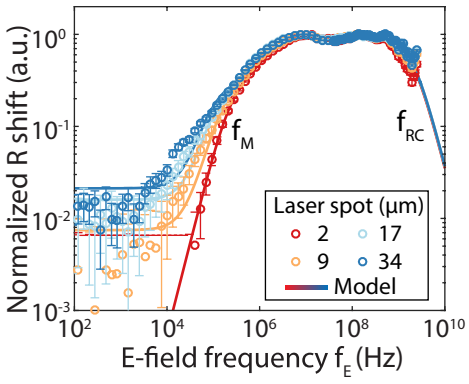

Figure 4.2: **Frequency dependence measurements.** Frequency response of the EOCC rate shift (normalized) for different laser spot sizes obtained by changing the microscope focus. At frequencies below f_{M}, the rate shift decays due to a lower effective electric field, while above f_{RC}, it decays due to the low-pass characteristics of the experimental setup and device impedance.

where $\Delta PL/\sigma_{\Delta PL}$ is the signal-to noise ratio (using standard deviation) for a given electric field and T_{exp} is the experiment time (i.e. PL integration time). Fig. 4.1d shows sensitivity values as a function of 976 nm pump power, optimized by using continuous 976 nm and 365 nm illumination while locking-in on the electric field turned periodically on and off. In this sample, we obtain a sensitivity at 10 MHz as high as 41 ± 8 $(\mathrm{V/cm})^2/\sqrt{\mathrm{Hz}}$ for an estimated ensemble of 10^4 VVs within the confocal spot size. Similar sensitivities have been demonstrated with DC and low frequency (< 1 MHz) spin sensing [45, 91], though the quadratic dependence in E makes it hard to properly compare EOCC and spin-based sensing (linear dependence). Higher sensitivities may be achieved with higher defect densities, e.g. with larger depth profile and higher implantation doses, to the limit of strong pinning of the charge state. Higher laser power may also improve the sensitivity by one to two orders of magnitude by increasing the decay rate R. Resonant optical excitation on the zero-phonon line may also enhance the charge conversion rate due to two-photon ionization [82], and alternative defects with higher ionization cross-section could be investigated. Sensitivities down to $0.1 - 1$ $(\mathrm{V/cm})^2/\sqrt{\mathrm{Hz}}$ should be achievable with commercially available materials. The measured sample and VV concentration are similar to that used for typical spin experiments, readily allowing EOCC to be combined with other spin sensing techniques.

4.2 Frequency Spectroscopy with EOCC

We then characterize in Fig. 4.2 the frequency response of the EOCC technique by looking at the rate shift ΔR as a function of electric field frequency, from quasi-DC (100 Hz) to 2 GHz. Above 1 GHz, ΔR diminishes as expected from parasitic capacitances of the device (RC filtering). Below 1 MHz, ΔR also decreases possibly owing to the creation of a steady state space charge defined by the laser spot and the applied electric field. At low frequency, the optical pumping ionizes VV and other defects, resulting in free carriers that redistribute to locally compensate the applied electric field. The decrease in signal is therefore attributed to a lower effective electric field seen by the defects and not a lower EOCC sensitivity. At high enough frequency, the carrier distribution never reaches its steady state and the space charge is not created. The characteristic timescale for space charge formation is the Maxwell relaxation time $1/f_{\mathrm{M}} = (\epsilon_0 \epsilon_r \rho)/2$, where ϵ_0 and ϵ_r ($\approx$ 10 for 4H-SiC) are the vacuum and relative permittivity and ρ is the resistivity [92]. Within this description and using the fitting function for f_{M} described in the Methods section, we measure $f_{\mathrm{M}} \approx 0.3$ MHz with a corresponding resistivity equal to $\approx 10^7$ Ω cm, as expected from typical resistivity values quoted for high purity semi-insulating 4H-SiC wafers. The space charge creation is also expected to depend on the initial charge distribution which we effectively modify by increasing the laser spot size (Fig. 4.2). The fit works well in all cases, and in particular for large spot sizes the low frequency rate shift is non-zero (above noise level).

Having characterized the EOCC frequency response, we now demonstrate the ability to resolve the frequency and phase of the applied RF electric field as shown in both Fig. 4.3a,b, respectively. These experiments are enabled by pulsing the 976 nm pump light with a given frequency f_{laser} and duty cycle (pulse duration). First, we fix f_{laser} while sweeping f_E with a random initial phase between the two frequencies. This sequence measures the effective filter function of the pulse sequence, and shows dips of decreasing intensities for f_E equal to increasingly higher harmonics of f_{laser} (Fig. 4.3a). The dips arise from the light pulse always overlapping with equal electric field values when f_E matches a harmonic of f_{laser}; the RF

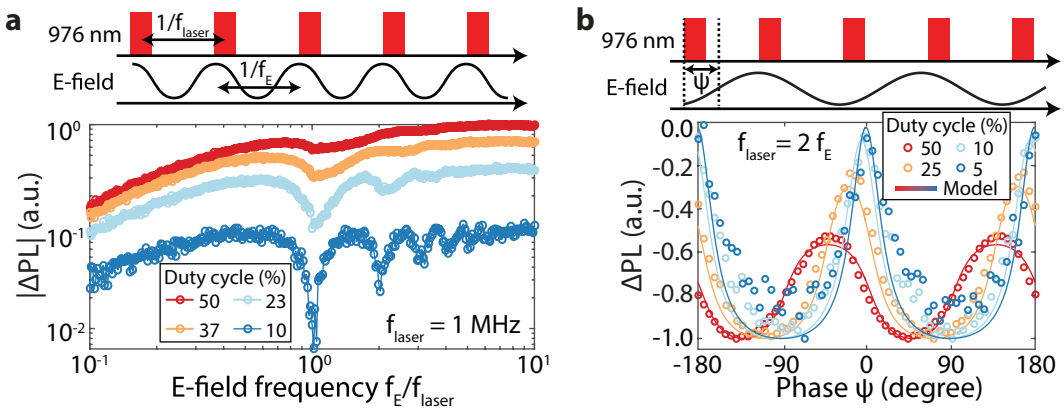

Figure 4.3: **Frequency spectroscopy and phase domain measurements. a**. Frequency response of the EOCC contrast under pulsed 976 nm light, corresponding to a filter function for RF electric field spectroscopy. The laser pulse periodicity is f_{laser}. The electric field has a random phase with respect to the laser pulse. The total measurement duration is fixed for all duty cycles. **b**. Phase measurement of the RF electric field using the sequence shown on top. The laser is pulsed at twice the electric field frequency and related by a phase Ψ. $\Psi = 0$ is defined as the laser pulse coinciding with $E = 0$; due to finite laser pulse length, this results in asymmetry of the EOCC signal around $\Psi = 0$. For both (**a**) and (**b**), a 405 nm reset pulse is used before the sequence.

electric field effectively becomes static in this condition and the EOCC signal diminishes as expected from Fig. 4.2. The effect is gradually more prominent for decreasing duty cycle as the filter function sharpens. For phase resolution (Fig. 4.3b), we fix the relative phase Ψ between the laser pulse and electric field oscillations and set $f_{\text{laser}} = 2f_E$. Alternating light pulses encounter electric fields with alternating signs but equal amplitude depending on the phase Ψ, and sweeping Ψ hence maps the time evolution of the electric field (E^2) oscillation. The model in the figure is calculated without any free parameters using eq. (4.1) and the overlap between the electric field wave and the laser pulse.

4.3 Applications to Other Defects and MEMS Sensings

The electrometry technique we have outlined is broadly applicable to other defects with known charge dynamics. For example, V_{Si} can be optically charge converted and, unlike VV, is optically active even at room temperature. The combination of 365 nm (pumping

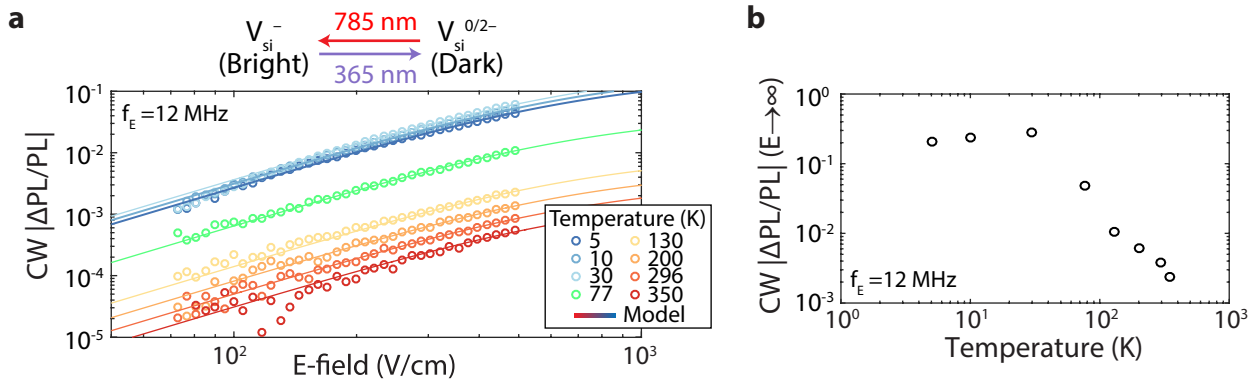

Figure 4.4: **EOCC in silicon vacancies (V_{Si}) in 4H-SiC. a**. EOCC contrast $|\Delta PL/PL|$ as a function of electric field for temperatures ranging from 5 to 350 K. Lines are fit to eq. 4.1, with E_{sat} fitted to be 610 ± 80 V/cm independent of temperature. **b**. Extrapolated EOCC contrast for $E \to \infty$ as a function of temperature, with 95% confidence intervals (not shown) equal to about 5% of the contrast.

to a dark state) and 785 nm (pumping to a bright state) lasers allows for OCC [82] and therefore the application of EOCC as shown in Fig. 4.4a,b. Under continuous illumination at both wavelengths, the electric field modifies the V_{Si} PL for temperatures ranging from 5 K to 350 K. The EOCC contrast is present at all temperatures, though it is strongly reduced above 30-77 K; this behavior could be explained by the thermal activation of shallow impurities or capture barriers. The EOCC frequency dependence was found to be identical between V_{Si} and VV (see Fig. 4.8). We do not compare here V_{Si} and VV sensitivities as the experimental setup and the sample were only optimized for VV defects.

To conclude this work, we demonstrate the application of EOCC to map surface acoustic wave (SAW) modes in an electro-mechanical resonator in 4H-SiC. As SiC is slightly piezoelectric, any strain or shear wave simultaneously produces a corresponding measurable electric field. The SAW resonator is displayed in Fig. 4.5a (see Methods section and Figs. 3.18,3.19 for further details) with an interdigital transducer (IDT) fabricated on top of a 500 nm AlN layer on top of the SiC substrate. The resonator is composed of Bragg gratings made from grooves in the AlN that act as reflective mirrors, while the IDT couples the electrical drive to the SAW mode. All PL measurements are realized away from the IDT to avoid contribution from the drive electric field. Fig. 4.5b presents a longitudinal (x-z) cross-section in

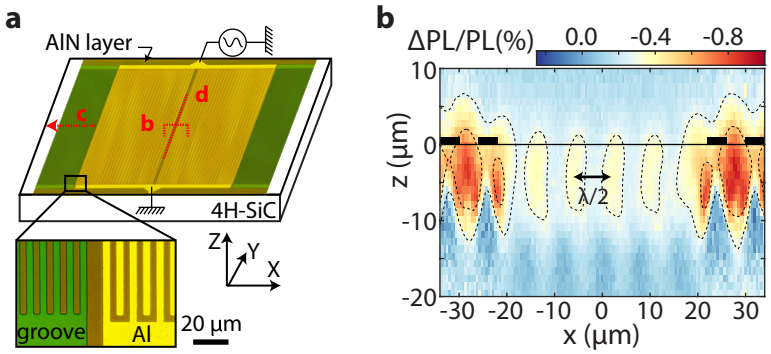

Figure 4.5: **Surface acoustic wave (SAW) mapping. (a)**. Schematic of the SAW device with partial microscope images. The red lines are scans with corresponding panel letters. The AlN grooves extend for 5.4 mm on each side. **(b)**. EOCC contrast of a cross-section (x-z) centered at the window of the resonator. The black line indicates the surface and the black boxes the metal from the interdigitated fingers (not to scale). The map taken at 0 dBm input power.

the center of a device where there is a window in the IDT. In Fig. 4.6a,b we show a cut (x) across the AlN grooves and a transverse cut (y) in the central window, respectively. In the cross-section of the window, we observe wave crests separated by half of the SAW wavelength λ ($\lambda = 16$ μm, cavity frequency is 421 MHz), as expected from a quadratic response in electric field. Numerical simulations confirm the contrast to likely originate from the E_x electric field component of the resonator mode (see Fig. 4.9). From the data in Fig. 4.6b, we observe oscillations in the Bragg grating's grooves from the SAW modulated by an exponential decay. The characteristic decay length is measured to be $L = 0.78 \pm 0.03$ μm, and directly related to the reflectivity per grating strip $|r_s| = \lambda/4L = 0.51 \pm 0.02$ %.

A transverse sweep across the central window measured as a function of drive frequency allows for direct observation of various transverse modes of the SAW resonator. Fig. 4.6b shows modes with 1 to 5 peaks (i.e. electric field extrema); their respective signals are separately integrated, plotted (bottom) and compared with a direct reflection ($|S_{11}|^2$) measurement of the cavity. The $|S_{11}|^2$ signal only provides the total contribution from all modes, whereas the EOCC technique fully separates each mode in spatial and in frequency domains. Overall, EOCC offers complementary information to common MEMS characterization methods such as laser Doppler vibrometry [93] and various surface techniques (scanning electron

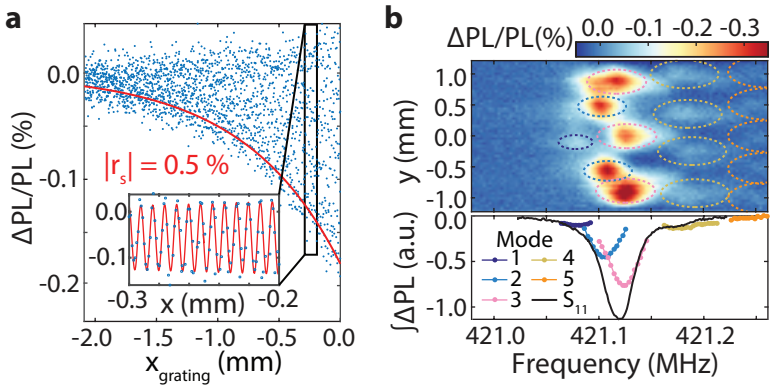

Figure 4.6: **Characterizing a planar SAW resonator with EOCC. (a)**. EOCC contrast near the AlN grooves (reflectors) allows for direct measurement of their reflectivity r_s. $x_{\text{grating}} = 0$ corresponds here to the position of the first groove. In inset, a zoom is shown to emphasis the oscillations from the SAW. **(b)**. SAW drive frequency as a function of transverse (y) position. 5 modes are observed and integrated according to the colored ellipses. The integrated signals for each mode are shown as a function of frequency and compared to the $|S_{11}|^2$ intensity from a Schottky diode. All maps were realized at 0 dBm input power.

microscope, atomic force microscopy, etc.) [75]. In particular, 3D spatial and high frequency (GHz) sensing available with EOCC are much harder to achieve with these alternative techniques.

4.4 Conclusions

In summary, we present a new electric field sensing technique for optically-active defects in 4H-SiC. This method is purely optical and has a quadratic dependence in the applied electric field, i.e. measures the electric field energy density, whose frequency can be as high as a few GHz, likely limited by the experimental setup. Electrometry at such frequencies would be hard to achieve with spin sensing techniques. We further demonstrate spectroscopy in both the frequency and phase domain. These methods were tested in 4H-SiC for both ensembles of divacancies and silicon vacancies, from cryogenic to room temperature, and with a measured sensitivity of 41 ± 8 $(\text{V/cm})^2/\sqrt{\text{Hz}}$. The ability to measure electric field vectors (3-axis) could be realized by taking advantage of the non-linear (quadratic) response in electric field. Finally, we demonstrate mapping of a SAW resonator due to the piezoelectricity of

SiC, offering a new characterization tool for related MEMS. Further improvements in the sensitivity could be achieved by higher defect densities, which should not drastically affect the charge state dynamics contrary to the spin coherence, or toward high spatial resolution by using single impurities. This technique is likely applicable to defects in other materials, in particular large bandgap crystals such as diamond and other substrates for high power electronics and high frequency MEMS.

4.5 Materials and Methods

4.5.1 Samples

The coplanar capacitor device was fabricated on a semi-insulating 4H-SiC commercial wafer from Norstel AB. VV and V_{Si} defects were created by carbon (^{12}C) implant with a 1×10^{12} cm^{-2} dose at 170 keV with a 7° tilt ($\approx$ 300 nm depth), followed by annealing at 900°C in Ar for 2 hours. 10/90 nm of Ti/Au was used for the metal gates. The device design is shown in Fig. 4.7 and has multiple capacitors in parallel, though the laser spot in all experiments was confined to a single capacitor (with 17.1 μm spacing). We confirmed the EOCC effect using other device geometries, including measurements of the electric field produced by a microwave stripline on a printed circuit board a few micrometers away from the sample, as well as devices fabricated on different 4H-SiC wafers (Norstel AB and Cree Inc.). The electric field sensitivity was found to vary between the wafers, mainly due to the OCC efficiency. Indeed, for some samples, the local Fermi level might be pinned by a dominant trap, including VV, preventing charge conversion from occurring, as previously observed in [82]. For example, carbon (^{12}C) implant at 1×10^{12} cm^{-2} dose was found to give higher sensitivity than at 1×10^{13} cm^{-2} dose in semi-insulating wafers. The total change in PL after charge conversion between the bright and dark states was reduced from a factor of 1000 in the first sample to a factor of 20 only in the second sample, and consequently the EOCC contrast was similarly reduced. Careful consideration of all impurities present in the

substrate is therefore necessary to optimize EOCC.

The SAW resonator (see Figs. 3.18,3.19) was fabricated on a semi-insulating 4H-SiC commercial wafer from Cree Inc.. Defects were created by carbon (^{12}C) implant with a 1×10^{12} cm^{-2} dose at 170 keV with a 7° tilt ($\approx$ 300 nm depth), followed by annealing at 900°C in N_2 for 2 hours. 500 nm of AlN was sputtered on the Si face of the wafer by OEM Group Inc. The AlN layer has $\approx$ 40 MPa film stress with a rocking curve for AlN (0002) of 1.52° full width at half maximum (XRD). 150 nm of Al was used for the interdigital contacts (80 finger pairs, with a window in the center equal to 3λ of missing fingers). Al and AlN were etched by inductively coupled plasma (ICP) with 10 sccm Ar, 30 sccm Cl_2, 30 sccm BCl_3, 50 W bias and 400 W ICP power. The grooves in the AlN were patterned by optical lithography and etched 270 nm deep.

4.5.2 Experimental setup

Samples are mounted on printed circuit board inside a closed-cycle cryostat. All measurements were realized using a single confocal microscopy setup (50x objective, 0.65 numerical aperture) with optics optimized for near-infrared. For VV, OCC was realized using a 365/405 nm and 976 nm laser diode, with 976 nm simultaneously exciting the VV^0 photoluminescence (> 1000 nm). For V_{Si}, OCC was realized using the same 365 nm and a 785 nm laser diode, with 785 nm simultaneously exciting the V_{Si}^- photoluminescence (875-1075 nm filtering). For pulsed laser experiments, the 976 nm laser was modulated using an acousto-optic modulator ($\ll$ 100 ns rise time) while 405 nm was directly modulated by a current driver (250 kHz).

Detection was realized using two separate configurations. For continuous measurements, an InGaAs photodiode with 1 kHz bandwidth was combined with a lock-in amplifier set at the frequency of the electric field amplitude modulation or switching (typically 400 Hz). For direct transient detection, an InGaAs avalanche photodiode (Thorlabs APD410C) in linear regime (M factor = 20) with 10 MHz bandwidth was used with a fast (125 MHz) acquisition

card. Transient signals were acquired with a 50 MHz sampling rate and binned into 2 μs samples; differential measurements for ΔPL are numerically processed during acquisition.

All maps were taken using a 3-axis linear stage. AC electric fields are generated by two separate sources below and above 40 MHz. Above 40 MHz, the input power is calibrated to be flat across all frequencies by measuring the reflected power from the sample with a Schottky diode.

4.5.3 Low frequency response

In order to understand the low frequency response, we also tested a simpler coplanar capacitor design and a coplanar waveguide design patterned on two different 4H-SiC wafers. We also measured electric fields coming from a coplanar waveguide on a printed circuit board, separate from The effect of device impedance at low frequencies is disregarded as we did not observe any change using these various device configurations.

The low frequency behavior can be modeled by an effective electric field with the following linear frequency response:

$$E(f_E) = E_{\mathrm{HF}} \left| 1 - c \times \frac{(1 - i f_E/f_{\mathrm{M}})}{(1 + a - i f_E/f_{\mathrm{M}})(1 - b - i f_E/f_{\mathrm{M}})} \right| \tag{4.3}$$

where E_{HF} is the electric field value at high frequency, i is the imaginary unit and a, b, c and f_{M} are free parameters. Though this equation is purely phenomenological, it is similar to theoretical calculations for the conductivity response from the creation of a space charge (but for different conditions from our experiments) [92]. In this case, the parameter f_{M} is the Maxwell relaxation rate and a and b are related to the inhomogeneous distribution of free carriers due to photoionization.

4.6 Supplementary Data and Figures

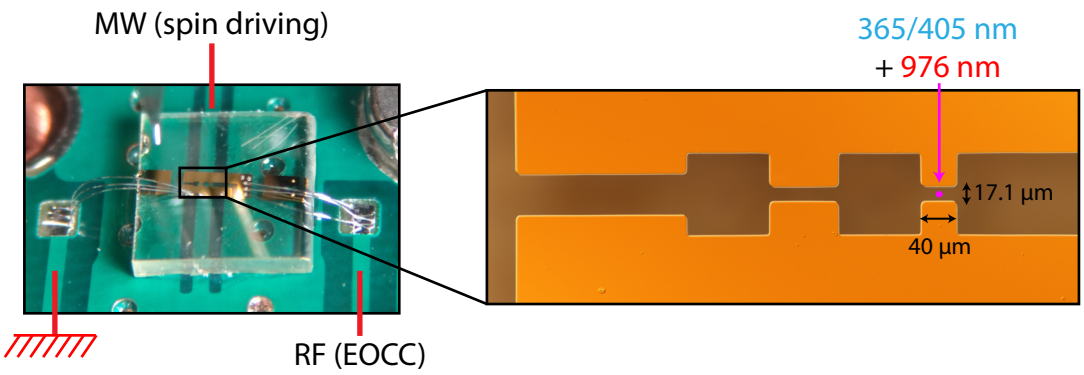

Figure 4.7: **Optical micrographs of the capacitor device for EOCC characterization.** 4H-SiC sample with electrodes (capacitor) mounted on a printed circuit board with radio-frequency (RF) input for the EOCC electric field signal. A shorted microwave coplanar stripline is directly beneath the sample to allow spin measurements for testing purposes (e.g. confirming the PL signal comes only from VV). The 976 nm laser, 365 nm light emitting diode and 405 nm laser are all focused between two metal gates separated by 17.1 μm.

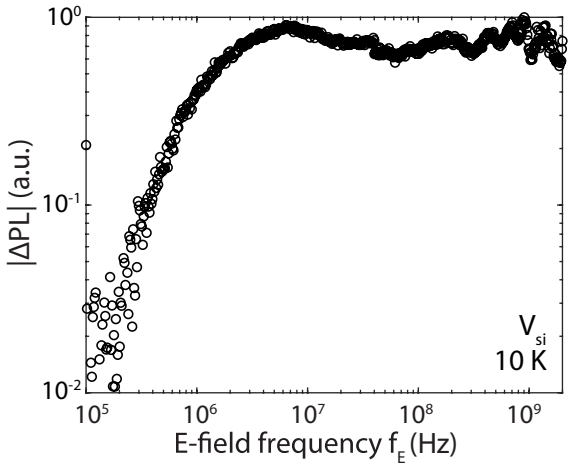

Figure 4.8: **Frequency dependence of EOCC using V_{Si} in 4H-SiC.** Measurement was realized using continuous-wave 785 nm and 365 nm illumination. No significant difference was observed between V_{Si} and VV, showing that the electrometry mechanism is likely identical.

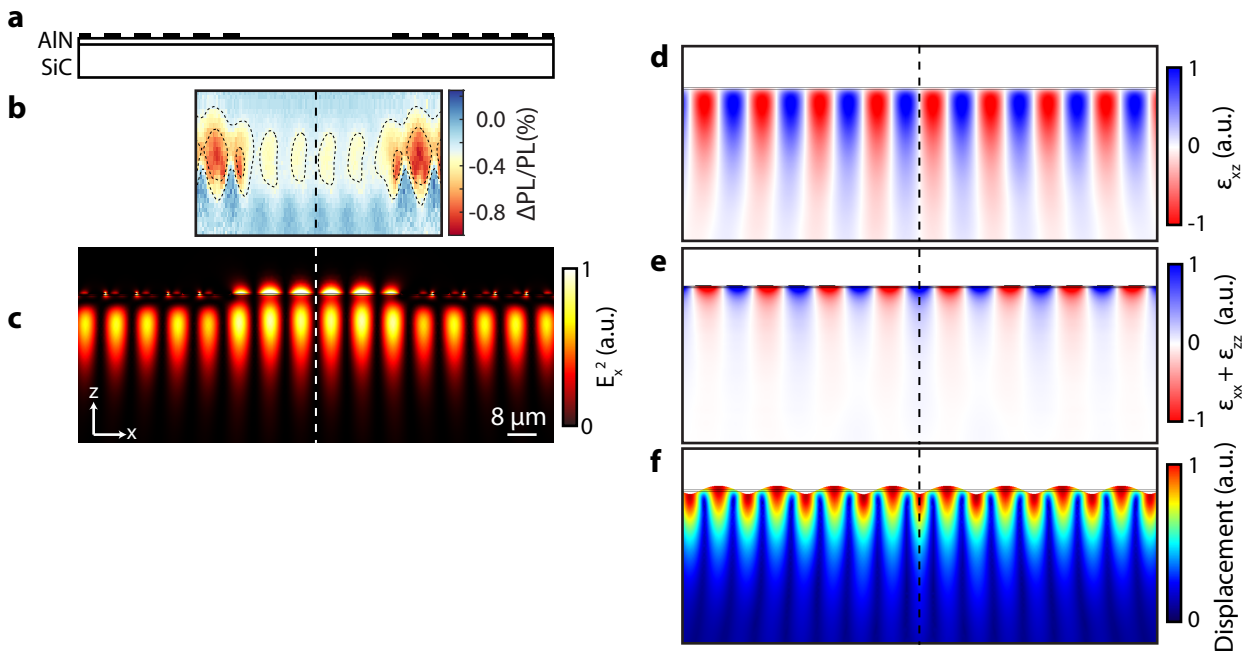

Figure 4.9: **Numerical simulations of the electro-mechanical SAW resonator mode.** **a**. Schematic of layers in de SAW device. **b**. EOCC contrast (see Figure 4. of the main text). COMSOL simulations are given in (c-f): **c**. x component of the electric field (square). **d**. ϵ_{xz} shear. **e**. Volumetric strain. **f**. Displacement. The dashed lines indicate the center of the IDT. All simulations were obtained when the voltage across the IDT is close to zero. In this case, the dominant contribution is the strain/shear and piezoelectric field of the SAW resonator. This is in contrast with the experimental result in (b) where the amplitude is larger beneath the metal. In addition, the simulation does not take into account all interdigitated fingers and reflectors of the resonator. We determine that (c) exhibits the closest resemblance to the spatial map of (b), from Fig. 4.5b, so mechanical-EOCC contrast results from piezoelectric effects in the 4H-SiC substrate.

Chapter 5

Direct Imaging of Dynamically Driven Strain using X-rays

The following chapter is adapted from previously published work in reference [94].

5.1 The Hard X-ray Nanoprobe

Strain provides a fundamental route to control diverse material properties such as electrical transport [95], chemical reactivity [96], and electromagnetic ordering [97]. In quantum systems, the manipulation of strain near isolated point defects and engineered structures has shown the potential to significantly improve performance characteristics of solid-state qubits for quantum information processing [98, 99, 5, 100, 101]. Among potential degrees of freedom in solid-state quantum devices, mechanics has the ability to nearly universally interact with various types of qubits [1, 102] and be confined to sub-micron length scales. Near-defect lattice strain can be used either statically, to tune quantum energy levels and degeneracy, or dynamically, to mechanically drive coherent spin transitions [44, 43, 103] and engineer hybrid system responses. From this, mechanical systems have the potential to play a transformative role in quantum information transfer, but the degree and nature of strain coupling to local properties, such as defect electronic energy levels are often not well understood [104, 17] due

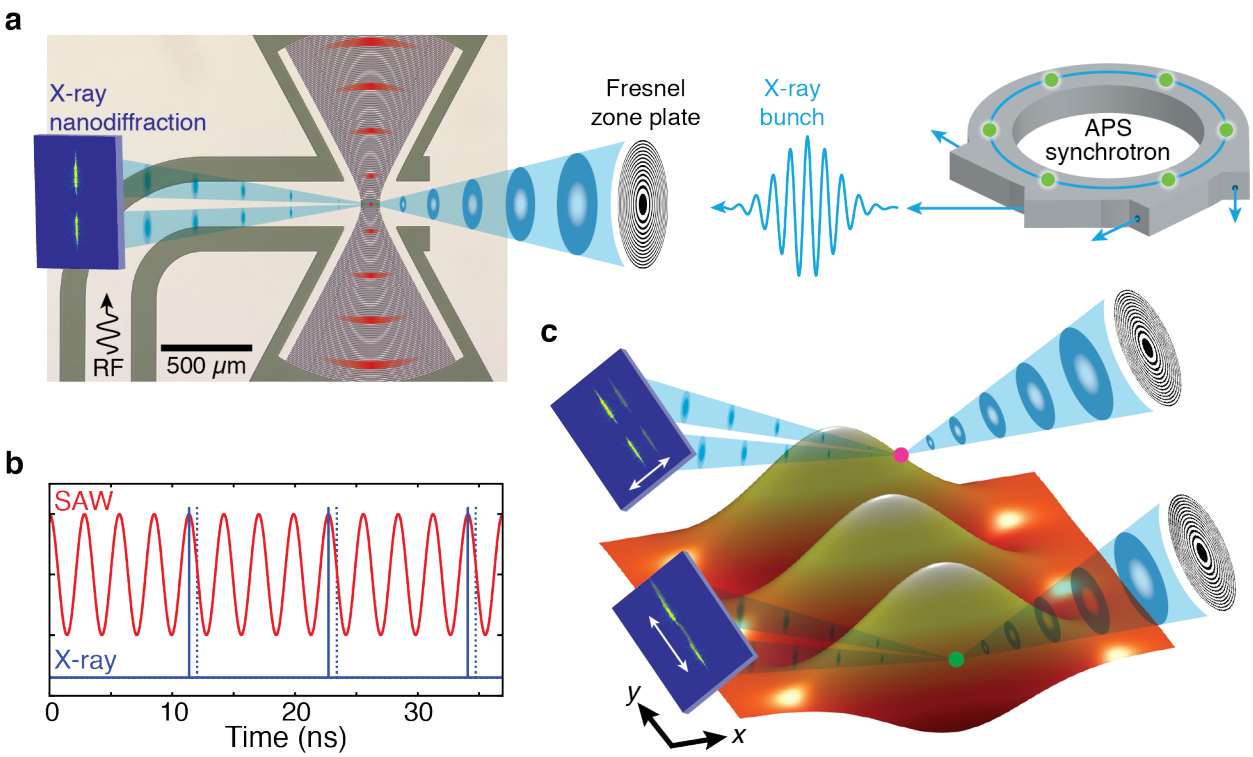

Figure 5.1: **Stroboscopic Scanning X-ray Diffraction Microscopy (s-SXDM) geometry.** **a**. Periodic bunch patterns of the Advanced Photon Source (APS) synchrotron are frequency matched to RF continuous wave excitation of a SAW (illustrated in red). Stroboscopic illumination allows for nanoscale SXDM of a virtually frozen wave. **b**. The time domain surface displacement of the SAW (red curve - 1 nm peak-to-peak displacement at 352 MHz) is synchronized to the time structure of the X-ray illumination (blue curve - 22 ps rms width at approximately 88 MHz). This allows a flexible measurement of the SAW amplitude by varying either time (detuned near-frequency match) or RF phase (at frequency match) to relatively displace the measurement to a new time slice (dotted blue line). **c**. The out-of-plane displacement of the SAW at a fixed point in time is represented by the orange isosurface, exhibiting both periodic lattice curvature along the wave longitudinal propagation direction $\boldsymbol{y}$ and transverse curvature along $\boldsymbol{x}$, at the magenta and green dots respectively, induced by Gaussian focusing of the standing wave. These curvatures induce orthogonal shifts in the far field diffraction pattern that oscillate as a function of the relative phase between the synchrotron time structure and the RF SAW excitation.

to the difficulty of directly measuring local nanoscale strain. Quantifying this coupling is especially important in the time domain, where dynamic sources of strain such as resonant acoustic waves can be used to manipulate spin states or control the transmission of single electron currents between qubits [105, 106].

Surface acoustic waves (SAWs) have been previously observed with frequency-matched

synchrotron X-ray diffraction, historically with diffraction micro-topography [107, 108] and with iterative phase retrieval of surface structure utilizing SAW satellite peaks [109, 110]. We report the development of a new approach to imaging dynamic bulk crystal strain using recent advances in nanoscale hard X-ray microscopy techniques at 3rd generation synchrotron sources, which have enabled the visualization of sub-picometer embedded crystal strain with nanometer scale spatial resolution [111]. Using Bragg diffraction contrast as a scattering mechanism, our approach gives access to femtometer atomic displacements ($\Delta c/c \sim 10^{-5}$) in crystalline materials with a real-space, in-plane spatial resolution given by a beam focus on the order of tens of nanometers and at depths from tens to hundreds of microns. By virtue of the high monochromaticity of the light, tuning the scattering specifically to the diffraction condition of the host material for quantum systems allows a strain contrast signal uncontaminated by the presence of capping material, transducer layers, or electrodes. This ability to access far-from-surface lattice perturbations in complex systems is combined with an ultrafast pulsed X-ray illumination, which is determined by the bunch structure of the synchrotron storage ring [112].

Here, we investigate acoustic strain modulation using 22 ps rms X-ray pulses separated by 11.37 ns synchronized to a SAW excitation that penetrates microns into the surface. In conventional pump-probe X-ray measurements, the synchrotron timing structure is used to synchronize an optical pump during pulsed stimulation of the sample [113]. Our measurement instead uses a frequency match of continuous radio frequency (RF) surface acoustic wave excitation to the ring time structure, in order to virtually slow or freeze periodic lattice fluctuations generated by a transducer fabricated on the 4H silicon carbide (SiC) host material without the need for a stimulation pulse. We demonstrate the impact of this approach by correlating the dynamic lattice curvature measurement of driven lattice fluctuations with photoluminescence changes from point defects caused by acoustic driving and piezoelectric effects near a etched microscopic structure.

5.2 Gaussian Focusing of Surface Acoustic Waves in SiC

Silicon carbide is a versatile and increasingly relevant material for quantum sensing and technological applications due to a rich variety of optically accessible defect spins with exceptionally long (millisecond) coherence times that are controllable up to room temperature [104, 6, 7, 15]. In comparison to diamond, SiC is available commercially on the wafer-scale with industrial growth processes established along with well understood micro and nanofabrication steps for the creation of electronic, mechanical, and optical functionality [114, 10]. As robust as SiC neutral divacancy ground state spins are for storing quantum information, their excited state electronic energy levels can be manipulated and split with small amounts of crystalline strain ($< 10^{-6}$) in the host material [17]. SAW phonons have been used to demonstrate quantum manipulation of defect electronic orbitals in diamond [115, 116] and spin states in SiC [103]. For the first time this study demonstrates a local measurement of the lattice perturbations created by a SAW near a fabricated microscale structural defect in SiC, responsible for locally enhancing strain fluctuations around divacancies.

Propagating and stationary SAWs have widespread usage in RF signal processing and electronics applications [117] and are typically realized using an interdigitated transducer (IDT) on a piezoelectric crystal surface. In this study we use a 500 nm thick piezoelectric transduction layer of sputtered aluminum nitride (AlN) on a 4H-SiC substrate with low film stress and fabricate an IDT to drive the SAWs. The IDT contains a Ti under-metal layer for both improved metal-AlN adhesion and X-ray fluorescence mapping. Considering that both 4H-SiC and AlN have isotropic Rayleigh wave velocities in their respective crystal planes, we apply Gaussian geometries, inspired by Gaussian optics and electromagnetism, to the IDT so as to form a nearly diffraction limited SAW spot size (Fig. 5.1a). Gaussian focusing provides increased acoustic power near the focus, which is useful for increasing spin-phonon coupling in hybrid quantum systems while minimizing SAW diffraction losses

in resonators [103]. The Gaussian IDT is geometrically designed to have a 1.25λ spot size (SAW wavelength $\lambda = 19.03$ μm) and Guoy phase incorporated for the lowest order Hermite-Gauss mode. Additionally, the piezoelectric AlN film is etched away at the SAW beam waist where 3λ of electrodes are removed to expose a window. The purpose of the window is to remove extraneous microstructures in the 4H-SiC caused by the internal film stress in the AlN epilayer clamping the substrate surface. Inside the IDT array, there is a standing wave produced by constructive interference from each of the individually phase matched electrodes.

5.3 Stroboscopic Scanning X-ray Diffraction Microscopy

The diffraction microscopy experiment sketched in Figure 5.1 consists of 8 keV X-rays generated by the Advanced Photon Source focused to a 25 nm FWHM beam spot by an interlaced double Fresnel zone plate [118] at the Hard X-ray Nanoprobe operated by the Center for Nanoscale Materials, Argonne National Laboratory. The sample is aligned to the 4H-SiC [0004] diffraction condition and the zone plate is raster scanned in real space relative to the sample position using an optomechanical nanopositioning system, allowing differential scanning of the nanofocused X-ray beam across the sample volume (Supplementary Fig. 2) [119]. The RF excitation for producing SAW phonons is matched to a multiple of the synchrotron storage ring frequency (~ 352 MHz). This creates Bragg diffraction from a virtually frozen wave curvature and strain that can be temporally swept by adjusting the relative phase of the RF signal generator to the synchrotron source using an RF IQ modulator (Fig. 5.1b). In a second approach for phase sampling we add a small detuning to the SAW frequency relative to the ring frequency, which causes the signal to beat and evolve in phase at the detuning frequency. The resulting slow, time varying diffraction allows the SAW oscillation amplitude to be efficiently and periodically sampled without adjusting the electronics. Both approaches yield similar results as a measure of local lattice distortion amplitude (Supple-

mentary Fig. 7). Here, the data we present are acquired in stroboscopic (time-sampled) mode with frequency detuning ($f_{ring} - f_{SAW} = 1 \pm 0.05$ Hz). The far-field diffraction patterns are sensitive to strain components along the diffraction condition and lattice curvature or slope. The two characteristic positions of high curvature on the Gaussian focused surface acoustic wave are marked as magenta and green dots in Fig. 5.1c. It is important to note that the directions of the lattice curvature gradient at the magenta and green points are mutually orthogonal, creating distinct oscillatory motions of the far-field diffraction patterns on the detector shown exaggerated in Fig. 5.1c. These diffraction pattern oscillations are maximized at a characteristic set of positions where the curvature gradient reaches a maxima along the wave - either inflection points along the SAW propagation direction (longitudinal lattice slope - magenta dot) or gradient maxima of the Gaussian focusing (transverse lattice slope - green dot).

Results of the s-SXDM measurement are shown in Figure 5.2. The IDT shown in Fig. 5.2a is aligned relative to the scanning directions using X-ray fluorescence (XRF) from the Ti under-metal layer of the Al patterned electrodes as in Fig. 5.2b. At each scanning position twenty images of the far field diffraction pattern are acquired at a 50 millisecond detector exposure time, allowing for stroboscopic sampling of two full periods. Oscillatory motions of the diffraction patterns are then separated into two components, one lying within the diffraction plane ($\boldsymbol{x}$-axis) and one orthogonal to the diffraction plane ($\boldsymbol{y}$-axis). These motions were primarily due to curvature inversion in the transverse and longitudinal (propagation) directions of the SAW, respectively. The images in Fig. 5.2c are calculated from peak-to-peak dynamic X-ray diffraction centroid shifts relative to the mean value at each position. This measure is used to remove spatially varying, time-independent lattice strain and curvature components in order to highlight SAW dynamics. Disorder visible in the longitudinal picture is primarily due to complex internal reflections from the AlN film windowing visible near the edges of both maps in Fig. 5.2c. Peak-to-peak displacement measurements fit to this curvature are consistent with a wave of $\sim$1 nm surface displacement amplitude over a 10 μm

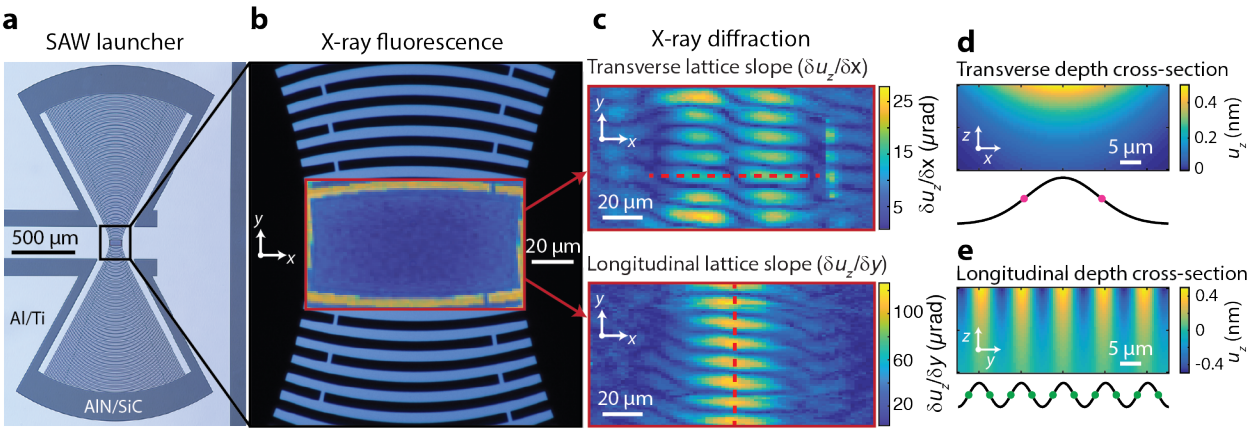

Figure 5.2: **Imaging of a Gaussian SAW. a**. with the wave propagation direction $\boldsymbol{y}$ aligned orthogonal to the scattering plane $\boldsymbol{x}$. **b**. The scanning X-ray Bragg diffraction measurements are registered relative to the patterned IDT using fluorescence from the Ti adhesion layer of the Al electrodes. The device background image is a dark field optical micrograph. **c**. The far-field X-ray diffraction pattern is sensitive to the local curvature (tilt) of the lattice planes calculated as the gradient of the displacement in two ordinal components. The oscillatory transverse and longitudinal shifts of the X-ray diffraction pattern oscillation are independently detected as peak-to-peak displacements in the centroid position spot relative to the X-ray scattering plane. **d,e**. The expected depth dependence of an ideal Gaussian surface acoustic wave displacement (u_z) along the transverse $\boldsymbol{x}$ (**d**) and longitudinal $\boldsymbol{y}$ (**e**) directions at the dashed red lines in (**c**). The transverse (longitudinal) curvature maxima, signified with magenta (green) dots, correlate with the double (single) lobed periodic features, respectively, experimentally observed in (**c**). The calculated displacements correspond to the experimentally observed curvature amplitude.

half-period (Fig. 5.2d,e). The curvature is sampled along a ~ 3 μm X-ray extinction length expected at the [0004] reflection oriented at a scattering angle of $\approx 18°$, resulting in a 1 μm depth sampling of the transverse and longitudinal curvature fluctuations. No fluctuations are measured when the SAW power was reduced to zero (Supplementary Fig. 6).

5.3.1 Imaging Structural Defects

Acoustic waves are often scattered by interactions with fabricated objects or lattice defects. In order to assess the divacancy response to locally induced curvature and strain, we fabricate a structural defect into the center of the SiC scanning window (Fig. 5.3a) to perturb the Gaussian SAW. This structural defect consists of a pit dry etched (~2.7 μm diameter, 1

μm deep) into the SiC surface. The dynamic (time-dependent) strain perturbation of the etch pit in response to the acoustic wave is expected to be relatively large, as shown by a mechanical model in Fig. 5.3b. This effect results in locally enhanced strain and piezoelectric effects in the 4H-SiC when the SAW is present, as simulated in Fig. 5.3c. Next, we probe the optical response of native divacancy defect ensembles, which emit photoluminescence (PL) in the near-infrared. By employing the technique Electrometry by Optical Charge Conversion (EOCC) [73], we all-optically map the divacancy ensemble charge state population in order to probe dynamic electric fields induced piezoelectrically in the vicinity of the microscopic structural defect. In this methodology, the optical charge conversion rates are sensitive to fluctuations in the local electric field (E^2), which we measure in the steady state by simultaneously illuminating the divacancy ensembles with both ultraviolet and near-infrared light. We find that PL contrast during SAW excitation is spatially maximized near the structural defect (Fig. 5.3d). These results correlate with the s-SXDM measurements of dynamic lattice curvatures where internal acoustic strains, detected by electric fields in the piezoelectric bulk 4H-SiC, are strongly enhanced near the etch pit corners. Furthermore, the depth dependence of PL contrast from the divacancies (Supplementary Fig. 4c) indicates that the dynamic strain and electric fields are located microns away from the SiC surface. This is in agreement with our numerical simulations (Fig. 5.3c) that reveal the linear strain amplitude near the structural defect base is over three times greater compared to strain from the propagating SAW amplitude alone.

We directly measure the dynamic transverse curvature amplitudes near the etch pit by s-SXDM (Fig. 5.4a). The expected instantaneous curvature of an unperturbed SAW is predicted with a simple phenomenological model assuming only Hermite-Gauss modes from the IDT. We find that an additional rotation degree of freedom relative to the scattering plane explains the weak S-shaped connections of the bimodal transverse curvature. This prediction is subtracted from the experimentally observed curvature amplitude in order to highlight the near-defect behavior, the results of which are shown in Fig. 5.4b. The etch pit

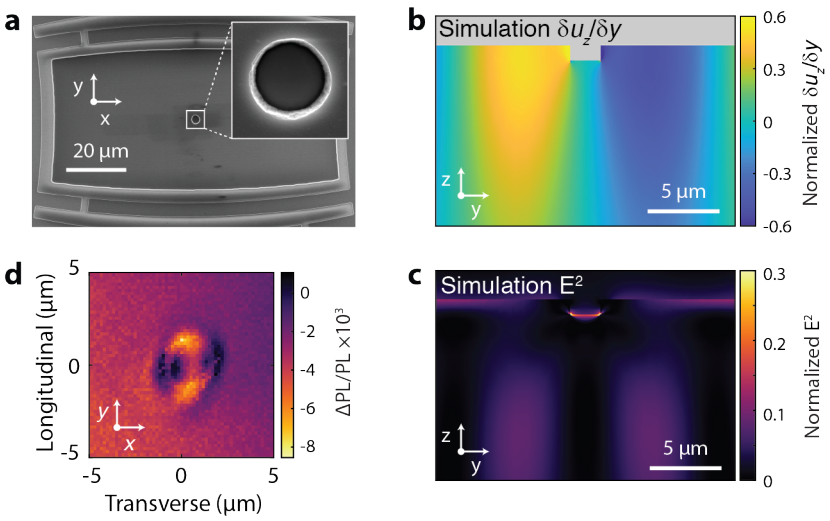

Figure 5.3: **Structural defect and internal piezoelectric response. a**. SEM image of model structural defect, an etched pit, located at the center of the SAW beam waist. **b,c**. Simulated depth cross-section of the longitudinal lattice curvature and electric field magnitude (E^2) in the SiC substrate. The finite element models are computed using COMSOL Multiphysics and show a time slice during continuous RF excitation of the SAW. Although the etch pit is located at a node in longitudinal curvature, increased strain and piezoelectric effects happen at the pit's base and corners. **d**. Enhanced dynamic piezoelectric effects at the pit are independently and all-optically mapped by native quantum defects using Electrometry by Optical Charge Conversion [73], which is sensitive to the local E^2. Peaks of signal are visible at the longitudinal pit edges, and the background is from stray electric fields (see Supplementary Fig. 4 for depth dependence of PL contrast).

is intended to create an outgoing secondary wave or a local reflection of the wave, which is weakly visible as patches of excess transverse amplitude and distortions of the longitudinal amplitude circularly surrounding the central position at a $\sim \lambda/2$ (9.5μm) radius.

Combining the nanometer-scale spatial resolution and stroboscopic feature of our X-ray imaging technique allows us to locally image both the static and actively driven lattice distortions around the etch pit. Static local strain induced by the dry etch process is relatively small and nonetheless can be directly visualized by the mean (time independent) diffraction pattern recorded at each scanning position (Fig. 5.4c,d). The static bound strain results can be understood as compressive (tensile) strain in the upper (lower) pit corners, respectively, which average and cancel each other when scanning through the center. At a higher degree of visibility in the dynamic variations (Fig. 5.4e) compared to an outgoing wave, and trapped

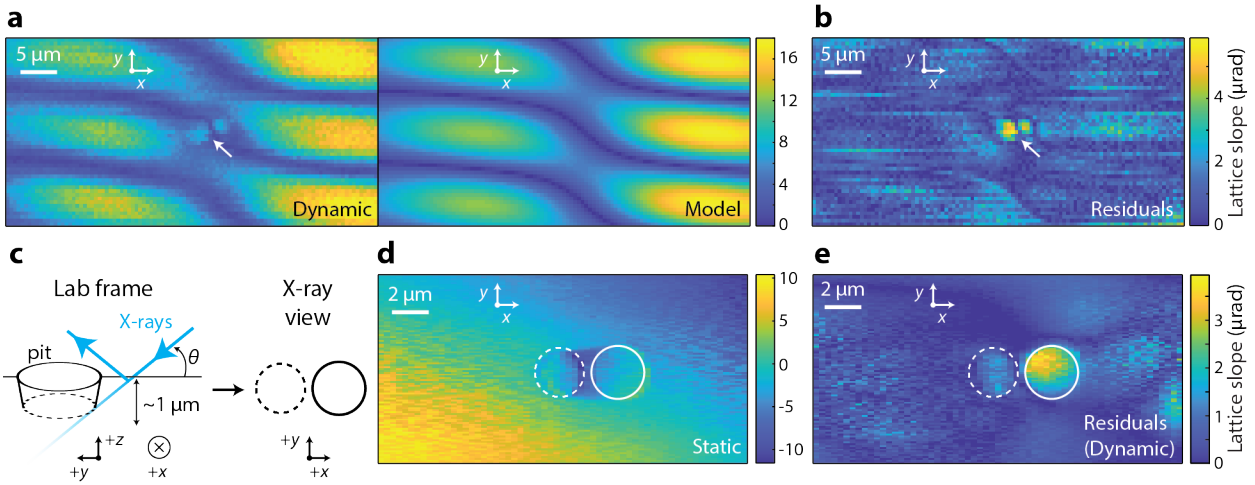

Figure 5.4: **Near structural defect dynamic curvature measured via s-SXDM. a**. (Left) Real - space maps of diffraction oscillation amplitude, gray circle show presence of the fabricated pit in the SiC surface. (Right) The expected instantaneous curvature predicted with a simple phenomenological model including Gaussian focusing and wave periodicity as free parameters. The weak S-shaped connection of the bimodal transverse curvature originates from a small (~ 2 deg) misalignment of the diffraction plane to the wave propagation direction. **b**. The best fit of the model parameters were then used to subtract the curvature of the unperturbed SAW, allowing approximate visualization of the outgoing secondary wave and clear visualization of a locally trapped high amplitude wave near the pit (dashed circle). The spatial step size in (a,b) is 500 nm, with a 25 nm spot size. **c**. SXDM sketch of the fabricated structural defect with a scattering angle $\Theta \approx 18$ degrees. The surface coordinate scanning is corrected for sample angle relative to X-ray beam. **d**. Nanoscale imaging near the pit of static strain, or lattice curvature, from the mean $\boldsymbol{x}$ centroid shift. **e**. Dynamic transverse curvature from the r.m.s. $\boldsymbol{x}$ centroid shift during stroboscopic imaging. The spatial step size in (d,e) is 50 nm, with a 25 nm spot.

within the diameter of the etch pit, we observe a strong bimodal peak. By raster scanning the beam and correlating the resulting bound strain, we determine that this trapped acoustic feature is microns below the surface and varying in time, demonstrating the value of this synchrotron microscopy method as a local direct measurement of defect interactions with acoustic waves. Such an effect could in principle be used to locally focus acoustics near quantum relevant defects within a nanostructure in order to achieve stronger time-varying distortions for state manipulation.

5.4 Conclusions

We demonstrated nano-focused, direct-space Bragg diffraction microscopy using the synchrotron timing structure to stroboscopically image lattice curvature. This new methodology enables three orders of magnitude higher spatial resolution versus previous topographic methods and access to independent ordinal components of lattice curvature and strain [120] rather than a single scalar projection of these quantities as in previous X-ray topographic studies. This is a necessary step towards the goal of simultaneous picosecond and nanoscale imaging of a single defect interacting with resonant local phonons. Future directions include the development of methods using nano-focused coherent diffraction imaging techniques such as 3D Bragg Projection Ptychography [121] in the dynamical diffraction regime, which has the potential to image dynamic strain at sub-10 nm 3D resolution near far-from-surface lattice defects.

We imaged local dynamic lattice perturbations induced by a Gaussian focused SAW interacting with a fabricated structural defect in 4H-SiC and correlated these perturbations with divacancy defect optical measurements. Our nano-focused hard X-ray diffraction imaging approach, based on the frequency matching of a synchrotron X-ray pulse structure to a RF transducer, can be extended to real-space imaging of crystal strain in the time domain with full control over the acoustic phase. The induced strain and dynamic lattice fluctuations observed hold important consequences for nanomechanical system engineering with local quantum defects, as indicated by the EOCC photoluminescence contrast enhancement near the structural defect. A key feature enabled by this methodology is removing ambiguity in assessing quantum structure-function relationships, through the congruent ability to image in real-space lattice fluctuations that directly relate to photoluminescence changes from optically-active point defects. Beyond quantum materials, this method is generally applicable to acoustically manipulated structures and crystallographic defects where simultaneous picosecond time, nanoscale spatial, and sub-picometer strain displacement sensitivity can be used for unique local visualization of mechanical energy transduction.

5.5 Materials and Sample Fabrication

The high purity semi-insulating 4H-SiC substrate from Cree Inc. had ∼500 nm AlN sputtered by OEM Group Inc. onto the wafer Si-face with low film stress. The IDT, comprising of 20 nm thick Ti and 150 nm thick Al, was fabricated on the AlN/SiC substrate. The circular pit (Fig. 5.3a) was measured to be ≈ 950 nm deep by AFM using an Asylum Research Cypher S and the depth was also confirmed with laser confocal microscopy using an Olympus LEXT OLS5000. All layers were processed by optical lithography techniques and inductively coupled plasma etching. Extensive fabrication and device characterization details are shown in the supplementary materials.

5.6 Supplementary Data and Analysis

5.6.1 Electronic schematic

The stroboscopic Scanning X-ray Diffraction Microscopy experiment uses a radio frequency (RF) signal generator matched to a multiple of the Advanced Photon Source (APS) synchrotron storage ring frequency (f_{ring}) to drive the interdigitating transducer device. The ring frequency in Fig. 2 is calibrated to be roughly $f_{ring} = 351,934,790$ Hz with a long term drift of a few Hz per hour and a short term drift in a random walk of < 0.1 Hz/s. Over a few months, we found that f_{ring} can changed less than 20 Hz. As the current synchronization signal from the APS control room in this experiment is too jittery to use directly as a trigger input, the signal generator is manually set to f_{ring} with a reference and connection to the APS control room via an ethernet connection. This allows for independent control over the center frequency (f_0) while continuously obtaining appropriate offsets to remain stroboscopic with respect to the storage ring timing. The frequency offset from the APS control room is accurate to within 0.1 Hz and mitigates most of the long term drift of the ring frequency. The short term drift, from APS doing feedback and adjusting the ring frequency, as well as

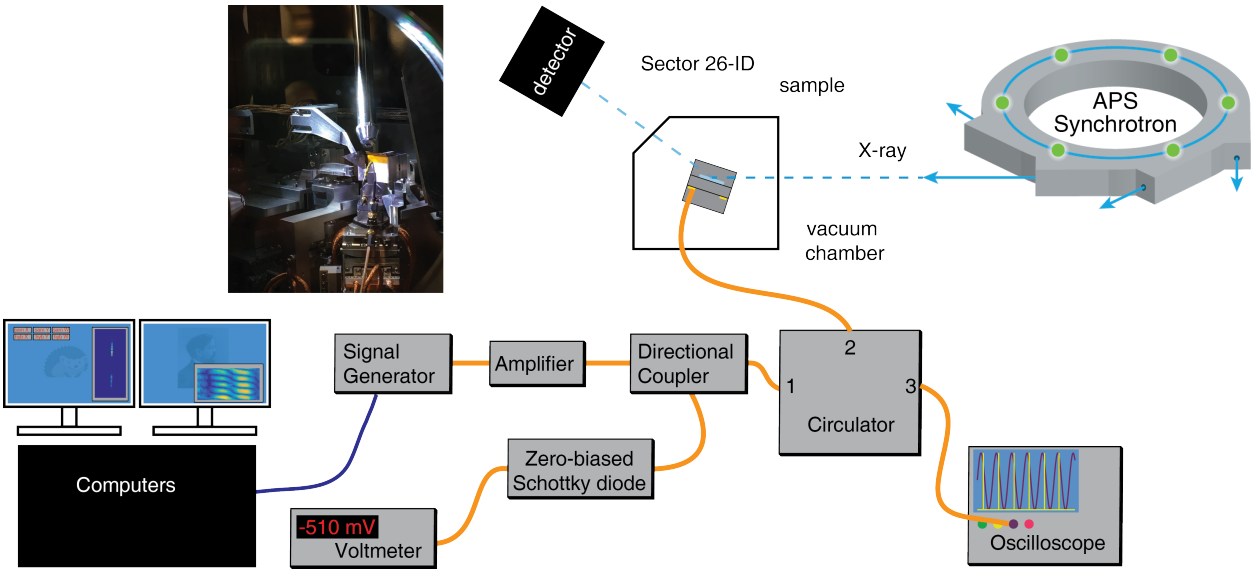

Figure 5.5: **Electronic schematic of the stroboscopic experiment.** Matching the frequency of the X-ray bunches from the Advanced Photon Source with the signal generator requires setting the frequency of the signal generator with a real-time frequency offset using a reference from the APS control room. The RF signal is then amplified, coupled to a Schottky diode, and sent through a circulator before entering the sample chamber. The Schottky diode is used to verify the approximate RF power at the device and a circulator minimizes back reflections along with sends the outgoing signal to an oscilloscope.

the inability to trigger the RF signal directly causes variations in the phase delays, which currently limits this imaging technique to only to non-propagating acoustics. Improved fiber connections from the APS control room to the beamline are planned to improve the timing accuracy in order to allow for full phase control imaging of the acoustic waves.

From the signal generator (SRS SG396), the RF signal goes to an Amplifier (Minicircuits ZHL-20w-13s+), a directional coupler (Fairview Microwave MC51008-20), and finally a RF circulator (Fairview Microwave SFC3340S) before entering the vacuum chamber to the sample. The -20 dB coupling port from the directional coupler is connected to a zero-biased Schottky diode (Fairview Microwave SMD0112) to measure the RF power at the sample, and the reflections from the sample are sent via the circulator to an oscilloscope to verify the RF timing with the APS ring, and X-ray experiment. Typical RF power at sample was 27-30 dBm. An RF electronic schematic of the experiments device is shown in 5.5.

5.6.2 Layout of Hard X-ray Nanoprobe

The CNM/APS Hard X-ray Nanoprobe (HXN) facility at beamline 26-ID of the Advanced Photon Source (APS), Argonne National Laboratory (ANL) delivers a hard X-ray beam tunable over the 6-12 keV spectral range and focused to 25 nm spot size in-plane onto the sample. The HXN uses interferometric control to maintain relative positional drift of the focusing optics and sample less than 10 nm/h. The working distance between the X-ray focusing optics and the sample is typically a few millimeters. This enables a variety of *in situ* and *operando* experiments with variable temperature, applied electric and magnetic fields, and liquid and gaseous environments. Nanoscale structural information, such as crystallographic phase, strain, and texture, are measured at the HXN at a ∼25 nm real-space spatial resolution by recording how a crystalline sample diffracts the incident nanofocused X-ray beam while on the Bragg condition as the focus is scanned over the sample. Bragg ptychography, a scanning coherent diffraction imaging technique that exploits the coherence of the nanofocused x-ray beam combined with iterative phase retrieval methods, provides nanoscale structure and lattice strain information within crystalline samples at a demonstrated resolution extending to 5 nm, well beyond the resolution of current hard X-ray focusing optics. Both the scanning nanodiffraction methods and future, time-resolved studies with the HXN will provide new abilities tools for probing acoustic interactions with crystal ordering, defects, and phase transitions in nanomaterials.

5.6.3 Microfabrication

The 4" diameter 4H silicon carbide (SiC) wafer had ∼ 500 nm of aluminum nitride (AlN) sputtered on the surface by OEM Group Inc. The AlN film had a X-ray diffraction rocking curve of 1.52° FWHM on the [0002] peak and the film stress was -42 MPa. All device layers were fabricated by optical lithography and dry etching with inductively coupled plasma (ICP) in a PlasmaTherm Apex SLR.

The IDT device layer was formed by electron-beam evaporation with 20 nm of titanium

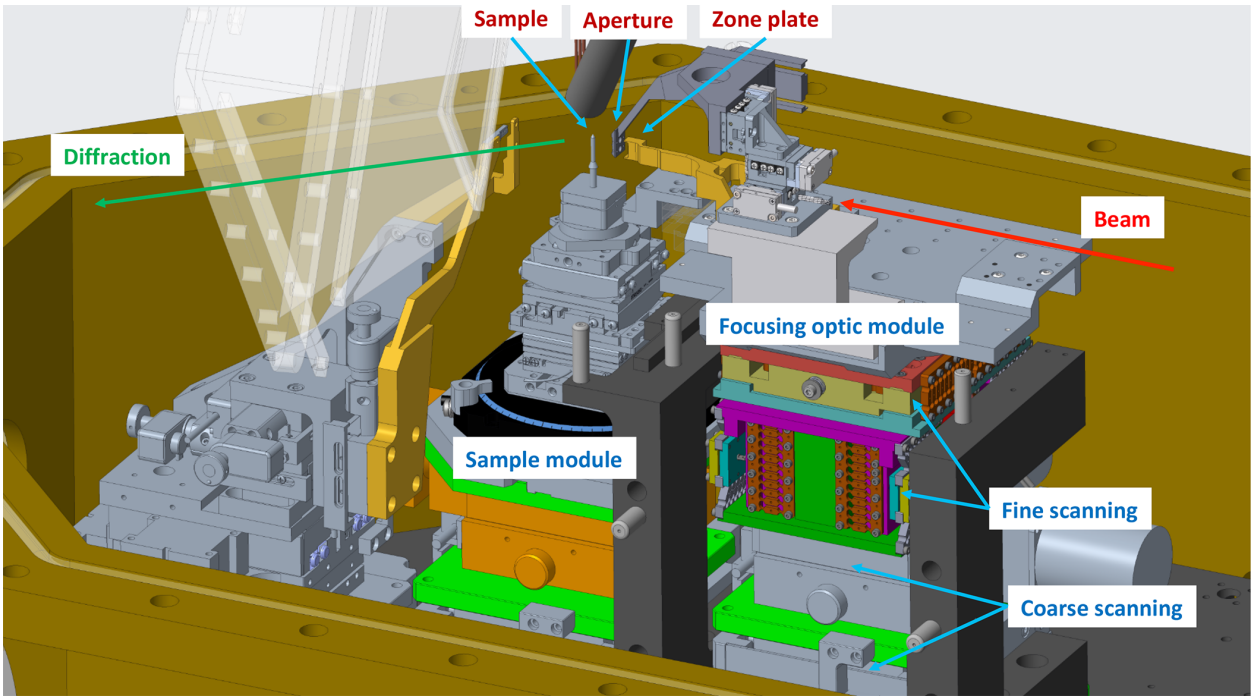

Figure 5.6: **Nanoprobe chamber and instrument schematic.** X-rays from the Advanced Photon Source are downselected to a monochromatic coherent fraction prior to being focused onto the sample by a hard X-ray Fresnel zone plate focusing optic. The sample scanning directions are vertically upwards and downstream (along the X-ray beam, in the plane of the sample surface) - rotating about the X-ray downstream vector at the zero diffraction angle.

(Ti) and 150 nm of aluminum (Al) using an Angstrom EvoVac. The Ti serves both as an adhesion layer for the Al and as a luminescent layer for X-ray fluorescence mapping. Optical lithography, utilizing a 0.9 μm thick photoresist, for the interdigitated transducer (IDT) pattern was subsequently performed using a GCA AutoStep 200. To direct write the autostepper reticle for this process, we used a Heidelberg MLA150. The IDT pattern was transfered to the Ti/Al metal device layer by ICP etching with $Cl_2/BCl_3/Ar$ with flow rates of 30/30/10 sccm, respectively, and 400 W ICP power. Next, we define a "film window" at the acoustic beam waist in the AlN piezoelectric transduction layer by direct-write optical lithography, using the Heidelberg MLA150. This releases inhomogeneous SiC strain caused by the AlN. ICP etching of the AlN film window was accomplished using $Cl_2/BCl_3/Ar$ with flow rates of 30/30/10 sccm, respectively, and 400 W ICP power. Finally, direct write optical

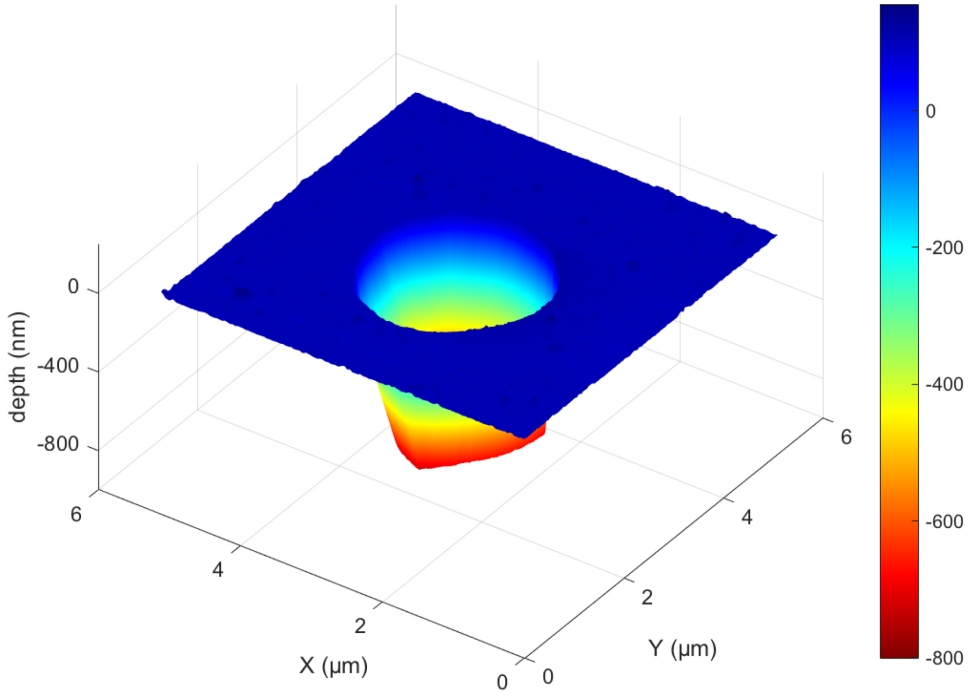

Figure 5.7: **Atomic force microscopy (AFM) measurements of the etch pit.** The pit depth is $\sim$ 950 nm deep. This is the same sample and pit that is shown in Figs. 3,4. Since the AFM tip's triangular shape distorts the in-plane dimensions, the SEM images in Fig. 3a should be consulted for the pit shape and diameter. The color scale is in nanometers.

lithography for the circular pit employed a $\sim$ 2.9 μm thick photoresist and purposefully over-exposing a 1 μm circle. The circular pit pattern was transferred to the 4H-SiC by ICP etching using SF_6/Ar with flow rates of 40/10 sccm, respectively, and 500 W ICP power. We characterized the etched pit depth by atomic force microscopy (AFM) measurements (Fig. 5.7). Our AFM measurements also found that the SiC surface had up to 5 nm of increased roughness after ICP etching, which was transferred from the rougher AlN film when fabricating the film window.

5.6.4 Divacancy photoluminescence response

Optically-active point defects in the 4H-SiC substrate provide numerous spin and electronic properties, sensitive to environmental perturbations. While the ground state spins of point

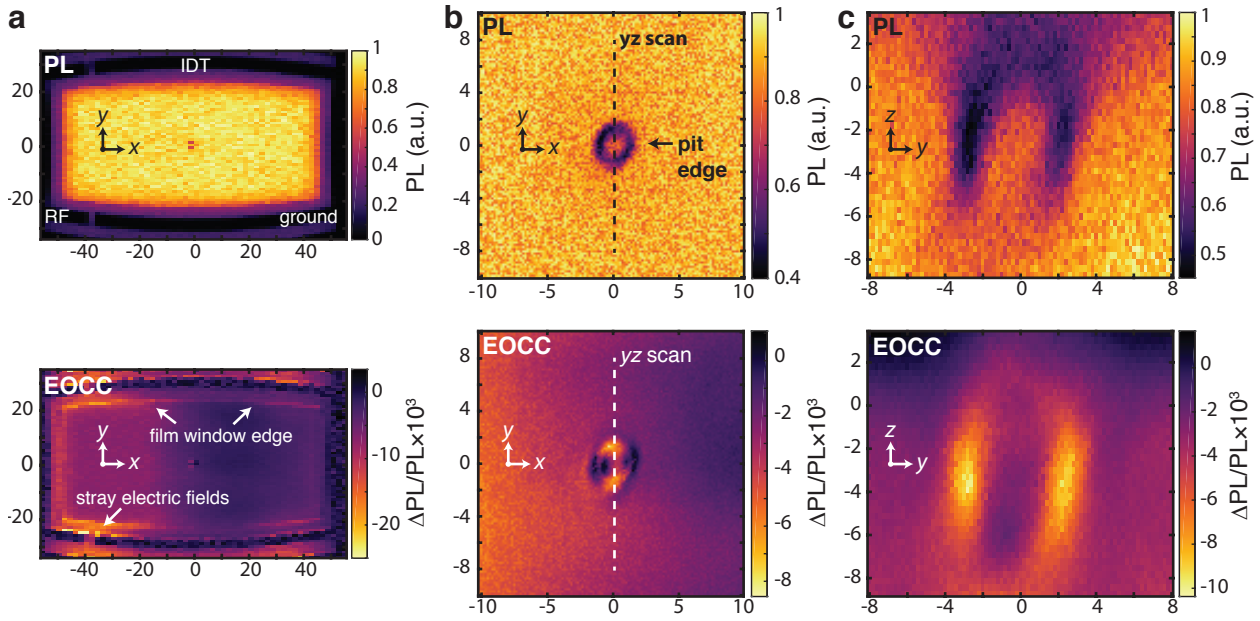

Figure 5.8: **Divacancy photoluminescence (PL) mapping and electrometry near the fabricated structural defect. a**. Overview (***xy*** map) of the Gaussian SAW beam waist region of the device. **b**. Scan (***xy*** map) near the etched pit. A reduction in PL near the pit is slightly visible in a 2 μm radius about $(x, y) = (0, 0)$. EOCC mapping shows two lobes of contrast (reduced PL during SAW driving) near the longitudinal edges of the pit. **c**. Depth cross-sectional scan (***xz*** map) through the pit at the dashed line in (**b**). In all panels the upper image is PL from divacancy defects in the SiC substrate, and the lower image is continuous-wave EOCC of the divacancies. The ***x***, ***y***, and ***z*** directions correspond to longitudinal, transverse, and sample c-axis directions, matched to sample orientations in the s-SXDM experiments.

defects, including the neutral divacancy (VV^0) and negatively charged silicon vacancy (V_{Si}^-), in SiC can be used to sense small magnetic fields [5], their charge state provides a straightforward means of measuring and imaging internal electric fields [73]. Here, we use the technique Electrometry by Optical Charge Conversion (EOCC) on native VV defect ensembles in the SiC substrate as local sensors of mechanics. In our implementation of EOCC, we use two laser colors on VV ensembles: 405 nm to perform charge state resets and 976 nm for optical charge conversion as well as read out. While illuminating with 976 nm, the rate of optical charge conversion, detected by photoluminescence (PL) from the VV on a photodiode, is dependent on the radio frequency electric field at the VV defects. Since SiC is piezoelectric, bulk strain will generate an internal electric field and be detected in three dimensions via

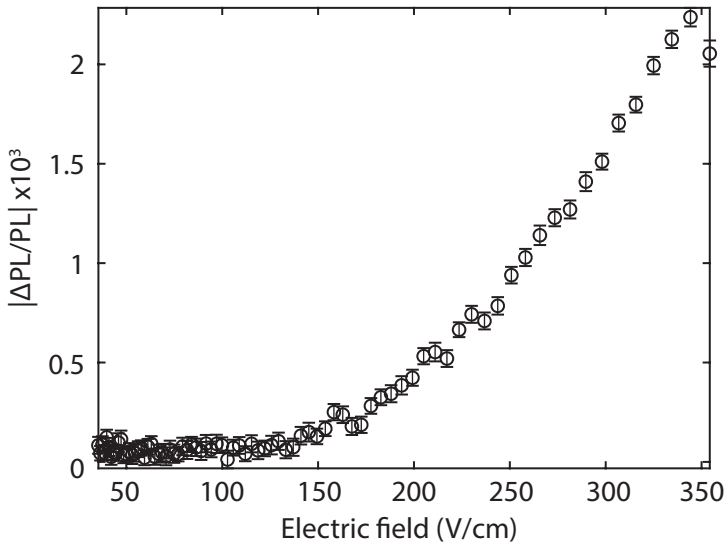

Figure 5.9: **Sensitivity calibration for electrometry by optical charge conversion (EOCC).** Measured magnitude of EOCC optical contrast as a function of linear electric field amplitude (converted from input power) in between the coplanar waveguide gap. Error bars are one standard deviation.

EOCC.

In the absence of RF driving of the Gaussian SAW, PL from the VV ensembles is spatially homogeneous over the SiC in the region where an AlN was removed to create a film window (Fig. 5.8a). Over the AlN, we observe that the PL is reduced by $\approx 70\%$, which is likely due to lower optical transmission through the sputtered polycrystalline AlN layer. An overview map of EOCC (Fig. 5.8a) yields 'hot spots' near the electrodes and film window edge, along with a gradient across the device center originating from the RF side - we attribute all of these EOCC features to stray electric fields from the IDT and RF drive. EOCC from the SAW far away from the pit is too weak to be measured on top of the background from stray electric fields.

Next, we zoom in near the pit and take finer in-plane images of PL and EOCC contrast (Fig. 5.8b). Even though the pit walls cause laser scattering and induce an optical shadow, the EOCC map reveals two maxima spatially resolved near the longitudinal ($\pm\boldsymbol{y}$) pit edges. Therefore, the SAW standing wave generates dynamic strains near the structural defect edges in the direction of acoustic propagation. Additionally, the EOCC contrast near the

pit qualitatively agrees with s-SXDM results (Fig. 4), which show the structural defect's dynamic strain is enhanced over the regular Gaussian SAW mode. The background EOCC contrast gradient from stray RF electric fields is visible even micrometers away from the pit (Fig. 5.8b). From depth cross-sectional scans, we find that the two lobes of EOCC contrast are maximized beneath the SiC surface and correlate to lower pit corners, in agreement with the phenomenological simulation in the main text Fig. 3c.

In order to calibrate the EOCC signal, we measure the EOCC response in the capacitor gaps (center pin to ground) formed by the input coplanar waveguide near the Gaussian IDT (Fig. 1a). The calibration is obtained by combining the EOCC contrast as a function of input microwave power with finite-element (COMSOL) simulations of the electric field. In turn, we estimate that the peak electric field measured near the pit is approximately 300 V/cm at 400 mW of drive power after background corrections. Using knowledge of strain and electric field distributions in the 4H-SiC caused by mechanics (Figs. 3 and 5.10), we can convert the estimated peak electric field of 300 V/cm to an estimated strain amplitude. We can see that electric field and strain scale together linearly from the piezoelectric equations (stress-charge form),

$$\begin{aligned} \boldsymbol{\sigma} &= \mathbf{c}^{\mathrm{E}}\mathbf{S} - \mathbf{e}\mathbf{E}\,, \\ \mathbf{D} &= \boldsymbol{\epsilon}\mathbf{E} + \mathbf{e}\mathbf{S}\,, \end{aligned} \tag{5.1}$$

where the tensors $\boldsymbol{\sigma}$ is stress, $\mathbf{S}$ is strain, $\mathbf{D}$ is the electric displacement field, $\mathbf{E}$ is the electric field, $\boldsymbol{\epsilon}$ is the matrix of dielectric constants, and $\mathbf{c}^{\mathrm{E}}$ is the elasticity (i.e. stiffness tensor). Note that normally we use $\varepsilon_{ij} = \frac{1}{2}(\frac{\partial u_i}{\partial x_j} + \frac{\partial u_j}{\partial x_i})$ in the paper and supplement to represent strain, although this equation shows $\mathbf{S}$ to distinguish the variables more easily. By applying a linear scale factor found from COMSOL simulations in the time-domain, we find the estimated uniaxial strain near the pit from 400 mW of RF drive power is $\varepsilon_{zz} = 8.3 \times 10^{-5} \pm 4.7 \times 10^{-5}$. The uncertainty in this estimation in part comes from which spatial

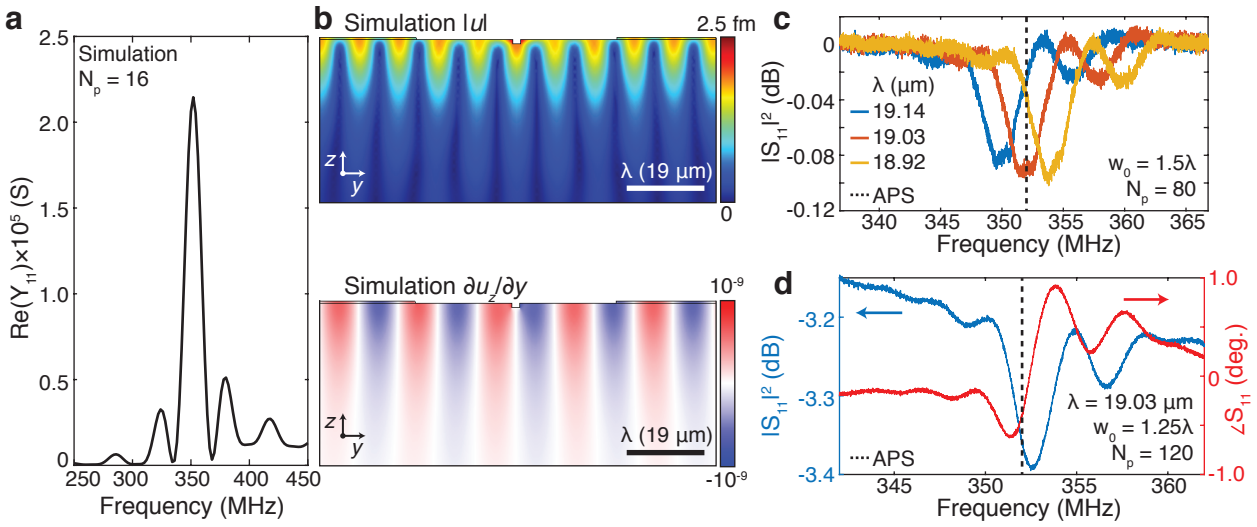

Figure 5.10: **RF characterization of Gaussian IDT. a**. Frequency domain simulated admittance of a planar IDT using COMSOL Multiphysics 2D (yz) cross-section. The simulation accurately predicts the IDT center frequency (352 MHz), and therefore acoustic velocity $v_{SAW} = \lambda f_0$, for a wavelength of 19.03 μm. **b**. Time domain simulated absolute displacement (upper image) and longitudinal lattice slope (lower image). The applied IDT voltage is 1 mV. The simulations confirm that the etched film window have a negligible effect on the standing wave mode and displacements are enhanced at the structural defect walls and corners. **c**. RF reflection measurements for Gaussian IDTs of varying the acoustic wavelength, plotted with subtracted magnitude offsets. While keeping the Gaussian geometry factors (e.g. spot size w and electrode finger pairs Np) constant, the IDT center frequency f_0 is easily tunable by changing λ. **d**. RF measurement of the Gaussian IDT used in s-SXDM experiments, wirebonded to a printed circuit board. The Gaussian IDT geometry appears to induce an asymmetric relative amplitude of the sinc-squared side peaks. Sub-MHz errors in f_0 may come from non-uniform AlN thickness across the wafer. The target frequency of Advanced Photon Source (APS) synchrotron timing structure is shown as a black dashed line.

locations in the simulation are used for the linear scale factor, therefore, one the dynamic strain near the pit corner should be treated as 10^{-4} order of magnitude.

5.7 SAW characterization and modeling

In order to find the proper SAW wavelength (λ) for s-SXDM experiments, we first by fabricate planar, single transducer planar IDTs (no Gaussian focusing) using single layer lithography. By attempting various acoustic wavelengths, such as 8, 12, 16 μm (not shown), and per-

forming RF characterization with a vector network analyzer (VNA), we can estimate that we require an IDT with $\lambda \sim 19 \pm 0.1$ μm to get a center frequency $f_0 \sim 352$ MHz. This agrees with an planar IDT simulation (Fig. 5.10a). Simulated 2D cross-sections ($\boldsymbol{yz}$) of Rayleigh wave produced at this f_0 and λ are shown in Fig. 5.10b, including the structural defect and AlN film window. Between multiple rounds of device fabrication, we find that chips from the middle of the wafer and 1 cm from the wafer's edge (containing the same IDT designs) produce center frequency variations $\leq 0.3\%$. This suggests that the effective Rayleigh waves velocities between devices are reproducible and the AlN film thickness is sufficiently uniform across the wafer.

The high degree of device repeatability and AlN thickness uniformity allows us to easily fabricate many IDTs and vary their geometry until the frequency performance is optimal for s-SXDM. We fabricate Gaussian IDTs ($w_0 = 1.5\lambda$ and 80 electrode finger pairs) and vary the acoustic wavelength λ in the mask design between devices by 11 nm. Even though optical lithography has limited resolution for a single feature, the increments in electrode periodicity work well enough to experimentally find the λ needed for s-SXDM (Fig. 5.10c). Using $\lambda = 19.03$ μm for s-SXDM, we fabricate Gaussian IDTS with extra electrodes for improved SAW admittance and a smaller SAW focus ($w_0 = 1.25\lambda$). Small structural defects, like an etch pit, had little to no impact on RF reflection results. The 1 port reflection measurement with VNA for the device used in experiments is shown in Fig. 5.10d. The IDT could not be impedance matched to 50 Ω because AlN and SiC are strong piezoelectric substrates, and we did not want to use even more electrode finger pairs, which could have risked making the IDT bandwidth too narrow and cause f_0 to miss the APS synchrotron bunch frequency.

We show a full three-dimensional simulation of a SAW wave interacting with a pit in 5.11. This simulation uses approximately planar (non-curved) electrodes with an aperture similar to the Gaussian acoustic focal spot, and a symmetry plane is used at $x = 0$ because the device design is in fact symmetric. All scalebar values are from the simulation and can be

globally, linearly scaled together in order to compare to experimental values (1 nm maximum displacement expected in experiments). The strain distributions and E^2 field from the SAW in this model qualitatively agreed with the 2D model shown in the main text (Fig. 3). EOCC enhanced by the pit is expected to be detected on the longitudinal ($\pm y$) sides of the pit at the lower corner from (5.11d,e). Curvature (i.e. variations in lattice slope) enhancements are predicted from the simulation (5.11c), however, this effect is much more noticeable in the transverse curvature map near the pit (5.11f) because there is a node in $\frac{\partial u_z}{\partial y}$ at $x = 0$ due to the mirror plane symmetry.

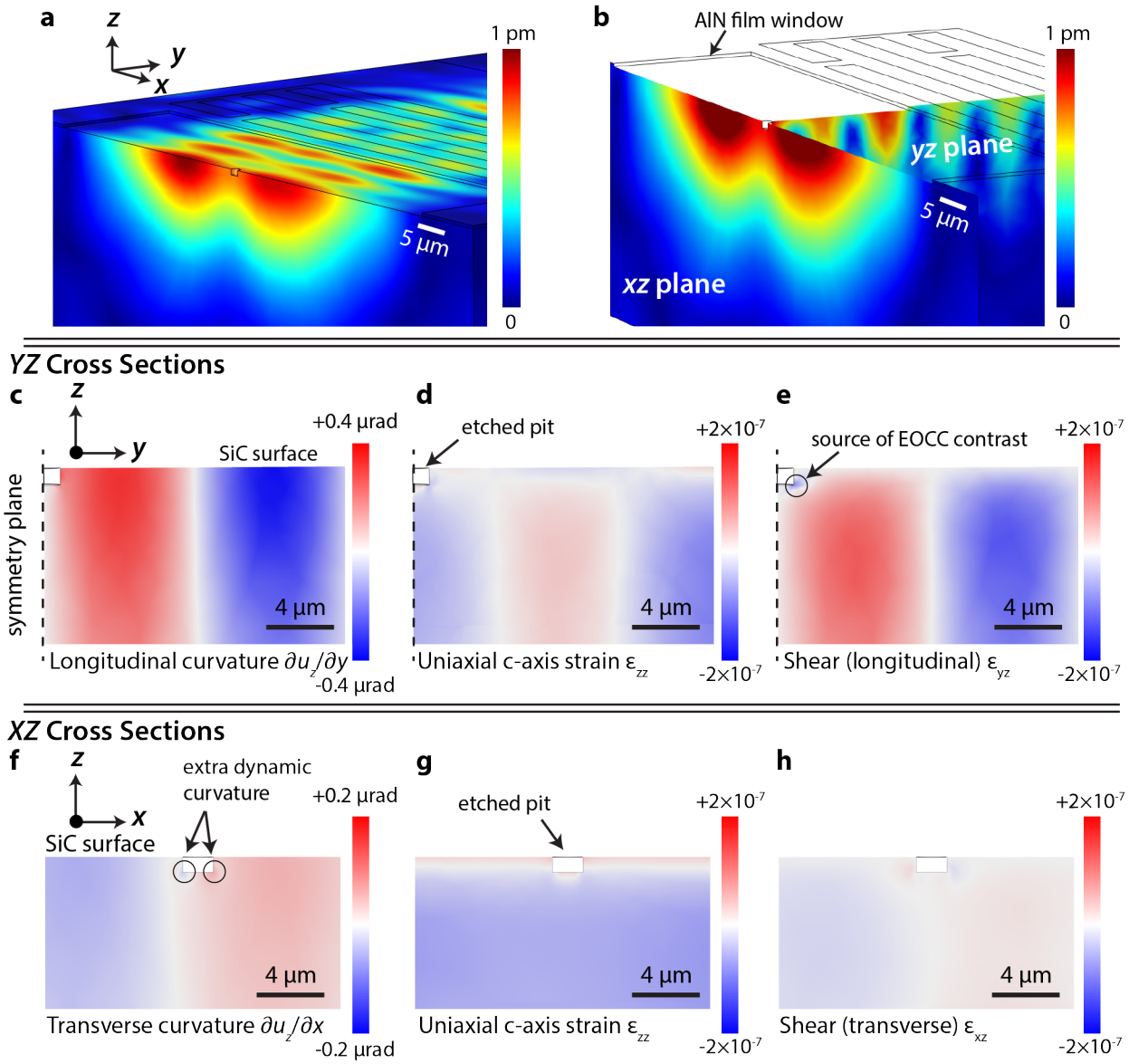

Figure 5.11: **Finite Element Model (COMSOL Multiphysics) in 3D of SAW interacting with pit. a**. Surface displacement profile of the AlN/SiC. The SAW is generated in the time domain with linear (non-Gaussian shaped) electrodes for simplicity for 4 oscillations. The models boundary conditions (x confinement) and finite planar electrode size distort the SAW transverse mode profile into have two lobes. This is not the case for our experimental Gaussian IDT. **b**. Cross-sectional view of the SAW illustrating the longitudinal yz-plane and transverse xz-plane. **Longitudinal Cross-Sections (yz)**: **c**. Longitudinal curvature. **d**. Uniaxial strain along SiC [0001]. **e**. Shear in the yz-plane (couples piezoelectrically to in-plane electric fields). **Transverse Cross-Sections**: **f**. Transverse curvature. (**g**) Uniaxial strain along SiC [0001]. **h**. Shear in the xz-plane (couples piezoelectrically to in-plane electric fields).

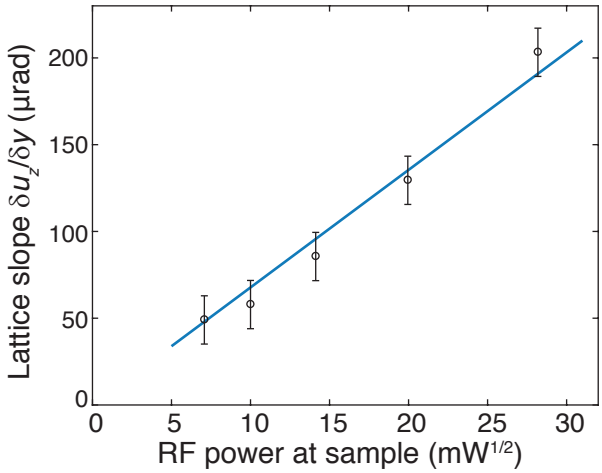

Figure 5.12: **RF power dependence of the SAW detected by s-SXDM.** Linear fit of longitudinal lattice slope ($\delta u_z/\delta y$) to the square-root of applied RF power. This is consistent with SXDM measuring lattice distortions from the SAW displacement and strain amplitude. SXDM measurements are performed at the SAW's maximum curvature near an IDT for consistency. Dynamic lattice slope was obtained from the Bragg peak X centroid standard deviation. Each data point is collected after waiting at least 15 minutes for the sample to thermally stabilize.

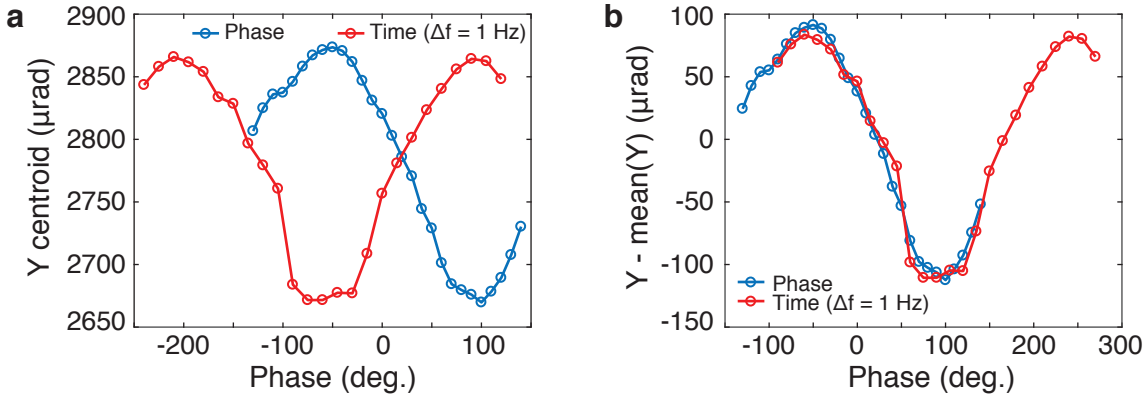

Figure 5.13: **Stroboscopic phase sweeps of the SAW. a**. Analyzed longitudinal X-ray diffraction centroid as a function RF phase. We show results with no frequency detuning while adjusting the signal generator (blue) and results using a 1 Hz frequency detuning with a time delay defining the SAW phase (red). **b**. Centroid data with the mean subtracted. The red trace has an arbitrary phase offset in order to overlay the two datasets.

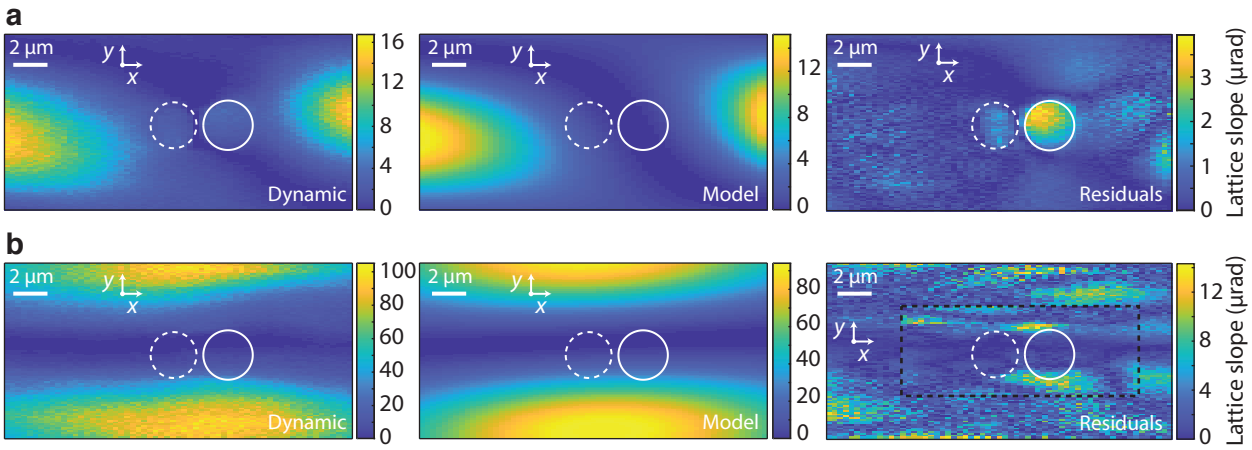

Figure 5.14: **Dynamic transverse and longitudinal curvatures near the structural defect.** From left to right the images are the raw data of stroboscopic SXDM, model of curvature produced by a surface acoustic wave containing a small rotation in-plane, and difference. The pit location is marked by dashed and solid white circles, representing the lower and upper portions the pit (see Fig. 4c). **a**. Transverse curvature plotted as the lattice slope $\partial u_z/\partial x$. **b**. Longitudinal curvature plotted as the lattice slope $\partial u_z/\partial y$. A second scan was taken close to the pit for lower noise, which is inset inside the dashed black box.

Chapter 6

Spin-Phonon Interactions Addressed by Gaussian Acoustics

The following chapter is adapted from previously published work in reference [103].

6.1 Introduction

Hybrid quantum systems [1] leverage the strengths of various modalities of representing quantum information, including optical photons for sending quantum states across long distances, spins for information storage, and microwave superconducting circuits for computation, with the potential of using nanomechanics as an intermediary quantum bus. For instance, coherently exchanging quantum information between optically active defect spins and mechanical resonators [122] provides a route to couple optical photons to microwave frequency phonons in a hybrid quantum system. Optically active defect spins in SiC, such as the neutral divacancy [6], have recently been shown to support long-lived spin states [7, 15, 123] a variety of quantum controls [5], and spin-photon interfaces [20] compatible with quantum entanglement protocols. Importantly, SiC is a piezoelectric material and supports mature fabrication processes for production of high quality micro-electromechanical systems (MEMS). Although progress has been made coupling spins to mechanics in similar

defect systems, including the NV center in diamond with coherent sensing using single spins [124, 125], strain tuning[40, 39], and mechanical driving [42, 44, 43, 54] defects in SiC are well positioned to solve the materials challenges of coherently manipulating spins with strain and strong coupling of spins with phonons.

While static strain will generate shifts in ground state ($s = 1$) energy sublevels, resonant a.c. strain can coherently drive electron spin transitions. Large in-plane dynamic strains can be generated by surface acoustic wave (SAW) devices, which are well developed for radio frequency filters and offer simple engineering approaches for fabricating low loss resonators. SAW devices have also been proposed as hybrid quantum transducers [102] and used to demonstrate coupling to superconducting qubits [126, 127, 8] along with optomechanical interactions involving defect excited states [115, 128].

Here, we demonstrate acoustically driven $\Delta m_{\mathrm{s}} = \pm 1$ spin transitions, where $m_{\mathrm{s}} = 0, \pm 1$ is the spin projection, on divacancy spin ensembles in 4H-SiC. We further demonstrate $\Delta m_{\mathrm{s}} = \pm 2$ spin transitions through the Autler-Townes effect, mechanical Rabi oscillations, and comparing the relative coupling strengths of inequivalent divacancy defects. These results are well described by our theoretical model developed from a combination of direct experimental observations and Density Functional Theory (DFT) calculations of anisotropic spin-strain coupling coefficients. We find that uniaxial strain and shear drive divacancy spins with coupling strengths of similar magnitude, but with generally different relative phase and selection rules. These experiments utilize a patterned Gaussian SAW phonon resonator that focuses strain and reduces resonator mode volumes in analogy to Gaussian optics. To image the mechanical modes of our Gaussian SAW devices, we use a unique nanoscale scanning X-ray diffraction technique that directly measures acoustic lattice perturbations. In addition, spatial responses of Autler-Townes splittings are well explained by ensemble averaging shear and uniaxial strain from the SAW mode. Shear provides an important way of controlling three-level spins (qutrits) with phonons and opens avenues for coupling spins with MEMS.

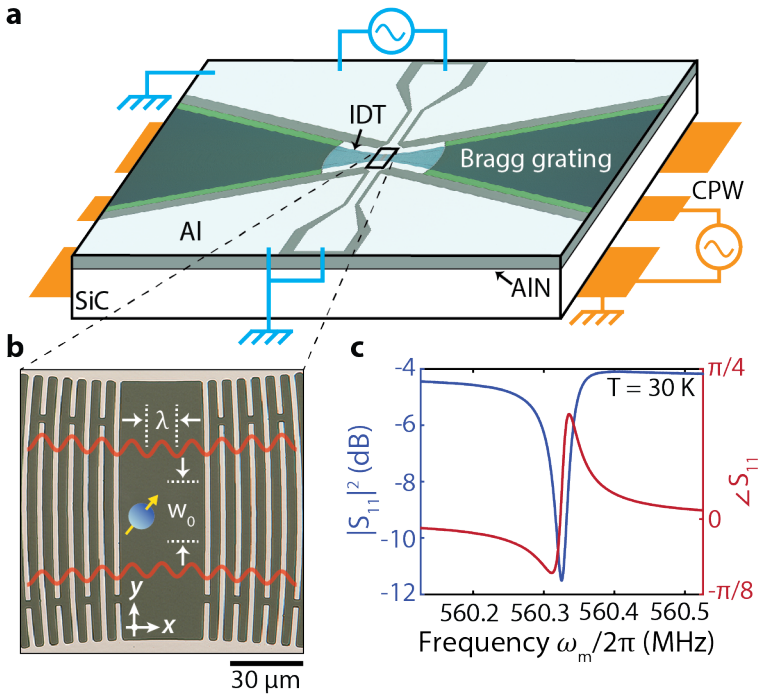

Figure 6.1: **Strain focusing with a Gaussian SAW resonator.** **a**. Schematic of the SAW device geometry fabricated on sputtered AlN on a 4H-SiC substrate. Microwaves drive spin transitions mechanically through the SAW resonator (cyan) and magnetically from the backside coplanar waveguide (orange). **b**. Optical micrograph of the Gaussian SAW resonators acoustic focus ($\lambda = 12$ μm, $w_0 = 2\lambda$) with red lines illustrating the waves out-of-plane displacement (u_z). **c**. Magnitude (blue) and phase (red) measurements of the 1-port reflection of the Gaussian SAW resonator used in spin experiments.

6.2 Gaussian SAW Devices for Spin Manipulation

We first describe device design and characterization with a nanoscale X-ray diffraction imaging method, followed by spin manipulation. To amplify the piezoelectric response of the SiC substrate, we use a thin, sputtered aluminum nitride (AlN) layer on the SiC surface before fabricating a SAW resonator to create radio frequency mechanical strain. Standard planar SAW resonator designs span wide apertures, often greater than 100 acoustic wavelengths (λ), distributing the strain across large crystal areas. Since AlN and 4H-SiC have isotropic in-plane Rayleigh wave velocities [59] (5790 and 6830 m/s, respectively), we fabricate simple Gaussian geometries, inspired by Gaussian optics, to focus strain while also suppressing acoustic diffraction losses (Fig. 6.1a,b). A patterned aluminum interdigitated transducer

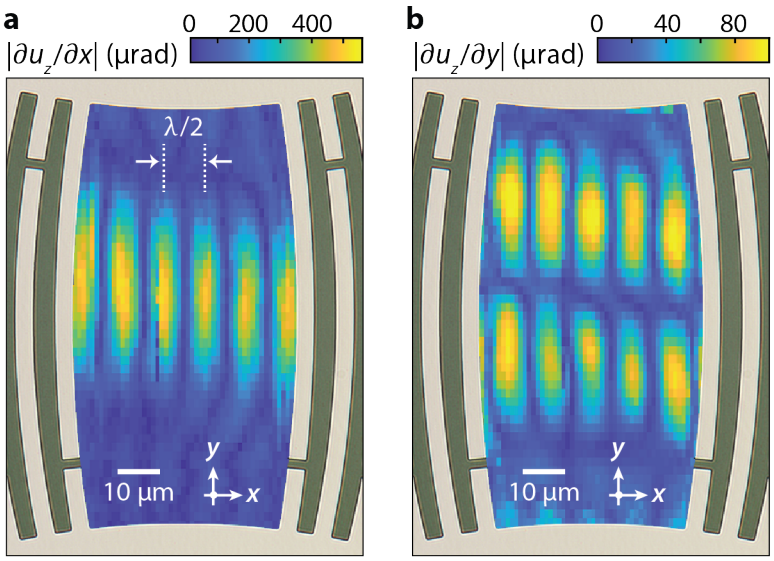

Figure 6.2: **Nanoscale X-ray imaging of the Gaussian acoustic mode.** Mechanical mode from a similar Gaussian SAW device ($\lambda = 19$ μm, $w_0 = 1.25\lambda$), directly measured with s-SXDM using the 4H-SiC [0004] Bragg peak. This quantifies the SAW peak-to-peak longitudinal (**a**) and transverse (**b**) lattice slopes at the acoustic beam waist. The image is skewed vertically due to sample drift during measurements.

transmits SAWs ($\lambda = 12$ μm), while grooves in AlN form Bragg gratings that act as SAW cavity mirrors to support a resonator frequency $\omega_m/2\pi \approx 560$ MHz and loaded quality factor of $\sim 16,000$ (Fig. 6.1c) at 30 K. The Gaussian SAW resonator internal quality factor ($Q_i \approx 22,400$ at 30 K) is likely limited by the polycrystalline AlN layer at low temperatures (analysis shown in Fig. 6.15). In our experiments the Gaussian geometries for enhanced strain focusing and reduced resonator mode volumes facilitate larger strains for fast coherent manipulation of electron spin states.

To directly visualize the Gaussian mechanical mode, we use stroboscopic scanning X-ray diffraction microscopy (s-SXDM) to image the phonons with nanoscale resolution (see Ch. 5). This technique utilizes coherent X-rays from a synchrotron radiation light source, generated at 8.00 keV and focused to a 25 nm spot size (3σ), and Bragg diffraction contrast to enable local measurements of lattice curvature and strain along a particular crystal orientation [111, 121]. We frequency match the radio frequency excitation to a Gaussian interdigitated transducer with the timing structure of the synchrotron storage ring in order to measure

the peak-to-peak amplitude of the acoustic standing wave. Due to the frequency matching requirements for s-SXDM, we use a SAW transducer without a cavity (see Methods for device specifications), which is designed to produce a spatial strain mode similar to resonators used in spin experiments. Scanning the nano-focused X-ray beam in real space clearly shows the SAW profile (Fig. 6.2a) is consistent with the fabricated geometry and approximately nanometer Rayleigh wave displacements. The dynamic transverse lattice slope (Fig. 6.2b), caused by a local lattice plane tilt towards the $\pm y$ direction, is expected from a Gaussian focus and SAW confinement. These X-ray measurements confirm that the SAW out-of-plane displacement (in phase with the in-plane uniaxial strain required for spin driving) is maximized at the resonators precise center and demonstrate the value of using X-ray diffraction microscopy for studying quantum devices [129] and materials.

6.3 Optically Detected Acoustic Paramagnetic Resonance

Electron spin ground state sublevels of divacancy defects are typically measured using optically detected magnetic resonance (ODMR) with $\Delta m_{\mathrm{s}} = \pm 1$ transitions magnetically driven by microwave fields. Due to the defects intersystem crossing, ODMR probes the spin projections of $|\pm 1\rangle$ versus $|0\rangle$ through changes in photoluminescence. The ground state spin Hamiltonian neglecting hyperfine interactions takes the form, z z

$$H/h = \gamma \mathbf{B} \cdot \mathbf{S} + \mathbf{S} \cdot \mathbf{D} \cdot \mathbf{S} \tag{6.1}$$

Where h is the Planck constant, γ is the electron gyromagnetic ratio ($\mu_{\mathrm{B}} \approx 2.8$ MHz/G), $\mathbf{B}$ is the external magnetic field vector, and $\mathbf{D}$ is the zero-field splitting tensor (also referred to as D_{ij}). In the absence of lattice strain, the divacancy spin-spin interaction simplifies to $D_0 S_z^2$ where $D_0 \approx 1.336$ and 1.305 GHz, depicted in Fig. 6.3a, for c-axis oriented defect

configurations [18] hh and kk, respectively. The zero-field splitting Hamiltonian is sensitive to local lattice perturbations [17] such as thermal disorder, an applied electric field, or strain. When the lattice is perturbed by a small strain, characterized by a tensor ϵ_{kl}, the zero-field splitting tensor is generally modified by $\Delta D_{ij} = G_{ijkl}\epsilon_{kl}$, where G_{ijkl} is the spin-strain coupling tensor. The symmetry of the spin-strain coupling tensor is determined by the local C_{3v} symmetry of the hh and kk configurations for divacancy (Fig. 2.6) and also applies to the NV center in diamond [47]. We utilize off-diagonal Hamiltonian elements containing ΔD_{ij} to drive resonant spin transitions with phonons, and consider both $\Delta m_s = \pm 1$ and ± 2 transitions for full ground state $s = 1$ spin control.

We first demonstrate mechanical driving of $\Delta m_s = \pm 1$ spin transitions with the Gaussian SAW resonator. The point group symmetries of the divacancy in SiC allow for non-zero spin-strain coupling coefficients for zero-field splitting terms that contain the anticommutators $\{S_x, S_z\}$ and $\{S_y, S_z\}$ (derivation in Ch. 2). In order to probe acoustic paramagnetic resonance, we tune the axial magnetic field (B_0) such that the spin $|0\rangle$ to $|-1\rangle$ transition frequency is matched with the SAW resonator (Fig. 6.3a). It is critical to design an experimental measurement sequence insensitive to stray magnetic fields from electrical currents in the interdigitated transducer. To disentangle these effects, we use an interlaced pump/laser probe sequence as well as lock-in amplification to measure the difference in luminescence when the spin resonance frequency is shifted away from the cavity resonance via modulation of B_0 with a small coil. Spin rotations are primarily driven and detected during the SAW cavity ring down period without radio frequency driving, although the spin ensemble will also encounter some residual magnetic resonance when the drive is turned back on due to lingering optical-spin polarization. We detect higher photoluminescence contrast when the radio frequency drive is matched to our SAW cavity resonance (Fig. 6.3b), whereas smaller, residual contrast is detected when the drive is far off the SAW resonance. When the photoluminescence contrast is normalized by ODMR experiments from magnetic driving, the kk/hh mechanical drive rate ratio is 0.89 ± 0.10, which agrees with our theoretical model and DFT

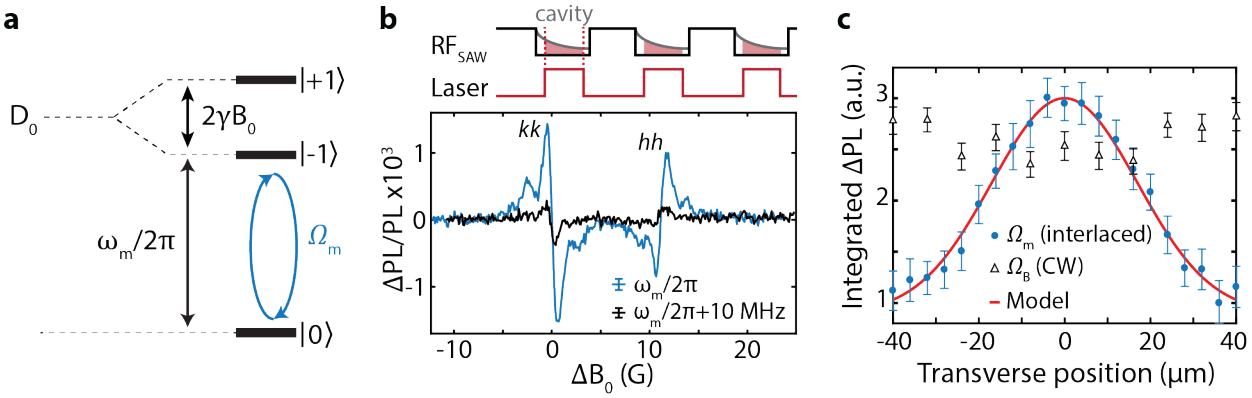

Figure 6.3: **Optically detected acoustic paramagnetic resonance in silicon carbide.** **a**. Energy level diagram showing the SAW frequency on resonance with the spin transition between the $|0\rangle$ and $|-1\rangle$ states. **b**. (Top) Interlaced pump-probe sequence during magnetic field-modulation. (Bottom) Photoluminescence (PL) contrast at 30 K when electrical excitation is on and off cavity resonance ($\omega_{\mathrm{m}}/2\pi = 559.6$ MHz). Radio frequency power is 32 mW at sample, and $\Delta \mathrm{B}_0$ is in reference to the drive frequency. **c**. Integrated photoluminescence contrast from kk resonance (evaluated at $\Delta \mathrm{B}_0 = 0$) as a function of the SAW resonator transverse position. Driving on-resonance (Ω_{m}) uses the interlaced sequence from (**b**), whereas off-resonance data (Ω_{B}) uses a continuous, non-interlaced sequence. The radio frequency power is 200 mW at the sample, and the beam waist model is $\exp[-y^2/(w_0^2)]$, using fabrication parameters and a scaled amplitude. All error bars are 95% confidence intervals.

calculations (ratio ~ 1.0) where shear couples more strongly to $\Delta m_{\mathrm{s}} = \pm 1$ transitions than does uniaxial strain (Table 6.2). The transverse spatial dependence (Fig. 6.3c) confirms that the photoluminescence contrast we measure on resonance matches our Gaussian resonators mechanical mode shape. Magnetic field driving from the transducer, on the other hand, results in a flat profile (two-dimensional spatial mapping is shown in Fig. 6.9). The long cavity ring up time prevents us from performing pulsed Rabi oscillations, though this could be solved using fast B_0 pulses to tune the spin resonance frequency. Our demonstration of $\Delta m_{\mathrm{s}} = \pm 1$ transitions by phonons enables direct photoluminescence contrast (optical detection) of resonant spin-strain coupling for sensing applications without electromagnetic microwaves.

6.4 Coherent Magnetically Forbidden Spin Transitions

To complement $\Delta m_s = \pm 1$ spin driving, we further use the strain coupling terms $S_x^2 - S_y^2$ and $\{S_x, S_y\}$ in the zero-field splitting Hamiltonian to show $\Delta m_s = \pm 2$ spin transitions. For these transitions, photoluminescence contrast from ODMR cannot directly measure resonant strain without extra electromagnetically driven spin resonance because photoluminescence contrast is insensitive to differences between $|+1\rangle$ and $|-1\rangle$ states. The mechanical transition rate (Ω_m) is instead measured using Autler-Townes (AC Stark) splittings, where in the dressed basis, the new eigenstates are split in energy by Ω_m. This splitting can be observed in the ODMR spectrum. We use a continuous magnetic microwave pump (Rabi frequency $\Omega_B : \pm 1 \sim$ MHz) for $|0\rangle$ to $|\pm 1\rangle$ transitions while the SAW is driven at a constant frequency $\omega_m/2\pi$ (Fig. 6.4a). Dressed state level anti-crossings are most clearly seen when the $|\pm 1\rangle$ spin sublevels are tuned to the SAW resonance frequency. The dressed spin eigenstate energies observed for a 400 mW drive power on the Gaussian SAW resonator closely match predictions for $\Omega_m/2\pi \approx 4$ MHz (Fig. 6.4b). Additionally, the Autler-Townes splitting scales linearly with square-root of radio frequency drive power delivered to the SAW, which is expected as Ω_m is linearly proportional to strain (Fig. 6.4c). The resolved Autler-Townes splitting shows that the mechanical drive rate is faster than the ensemble spin inhomogeneous linewidth (decoherence rate), allowing for measurement of coherent Rabi oscillations.

We mechanically drive coherent Rabi oscillations of kk electron spins using the pulse sequence in Fig. 6.4d to differentiate between populations transferred to $|+1\rangle$ versus $|-1\rangle$ spin states. The spin ensemble inhomogeneous linewidth ($\sim$ 1 MHz) and relatively long cavity ring up time ($2Q_i/\omega_m \approx 16\mu$s) prevent fast mechanical pulsing, so we keep the mechanical drive on continuously. A pair of magnetic microwave π pulses defines the effective mechanical pulse time τ seen by the spin ensemble (Fig. 6.4d). Using this pulse sequence and positive ODMR contrast of kk defects, normalized photoluminescence values of ± 1 can be interpreted as $|\mp 1\rangle$ spin populations, respectively, before the second magnetic π pulse. We find that three-level system dynamics are necessary to explain the observed

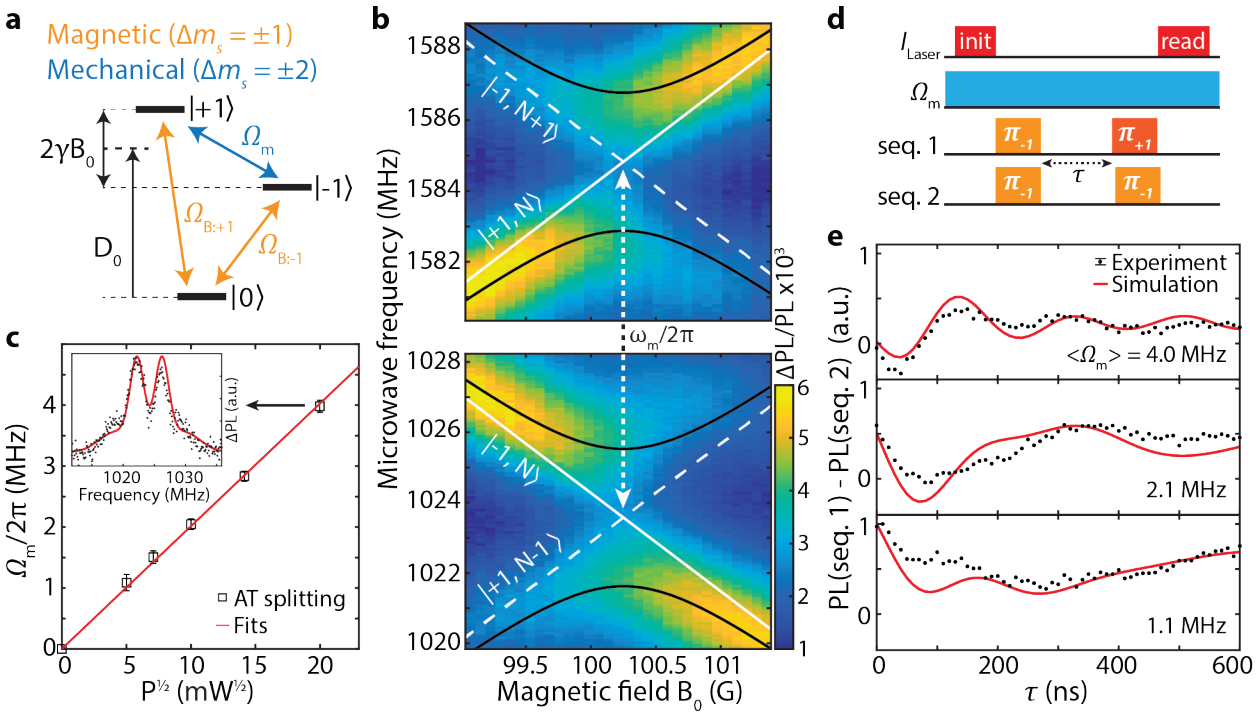

Figure 6.4: **Coherent mechanical driving of kk spin ensembles. a**. Divacancy ground state illustration with magnetic ($\Omega_{\mathrm{B:}\pm1}$) and electromechanical (Ω_{m}) drives shown. **b**. Autler-Townes measurement on a kk ensemble at 30 K; dressed for N phonons (black) and undressed (white) spin transitions. The mechanically dressed eigenstates and corresponding transitions are split by Ω_{m}. **c**. Mechanical transition rates obtained from Autler-Townes splittings agree with a linear fit to the square-root of drive power. Error bars are 95% confidence intervals from fits. Inset shows an Autler-Townes splitting measurement (black) at $B_0 \approx 100$ G, with Gaussian fits (red) to the divacancy electron spin and weakly coupled nearby nuclear spins. **d**. Pulse sequence for mechanically driven Rabi oscillations. **e**. Mechanically driven Rabi oscillations at ∼400, 100, and 25 mW, respectively, and typical error bars are 95% confidence intervals. The photoluminescence signal for each Rabi oscillation is normalized by a global factor, and simulations are ensemble average predictions with inhomogeneous strain distributions from finite element modeling.

mechanical Rabi oscillations shown in Fig. 6.4e, in particular the ensemble population at $\tau = 0$. Specifically, during each magnetic pulse, the simultaneous mechanics Ω_{m} drives some unintended population transfer between the $|+1\rangle$ and $|-1\rangle$ spin states, which leads to a modified initial projection of the population at $\tau = 0$.

The observed Rabi oscillations qualitatively agree with spin simulations predicted using a physical model consisting of spin-strain coupling parameters from DFT calculations and experimental knowledge, including (i) the ensemble spin resonance spectrum from ODMR,

(ii) spin-mechanical drive amplitudes from fitted Autler-Townes splittings, (iii) spatial distribution of spins in the SiC bulk and implanted layer, (iv) finite element analysis of strain and shear distributions from Rayleigh waves, and (v) optical point spread function (Fig. 6.11). Our physical model reproduces the mechanically driven Rabi oscillation rates, asymmetric decay shape, higher frequency features from hyperfine detuned spins, and initial spin population at $\tau = 0$. This demonstrates we can mechanically drive $\Delta m_s = \pm 2$ transitions with a Rabi frequency about four times greater than the ensemble ODMR linewidth. During Rabi oscillations with 400 mW radio frequency power, we estimate from input-output theory applied on a SAW model (derivation shown in Section 6.8) that the mechanical field strength is approximately 10^{-3} strain order of magnitude, in agreement with DFT simulation results. Short Rabi decay times are primarily explained by SAW strain inhomogeneity across the ensemble, though another source of damping may be present in the experiments. Manipulation of single divacancies [7, 20] will offer the opportunity to extend coherent Rabi oscillations up to or beyond the spin T_2^*. Coherent Rabi oscillations in ensembles for quantum phononics applications could be improved by using higher quality material and controlled aperture implantations [130] for more homogeneous strain distributions.

6.5 Quantum Sensing of Gaussian Acoustics

We spatially map the Gaussian SAW mode in order to show that $\Delta m_s = \pm 2$ transitions occur due to the mechanical driving and not due to any stray electromagnetic fields [131]. We map changes in the Autler-Townes splitting, shown in Fig. 6.5a, at a constant magnetic field while sweeping the laser position across the SAW beam waist. In the resonators transverse direction, a clear Autler-Townes splitting maximum, and therefore resonant strain amplitude, is observed at the Gaussian acoustic focus. Ω_m as a function of transverse position is well described by a model Gaussian beam waist of the fundamental mode in the device geometry (FWHM = 3.3λ) and not due to predicted stray electric fields (Fig. 6.10). Scanning the

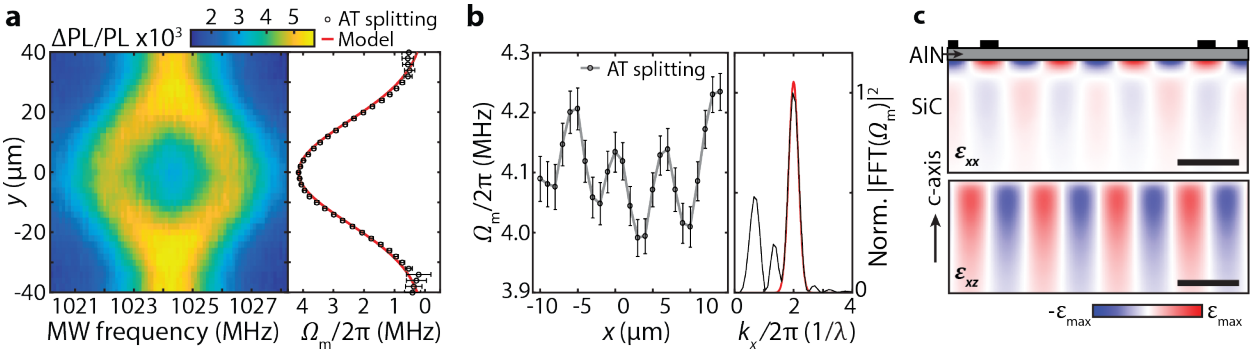

Figure 6.5: **Spatially mapping mechanical spin drive rates. a**. Autler-Townes splitting of kk $|-1\rangle$ sublevel as a function of transverse position (left) at $x = 0$ and the analyzed mechanical transition rates (right). The beam waist model only uses fabrication parameters with a scaled amplitude. **b**. Mechanical transition rate (left) as a function of longitudinal position at $y = 0$, plotted with a line through the experimental data. FFT (right) shows a peak and Gaussian fit in red at the expected acoustic periodicity $\lambda/2$ (6μm). **c**. Strain ϵ_{xx} and ϵ_{xz} of the SAW modeled with COMSOL Multiphysics.

laser spot longitudinally (Fig. 6.5b), along the SAW propagation, reveals oscillations in the Autler-Townes splitting at the resonators acoustic half wavelength. Surprisingly, in conflict with assumptions of a simple sinusoidal standing wave containing uniaxial strain nodes (Fig. 6.2a,b), we observe the mechanical drive rate oscillations are less than 5% peak-to-peak. This is contrary to expectations from previous theoretical work [46] neglecting the full strain tensor, so we interpret our experimental results using a spin Hamiltonian under anisotropic strains also including shear.

The spatial mapping results can be understood by employing a combination of finite-element simulations in conjunction with DFT calculations of spin-strain interactions. The $\{\bar{1}\bar{1}20\}$ mirror plane symmetry in 4H-SiC is broken by shears ϵ_{xz} and ϵ_{xy}, which drive the spin out-of-phase with $\epsilon_{xx} - \epsilon_{yy}, \epsilon_{yz}$ (mirror symmetry preserving). In our experiments, the Gaussian SAW beamwaist is oriented to propagate in the $\{1\bar{1}00\}$ plane (defined as the xz-plane). The mechanical transition rate is $\Omega_{\mathrm{m}} = \frac{1}{2}(G_{11} - G_{12})\epsilon_{xx} - 2iG_{14}\epsilon_{xz}$ corresponding to $\Delta m_{\mathrm{s}} = \pm 2$ transitions, where the spin-strain coupling tensor $\mathbf{G}$ is written in Voigt notation. In Fig. 6.5c we show finite element simulation results for uniaxial strain ϵ_{xx} and shear ϵ_{xz} for a Rayleigh wave propagating along the x direction. We model the experimental

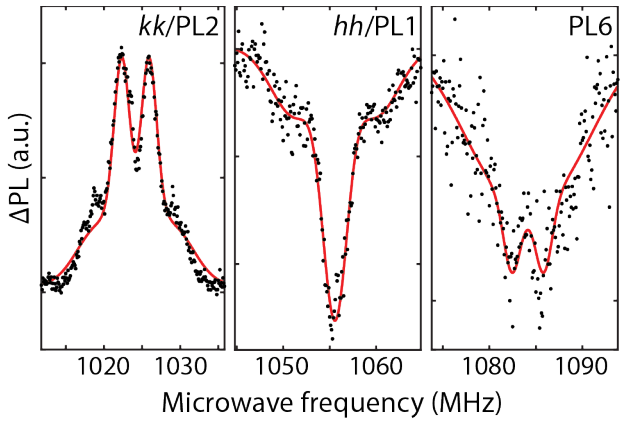

Figure 6.6: **Divacancy defect comparisons of mechanical drive rates.** Autler-Townes splitting measurements (black points) for kk, hh, and PL6 with Ω_m ~4.0, 1.1, 3.4 MHz, respectively, under the same conditions. The fits (red lines) are from simultaneously fitting the data with ODMR spectra to common Gaussian distributions (Fig. 6.14). All error bars are 95% confidence intervals from fitting and measurements are performed at 30 K.

results by converting the strain maps to Ω_m using G calculated from DFT, which is then convolved with both an optical point-spread function and estimated spatial distribution of the spins (Fig. 6.11). In our model, spatial averaging causes the spin ensemble to experience similar transition rate magnitude $|\Omega_m|$ from $(G_{11} - G_{12})\epsilon_{xx}$ and $G_{14}\epsilon_{xz}$ contributions at their respective spatial maxima. These uniaxial strain and shear components, which are spatially offset, do not interfere destructively since Ω_m is proportional to a linear combination of $\epsilon_{xx}(S_x^2 - S_y^2)$ and $\epsilon_{xz}(S_xS_y + S_yS_x)$. Consequently, in qualitative agreement with our calculations (Fig. 6.12), we always experimentally measure a non-zero Autler-Townes splitting in Fig. 6.5b. Furthermore, our model explains the relative Ω_m amplitudes between kk and hh (4.0 : 1.1) observed in Fig. 6.6, and the results for $\Delta m_s = \pm 2$ transitions are well described by the zero-field splitting tensor when the full strain tensor is taken into account. Lastly, we measure mechanical-spin driving on the PL6 defect species in SiC, previously used to demonstrate electron-nuclear spin entanglement in ambient conditions [25]. We find that PL6 experiences similar mechanical transition rates compared to hh and kk (Fig. 6.6); therefore, mechanical control of SiC spin ensembles should be possible at room temperature.

6.6 Conclusions

We established a Gaussian surface acoustic wave platform for ground state spin control and imaged the phononic modes using a novel nanoscale X-ray imaging technique. Local defect symmetries are critical to understanding spin-phonon interactions in a general model of anisotropic lattice perturbations that we developed based on ab initio calculations. Surprisingly, shear and uniaxial strain couple to the ground state spin with equivalent magnitudes and different relative phases depending on the strain tensor component. This property could be used to engineer material and device designs that capitalize on mechanical interactions. Since a complete model of spin-strain coupling with C_{3v} symmetry requires six independent coupling parameters, strain cannot necessarily be treated as an equivalent electric field vector. Even so, the zero-field splitting tensor is also affected by electric fields with three independent coupling parameters and can be used for both $\Delta m_s = \pm 1$ and $\Delta m_s = \pm 2$ spin transitions. In order to further enhance defect-phonon interaction strengths for hybrid quantum systems, defect excited state electronic orbitals [132, 116] and spins [133] could be utilized as opposed to ground state spins [134], and strain effects on defect hyperfine couplings have not been well explored. In addition, new defects [135] with greater spin-spin or spin-orbit coupling, with minimal cost to their spin coherence, may greatly improve spin-phonon coupling strengths and be advantageous for quantum control of phonons with optically addressable spins. Our combined theoretical understanding and demonstrations of spin-strain coupling with SiC divacancies provide a basis for quantum sensing with MEMS [48] as well as engineering strong interactions with single phonons for quantum transduction [1], spin squeezing [136], and phonon cooling [137] applications.

6.7 Materials and Methods

6.7.1 Samples and Devices

The substrate was an on-axis, high-purity semi-insulating 4H-SiC commercial wafer (Cree Inc. serial no. W4TRF0R-0200). Defects were created in the 4H-SiC wafer by carbon-12 implantation with a dose of 10^{12} cm^{-2} at 170 keV and 7° tilt, which generated vacancies $\sim$ 300 nm deep calculated using the Stopping and Range of Ions in Matter software; however, there was a high defect density in the SiC bulk from material growth. After annealing the wafer at 900 °C in N_2 for 2 hr, the substrate was then cleaned sequentially with organic solvents, nanostrip and HF BOE before AlN was sputtered 500 nm thick on the wafer Si face by OEM Group Inc. The sputtered AlN layer had a film stress of -42 MPa and a rocking curve of 1.52° full-width at half-maximum on the AlN [0002] X-ray diffraction peak. The interdigitated transducer, consisting of 80 finger pairs with a window at the SAW focus spanning 3 wavelengths of missing fingers, was fabricated with 10 nm Ti and 150 nm Al. The Ti/Al and AlN device layers were each dry-etched by inductively coupled plasma (ICP) with 10 sccm Ar, 30 sccm Cl_2 and 30 sccm BCl_3, 400 W ICP power. AlN grooves (650 strips for each grating) in all SAW devices were etched nominally 180 nm deep. The SAW resonator for spin transitions for Figs. 6.1, 6.4 and, 6.5 was oriented longitudinally (SAW propagation direction) along $[\overline{1}\overline{1}20]$, and the resonator for Fig. 6.3 was oriented along $[1\overline{1}00]$. The x, y, z crystal directions are $[11\overline{2}0]$, $[1\overline{1}00]$ and [0001], respectively. Both devices had Gaussian geometry parameters $\lambda = 12$ μm and $w_0 = 2\lambda$, containing 80 electrode finger pairs and 650 grating strips. All interdigitated transducer electrodes and grating strips were overlapped $3\sigma = 3w/\sqrt{2}$ in the transverse direction, where w is the Gaussian spot size [68] along the axis of SAW propagation, while electrodes were apodized by only 2σ. Since the X-ray imaging experiments require specific frequencies for stroboscopic X-ray diffraction, the results in Fig. 6.2a,b used a similar transducer geometry and without AlN grooves for increased frequency bandwidth. This transducer was less impedance matched to 50

Ω compared to the Gaussian SAW resonators. Figure 6.2a,b used a Gaussian transducer with $\lambda = 19.03$ μm, $w_0 = 1.25\lambda$ and 120 electrode finger pairs, yielding an interdigitated transducer center frequency $f_0 \approx 352$ MHz with 1 MHz bandwidth. This was purposefully matched to an integer multiple of the Advanced Photon Source electron bunch frequency (~ 88 MHz) at Argonne National Laboratory.

6.7.2 Measurements

All divacancy spin manipulation experiments in this study were carried out in a closed-cycle cryostat from Montana Instruments Corp. operated with the sample temperature at 30 K. The sample is illuminated using 405 nm and 976 nm laser diodes, with the 405 nm acting as a charge-state reset[82] for neutral divacancies and 976 nm for exciting photoluminescence (>1,000 nm) and initializing the spin state. For pulsed laser experiments, the 976 nm laser is modulated using an acousto-optic modulator (< 50 ns rise time), while the 405 nm laser diode is directly modulated by a current driver (250 kHz bandwidth). Emitted photoluminescence was separated by a dichroic and passed through a 1,000 nm long-pass filter, and then collected into a 62.5 μm core optical fibre. Measurements were realized with an InGaAs photodiode at 1 kHz bandwidth, combined with a lock-in amplifier set at a reference frequency of ~ 400 Hz for all experiments. Spin ensembles of divacancies near the Gaussian resonators beam waist (defined by the acoustic focal spot w_0) are initialized and read out optically. To tune the ground-state spin sublevels, we use a combination of a permanent magnet and a wire loop on a printed circuit board to produce static magnetic fields (B_0) oriented along the 4H-SiC c-axis. A coplanar waveguide behind the sample provides microwaves for in-plane magnetic spin control.

6.7.3 Mitigating Outgassing and Device Heat Fluctuations

Resonator frequency (f_0) and internal quality factor (Q_i) stability are critical for the experiments described in the main text. These parameters in SAW resonators are sensitive to mass

loading and viscous dampening effects at the surface: any out-gassing in cryogenic systems can cause unwanted condensation on the resonator. At low temperatures, e.g. T $<$ 50 K, we observed drifts in the Gaussian SAW resonator frequency of $\geq$ 1 kHz/min towards lower frequencies only. We attributed the drop in resonance frequency to mass loading from condensation, thereby decreasing the SAW velocity.

In order to minimize surface area and organic contaminants, the cryostat chamber interior shielding and machined aluminum components were polished by hand, followed by degreasing with organic solvents. The chamber pressure at low temperatures was further reduced by adding zeolite, thermalized to T = 30 K, with $<$ 10 Å pore size. Inside the cryostat, a secondary 0.2 mm thick quartz window was added to effectively shield the sample, blocking any direct path between out-gassing components or o-rings and the sample.

Additionally, resonator Q_i and f_0 were sensitive to microwave powers over $\sim$10 mW. We observed f_0 shifts toward lower frequencies, which can be interpreted as the wavelength increasing from thermal expansion. In order to keep f_0 stable and eliminate temperature variations, microwave power to the SAW resonator was continuous at constant power. The microwave frequency was also corrected with a PID loop using the resonator's f_0, measured by microwave reflection with a Schottky diode. During Rabi oscillations and pulsed experiments, the PID loop was disabled.

6.8 Supplementary Data and Analysis

6.8.1 Density Functional Theory Calculations of G Parameters

In this section we discuss the spin-strain coupling tensor and its values predicted by density functional theory (DFT). We mainly focus on the experimentally relevant divacancies (hh, kk)-VV in 4H-SiC (Fig. 6.7). To validate the computational protocol of our DFT calculations, we also report the spin-strain coupling tensor for the NV center in diamond and compare with existing literature values.

In the following discussion we use the Cartesian frame for 4H-SiC and diamond defined in Ch. 2. Under this convention, there is a mirror plane perpendicular to the x axis for both 4H-SiC and diamond. The structures of (hh, kk)-VV and NV in their respective frames are shown in Fig 2.6. To compute the numerical values of $\mathbf{G}$ components, we assume that the zero-field splitting effects for VV and NV are dominated by the magnetic dipole-dipole interaction, and we neglect the spin-orbit coupling effect. The magnetic dipole-dipole interaction between the two unpaired electrons in the defect ground state is given by

$$\mathcal{H}_{\mathrm{dd}} = \frac{\mu_0}{4\pi}(\gamma_{\mathrm{e}}\hbar)^2 \frac{r^2 \boldsymbol{s}_1 \cdot \boldsymbol{s}_2 - 3(\boldsymbol{s}_1 \cdot \boldsymbol{r})(\boldsymbol{s}_2 \cdot \boldsymbol{r})}{r^5}, \tag{6.2}$$

where μ_0 is the vacuum magnetic permeability, γ_{e} is the electron gyromagnetic ratio, $\hbar$ is the reduced Planck constant, $\boldsymbol{s}_1$ and $\boldsymbol{s}_2$ are spin-1/2 operators for the two unpaired electrons, $\boldsymbol{r}$ and r are the relative coordinate between two electrons and its norm, respectively. The $\mathbf{D}$ tensor can be computed as the expectation value of the dipole-dipole interaction on the ground state from Kohn-Sham DFT calculations

$$D_{ab} = \frac{1}{2}\frac{1}{s(2s-1)}\frac{\mu_0}{4\pi}(\gamma_{\mathrm{e}}\hbar)^2 \sum_{i\leq j}^{\mathrm{occ.}} \chi_{ij} \left\langle \Psi_{ij}\right| \frac{r^2\delta_{ab} - 3r_a r_b}{r^5} \left|\Psi_{ij}\right| \left|\Psi_{ij}\right| \frac{r^2\delta_{ab} - 3r_a r_b}{r^5} \left|\Psi_{ij}\right\rangle \tag{6.3}$$

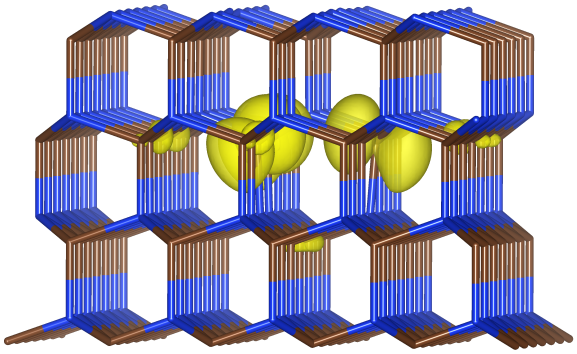

Figure 6.7: **Electron spin wavefunction of the *kk* in 4H-SiC.** Spin polarization density of a divacancy modeled in 4H-SiC supercell. The centers of blue vertices are Si atoms and the brown vertices are C atoms

where s is the effective electron spin ($s = 1$ for triplet defects like the neutral VV or negatively charged NV center). The summation runs over all pairs of occupied Kohn-Sham orbitals, and $\chi_{ij} = \pm 1$ for parallel and anti-parallel electrons respectively. Ψ_{ij}'s are 2×2 Slater determinants of occupied Kohn-Sham orbitals, and expectation values of dipole-dipole interaction are evaluated following the recipe in Ref [138].

We performed DFT calculations for the (hh, kk)-VV in 4H-SiC and NV in diamond with the PBE exchange-correlation functional[139]. The Projector Augmented Wave (PAW) method[140] with datasets compiled in the PSL1.0 library[141] are used to represent electron-ion interactions. When evaluating the expectation values in Eq. 6.3, we used the normalized pseudo-wavefunctions [142, 17, 21]. We used 55 Ry. kinetic energy cutoff and Γ-point sampling of the Brillioun zone. Furthermore, the structures are relaxed until forces on atoms are smaller than 5×10^{-4} eV $\cdot$ Å^{-1}, and all DFT calculations are performed with the Quantum ESPRESSO code[143].

To simulate isolated defects, we create point defects in large supercells built by periodic replication of hexagonal unit cells of 4H-SiC or diamond. Figure 6.8 shows the convergence of D_0 value with respect to supercell size. For all of the following results reported, $7 \times 2 \times 2$ supercells are adopted, which contain 782 and 588 atoms for pristine 4H-SiC and diamond, respectively. With the computational formalism described above, the D values obtained for (hh, kk)-VV in 4H-SiC and NV in diamond agree very well with experimental results [144][18].

Table 6.1: **Calculated D_0 values for the (hh, kk)-VV in 4H-SiC and NV in diamond.** All values are in GHz.

	This work (DFT)	Ref (Exp.)[144][18]
hh-VV	1.41	1.34
kk-VV	1.36	1.31
NV	2.92	2.88

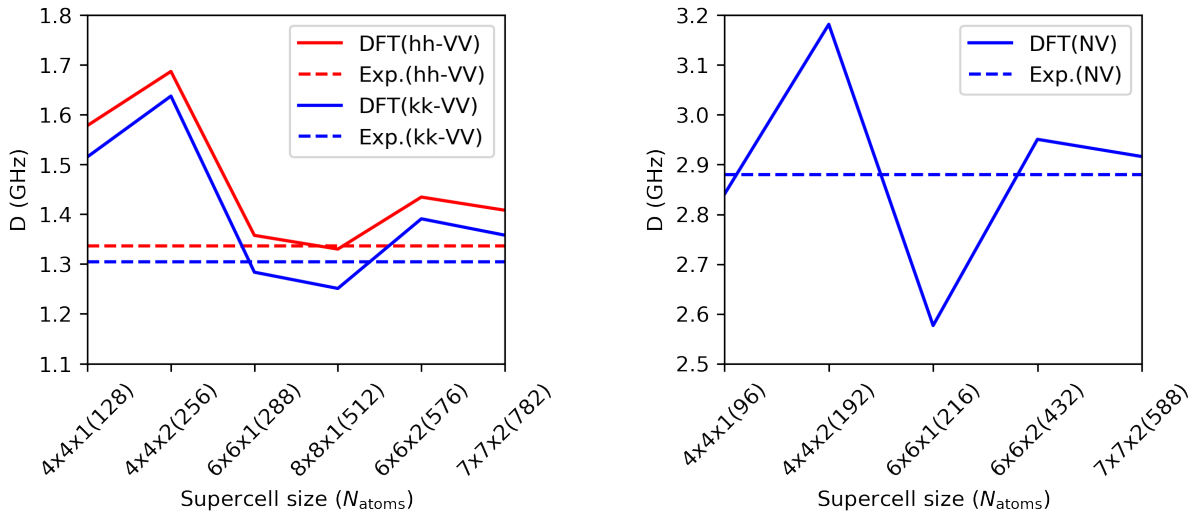

Figure 6.8: **Super-cell size convergence of the zero-field splitting.** D_0 value ($\frac{1}{2}(D_{xx}+D_{yy})-D_{zz}$) for VV in 4H-SiC (left) and NV in diamond (right) as functions of supercell sizes. Calculations are done without strain and thus all defects have C_{3v} symmetry. E values ($\frac{1}{2}(D_{xx}-D_{yy})$) are smaller than 2 MHz for all calculations.

To compute the spin-strain coupling tensor $\mathbf{G}$, the zero-field splitting $\mathbf{D}$ tensor is computed for defects in strained lattices with 0.0%, $\pm$ 0.25%, $\pm$ 0.5%, $\pm$ 0.75%, $\pm$ 1.0% amount of each strain component $\{xx, yy, zz, yz, xz, xy\}$. We extract each component of $\mathbf{G}$ by performing a linear fit for individual components of $\mathbf{D}$ to each applied strain. Due to numerical noises, $\mathbf{G}$ tensors predicted by DFT do not exactly obey the symmetric form in (2.36). Therefore, we symmetrized $\mathbf{G}$ tensor results from DFT by projecting them onto the A_1 irreducible representation of the C_{3v} group. Table 6.2 presents the 6 independent symmetrized components of $\mathbf{G}$. For all values reported, the standard deviations from linear fitting are smaller than 0.1 GHz/strain. It is assumed that the numerical noises from linear fitting for different $\mathbf{G}$ components are independent to each other, so the variances of different $\mathbf{G}$ components are additive.

Table 6.2: **Spin-strain coupling parameters from *ab initio* calculations.** Independent components of spin-strain coupling tensors for (hh, kk)-VV in 4H-SiC and NV in diamond. All values are given in GHz/strain.

	hh-VV	kk-VV	NV
G_{11}	-3.99	-3.35	-4.63
G_{12}	-0.42	-0.93	-1.67
G_{13}	1.74	1.26	1.23
G_{14}	0.34	1.93	-4.68
G_{41}	0.30	-0.10	0.48
G_{44}	0.46	0.47	0.80

6.8.2 Spatial Mapping of $\Delta m_s = \pm 1$ Transitions in SAW Resonator

To further study the effects of ODMR and strain induced spin contrast, we map the PL contrast spatially mode in two dimensions (x, y) . By scanning our confocal microscope and imaging VV^0 PL, we locate the device geometry (Fig. 6.9a,b top). If the SAW is driving $\Delta m_s = \pm 1$ transitions then spatial mapping should reveal the mechanical mode. Magnetic field driving, on the other hand, would show a more homogeneous spatial map across the IDT region, caused by a wider distribution of current (throughout all IDT fingers and the CPW) and compared to the Gaussian mechanical mode. While the RF mechanical drive frequency is on cavity resonance ($\omega_m/2\pi$) we use the interlaced measurement sequence from Fig. 6.3b, containing 1 μs buffer times between RF drive and optical measurement ($\sim$10 μs). Spatial mapping with RF on-resonance reveals the Gaussian SAW mode (Fig. 6.9a). Mapping with RF drive off-resonance ($\omega_m/2\pi + 10$ MHz) shows an overall flat 2D profile and higher PL contrast near the IDT fingers due to stronger magnetic driving close to the wires/electrodes. In conclusion, the spatial mapping confirms that we are measuring an effect from mechanics at the drive frequency ($\omega_m/2\pi$). All PL contrast measurements here were taken at static

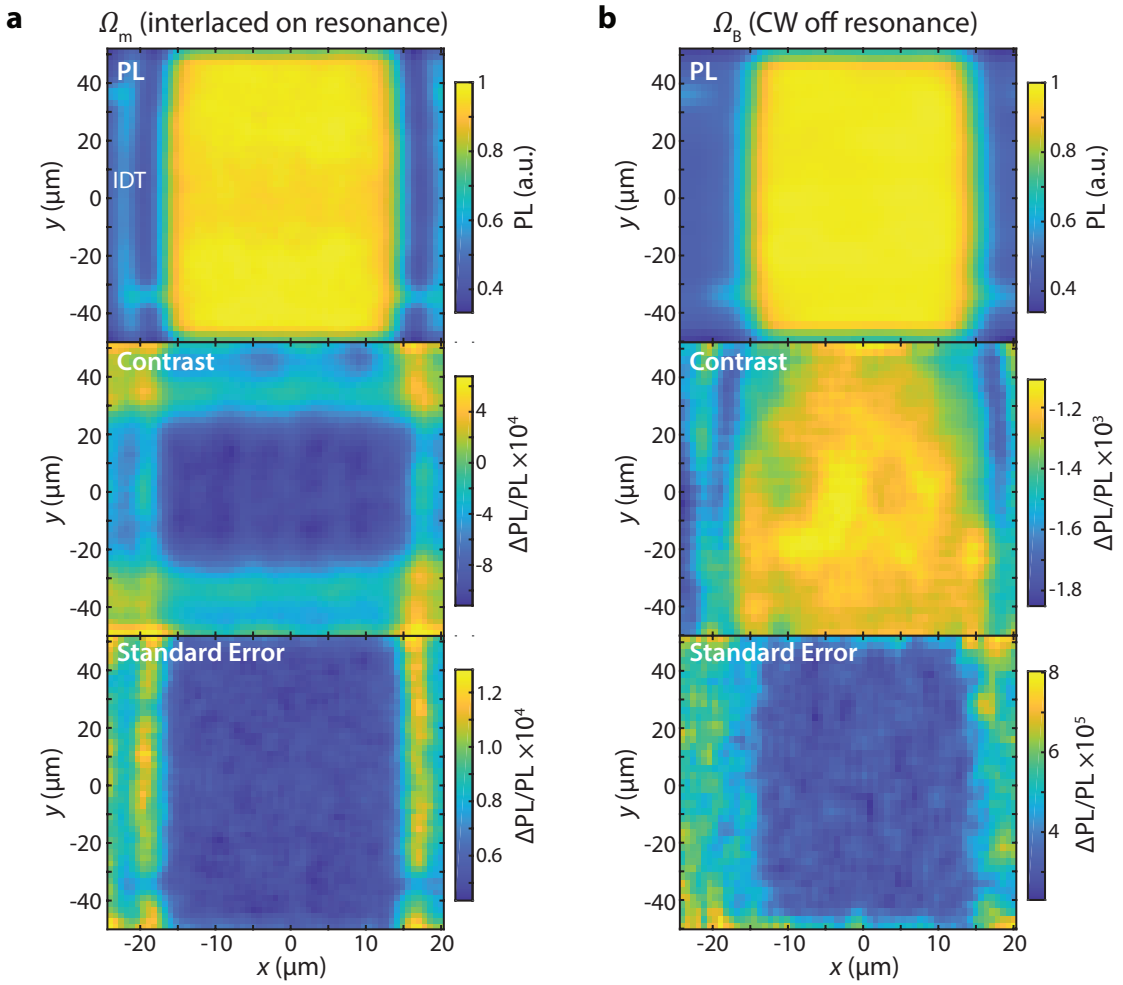

Figure 6.9: **Two-dimensional spatial mapping of acoustic paramagnetic resonance.** **a**. *kk* PL contrast from SAW resonator when driven on cavity resonance ($f_{MW} = \omega/2\pi$), measured with interlaced sequence described in the main text (Fig. 6.3). The spatial mode at $x = 0$ is the Gaussian mechanical profile in Fig. 6.3c. **b**. *kk* PL contrast from ODMR when driven off cavity resonance ($f_{MW} = \omega/2\pi + 10$ MHz), measured in CW mode. The spatial mode is flat in the center, and there is stronger ODMR in between the electrodes. Uncertainties are σ from PL contrast measurements.

magnetic fields $B \approx 266.3$ Gauss for Fig. 6.9a and $B \approx 262.7$ Gauss for Fig. 6.9b with magnetic field modulation.

Another possible explanation for the optically detected acoustic paramagnetic resonance, i.e. mechanical driving of $\Delta m_s = \pm 1$ transitions, is misalignment of the static magnetic field with respect to the defect axis, which would cause a first-order mixing of the $|0\rangle$ and $|\pm 1\rangle$ states and a second-order mixing of $|-1\rangle$ and $|+1\rangle$ states. Spin mixing could then permit spin-strain interactions from $\Delta m_s = \pm 2$ transitions to couple and show up as $\Delta m_s = \pm 1$

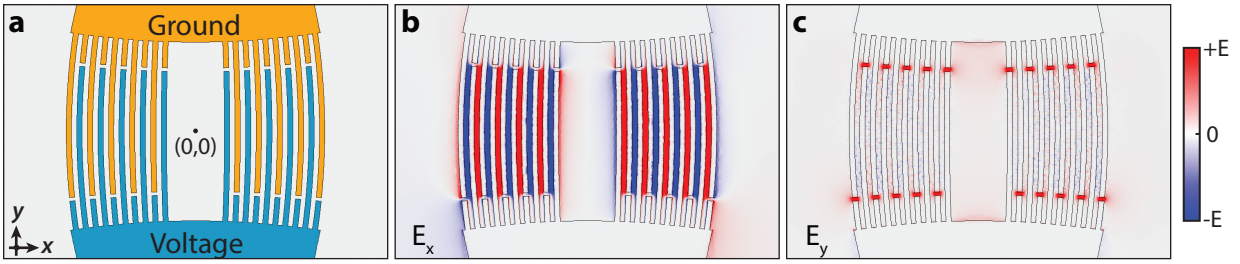

Figure 6.10: **Simulated electric fields produced by a Gaussian IDT. a**. Top-down view of the Gaussian IDT used in experiments (partial device mask file imported into COMSOL); 3D electrostatics simulation using 1 V. **b**. E_x simulation results. Most of the field lines are concentrated between the IDT electrode fingers. **c**. E_y simulation results. $E_\perp = \sqrt{E_x^2 + E_y^2}$ in the center of the IDT is minimal and the spatial profile of $E_\perp$ does not match a Gaussian SAW/mechanical mode. All results are plotted 100 nm below the SiC surface. The color bar scale is saturated at ± 2000 V/cm; the maximum value of E_x is 7100 V/cm.

transitions. However, $\Delta m_s = \pm 2$ characterized earlier showed an Autler-Townes splitting ratio ≈ 4.0 for $kk : hh$. Since the $\Delta m_s = \pm 1$ transitions have a $kk : hh$ drive strength ratio ≈ 0.9 experimentally and ~ 1.0 theoretically, we conclude that the $\Delta m_s = \pm 1$ transitions are not due to spin mixing, which would also be a much weaker effect.

6.8.3 In-Plane Electric Fields from a Gaussian IDT

The electric field distributions near the center of the Gaussian IDT are shown in Fig. 6.10. The mask design is directly imported into COMSOL MultipPhysics and used in an electrostatics simulation.

6.8.4 Numerical Models and Simulations

In order to compare the various experimental results and theoretical calculations of spin-strain tensors, we have to take into account various spatial distributions:

1. The spatial distribution of the various strain components
2. The defect distribution in the sample
3. The optical point-spread function from the confocal microscopy setup

These will described and quantified in sections 5.1 and 5.2, then the model results are summarized as well as compared with both Autler-Townes and mechanically driven Rabi oscillation experiments.

6.8.5 Surface Acoustic Wave Model

We perform simulations with COMSOL Multiphysics to quantitatively understand the full strain tensors and their respective spatial distributions in our SAW resonators. We only consider strain tensor components $\varepsilon_{xx}, \varepsilon_{zz}, \varepsilon_{xz}$ near the acoustic beam waist because the SAW is collimated at the resonator's focus, assuming the wave acts according to Gaussian optics[68] analogies (partially confirmed by X-ray imaging phononic mode in Fig. 6.2a,b). The finite-element simulation is 2D (xz plane) and replicates the device geometry longitudinally, though it is non-Gaussian since the model is constant throughout the out-of-plane (y) direction. We use anisotropic elastic constants[58] and piezoelectric constants[145] for both AlN and 4H-SiC using 16 electrode finger pairs. In the frequency domain COMSOL predicts a maximum in real admittance (Y_{11}) at 556 MHz, along with the sinc-squared shape from an IDT (Fig. 6.11a). The 556 MHz resonance comes from Rayleigh waves, and this quantitatively matches with experimental values we've measured (556-560 MHz depending on Ti/Al thickness). The uniaxial strain (ϵ_{xx}) and shear (ϵ_{xz}) from a SAW are shown in Fig. 6.5c.

We transform the strain distributions into local spin drive rates Ω_{m} for $\Delta m_{\mathrm{s}} = \pm 1$ ($\propto \frac{D_{xz} - iD_{yz}}{\sqrt{2}}$) and $\Delta m_{\mathrm{s}} = \pm 2$ transitions ($\propto \frac{1}{2}(D_{xx} - D_{yy}) - iD_{xy}$) by using the G tensor from DFT, before performing convolutions and ensemble averaging due to our confocal microscope resolution.

6.8.6 Confocal Microscope and Spin Distribution

Understanding the ensemble average signal from the defects' photoluminescence requires taking into account the point-spread function (PSF) of the confocal microscope used in the

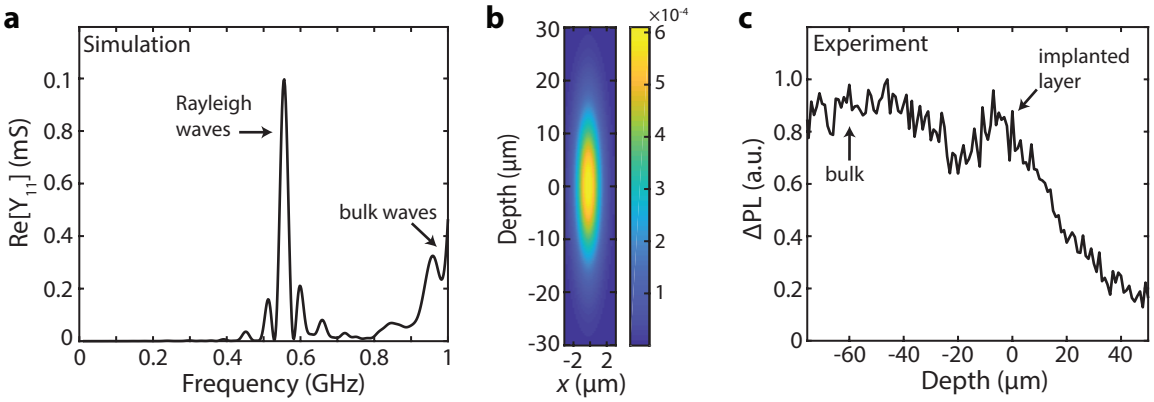

Figure 6.11: **Spin ensemble distribution and optical spot averaging. a**. Real admittance from an IDT, modeled in COMSOL with massless Al, using 150λ in y ($\lambda = 12$ μm). **b**. Model Gaussian optical spot from experimental parameters. **c**. Experimental ODMR on *kk* ensemble $|-1\rangle$ sublevel as a function of depth into the sample. Due to the index of refraction of SiC and the numerical aperture of the objective, the depth axis must be scaled up by a factor of 2.91 for $z < 0$. The sample surface is at $z = 0$.

experiments. The effective PSF was directly estimated from optical measurements on the sample: the interdigitated metallic contacts provided a knife-edge measurement of the in-plane resolution (≈ 2.5 μm FWHM), and the Raman signal from the thin AlN layer provided a depth resolution of ≈ 23 μm FWHM (taking into account the objective 0.65 numerical aperture and the index of refraction of SiC). The Gaussian optical spot model is plotted in Fig. 6.11b.

TRIM calculations show that our ion implantation (170 keV, 7° tilt) into SiC had a stopping range 300 ± 120 nm (2σ). Knowing that VV has about a 5% creation efficiency per ^{12}C ion from implantation[18] followed by annealing, we estimate a VV density $\approx 4 \times 10^{15}$ cm^{-3} in the implanted layer. Though the bulk VV defect concentration in our HPSI SiC material is smaller than the implanted concentration by about one to two orders of magnitude, poor depth resolution of the confocal microscope results in equal PL contributions from both bulk and implanted layer when focused near the surface. This approximation of $\sim 10^{14}$ cm^{-3} VV density in the bulk is consistent with ODMR scans versus depth (z), which show the *kk* PL contrast from the implanted layer is nearly equal to *kk* contributions from the bulk (Fig. 6.11c).

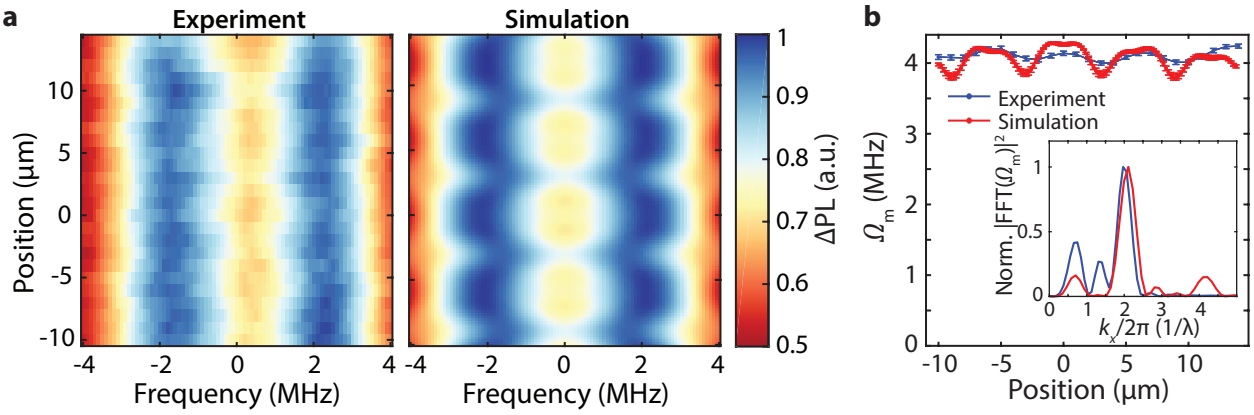

Figure 6.12: **Model of Autler-Townes splitting as a function of longitudinal position. a**. (Left) Autler-Townes splitting measurements on *kk* ensemble $|-1\rangle$ sublevel as a function of longitudinal (x) position in the Gaussian SAW resonator, where x is along $[\bar{1}\bar{1}20]$, and (right) simulated ensemble Autler-Townes splittings. **b**. Mechanical drive rate Ω_{m} and FFT analysis of the data in (**a**).

6.8.7 Autler-Townes Splitting vs. x Position

After computing the Ω_{m} spatial distributions for both *hh* and *kk* in the SiC, we simulate the ensemble Autler-Townes splittings for $\Delta m_{\mathrm{s}} = \pm 2$ transitions. The simulation shows the expected Ω_{m} after weighting the mechanical drive distributions by the spin spatial distribution and convolving it with the optical PSF. The experimental data and simulation of Autler-Townes splittings ($m_{\mathrm{s}} = -1$ sublevel) as a function of x position are plotted in Fig. 6.12a. To analyze the level of agreement, we compare the ensemble mechanical drive rates in the experimental data and simulation as a function of position (Fig. 6.12b). The experimental data shows Ω_{m} oscillations with $\approx 4\%$ contrast ($\Omega_{\mathrm{m}} \approx 3.99$ - 4.14 MHz near the center), and the simulation has $\approx 11\%$ contrast ($\Omega_{\mathrm{m}} \approx 3.85$ - 4.28 MHz near the center). Additionally, both data sets contain the $\lambda/2$ periodicity as shown by Gaussian peaks in their FFT spectra at $k_x/2\pi = 2\lambda$.

6.8.8 Rabi Simulations

To fully model $\Delta m_s = \pm 2$ mechanically driven Rabi oscillations, we use i) the physical model described above as an ensemble inhomogeneous mechanical drive distribution ii) ensemble

ODMR spectrum for transition frequency detunings and iii) three-level system dynamics due to simultaneous magnetic and mechanical drives. By propagating a pure spin state, beginning in $|0\rangle$ from optical initialization, through our pulse sequence we find the simulated change in photoluminescence and will directly compare this to experimental results. The simulation is repeated 101 times for different detuning values and 351 times for different mechanical drive rates using ensemble distributions described later on. Our simulations show good qualitative agreement and moderate quantitative agreement with important asymmetric features and oscillation rates in our experimental results.

The Hamiltonian in the rotating frame ($\{|+1\rangle, |0\rangle, |-1\rangle\}$ basis):

$$H_{\mathrm{RF}} = \begin{pmatrix} \Delta & \Omega_{\mathrm{B}_{+1}}/2 & \Omega_{\mathrm{m}}/2 \\ \Omega_{\mathrm{B}_{+1}}/2 & 0 & \Omega_{\mathrm{B}_{-1}}/2 \\ \Omega_{\mathrm{m}}/2 & \Omega_{\mathrm{B}_{-1}}/2 & \delta \end{pmatrix} \tag{6.4}$$

Where Ω_{m} is the mechanical transition rate, $\Omega_{\mathrm{B}_{\pm 1}}$ are the magnetic transition rates, Δ is the microwave one-photon detuning from $|0\rangle$ to $|1\rangle$, and δ is the one-photon plus one-phonon detuning from $|0\rangle$ to $|-1\rangle$ in our Λ system by convention (Fig. 6.13a). The diagonal elements of H_{RF} are consistent throughout the entire spin simulation so that relative phases are properly accounted for by staying in a single reference frame. Only the off diagonal elements of H_{RF} are changed between each propagator ($U_1(t)$,$U_2(t)$,$U_3(t)$) used for spin simulations (Fig. 6.13b). $\Omega_{\mathrm{B}_{+1}}$ and $\Omega_{\mathrm{B}_{-1}}$ are equivalent to the magnetic Rabi frequencies during magnetic driving. The transition frequencies during $\Delta m_{\mathrm{s}} = \pm 2$ Rabi experiments are $\omega_{\mathrm{m}} + \omega_{\mathrm{B}_{-1}} = \omega_{\mathrm{B}_{+1}}$.

For different parts of the pulse sequence we define the Hamiltonians:

$$H_{\pi_{-1}} = \begin{pmatrix} \Delta & 0 & \Omega_{\mathrm{m}}/2 \\ 0 & 0 & \Omega_{\mathrm{B}_{-1}}/2 \\ \Omega_{\mathrm{m}}/2 & \Omega_{\mathrm{B}_{-1}}/2 & \delta \end{pmatrix}, \tag{6.5}$$

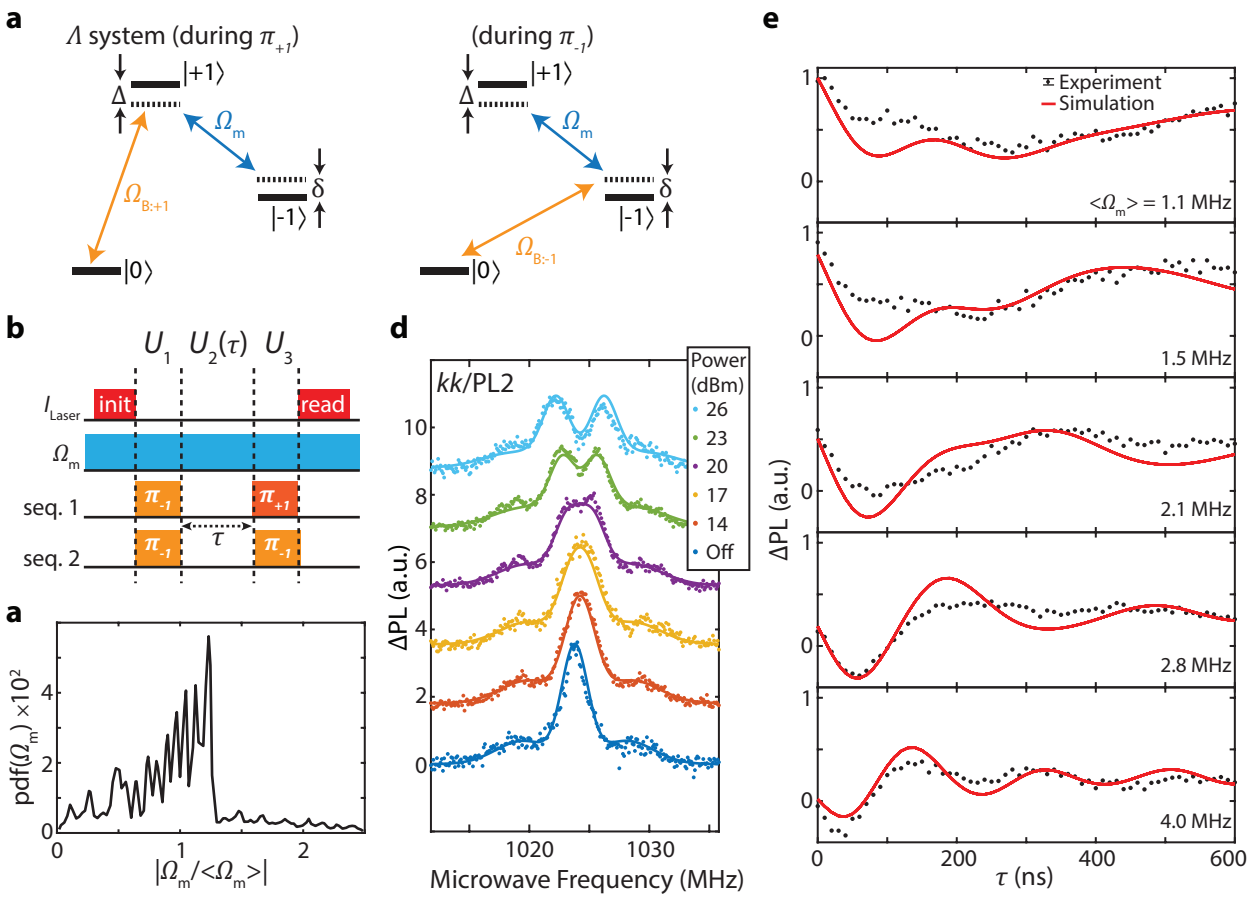

Figure 6.13: **Magnetically forbidden Rabi oscillations of *kk* spin ensembles.** **a**. Three-level system for ground state spin with mechanical drive (Ω_{m}) and magnetic drives ($\Omega_{\mathrm{B}_{\pm 1}}$). **b**. Pulse sequence for driving and detecting mechanical Rabi oscillations. Propagators $U_n, n \in \{1, 2, 3\}$ for simulations are depicted. **c**. Probability distribution function of normalized ensemble mechanical drive rates within one optical spot. **d**. Autler-Townes splitting measurements for various microwave powers to the SAW resonator. **e**. Mechanical Rabi oscillations between $|-1\rangle$ and $|+1\rangle$ using the sequence from (**b**) and same microwave powers as those used in (**d**). All simulations were globally scaled by a constant.

$$H_{\mathrm{m}} = \begin{pmatrix} \Delta & 0 & \Omega_{\mathrm{m}}/2 \\ 0 & 0 & 0 \\ \Omega_{\mathrm{m}}/2 & 0 & \delta \end{pmatrix}, \tag{6.6}$$

$$H_{\pi_{+1}} = \begin{pmatrix} \Delta & \Omega_{\mathrm{B}_{+1}}/2 & \Omega_{\mathrm{m}}/2 \\ \Omega_{\mathrm{B}_{+1}}/2 & 0 & 0 \\ \Omega_{\mathrm{m}}/2 & 0 & \delta \end{pmatrix}. \tag{6.7}$$

The final state $|\Psi(\tau)\rangle$ just before measurement is calculated from the initial state $|0\rangle$ by time-evolution operations:

$$|\Psi(\tau)\rangle = U_3 U_2(\tau) U_1 |0\rangle \tag{6.8}$$

Where $U_1 = e^{-iH_{\pi_{-1}}t_\pi}$ and $U_2(\tau) = e^{-iH_{\mathrm{m}}\tau}$. In the lock-in sequence, $U_3 = e^{-iH_{\pi_{+1}}t_\pi}$ for sequence 1 while $U_3 = e^{-iH_{\pi_{-1}}t_\pi}$ for sequence 2. Here, $\hbar$ has been set to 1, $\Omega_{B_{\pm 1}}$ are both 5.26 MHz, and $t_\pi = 85$ ns is the time to do a magnetic π pulse (found by performing two-level system Rabi oscillations and fitting to similar ensemble spin simulations).

The spin ensemble mechanical drive rates and detunings now are taken from experimental values. The Ω_{m} for > 9000 spins are calculated using the COMSOL and spin-strain coupling models described earlier. We bin Ω_{m} values, plotted in Fig. 6.13c, and use results from experimental Autler-Townes splitting for the expectation value $< \Omega_{\mathrm{m}} >$. The Autler-Townes data and fits are shown in Fig. 6.13d, and splitting frequency results are plotted in Fig. 3c. Detuning parameters Δ and δ are modeled from small static magnetic field fluctuations, which shift the eigenstates $|\pm\rangle$ by γB. Assuming negligible D shifts (e.g. temperature fluctuations), the detunings [1] simplify:

$$\Delta = -\gamma\ \Delta_B;\ \delta = \gamma\ \Delta_B \tag{6.9}$$

The ensemble distribution of magnetic field shifts ($\gamma\ \Delta_B$) are known directly from ODMR without mechanical driving, using Gaussian fits for electron and hyperfine coupled spins. The ensemble $< \Omega_{\mathrm{m}} >$ is known from Autler-Townes splitting measurements, which were simultaneously fit for Ω_{m} (Fig. 6.13d).

Finally, since ODMR measures an increase in PL for kk spins, the simulated PL contrast from $\Delta m_{\mathrm{s}} = \pm 2$ Rabi oscillations is:

1. The detunings Δ and δ acquired a minus sign relative to Ch. 2 because the transformation matrix used here was relative to $|m_{\mathrm{s}} = +1\rangle$ instead of $|m_{\mathrm{s}} = 0\rangle$.

$$\Delta \mathrm{PL} \propto |\left\langle 0|\Psi(\tau)_{\text{seq. 2}}\right|0|\Psi(\tau)_{\text{seq. 2}}\rangle|^2 - |\left\langle 0|\Psi(\tau)_{\text{seq. 1}}\right|0|\Psi(\tau)_{\text{seq. 1}}\rangle|^2 \tag{6.10}$$

Putting everything together, simulation results are shown in Fig. 6.13e plotted against the experimental data. The model results (red lines) have a globally scaled amplitude across all simulations, so the initial projection of the spin population at $\Delta\mathrm{PL}(\tau = 0)$ can be meaningfully compared between Rabi oscillation experiments. The simulations capture multiple unique features in the experimental data, such as the population at $\tau = 0$, oscillation rates, and overall shape. The reason that the population decreases at $\tau = 0$ for larger Ω_m values is because $\Omega_\mathrm{B} \sim \Omega_\mathrm{m}$, so more of the spin population gets transferred to $|{+1}\rangle$ during the first magnetic π pulse. The fast decay time in < 1 μs is due to the inhomogeneous Ω_m distribution (Fig. 6.13c). Additionally, the detuning also plays an important role. Although the pulse sequence would produce symmetric oscillations about $\Delta\mathrm{PL} = 0$ for a single spin, the Gaussian detuning spectrum combined with distribution for Ω_m produce an asymmetric decay. Ensemble detunings were also necessary to quantitatively obtain the observed oscillation rates. We note that there could be extra sources of damping our model does not take into account.

6.8.9 Summary of *kk:hh* Relative Mechanical Drive Strengths

We perform ODMR and Autler-Townes splitting experiments under similar conditions in order to accurately discern the relative spin-strain coupling for both c-axis oriented VV *hh* and *jj* (also called PL1 and PL2, respectively, in literature) as well as PL6. For each defect configuration we measure ODMR with the Gaussian SAW resonator drive off ($\Omega_\mathrm{m} = 0$), and then we measure the electron spin resonance again with the mechanical resonator driven to probe the Autler-Townes splitting and determine Ω_m. The results are shown in Fig. 6.6 and Fig. 6.14. We fit the ODMR and Autler-Townes splittings simultaneously with

2 unique Gaussian distributions (model of electron spin ensemble and hyperfine couplings) and a constant offset, so even a small Ω_{m} value is detectable as a broadening in the Autler-Townes measurement. We find the values of Ω_{m} for *kk*, *hh*, and PL6 to be 4.0 ± 0.1, 1.1 ± 0.2, and 3.4 ± 0.4, respectively (Fig. 6.14). Since optical spot and spatial distributions remain constant between each measurement, only variations in spin-strain coupling parameters can explain large differences in Autler-Townes splittings between each defect species.

We find that the simulations described above, using only DFT results and experimental parameters, can reproduce the experimentally observed ensemble Autler-Townes splittings ≈ 4.0 MHz (≈ 1.0 MHz) for *kk* (*hh*), respectively. Thus, we obtain quantitative experiment-theory agreement of the Ω_{m} ratio *kk:hh* ~ 4.0 for $\Delta m_{\mathrm{s}} = \pm 2$ transitions, and a ratio ~ 1.0 for $\Delta m_{\mathrm{s}} = \pm 1$ transitions. We note that our model is robust to small parameter changes, such as optical spot size and spin distributions. In general, the model always predicts Autler-Townes splitting ratios *kk:hh* trends $kk > hh$ for $\Delta m_{\mathrm{s}} = \pm 2$ transitions, and $kk \sim hh$ for $\Delta m_{\mathrm{s}} = \pm 1$ transitions when using strain distributions and from a Rayleigh wave and spin ensembles.

In addition, the results of Autler-Townes simulations with DFT spin-strain coupling tensors can be used to back-out strain values needed to achieve $\Omega_{\mathrm{m}} \approx 4$ MHz. This yields $\epsilon_{xx}, \epsilon_{xz} \sim 10^{-3}$ order of magnitude at the Gaussian resonator's beam waist during 400 mW RF power at sample - matching expectations from back of the envelope predictions (using theory discussed in [102]), which are detailed in Section 6.8.11.

6.8.10 RF Characterization of Gaussian SAW Resonators

We measure resonators the Gaussian SAW resonators by RF reflection using a Vector Network Analyzer (VNA). A SAW resonator can be modeled as a Butterworth-Van Dyke (BVD) [60], which is a capacitor (geometric capacitance of the IDT) in parallel with a series *RLC* circuit for the mechanical resonance. In the case of a small geometric capacitance, the circuit can be approximated as just the series *RLC* that we define as $Z_r = R + i\omega L + 1/(i\omega C)$,

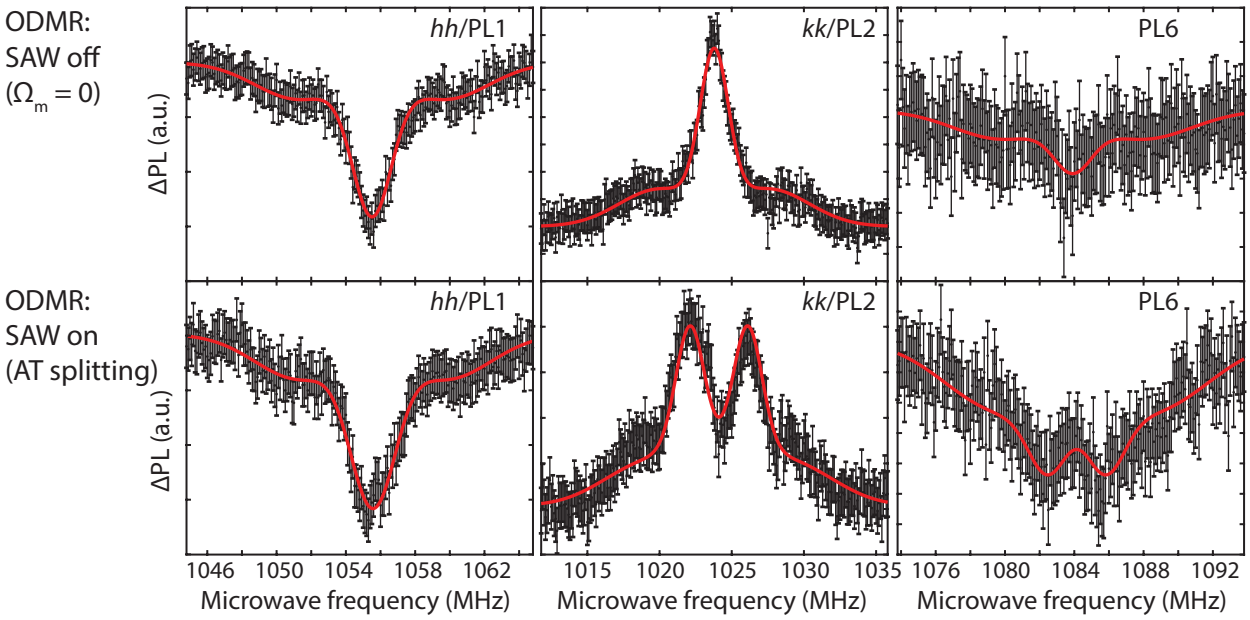

Figure 6.14: **Autler-Townes splittings and ODMR of *hh*, *kk*, and PL6.** Top row: ODMR when the Gaussian SAW resonator is disabled (no mechanics). Bottom row: ODMR signal, showing the Autler-Townes splitting, when the Gaussian SAW is driven with 400 mW power at sample. All experiments were performed under similar conditions and the sample temperature is 30 K. Only the static magnetic field (B_0) and frequency of the magnetic microwave drive ($\omega_{\mathrm{B}:-1}/2\pi$) is changed between experiments for each different defect site (*hh*, *kk*, and PL6). Black data points are experimental data with error bars representing two standard deviations of the mean, and the fits are shown in red.

which has a resonance at $\omega_0^2 = 1/(LC)$. Furthermore, an asymmetric resonance lineshape can result from impedance mismatches, for example, from cables, wirebonds, and improperly designed coplanar waveguides. We model an arbitrary impedance mismatch a short length of lossless transmission line with a characteristic impedance Z_c mismatched from $Z_0 = 50\Omega$ (Fig. 6.15a). The fit equation derived from ABCD matrix methods is,

$$S_{11}(\omega) = \frac{\kappa_i - \kappa_e^* e^{-i\phi} + 2i(\omega - \omega_0)}{\kappa_i + \kappa_e^* e^{-i\phi} + 2i(\omega - \omega_0)} \tag{6.11}$$

The loss rate κ_i (κ_e) is related to the internal (external) quality factors, by $\kappa_{i,e} = \omega_0/Q_{i,e}$. When $Z_c \neq Z_0$, the external quality factor is modified to $Q_e^* = Q_e A e^{i\phi}$ where the impedance mismatch terms A and ϕ are real constants. Notice that this equation is similar to that of a bare series RLC circuit [69], however, here the external quality factor is modified by a

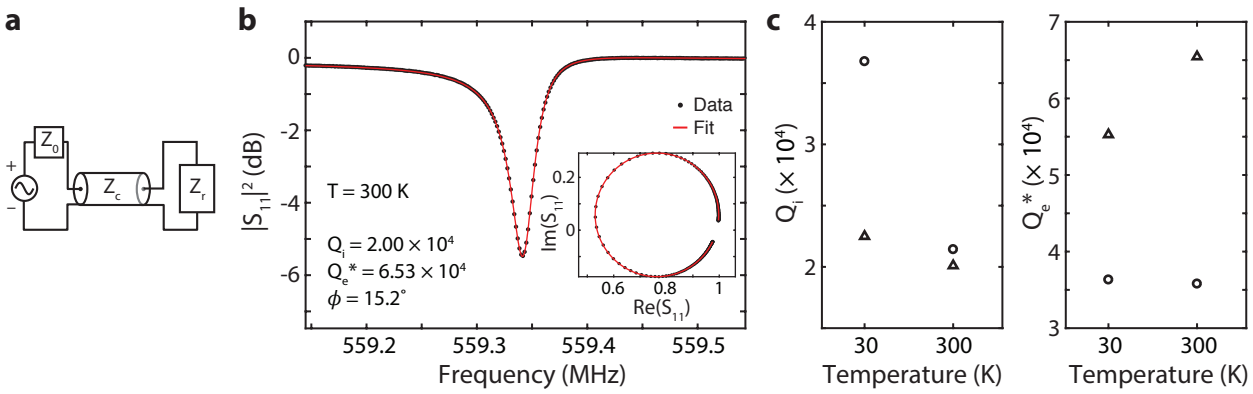

Figure 6.15: **RF reflection measurements of Gaussian SAW resonators quality factors. a**. Equivalent circuit model for fitting reflection data from SAW resonators. **b**. RF reflection measurement at room temperature and fit for the resonator oriented along $[\bar{1}\bar{1}20]$. **c**. Internal and external quality factors extracted from fits for the devices oriented along $[\bar{1}\bar{1}20]$ ($\triangle$) and $[1\bar{1}00]$ ($\circ$).

magnitude ($\kappa_e^* = \omega_0/Q_e^*$) and complex phase that causes a rotation of S_{11} in the complex plane. In addition to these fit parameters, we fit with magnitude and phase offsets on S_{11} to account for external losses and phase offsets from to the cables.

Our reflection data for Gaussian SAW resonators are well fitted by this model (Fig. 6.15b). The Q_i near room temperature for both devices used in experiments is $\sim 20,000$ order of magnitude. We always observe the mechanical resonator internal losses decrease (Q_i increases) as the temperature decreases (Fig. 6.15c). However, the absolute Q_i improvement between different resonators at cryogenic temperatures is not consistent. Additionally, Q_e^* typically stays constant as a function of temperature, and the resonance frequency increases by $< 0.2\%$ at cold temperatures due to thermal lattice contraction and changes in acoustic wavespeeds. The Q_e^* is smaller for one device ($\triangle$) in Fig. 6.15c at low temperatures because the cables and measurement setups had changed between experiments.

6.8.11 Theoretical Model of Strain Amplitude in a driven SAW Resonator

Zero-point strain fluctuations

In this section we estimate the amplitude of zero-point strain fluctuations in the SAW resonator while keeping in mind the anisotropic elastic constants of SiC and full strain tensor. A planar SAW resonator will be evaluated first, and then the effects of Gaussian geometry will be discussed. First, we will approximate the material as pure SiC in the absence of an AlN thin layer. This approximation greatly simplify the following calculations to Rayeligh waves in a half-space. The second approximation is we will neglect the effects of piezoelectricity because the piezoelectric constant $k^2_{\mathrm{SiC}} \leq 10^{-4}$ [59], which intuitively means about 0.01% of the energy is stored in the associated electromagnetic field.

We begin by defining the three dimensional displacements u_i using Eq. 3.8 for a planar Rayleigh wave propagating in the x_1 direction and constant in the x_2 direction given by,

$$\begin{aligned} u_1(x_1, x_2, x_3) &= k\phi_0(e^{\kappa_\ell x_3} - \tfrac{2\kappa_\ell\kappa_{\mathrm{t}}}{k^2+\kappa_{\mathrm{t}}^2}e^{\kappa_{\mathrm{t}} x_3})e^{i(kx_1-\omega t)}\,, \\ u_2(x_1, x_2, x_3) &= 0\,, \\ u_3(x_1, x_2, x_3) &= -i\kappa_\ell\phi_0(e^{\kappa_\ell x_3} - \tfrac{2k^2}{k^2+\kappa_{\mathrm{t}}^2}e^{\kappa_{\mathrm{t}} x_3})e^{i(kx_1-\omega t)}\,. \end{aligned} \tag{6.12}$$

where x_1 is the propagation direction in-plane and $x_3 > 0$ is the depth into the substrate. The constant $k = 2\pi/\lambda$ is the wavenumber in the propagation direction, $\kappa_{\mathrm{t}}^2 = k^2(1 - (v_{\mathrm{R}}/v_{\mathrm{t}})^2)$ and $\kappa_\ell^2 = k^2(1 - (v_{\mathrm{R}}/v_\ell)^2)$ are the decay coefficients, ϕ_0 is a scalar, and $\omega = kv_{\mathrm{R}}$ is the SAW angular frequency. Numerical values for the bulk wave velocities (v_ℓ, v_{t}) and Rayleigh wave velocities (v_{R}) for 4H-SiC can be found in reference 3.2.

The strain tensor is defined as,

$$\epsilon_{ij} = \frac{1}{2}(\partial u_i/\partial x_j + \partial u_j/\partial x_i) \tag{6.13}$$

The general form of the acoustic Hamiltonian [146] for an anisotropic, elastic material

that is homogeneous can be written as,

$$\mathcal{H} = \frac{1}{2}\int \mathrm{d}^3R[\rho(\frac{\partial u_i}{\partial t})^2 + \lambda_{ijkl}\epsilon_{ij}\epsilon_{kl}] \tag{6.14}$$

where ρ is the density and λ_{ijkl} is the tensor of elastic constants. Next, we treat the two terms as the kinetic and potential energies by analogy, which both contain half the total system energy, and we set $\mathcal{H} = \hbar\omega_0/2$ in order to calculate the amplitude of zero-point vacuum fluctuations of strain. It is simpler to perform the calculation in Voigt notation and matrix form. Additionally, we re-write the strain as a normalized standing wave by taking the real part $\mathrm{Re}[\epsilon_{ij}] \rightarrow \varepsilon_{\mathrm{zpf}}\widetilde{\varepsilon}_i$.

$$\frac{\hbar\omega_0}{2} = \frac{\varepsilon_{\mathrm{zpf}}^2}{2}\int \mathrm{d}^3R\ \widetilde{\varepsilon}_i\lambda_{ij}\widetilde{\varepsilon}_j \tag{6.15}$$

Here, ω_0 is the frequency of the resonator, $\varepsilon_{\mathrm{zpf}}$ is the amplitude of the zero-point fluctuations, $\widetilde{\varepsilon}_i$ are normalized strain wave functions, and the remaining factor of $1/2$ before the integral comes from averaging out the time dependence $\cos^2(\omega_0 t)$. Note that $\widetilde{\varepsilon}_{4,5,6} = 2\varepsilon_{yz,xy,xz}$ in Voigt notation. The bounds of the definite integral, which is over the entire mode volume of a planar SAW resonator, only depends on the cavity length (L_c) since the aperture of the SAW is a constant W (usually equal to the IDT overlap) and the strain is independent of x_2.

We estimate L_c from known dimensions of the SAW resonator. The total cavity length is the sum of the IDT length and penetration depth into each Bragg mirror ($L_\mathrm{c} = L_\mathrm{IDT} + 2L_\mathrm{p}$). The IDT longitudinal length L_IDT is 83λ for the resonators used in spin experiments. The SAW penetration depth into each Bragg mirror is $L_\mathrm{p} = \lambda/(4|r_\mathrm{s}|)$ [60], where $|r_\mathrm{s}| = 0.5\%$ is the magnitude of the reflection per grating strip measured for a similar SAW resonator on AlN/SiC [73].

$$\epsilon_{\mathrm{zpf}} = \sqrt{\frac{\hbar\omega_0}{W\mathcal{H}_s}} \tag{6.16}$$

$$\mathcal{H}_s = \int_{-L_c/2}^{L_c/2} \int_0^{\infty} \mathrm{d}x_1 \; \mathrm{d}x_3 \; \varepsilon_i \lambda_{ij} \varepsilon_j \tag{6.17}$$

The results for amplitude of zero-point vacuum fluctuations of in-plane uniaxial strain $\epsilon_{xx} \approx 3.3\text{x}10^{-13}$ at the crystal surface $x_1 = x_2 = x_3 = 0$ for a planar SAW resonator with $\lambda = 12$ μm and $W = 150\lambda$.

Mode volume reduction by applying a Gaussian geometry

In general, more Gaussian focusing will shrink the beam waist (w_0) at $x_1 = 0$. In addition, the power in a wave front is conserved at all positions along the propagation axis (x_1 direction) [68], so changing the beam waist parameter can be considered as modifying the total resonator mode volume. Gaussian resonator geometries also modify transverse mode frequencies, but we will not address that in this work. By changing the beam waist, for example from W to w_0, the strain field strength in eq. 6.16 gets multiplied by a factor of $\propto \sqrt{W/w_0}$.

Compared to the planar SAW resonator discussed above, a Gaussian SAW resonator with $w_0 = 2\lambda$ result in a larger ε_{zpf} by a factor $(\frac{150\lambda}{2.35(w_0/\sqrt{2})})^{1/2} \approx 6.7$. The denominator of this factor comes from approximating the new effective aperture as the Gaussian distribution's full width at half maximum. In summary a Gaussian SAW resonator, like the one used in our experiments, would have zero-point strain fluctuations $\epsilon_{xx} \approx 2.2\text{x}10^{-12}$ at the center and crystal surface.

High power strain and displacement

The strain magnitude in the resonator during coherent driving can be predicted from the zero-point vacuum fluctuation and drive power [147]. For a resonator with one port and RF drive power P, the number of phonons in the mechanical resonator is,

$$N_{\mathrm{ph}} = \frac{4\kappa_{\mathrm{e}} P}{\hbar\omega_0(\kappa_{\mathrm{e}} + \kappa_{\mathrm{i}})^2}; \tag{6.18}$$

where the resonator loss rates κ_{e} and κ_{i} are defined in Section 6, and here we substitute κ_{e}^* into κ_{e} given external impedance mismatches. Finally, the a.c. strain is related to the number of phonons in the resonator by,

$$\epsilon = \varepsilon_{\mathrm{zpf}}\sqrt{N_{\mathrm{ph}}}; \tag{6.19}$$

Using characterized resonator properties for the device in Fig. 6.1 ($\omega_0/2\pi = 560.33$ MHz, $Q_{\mathrm{i}} = 2.24\text{x}10^4$, $Q_{\mathrm{e}}^* = 5.51\text{x}10^4$) and 400 mW of RF power at sample, we estimate the a.c. strain amplitude $\varepsilon_{xx} \approx 5.3\text{x}10^{-3}$. This strain calculation overestimates the acoustic strain in our resonator compared to DFT calculations for spin-strain coupling parameters with Aulter-Townes splitting experiments (expect $\varepsilon_{xx} \approx 10^{-3}$). Nevertheless, this back-of-the-envelope estimate agrees with our spin driving model outlined in Section 5.5 and should be treated only as an order of magnitude due to the approximations we made in 7.1. The corresponding displacement magnitude, using relations from eq. 6.12 and eq. 6.13, is $|u_3| \approx 70$ nm.

Appendix A

Device Fabrication Methods

A.1 Lift-Off Recipes with an Undercut

In lift-off processes for depositing metal and other materials by physical vapor deposition it is desirable to have an undercut in the mask. By using an undercut, it is possible avoid flagging and tearing caused by the metal forming a conformal coating around the mask. Two methods using optical photoresist are shown here quantum devices are negative photoresists and LOR for use with electron-beam evaporation and sputtering.

A.1.1 Negative Photoresist AZ nLOF series

1. **Spin nLOF2020.**

   On silicon and SiO_2 substrates, HMDS vapor prime should be used to promote photoresist adhesion. Spinning at 4500 RPM for 45 seconds usually results in ≈ 1.6 μm thick resist on a 4" wafer.

2. **Bake at 110 °C for 60 seconds.**[1]

3. **Expose.**

1. A bake temperature of 115 °C was often used due to convenience of available hotplates at the time instead of the optimal 110 °C.

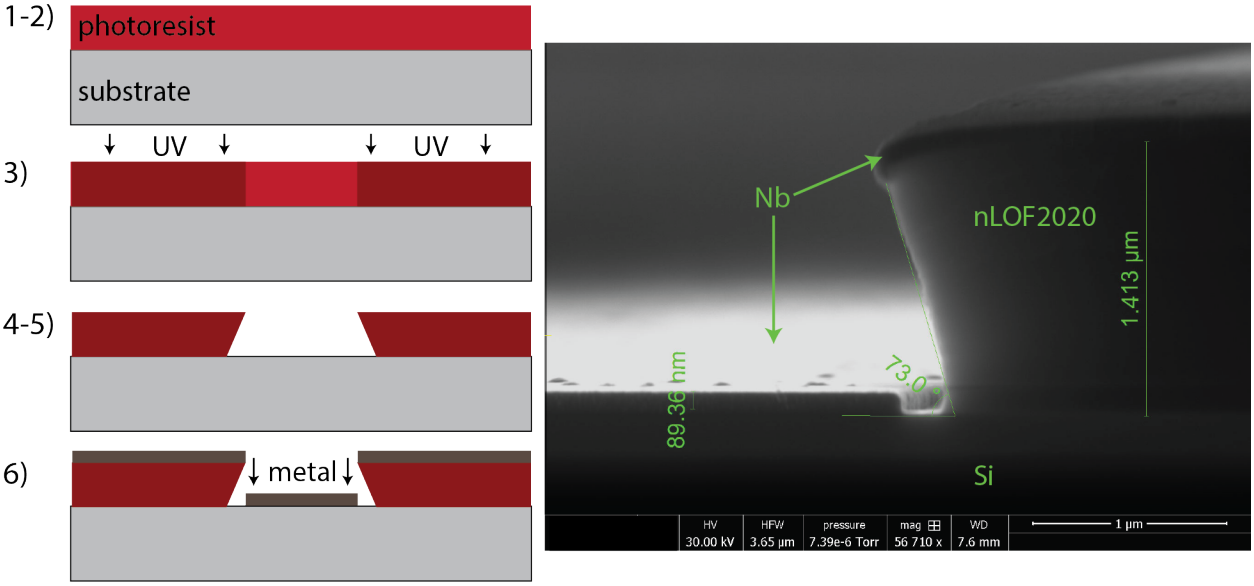

Figure A.1: **Lift-off of superconducting niobium (Nb) with nLOF2020 photoresist.** Fabrication steps are depicted on the left. The image on the right is a scanning electron micrograph (SEM) edge-on after step (4) by cleaving the sample, which directly shows the undercut.

Areas exposed to UV light (e.g. 365-375 nm) will harden and remain after development.

4. **Bake at 110 °C for 60 seconds (critical).**

5. **Develop for 60 seconds using AZ MIF 300.**

   Quench into a bath of DI water for ∼20 seconds and then rinse with copious amounts of fresh DI water for 30-60 seconds. If the sample is small, then placing it in a beaker of DI water and agitating/swirling may work well enough to avoid losing the sample in the sink. Perform an O_2 plasma descum before moving onto deposition.

6. **Deposit.**

   See Fig. A.1 (right) for the result of e-beam evaporated Nb at 0.5 Å/s onto Si with an nLOF2020 mask (exposed with 125 mJ/cm^2 from a 375 nm light source using a Heidelberg MLA150.). This film had a superconducting T_c of 8 K.

7. **Lift-off resist with organic solvents.**

   Recommended procedure: sonicate in NMP at 80 C for 30 minutes or greater, sonicate

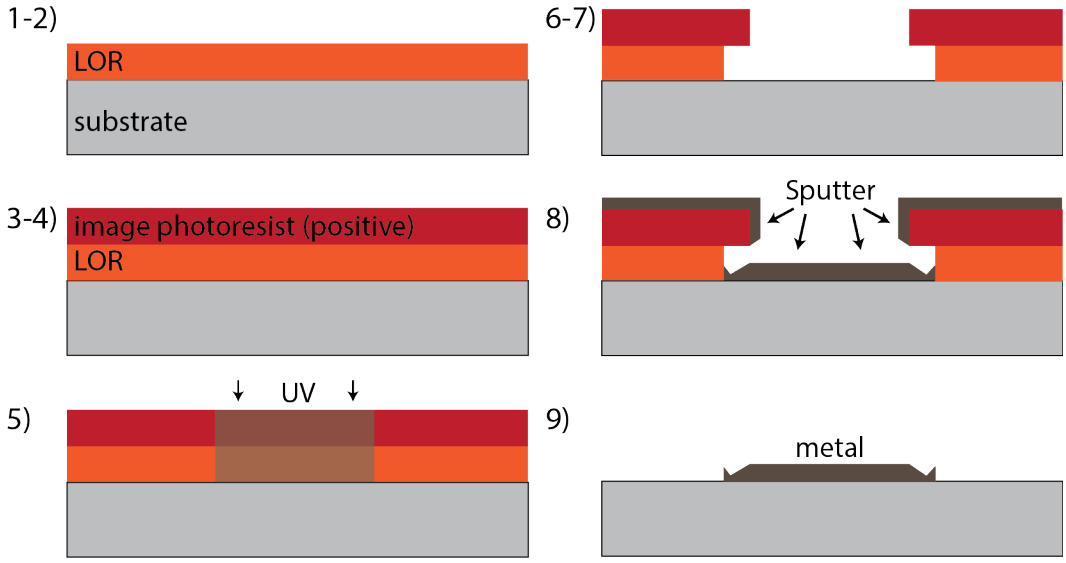

Figure A.2: **Process flow for sputtering with Lift-Off Resist (LOR).**

in IPA at room temperature for 10 minutes or greater, rinse with DI water, then N_2 or spin dry. If one wants to avoid sonication, it is possible to lift-off by soaking for much longer periods of time as long as there was a proper undercut.

A.1.2 Lift-Off Resist (LOR) & Sputtering Thick Copper

Sputtering, which uses a plasma to remove material from a target and deposit atoms on the substrate, often yields different material quality from e-beam evaporation and is more chemically versatile. Sputtering also offers more atmospheric control and sometimes less oxygen absorption into films for reasons like higher deposition rates and lower base pressures. The process flow below details a recipe for producing a ≈500 nm undercut and nearly micron thick resist underlayer. The undercut is tunable with development time and bake temperature while the resist thickness is tunable with spin speed.

1. **Spin LOR.**

   Adhesion promotion by HMDS is not necessary, and LOR typically has superior adhesion on most materials. One micron thick LOR can be accomplished with LOR5A spun at 2000 RPM or a thicker series at higher speeds. LOR3A is useful for thicknesses

of a few hundred nanometers.

2. **Bake at 180 °C for 3 minutes.**

   Consistent temperature between processes is critical. Wait for the sample to cool after this step.

3. **Spin the top layer of photoresist.**

   This 'image resist', which could be a high resolution photoresist like AZ 703 MiR, sets the feature size upon exposure/development. The LOR develops faster and should not be depended on for the final pattern.

4. **Bake (at temperature and time suitable for top resist layer, e.g. 95 °C for 60 seconds).**

5. **Expose.**

6. **Post-exposure bake suitable for top layer (image) photoresist.**

7. **Develop in AZ 300 MIF or 726 MIF for 60 seconds.**

   Gently agitate during development. In order to further clear out the undercut region, rinse in DI water for ∼30 seconds and then develop for another 15 seconds without drying. Afterwards, rinse with copious amounts of DI water and then dry. AZ Developer 1:1 will not develop LOR A or B series. Perform an O_2 plasma descum before moving onto deposition.

8. **Deposit.**

   Before sputtering onto the sample, run a short deposition on a dummy wafer in order to clean and prime the chamber. A longer Ti deposition on a dummy wafer is also recommended to decrease the chamber base pressure. Figure A.3a shows an SEM of a cleaved sample (cross sectional view) of 20 nm Ti/∼200 nm Cu sputtered on silicon with an AZ 703 MiR/LOR5A mask. The LOR5A was spun at 2000 RPM for 75 seconds

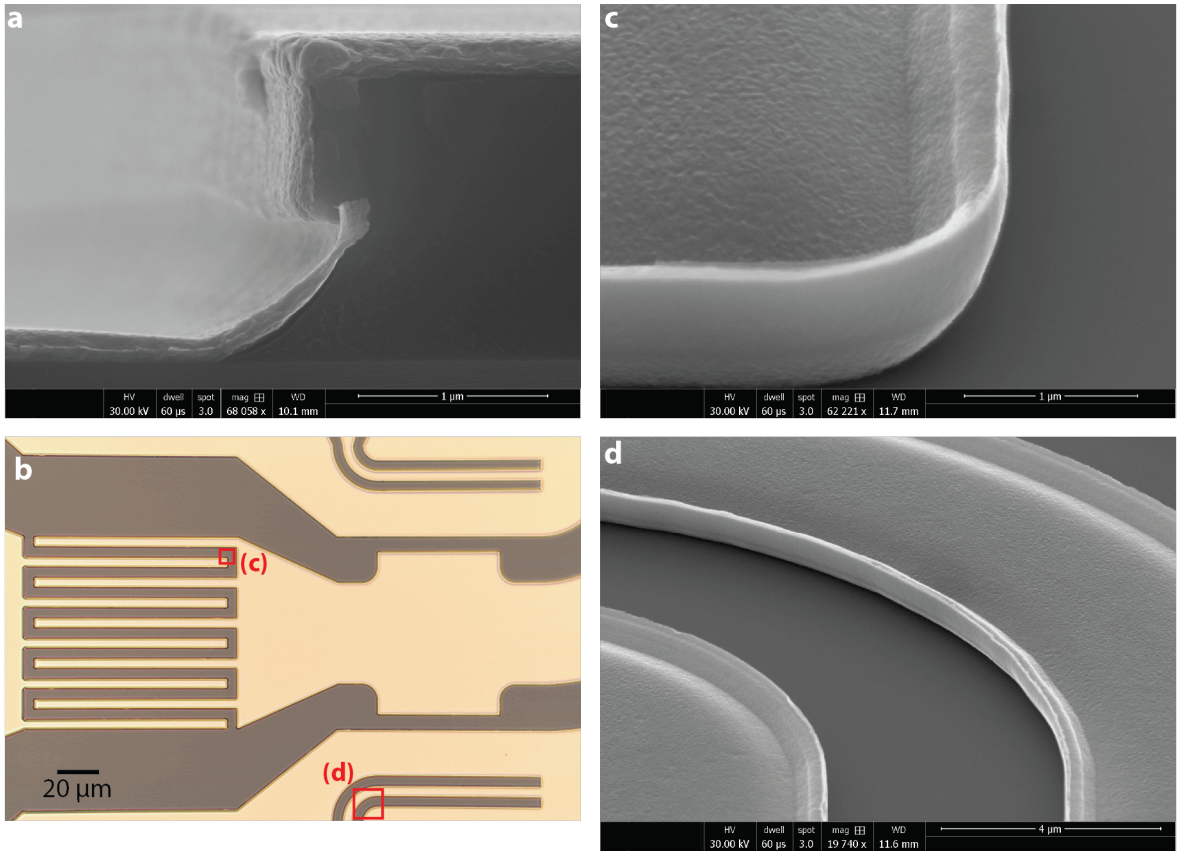

Figure A.3: **Sputtering thick (0.8 μm) copper with lift-off.**

and baked at 190 °C for 3 minutes, so the undercut was unsufficient to protect material from sputtering underneath the image resist overhang. Sputtering is semi-conformal, so it is nearly impossible to prevent deposition on the LOR.

9. **Lift-off resist.**

   See sections on nLOF2020 for recommendations and details.

Results of thick Cu sputtering are shown in Figure A.3. In the optical micrograph in Fig. A.3b, we see that there is no dramatic flagging (tearing), roughness on the metal features or edges at this resolution. The metal edge is imaged with scanning electron microscopy in Fig. A.3c-d, which reveal that the a couple hundred nanometers within the edge exhibit large variations in metal thickness. These Cu thickness variations result from metal deposition directly onto the LOR without connecting the metal outside the image resist, top layer.

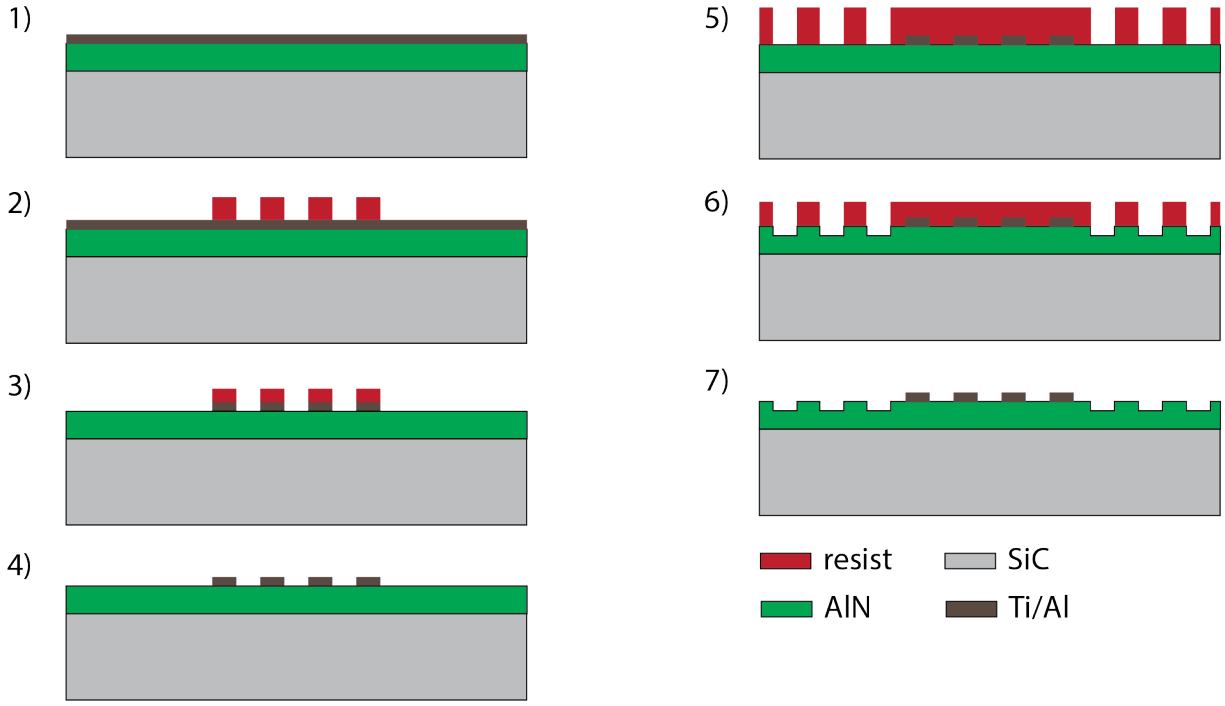

Figure A.4: **SAW device layers with inductively coupled plasma (ICP) etching.**

A.2 Etching with Inductively Coupled Plasmas

In this section we discuss the process for fabricating device layers, specifically for surface acoustic wave devices on AlN/SiC (Fig. A.4). This process is generalizable for different systems and layers barring chemistry and material constraints.

0. **Clean the sample.**

   Organic solvent cleaning with acetone, isopropanol (IPA), DI water consecutively with sonication is recommended at a minimum to ensure there are neither organic residues nor dust on the substrate prior to fabrication. After solvent or acid cleaning, bake the sample at a temperature of 115 °C or greater (180-200 °C recommended) for 3 minutes in order to dehydrate the material surface. More aggressive cleaning options include 'TAMI' (toluene, acetone, methanol, isopropanol), oxygen downstream plasma with heat, RCA cleaning (pirhana acid, DI, hydrofluoric acid, DI), or hydrofluoric & nitric acid 1:1 for SiC.

1. **Electron-beam evaporate device layer.**

   Our AlN/SiC SAW devices typically used 20 nm Ti and 150 nm Al in that order, evaporated at 1 Å/s and 3 Å/s, respectively. The Ti undermetal layer provides improved adhesion (empirically observed to reduce pitting and roughness in the Al) as well as a source of X-ray fluorescence for synchrotron experiments.

2. **Optical lithography for the metal layer etch mask.**

   If necessary to promote photoresist adhesion (e.g. on SiO_2), oven vapor prime with HMDS. Spinning HMDS is possible but may reduce the device yield or have worse effects on non-Si substrates. Afterwards, spin photoresist on the sample. For AZ1512 and AZ 703 MiR positive photoresists spinning at 4500 RPM results in approximately 1.2 and 0.85 μm thick resist, respectively. Bake the sample at 95 °C for 60 seconds after spinning. Pattern with direct write or mask-based optical lithography by exposure to UV light; bake at 115 °C for 60 seconds; let sample cool down for at least a minute to stabilize development time; develop in AZ Developer 1:1 (minimum Al attack compared to AZ MIF 300) for 120 seconds.

3. **Etch metal device layer.**

   Before etching, using an O_2 downstream plasma descum may improve sidewalls and etch results. O_2 plasma will oxidize more of the sample surface, so this step should be avoided for various materials and applications such as superconducting metals for low loss quantum circuits. Chlorine chemistry is efficient at etching Al: Cl_2, BCl_3, Ar with flow rates 30, 30, 10 sccm, bias power 50 W, ICP run power 400 W. The Al etch rate is ≈500 nm/min and photoresist etch rate is ∼200 nm/min. Chamber cleaning and priming is recommended by running an O_2 plasma clean for 10 minutes and then the desired etch recipe for 3 minutes on a dummy wafer.

4. **Lift-off resist with organic solvents.**

   An O_2 descum (mildly aggressive at 70 °C and higher power to remove ∼100 nm of

photoresist) can help remove a cross-linked layer from plasma etching. For maximum yield, soak the sample in N-Methyl-2-Pyrrolidone (NMP) at 80 °C with the sample supported upside down for > 4 hours, transfer the sample to a new beaker of fresh NMP and sonicate at 80 °C for 30 minutes, transfer to a beaker of IPA and sonicate for > 10 minutes, rinse with DI water and then N_2 or spin dry.

5. **Optical lithography for the AlN Bragg gratings.**

   See previous optical lithography step for further details. AZ Developer 1:1 is recommended again for minimal attack of AlN as well as any potentially exposed Al.

6. **Etch grooves into the AlN layer.**

   Before etching, using an O_2 downstream plasma descum may improve sidewalls and etch results. O_2 plasma will oxidize more of the sample surface, so this step should be avoided for various materials and applications such as superconducting metals for low loss quantum circuits. Chlorine chemistry is efficient at etching Al: Cl_2, BCl_3, Ar with flow rates 30, 30, 10 sccm, bias power 50 W, ICP run power 400 W. The AlN etch rate is ≈100 nm/min.

7. **Lift-off resist.**

   See previous lift-off step for further details.

A.3 Film Stress

Thin film stress is an important metric when considering material performance, stability or adhesion, and resonator quality factors. When a newly deposited thin film is too stressed, it can lead to buckling if highly compressive or cracking and delamination (decohesion) if highly tensile [148]. Localized buckling or 'hillocks' in the film are points of stress relief as shown in Figure A.5 in low and high magnification optical micrographs of AlN sputtered on 4H-SiC.

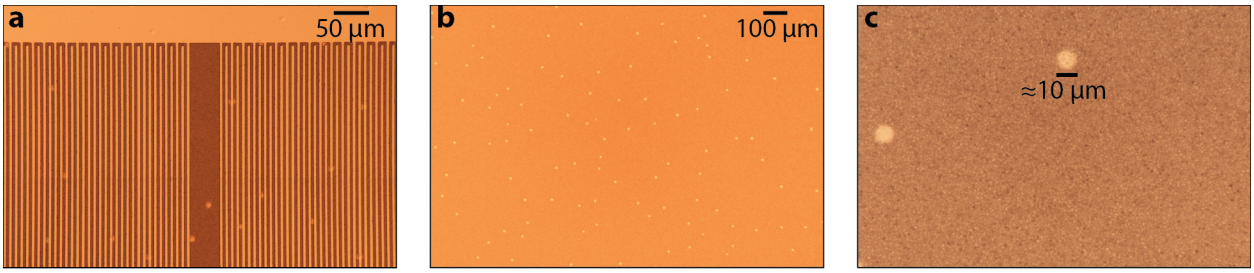

Figure A.5: **Defects in highly stressed AlN.** Hillocks form randomly distributed in the 1 μm thick AlN film on the 4H-SiC substrate.

In membrane mechanical resonators, it can be shown that the quality factor is directly proportional to the tensile film stress, so highly stressed SiN films in fact have enabled ultrahigh quality factors at megahertz frequencies [149]. Therefore, we usually want to deposit slightly thicker films on bulk substrates, such as piezoelectric AlN, with close to zero stress in order to avoid mechanical failures while at the same time remaining tensile.

Measurement of film stress is easily accomplished by comparing the substrate radius of curvature before and after deposition. Assuming that the film thickness (t_f) much smaller than that of the substrate (t_s), the radius of curvature is inversely proportional to the internal film stress in the *Stoney Equation*,

$$\sigma_\mathrm{f} = \frac{t_\mathrm{s}^2 E_\mathrm{s}}{6 t_\mathrm{f}(1-\nu)R} \quad \text{(isotropic substrate)}, \tag{A.1}$$

where E_s and ν are the Young's modulus and Poisson's ratio of the substrate. This

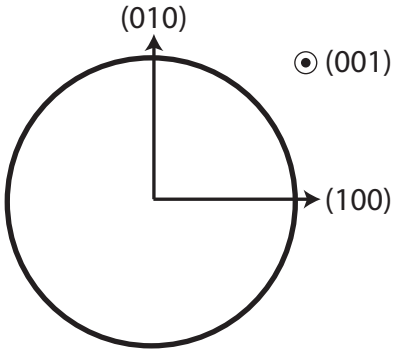

Figure A.6: **Wafer crystal axes.** Corresponding substrate schematic for Eq. (A.2).

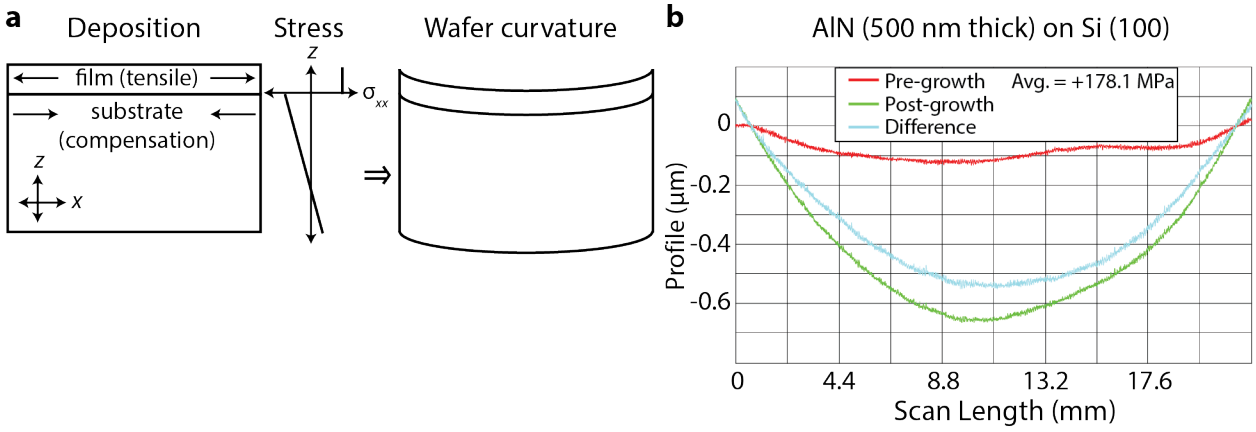

Figure A.7: **Film stress measurement by substrate curvature. a**. Sketch of a stressed thin film and the initial lateral stress distribution ($\sigma_{zz} = 0$ at the surface boundary condition). The stress causes a change in wafer curvature. **b**. Stress measurement on a 500 μm thick Si (100) wafer performed using a KLA Tencor profiler. The wafer surface profile, which must be measured in the same location (position and orientation) is fit to a 5th order polynomial.

formula takes the substrate's radius of curvature before deposition to be infinity (flat wafer) and R is the radius of curvature after deposition.

Anisotropic substrates, which includes all crystalline materials such as silicon, have direction dependent elastic moduli and Poisson's ratio. It can be shown that for a wafer with cubic symmetry and the surface normal along (001) as depicted in Fig. A.6 that the Stoney Equation takes the form [150],

$$\sigma_{\mathrm{f}} = \frac{t_{\mathrm{s}}^2}{6t_{\mathrm{f}}(s_{11} + s_{12})R} \quad \text{(anisotropic substrate)}, \tag{A.2}$$

where s_{11} and s_{12} are elements of the compliance tensor s^{E} ($c^{\mathrm{E}}s^{\mathrm{E}} = s^{\mathrm{E}}c^{\mathrm{E}} = 1$ where c^{E} is the elasticity tensor). We can see that a positive radius of curvature corresponds to tensile film stress (illustrated in Fig. A.7a) that we define as $\sigma_{xx} > 0$ in this convention. Figure A.7b shows an example stress measurement on a Si (100) square sample that is 35 mm x 35 mm large with 500 nm thick of sputtered AlN.

Using some handy relations from Nye, "Physical Properties of Crystals" Chapter 8.7 [56], one finds that $s_{11} + s_{12} = 180.65$ GPa for Si (100). Many other literature values range

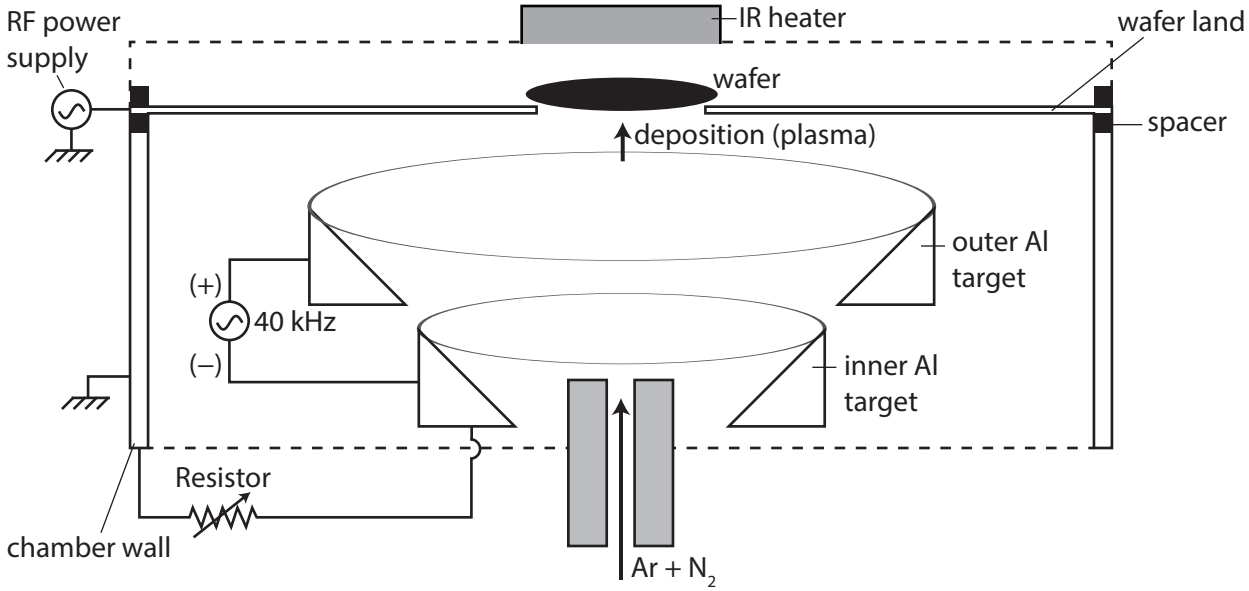

Figure A.8: **Schematic of reactive a.c. magnetron sputtering tool for AlN.** Ultra-high purity aluminum targets receive a.c. power at 40 kHz and usually kilowatts of power, which allows the inner and outer targets to each act as the anode and cathode. This diagram is adapted from Ref. [151].

from 180.3 GPa [150] to 180.7 GPa probably varying because of rounding and precision errors on the compliance tensor elements. For Si (111) we must rotate the system, yielding $s_{11} + s_{12} \rightarrow 4s_{11} + 8s_{12} + s_{44} = 229.1$ GPa. Since hexagonal 4H-SiC has a crystal class 6mm, there are similarities between the elasticity/compliance tensors of Si and 4H-SiC, so Eq. (A.2) is again applicable. We find that $s_{11} + s_{12} = 602.2$ GPa for 4H-SiC.

A.4 Aluminum Nitride

A.4.1 Reactive Sputtering

Reactive sputtering is among the most common deposition methods for depositing piezoelectric AlN for electromechanical devices [152]. We use an OEM Endeavor to reactively sputter AlN on 4" wafers or smaller samples by using metal wafer adapters. The system has

a load-lock and has a robotic system to transfer samples into the process module. Inside the process module (Fig. A.8) the sample surface faces downward towards the cylindrical targets shaped like annuli. Unlike d.c. sputtering, which is prone to arcing and dielectric build-up on the targets, a.c. sputtering keeps the target corners clean by alternating each Al targets role as the anode or cathode. Radio frequency (RF) biasing at 13.6 MHz offers Ar^+ plasma etching, and infrared (IR) heater directed towards the sample through a quartz window provides temperature control up to 500 °C maximum, and the constant, tunable resistor box (5-50 Ω or open) allows the grower to set a relative voltage between the targets allowing some control of ion bombardment and therefore independent film stress tunability. Summarized below are the typical process flows for sputtering polycrystalline (002)-oriented AlN on Si and 4H-SiC substrates.

Table A.1: **Reactive sputtering of AlN - typical parameters.** These deposition parameters demonstrate reasonably good oriented AlN growth on Si and provide a starting place for creating new recipes.

Ar flow	N_2 flow	Power	Pressure	Resistor box
5 sccm	17 sccm	6,000 W	5 mTorr	15 or 20 Ω

Silicon:

1. **Precondition chamber on a dummy sample.**

   This process step interleaves Al and AlN sputtering steps for a few hundred nanometers of each material. The dummy sample should be etched if it has not been used before to improve adhesion and avoid material flaking. Do not re-use the same Si sample for more than 5 microns of conditioning growths, and run a longer condition if the tool has not been used for more than 24 hours.

2. **Etch.**

   RF bias at 200 W of power with 4 sccm of Ar for 180 seconds.

3. **Heat.**

   Power at 100%, that we believe corresponds to ~ 450 °C, for 60 seconds.

4. **Sputter AlN.**

   Sputter with the parameters from Table A.1 without heat.

5. **Wait.**

   This step allows the wafer to cool down before transferring in order to avoid thermalization effects on the film from rapid thermal expansion or contraction. This is particularly important for thick aluminum electrodes because aluminum is soft and prone to migration. Approximately 60 seconds is sufficient.

Silicon carbide:

1. **Precondition chamber on a dummy sample.**

   See silicon recipe above for details.

2. **Etch (heated).**

   RF bias at 200 W of power with 4 sccm of Ar for 600 seconds with the IR heater at 100% power (~ 450 °C). Occasionally the RF impedance matcher, which is near the chamber wall and wafer land, has trouble keeping up with the heat, so this etch step could be broken up with intermittent wait steps.

3. **Heat.**

   Power at 100% (~ 450 °C) for 60 seconds.

4. **Sputter AlN (heated).**

   Sputter with the parameters from Table A.1 with heat at 100% power.

5. **Wait.**

   Approximately 60 seconds is sufficient.

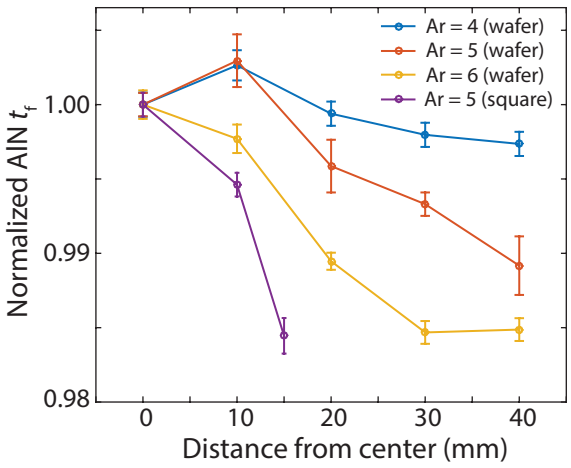

Figure A.9: **AlN uniformity as a function of Ar flow rate.** Ellipsometry measurements of AlN on Si (100) taken as a function of position. The error bars are the 95% confidence interval from fits.

In the results summary we show that more heating during the etch and growth steps result in better AlN. However, we have not run enough tests to prove which steps are essential and what is the optimal order. For example, it is possible that a long heat step before etching could improve the AlN (002) X-ray diffraction rocking curve (crystallinity).

A.4.2 Summary of Growths

Sputtering AlN on Si substrates with results detailed in Table A.2 show good crystallinity from X-ray diffraction peak rocking curve measurements that are robust to changes in Ar flow rate. The Ar flow rate tunes the deposition rate, uniformity, and stress. We first find the optimal Ar flow rate, which seems to be around 5 or 6 sccm for consistent AlN thickness that varies $< 1\%$ across the entire wafer (Fig. A.9). Using 5 sccm gives stress values closer to zero and a larger available dynamic range with the resistor box settings. On a separate set of samples, varying only the resistor box yields stress tunability from nearly zero at 25 Ω to highly tensile films nearly 1 GPa. If we wanted compressive AlN we could tune the resistor to > 25 Ω.

On 4H-SiC we observe that the AlN crystallinity (diffraction peak) is very sensitive to the etching step and heated growths. When the sputter step is performed under heated con-

ditions, we find that the AlN monotonically gets more crystalline, and furthermore heating during the etch step also improves the film crystallinity. This suggests that it is more difficult to etch SiC and expose fresh crystal substrate. Additionally, heated growth is needed in order to bring the rocking curve FWHM below 3° in our configuration (Table A.3). Interestingly, the film stress progressively becomes more tensile after using heat and correlates to the improved crystallinity, which may be due to interstitials or presence of larger gaps between grain boundaries [148] or thermal expansion effects.

Table A.2: **AlN sputtering results: Si (100) substrates.** The substrate size corresponds to either the diameter of a wafer (W) or side length of a diced square (S), manufactured by Nova Electronic Materials. Samples were solvent cleaned prior to sputtering. The AlN film thickness (t_f) was measured by ellipsometry and X-ray diffraction rocking curves (FWHM) are measured using a Brucker D8 on the AlN (0002) diffraction peak and fit to a Gaussian distribution. The target AlN thickness was 500 nm for all samples. All uncertainties in parentheses are 95% confidence intervals from fitting on the last digit.

Size	Ar flow	Resistor (Ω)	t_f (nm)	Stress (MPa)	FWHM (°)
100 mm W	4	15	492.0(4)	-246.2	1.82(1)
100 mm W	5	15	507.9(4)	+29.2	1.77(2)
100 mm W	6	15	522.2(5)	+225.0	1.87(1)
35 mm S	5	10	501.7(4)	+800.9	1.91(1)
35 mm S	5	15	517.0(4)	+172.3	1.86(2)
35 mm S	5	20	498.1(4)	+139.7	-
35 mm S	5	25	493.8(7)	+81.3	1.87(2)

Table A.3: **AlN sputtering results: 4H-SiC substrates.** All substrates were diced from 100 mm wafers manufactured by II-VI Inc. for the N-type (16-28 mΩ cm), development grade and Norstel AB for the high purity semi-insulating (SI), production grade SiC. Samples were solvent cleaned prior to deposition and each sputtered with a resistor box value of 20 Ω and Ar flow rate of 5 sccm. X-ray diffraction rocking curves (FWHM) are measured using a Brucker D8 on the AlN (0002) diffraction peak and fit to a Gaussian distribution. The target AlN thickness was 500 nm for all samples. All uncertainties in parentheses are 95% confidence intervals from fitting on the last digit.

Type	Miscut	Etch w/o heat (s)	Etch w/ heat (s)	Sputter w/ heat (nm)	Sputter w/o heat (nm)	Stress (MPa)	FWHM (°)
N-type	4°	600	0	10	490	-223.7	3.20(5)
N-type	4°	600	0	50	450	-100.4	3.01(2)
N-type	4°	600	0	200	300	-25.3	3.04(2)
N-type	4°	420	180	50	450	-194.5	2.73(2)
SI	0	420	180	50	450	+124.5	5.2(6)
SI	0	0	600	50	450	+217.4	4.11(2)
SI	0	0	600	500	0	+310.7	2.65(1)
SI	0	0	600	500	0	+482.5	2.39(1)
SI	0	0	600	500	0	-	2.50(1)

Appendix B

Spin-Stress and Electric Field Coupling

The results in these sections were published in the supplementary materials of [103].

B.1 Comparison of Spin-Stress Coupling Parameters

In additional to checking the supercell convergence for zero-field splitting D_0 values, we validate the computational protocol by comparing our theoretical results for the NV center in diamond with the work by Udvarhelyi *et al.* [47] and Barson *et al.* [134]. Udvarhelyi *et al.* computed the spin-strain and spin-stress coupling coefficients of NV centers by DFT. Barson *et al.* measured the coupling strength between spin and stress for NV centers in a diamond nanomechanical structure.

To make a direct comparison, we converted the 6 spin-strain coupling coefficients for NV centers in Table 6.2 into the 6 spin-stress coupling coefficients a_1, a_2, b, c, d, e as defined in their work [47, 134]. In the conversion we used the compliance tensor ($s^{\mathrm{E}} = (c^{\mathrm{E}})^{-1}$) of diamond in Ref [153]. Table B.1 shows the comparison of spin-stress coupling coefficients from different works. Note that Ref [134] used a different sign convention for strain, and

therefore their results are multiplied by a negative sign in the table.

Table B.1: **Spin-stress coupling coefficients for the NV in diamond.** All values are in MHz/GPa.

	This work (DFT)	Ref (DFT)[47]	Ref (Exp.)[134]
a_1	-3.82	-2.65	-4.4
a_2	3.80	2.52	3.7
b	1.80	1.94	2.3
c	-2.77	-2.84	-3.5
d	-0.23	-0.12	
e	0.60	0.67	

From Table B.1 we find that our results match well with both references. The agreement is a validation for the computational setup we used for the calculations of **G**.

B.2 Electric Field Coupling to Spin Defects

The response of **D** to strain (2nd rank tensor) is different from its response to applied electric field (1st rank tensor). Similar to spin-strain coupling tensor, we can expand the effect of an electric field (**E**) perturbation on the **D** tensor,

$$D_{ij}(E_k) = D_0 S_z^2 + \frac{\partial D_{ij}}{\partial E_k} E_k + \mathcal{O}\Big(E^2\Big). \tag{B.1}$$

We can define a tensor **F** as the first-order coupling between **D** and the electric field vector **E**:

$$F_{ijk} = \frac{\partial D_{ij}}{\partial E_k}\,. \tag{B.2}$$

where i, j, k are indices, each representing the three Cartesian coordinates $\in x, y, z$. Simi-

lar to the previous discussions of spin-strain coupling, we define the Cartesian frame for kk, hh divacancies in 4H-SiC to be $\hat{x} \equiv [\bar{1}\bar{1}20], \hat{y} \equiv [1\bar{1}00], \hat{z} \equiv [0001]$, in consistence with the SAW experiment, and for the nitrogen-vacancy center diamond as $\hat{x} \equiv [\bar{1}10], \hat{y} \equiv [\bar{1}\bar{1}2], \hat{z} \equiv [111]$. In Voigt notation, the response of $\mathbf{D}$ to an applied electric field $\mathbf{E}$ is given by

$$\begin{pmatrix} \Delta D_{xx} \\ \Delta D_{yy} \\ \Delta D_{zz} \\ \Delta D_{yz} \\ \Delta D_{xz} \\ \Delta D_{xy} \end{pmatrix} = \begin{pmatrix} F_{11} & F_{12} & F_{13} \\ F_{21} & F_{22} & F_{23} \\ F_{31} & F_{32} & F_{33} \\ F_{41} & F_{42} & F_{43} \\ F_{51} & F_{52} & F_{53} \\ F_{61} & F_{62} & F_{63} \end{pmatrix} \begin{pmatrix} E_x \\ E_y \\ E_z \end{pmatrix} = \begin{pmatrix} & F_{12} & F_{13} \\ & -F_{12} & F_{13} \\ & & -2F_{13} \\ & F_{42} & \\ F_{42} & & \\ F_{12} & & \end{pmatrix} \begin{pmatrix} E_x \\ E_y \\ E_z \end{pmatrix} \tag{B.3}$$

where C_{3v} symmetry was considered in the last equality. Combining the above equation with $H = \sum_{i,j} S_i(\Delta D_{ij})S_j$, one can see that an applied electric field can drive $\Delta m_s = \pm 1$ and $\Delta m_s = \pm 2$ transitions, similar to the case of applying a strain. However, an electric field and a strain enters the Hamiltonian by dissimilar response tensors with different dimensions and rank. $\mathbf{F}$ is 6×3 matrix while $\mathbf{G}$ is 6×6 matrix in Voigt notation. For C_{3v} defects, $\mathbf{F}$ has only 3 independent components while $\mathbf{G}$ has 6 independent components; $\mathbf{F}$ also has completely different symmetric form as $\mathbf{G}$ even if only the first 3 columns of $\mathbf{G}$ (corresponding to normal strains ε_{xx}, ε_{yy}, ε_{zz}) are considered.

Appendix C

High-Q Superconducting SAW Cavities

In order to test the limits of silicon carbide (SiC) as a low loss mechanical material, piezoelectric properties without AlN, and applicability for future hybrid quantum systems with spin ensembles, SAW resonators are fabricated directly on 4H-SiC substrates. All 4H-SiC substrates are chemically-mechanically polished (CMP), high-purity semi-insulating (HPSI) sourced by Cree Inc. and are RCA cleaned before fabrication. Both niobium (Nb) and aluminum (Al) SAW devices are investigated separately with optical lithography methods (positive photoresist S1813) and lift-off using electron-beam evaporation in an Angstrom EvoVac. The Nb is evaporated at 1 Å/s to a thickness of 100 nm, while devices using Al was evaporated in at 2 Å/s rate to a thickness of 100 nm. Lift-off was performed by sonicating in NMP at 80 °C for at least one hour. An example of the final device is shown in Fig. C.1a, which has $N_\mathrm{p} = 50$ finger pairs in the IDT, 1100 grating strips in each Bragg reflector, aperture size W of 150λ, the acoustic wavelength is 16 μm.

All radio frequency (RF) reflection measurements are performed with a vector network analyzer (VNA). The samples are wirebonded to a PCB inside a copper box, placed in a Quantum Design PPMS for 1.8-300 K measurements or a dilution refrigerator for mea-

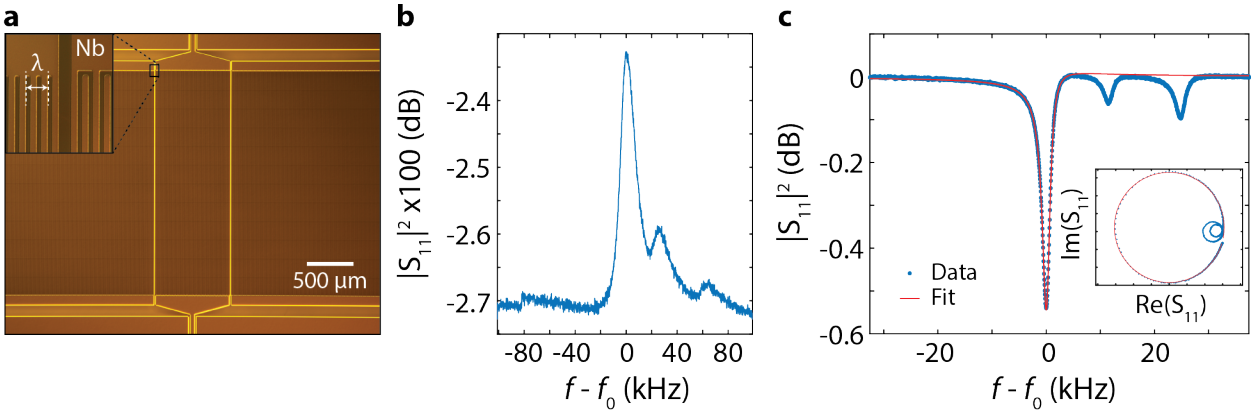

Figure C.1: **Result for superconducting niobium SAW resonator on 4H-SiC. a**. Optical micrograph of the device. The niobium metal was deposited on top of a clean 4H-SiC with optical lithography and lift-off. The IDT (inset) is made up of single finger interleaved electrodes. Faint horizontal patterns are from the direct write lithography where the pattern was stitched together with multiple passes (small dose variations). **b**. RF reflection measurement of the SAW resonator at room temperature with a calibrated VNA. Notice the y-axis is very close to 100% reflection. **c**. RF reflection measurement of the same resonator at a temperature of 1.8 K. This niobium superconducted at ≈ 8 K in a Quantum Design PPMS.

surements down to 26 mK, and the sample/PCB is connected via SMA cables. All SAW resonators experiments use a 1-port grounded configuration, such that one side of the IDT is connected to RF while the other side of the IDT is grounded. All grating reflectors are shorted and floating. At room temperature, the Nb SAW resonator is normal and has stray resistance in the IDT and CPW that is much greater than 50 Ω, so only a weak peak is observed (Fig. C.1b) at $f_0 = 421.735834$ MHz. The inferred acoustic wavespeed $v_\mathrm{f} = f_0\lambda = 6,748$ m/s is very close to the expected value from literature (6,830 m/s) Below 8K we observe that the Nb superconducts and yields a very high Q cavity. Using the fit equation (3.42) find a higher resonance frequency at $f_0 = 422.468665$ MHz due to thermal expansion/contraction and a change in acoustic wavespeed, internal quality factor $Q_\mathrm{i} = 2.41 \times 10^5$, external quality factor $Qe = 7.59 \times 10^6$, and asymmetry rotation angle $\phi = 13.7°$. This is among the highest internal quality factors reported to date for a SAW resonator at 1.8 K. Nonetheless, the result comes at a cost of the weak piezoelectric coupling provided by SiC, so this cavity is not as useful for strongly driving spins at high RF excitation powers. Our high-Q superconducting

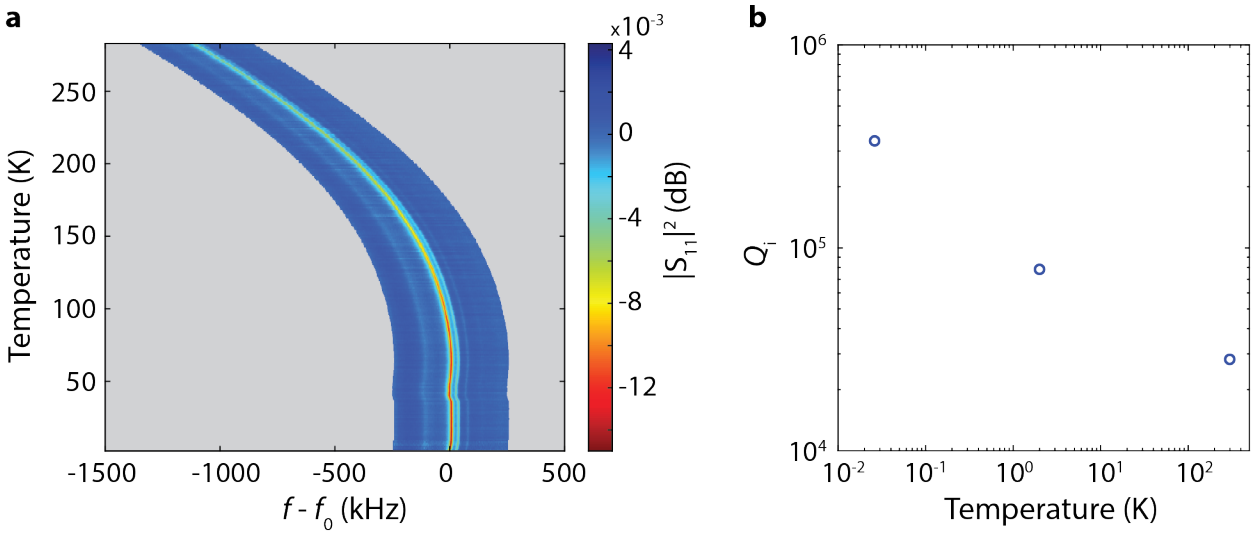

Figure C.2: **Temperature dependence of aluminum SAW resonators on 4H-SiC. a**. Temperature dependence of RF reflection measurement, performed in a Quantum Design Physical Property Measurement System. **b**. Analyzed internal quality factor Q_i as a function of temperature. The data point taken at T = 26 mK was performed in an Oxford dilution refrigerator with high microwave power (-50 dB attenuation on the input lines, low noise HEMT amplifier at 4K on the output, and a room temperature amplifier for a total of +40 dB gain on the output.).

Nb SAW cavity is well suited for hybridizing with spin ensembles as long the cavity does not need to be overcoupled to a transmission line.

The Al SAW resonators on SiC, which were actually the first ones to get fabricated after testing on ST-X quartz, are also found to yield internal quality factors. For the same temperature, the Q_i is slightly lower, and this is probably due to having rougher lithography from a hard contact aligner in the Searle cleanroom compared to direct writing that was used for Nb devices in the Pritzker Nanofabrication Facility. A temperature sweep of the RF reflection response (Fig. C.2a) clearly shows the resonator frequency shift as the temperature increases, and there is a dependence reminiscent of T^3 from thermal expansion. The Q_i reaches nearly 3×10^5 near 26 mK, and Q_i as a function of temperature appears to be linear on a log-log scale. Other materials including GaAs and ST-X quartz have also exhibited power-law behaviors for $Q_\mathrm{i}(T)$.

Appendix D

Creating Defect Ensembles and Annealing 4H-SiC

In this appendix we present the details and recipes for ion implantation by Cutting Edge Ions Inc. to create divacancy ensembles and chromium ion (substitutional Cr^{4+}) ensembles. All samples are annealed in tube furnaces with a gas controlled environment, which is usually argon (Ar) for an inert atmosphere[1]. We found that many atmospheres including argon and air worked similarly to create defect ensembles and did not notice photoluminescence differences with/without oxygen. Forming gas (4% H_2, 96% Ar) was found to damage SiC samples and create hexagonal shaped pitting above $\sim$ 1300 °C, in addition to causing charge unstable single divacancies (not shown here), so forming gas should be avoided during defect spin creation when possible.

D.1 Divacancy Ensembles

1. **Clean samples.** Organic solvent cleaning (acetone, isopropanol, DI water rinse) is sufficient to remove any organic residues. This step is to avoid thick residues and

1. The gas flow rates and pressures were not well controlled. The pressure was usually close to one atmosphere.

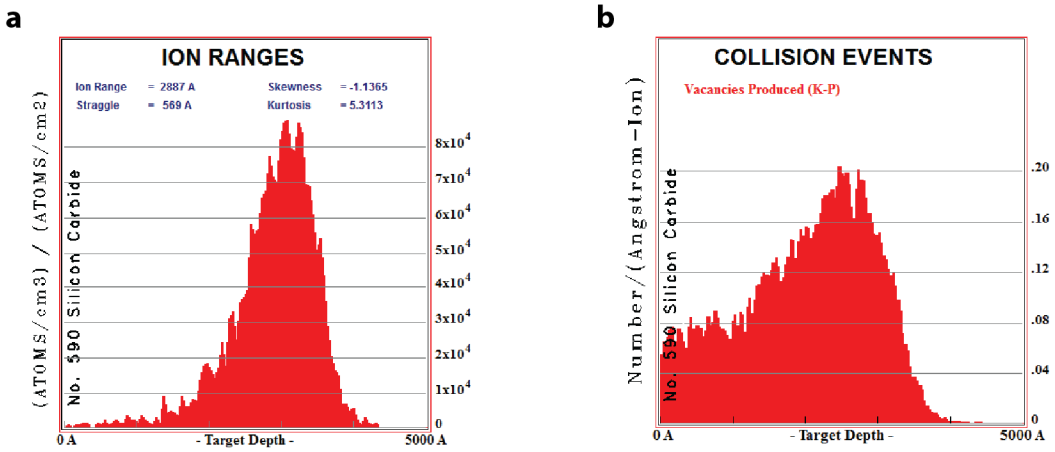

Figure D.1: **Stopping range of carbon-12 implanted into SiC.** Results of SRIM calculations for **a** the ^{12}C ions in the SiC lattice at 170 keV with a 7° tilt and **b** vacancy distribution produced by the implantation events. Approximately 500 vacancies are created per ion.

materials that could mask ion implantation, and additionally any materials or surface contamination that becomes heavily damaged could be very difficult to remove afterwards.

2. **Implant with carbon-12.** We use 170 keV energy (from a 170 kV accelerating potential) of the $^{12}C^{+}$ ions, tilt of 7°, dose of 10^{12} ions cm^{-2}. The tilt helps to prevent channeling, which would yield a less predictable distribution of deeper ions that avoided the lattice nuclei. The exact energy is not critical; we choose to use 170-190 keV in various experiments because we wanted to generate vacancies as deep as possible, but higher energies than 190 keV require double ionization and cost more money per batch.

3. **Anneal the sample at a temperature of ~ 850 °C.** We use ultra-high purity argon gas cylinder and a small over-pressure in the tube furnace to prevent oxygen leaking.

The implanted carbon ions are expected to penetrate into the SiC approximately 290 ± 57 nm deep (Fig. D.1a). The width of the implantation profile in depth is called the *ion*

straggle. The vacancies from these carbon ions are distributed more of a flat profile while still concentrated at a similar depth (Fig. D.1b). We can estimate the defect density formed by implantation and annealing. Using the straggle and 5% creation efficiency per carbon-12 ion found by A. L. Falk *et al.* in Ref. [18], we approximate a density of $\approx 10^{16}$ divacancies cm^{-3} from a dose of 10^{12} ions cm^{-2}. If, for comparison, we assume that each vacancy generated in the wider distribution has a 0.1-1% creation efficiency like nitrogen-vacancy centers in diamond, then we find a density of $\approx 2 \times 10^{16} - 10^{1}7$ divacancies cm^{-3} for the same dose.

D.2 Chromium Ensembles

This section details a recipe for implanting and annealing chromium defect ensembles for creating Cr^{4+} substitutional ions in semi-insulating 4H-SiC [154].

1. **Clean samples.** Organic solvent cleaning (acetone, isopropanol, DI water rinse) is sufficient to remove any organic residues. This step is to avoid thick residues and materials that could mask ion implantation, and additionally any materials or surface contamination that becomes heavily damaged could be very difficult to remove afterwards.

2. **Implant with chromium** ($\mathbf{I_{Cr-52} = 0}$, $\mathbf{I_{Cr-53} = 3/2}$.) We use 190 keV energy (from a 170 kV accelerating potential) of the $^{52}Cr^{+}$ ions, tilt of 7°, dose of 5×10^{11} ions cm^{-2}. The tilt helps to prevent channeling, which would yield a less predictable distribution of deeper ions that avoided the lattice nuclei. The exact energy is not critical; we choose to use 1190 keV in various experiments because we wanted to generate chromium defects as deep as possible, but higher energies than 190 keV require double ionization and cost more money per batch. Our first experiments also used a carbon co-implantation at 100 keV to generate defects at a similar depth because it is known to increase transition metal electrical activation [155], but it probably was not needed. The SRIM calculations are shown in Fig. D.2.

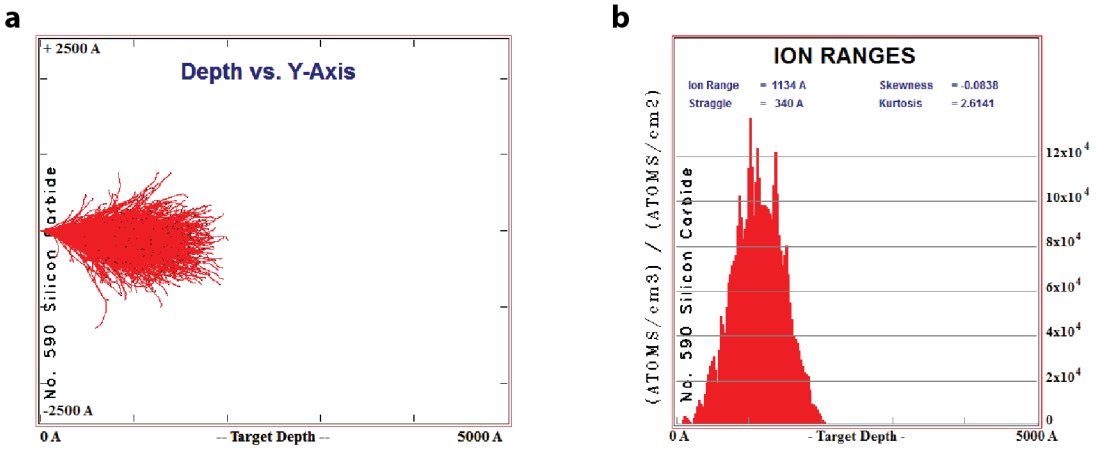

Figure D.2: **Stopping range of chromium-52 implanted into SiC. a** Ion ranges and paths taken shown in a depth cross section (horizontal is depth into the SiC substrate and vertical is the transverse direction if ions penetrated from a point at the surface). **b**. Results of SRIM calculations for the ^{52}Cr ions in the SiC lattice at 190 keV with a 7° tilt. Approximately 2000 vacancies are created per ion.

3. **Make a photoresist carbon cap on the SiC Si-face (implantation surface).** A simple recipe for example is to use a common optical photoresist (e.g. AZ1512 or AZ5214-E), spin coat (e.g. 3000 RPM for $\sim$ 2 μm thickness), bake at 95 °C for 60 seconds to harden the resist, and then bake at bake at 350 °C for 30 minutes to remove solvents. A carbon cap will prevent Si sublimation and roughening caused by annealing at temperatures over 1400 °C. Other materials unfortunately have been found to alloy with the SiC at high temperatures and then cannot be removed, whereas carbon will not react or mix with the SiC.

4. **Anneal the sample at a temperature > 1500 °C.** We use ultra-high purity argon gas cylinder and a small over-pressure in the tube furnace to prevent oxygen leaking. We use a tube furnace with $MoSi_2$ heating elements and an alumina tube rated up to a maximum temperature of 1700 °C. We ramp at 100 °C/hr to the desired temp, dwell for 30 minutes, and ramp at °C/hr to room temp. Higher temperatures ranging 1500-1900 °C have been performed at companies such as Centrotherm and Fraunhofer IISB in Germany and usually yield much smoother results because their furnaces ramp

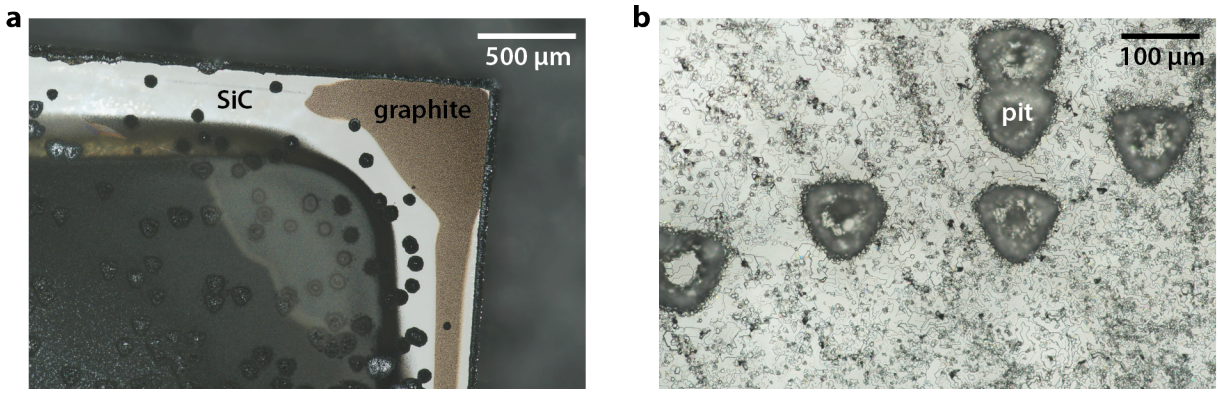

Figure D.3: **SiC anisotropic etching caused by annealing at 1600 °C. a**. Sample after annealing in a tube furnace for **b**. 4H-SiC surface that was not capped. All of these issues can be mitigated by annealing for minimal times with a proper graphite cap or by only using temperatures less than 1400 °C.

faster (50-75 °C/min) and have better atmosphere control.

5. **Remove the carbon cap by annealing at a temperature of $> \sim 750$ °C in oxygen or air.** The exact temperature is not critical as long as oxygen in the atmosphere can react with the graphite to turn C into CO_2. Downsteam oxygen plasma can also work for cap removal but the plasma is actually quite slow at etching graphite and more physically destructive to the substrate compared to a box furnace in air.

Some examples of bad outcomes are shown in Fig. D.3a. When the carbon cap is not made well or thick enough, pitting can occur simply from Si sublimation. The pits look either hexagonal or triangular because of the 4H-SiC crystal symmetry. Since any oxygen can remove the carbon (graphite) cap at high temperatures, a long anneal in nominally argon may eventually etch away the entire cap and expose fresh SiC. At that point, the surface will most certainly be roughened as shown in Fig. D.3b. In order to avoid losing the graphite cap during long, high temperature anneals, it can be helpful to collaborate with or pay another institution with access to advanced tools for rapid thermal processing.

Bibliography

[1] G. Kurizki, P. Bertet, Y. Kubo, K. Mølmer, D. Petrosyan, and P. Rabl. Quantum technologies with hybrid systems. *Proceedings of the National Academy of Sciences of the United States of America*, 112(13):3866–3873, 2015.

[2] M. Ziaei-Moayyed, S. D. Habermehl, D. W. Branch, P. J. Clews, and R. H. Olsson. Silicon carbide lateral overtone bulk acoustic resonator with ultrahigh quality factor. *2011 IEEE 24th International Conference on Micro Electro Mechanical Systems*, pages 788–792, 2011.

[3] Ou, H. and and Ou, Y. and Argyraki, A. and Schimmel, S. and Kaiser, M. and Wellmann, P. and Linnarsson, M. K. and Jokubavicius, V. and Sun, J. and Liljedahl, R. and Syväjärvi, M. Advances in wide bandgap SiC for optoelectronics. *The European Physical Journal B*, 87, 2014.

[4] M. W. Doherty, N. B. Manson, P. Delaney, F. Jelezko, J. Wrachtrup, and L. C. L. Hollenberg. The nitrogen-vacancy colour centre in diamond. *Physics Reports*, 528(1):1 – 45, 2013.

[5] F. J. Heremans, C. G. Yale, and D. D. Awschalom. Control of Spin Defects in Wide-Bandgap Semiconductors for Quantum Technologies. *Proceedings of the IEEE*, 104(10):2009–2023, 2016.

[6] W. F. Koehl, B. B. Buckley, F. J. Heremans, G. Calusine, and D. D. Awschalom. Room temperature coherent control of defect spin qubits in silicon carbide. *Nature*, 479(7371):84–87, 2011.

[7] D. J. Christle, A. L. Falk, P. Andrich, P. V. Klimov, J. U. Hassan, N. T. Son, E. Janzén, T. Ohshima, and D. D. Awschalom. Isolated electron spins in silicon carbide with millisecond coherence times. *Nature Materials*, 14(2):160–163, 2015.

[8] K. J. Satzinger, Y. P. Zhong, H.-S. Chang, G. A. Peairs, A. Bienfait, M.-H. Chou, A. Y. Cleland, C. R. Conner, É. Dumur, J. Grebel, I. Gutierrez, B. H. November, R. G. Povey, S. J. Whiteley, D. D. Awschalom, D. I. Schuster, and A. N. Cleland. Quantum control of surface acoustic-wave phonons. *Nature*, 563(7733):661–665, 2018.

[9] R. Manenti, M. J. Peterer, A. Nersisyan, E. B. Magnusson, A. Patterson, and P. J. Leek. Surface acoustic wave resonators in the quantum regime. *Physical Review B*, 93:041411, 2016.

[10] G. Calusine, A. Politi, and D. D. Awschalom. Silicon carbide photonic crystal cavities with integrated color centers. *Applied Physics Letters*, 105:011123, 2014.

[11] G. Calusine, A. Politi, and D. D. Awschalom. Cavity-enhanced measurements of defect spins in silicon carbide. *Physical Review Applied*, 6:014019, 2016.

[12] A. A. Lebedev. Deep level centers in silicon carbide: A review. *Semiconductors*, 33(2):107–130, 1999.

[13] M. Cabello, V. Soler, G. Rius, J. Montserrat, J. Rebollo, and P. Godignon. Advanced processing for mobility improvement in 4H-SiC MOSFETs: A review. *Materials Science in Semiconductor Processing*, 78:22 – 31, 2018.

[14] S. E. Saddow and A. Agarwal. *Advances in silicon carbide processing and applications*. Artech House, Inc., 2004.

[15] M. Widmann, S.-Y., T. Rendler, N. T. Son, H. Fedder, S. Paik, L.-P. Yang, N. Zhao, S. Yang, I. Booker, A. Denisenko, M. Jamali, S. A. Momenzadeh, I. Gerhardt, T. Ohshima, A. Gali, E. Janzén, and J. Wrachtrup. Coherent control of single spins in silicon carbide at room temperature. *Nature Materials*, 14(2):164–168, 2015.

[16] R. Nagy, M. Widmann, M. Niethammer, D. B. R. Dasari, I. Gerhardt, Ö. O. Soykal, M. Radulaski, T. Ohshima, J. Vuckovic, N. T. Son, I. G. Ivanov, S. E. Economou, C. Bonato, S.-Y. Lee, and J. Wrachtrup. Quantum properties of dichroic silicon vacancies in silicon carbide. *Physical Review Applied*, 9:034022, 2018.

[17] A. L. Falk, P. V. Klimov, B. B. Buckley, V. Ivády, I. A. Abrikosov, G. Calusine, W. F. Koehl, Ádám Gali, and D. D. Awschalom. Electrically and Mechanically Tunable Electron Spins in Silicon Carbide Color Centers. *Physical Review Letters*, 112(18):187601, 2014.

[18] A. L. Falk, B. B. Buckley, G. Calusine, W. F. Koehl, V. V. Dobrovitski, A. Politi, C. A. Zorman, P. X.-L. Feng, and David D. Awschalom. Polytype control of spin qubits in silicon carbide. *Nature Communications*, 4:1819, 2013. Article.

[19] Bockstedte, M. and Schütz, F. and Garratt, T. and Ivády, V. and Gali, A. Ab initio description of highly correlated states in defects for realizing quantum bits. *npj Quantum Materials*, 3(1):31, 2018.

[20] D. J. Christle, P. V. Klimov, C. F. de las Casas, K. Szász, V. Ivády, V. Jokubavicius, J. U. Hassan, M. Syväjärvi, W. F. Koehl, T. Ohshima, N. T. Son, E. Janzén, Á. Gali, and D. D. Awschalom. Isolated spin qubits in sic with a high-fidelity infrared spin-to-photon interface. *Phys. Rev. X*, 7:021046, 2017.

[21] H. Seo, H. Ma, M. Govoni, and G. Galli. Designing defect-based qubit candidates in wide-gap binary semiconductors for solid-state quantum technologies. *Physical Review Materials*, 1:075002, 2017.

[22] W. F. Koehl, H. Seo, G. Galli, and D. D. Awschalom. Designing defect spins for wafer-scale quantum technologies. *MRS Bulletin*, 40(12):11461153, 2015.

[23] J. R. Maze, A. Gali, E. Togan, Y. Chu, A. Trifonov, E. Kaxiras, and M. D. Lukin. Properties of nitrogen-vacancy centers in diamond: the group theoretic approach. *New Journal of Physics*, 13(2):025025, 2011.

[24] M. W. Doherty, N. B. Manson, P. Delaney, and L. C. L. Hollenberg. The negatively charged nitrogen-vacancy centre in diamond: the electronic solution. *New Journal of Physics*, 13(2):025019, 2011.

[25] P. V. Klimov, A. L. Falk, D. J. Christle, V. V. Dobrovitski, and D. D. Awschalom. Quantum entanglement at ambient conditions in a macroscopic solid-state spin ensemble. *Science Advances*, 1(10):e1501015, 2015.

[26] E. Zavoisky. Spin-magnetic resonance in paramagnetics. *Journal of Physics USSR*, 9:245, 1945.

[27] S. A. Al'tshuler. *Proceedings of the USSR Academy of Sciences*, 85:1235, 1952.

[28] A. Kaslter. *Experimentia*, 8:1, 1952.

[29] W. G. Proctor and W. H. Tanttila. Saturation of nuclear electric quadrupole energy levels by ultrasonic excitation. *Physical Review*, 98:1854–1854, 1955.

[30] W. G. Proctor and W. H. Tanttila. Influence of ultrasonic energy on the relaxation of chlorine nuclei in sodium chlorate. *Physical Review*, 101:1757–1763, 1956.

[31] E. H. Jacobsen, N. S. Shiren, and E. B. Tucker. Effects of 9.2-kmc/sec ultrasonics on electron spin resonances in quartz. *Physical Review Letters*, 3:81–83, 1959.

[32] E. B. Tucker. Attenuation of longitudinal ultrasonic vibrations by spin-phonon coupling in ruby. *Physical Review Letters*, 6:183–185, 1961.

[33] E. B. Tucker. Interaction of phonons with iron-group ions. *Proceedings of the IEEE*, 53(10):1547–1573, 1965.

[34] E. R. Feher. Effect of uniaxial stresses on the paramagnetic spectra of Mn^{3+} and Fe^{3+} in mgo. *Physical Review*, 136:A145–A157, 1964.

[35] E. B. Tucker. Spin-lattice coupling of a kramers doublet: Co^{2+} in MgO. *Physical Review*, 143:264–274, 1966.

[36] J. F. Clare and S. D. Devine. Superposition-model analysis of the spin-strain coupling tensor in ruby. *Journal of Physics C: Solid State Physics*, 16(22):4415–4423, 1983.

[37] Z. Wen-Chen. Theoretical explanation of the spin-lattice coupling coefficients G_{11} and G_{44} for d^3 (V^{2+}, Cr^{3+}) ions in MgO crystals. *Journal of Physics: Condensed Matter*, 1(43):8093–8098, 1989.

[38] S. A. Al'tshuler, B. I. Kochelaev, and A. M. Leushin. Paramagnetic absorption of sound. *Soviet Physics Uspekhi*, 4(6):880, 1962.

[39] P. Ovartchaiyapong, K. W. Lee, B. A. Myers, and A. C. Bleszynski Jayich. Dynamic strain-mediated coupling of a single diamond spin to a mechanical resonator. *Nature Communications*, 5:4429, 2014.

[40] J. Teissier, A. Barfuss, P. Appel, E. Neu, and P. Maletinsky. Strain coupling of a nitrogen-vacancy center spin to a diamond mechanical oscillator. *Phys. Rev. Lett.*, 113:020503, 2014.

[41] E. R. MacQuarrie, T. A. Gosavi, N. R. Jungwirth, S. A. Bhave, and G. D. Fuchs. Mechanical spin control of nitrogen-vacancy centers in diamond. *Physical Review Letters*, 111:227602, 2013.

[42] E. R. MacQuarrie, T. A. Gosavi, A. M. Moehle, N. R. Jungwirth, S. A. Bhave, and G. D. Fuchs. Coherent control of a nitrogen-vacancy center spin ensemble with a diamond mechanical resonator. *Optica*, 2(3):233–238, 2015.

[43] E. R. Macquarrie, T. A. Gosavi, S. A. Bhave, and G. D. Fuchs. Continuous dynamical decoupling of a single diamond nitrogen-vacancy center spin with a mechanical resonator. *Physical Review B*, 92:224419, 2015.

[44] A. Barfuss, J. Teissier, E. Neu, A. Nunnenkamp, and P. Maletinsky. Strong mechanical driving of a single electron spin. *Nature Physics*, 11(10):820–824, 2015.

[45] F. Dolde, H. Fedder, M. W. Doherty, T. Nöbauer, F. Rempp, G. Balasubramanian, T. Wolf, F. Reinhard, L. C. L. Hollenberg, F. Jelezko, and J. Wrachtrup. Electric-field sensing using single diamond spins. *Nature Physics*, 7(6):459–463, 2011.

[46] M. W. Doherty, F. Dolde, H. Fedder, F. Jelezko, J. Wrachtrup, N. B. Manson, and L. C. L. Hollenberg. Theory of the ground-state spin of the nv^- center in diamond. *Phys. Rev. B*, 85:205203, 2012.

[47] P. Udvarhelyi, V. O. Shkolnikov, A. Gali, G. Burkard, and A. Pályi. Spin-strain interaction in nitrogen-vacancy centers in diamond. *Physical Review B*, 98:075201, 2018.

[48] P. Udvarhelyi and A. Gali. *Ab initio* spin-strain coupling parameters of divacancy qubits in silicon carbide. *Physical Review Applied*, 10:054010, 2018.

[49] J. J. Sakurai. *Modern Quantum Mechanics*. Addison-Wesley, Reading, MA, 1994.

[50] S. N. Shevchenko, S. Ashhab, and F. Nori. Landau-Zener-Stückelberg interferometry. *Physics Reports*, 492(1):1–30, 2010.

[51] C. G. Yale, B. B. Buckley, D. J. Christle, G. Burkard, F. J. Heremans, L. C. Bassett, and D. D. Awschalom. All-optical control of a solid-state spin using coherent dark states. *Proceedings of the National Academy of Sciences of the United States of America*, 110(19):7595–7600, 2013.

[52] C. G. Yale, F. J. Heremans, B. B. Zhou, A. Auer, G. Burkard, and D. D. Awschalom. Optical manipulation of the berry phase in a solid-state spin qubit. *Nature Photonics*, 10:184, 2016.

[53] B. B. Zhou, A. Baksic, H. Ribeiro, C. G. Yale, F. J. Heremans, P. C. Jerger, A. Auer, G. Burkard, A. A. Clerk, and D. D. Awschalom. Accelerated quantum control using superadiabatic dynamics in a solid-state lambda system. *Nature Physics*, 13:330, 2016.

[54] A. Barfuss, J. Kölbl, L. Thiel, J. Teissier, M. Kasperczyk, and P. Maletinsky. Phase-controlled coherent dynamics of a single spin under closed-contour interaction. *Nature Physics*, 14(11):1087–1091, 2018.

[55] J. A. Weil and J. R. Bolton. *Electron Paramagnetic Resonance: Elementary Theory and Practical Applications*. Wiley, 2007.

[56] J. F. Nye. *Physical Properties of Crystals*. Oxford University Press, 1986.

[57] L. D. Landau and E. M. Lifshitz. *Theory of Elasticity (Second Edition)*. Pergamon Press, 1970.

[58] O. Madelung, U. Rössler, and M. Schulz, editors. *Landolt-Börnstein - Group III Condensed Matter*. Springer, 2001.

[59] Y. Takagaki, P. V. Santos, E. Wiebicke, O. Brandt, H.-P. Schönherr, and K. H. Ploog. Guided propagation of surface acoustic waves in aln and gan films grown on 4h-sic (0001) substrates. *Physical Review B*, 66:155439, 2002.

[60] D. Morgan and E. G. S. Paige. *Surface Acoustic Wave Filters*. Academic Press, 2007.

[61] Lord Rayleigh. On waves propagated along the plane surface of an elastic solid. *Proceedings of the London Mathematical Society*, s1-17(1):4–11, 1885.

[62] A. N. Cleland. *Foundations of Nanomechanics*. Springer, Berlin, Heidelberg, 2003.

[63] M. E. Levinshtein, S. L. Rumyantsev, and M. S. Shur, editors. *Properties of Advanced Semiconductor Materials: GaN, AlN, InN, BN, SiC, SiGe*. John Wiley & Sons, 2001.

[64] D. L. T. Bell and R. C. M. Li. Surface-acoustic-wave resonators. *Proceedings of the IEEE*, 64(5):711–721, 1976.

[65] R. C. M. Li, J. A. Alusow, and R. C. Williamson. Surface-wave resonators using grooved reflectors. *29th Annual Symposium on Frequency Control*, pages 167–176, 1975.

[66] P. S. Cross. Reflective arrays for saw resonators. *1975 Ultrasonics Symposium*, pages 241–244, 1975.

[67] J. P. Wolfe. *Imaging Phonons: Acoustic Wave Propagation in Solids*. Cambridge University Press, Cambridge, 1998.

[68] A.E. Siegman. *Lasers*. University Science Books, 1986.

[69] D. M. Pozar. *Microwave Engineering*. Wiley, 2004.

[70] M. C. Sanchez, E. Martin, and J. M. Zamarro. New vectorial automatic technique for characterisation of resonators. *IEE Proceedings H - Microwaves, Antennas and Propagation*, 136(2):147–150, 1989.

[71] P. J. Petersan and S. M. Anlage. Measurement of resonant frequency and quality factor of microwave resonators: Comparison of methods. *Journal of Applied Physics*, 84(6):3392–3402, 1998.

[72] A. Megrant, C. Neill, R. Barends, B. Chiaro, Y. Chen, L. Feigl, J. Kelly, E. Lucero, M. Mariantoni, P. J. J. OMalley, D. Sank, A. Vainsencher, J. Wenner, T. C. White, Y. Yin, J. Zhao, C. J. Palmstrøm, J. M. Martinis, and A. N. Cleland. Planar superconducting resonators with internal quality factors above one million. *Applied Physics Letters*, 100(11):113510, 2012.

[73] G. Wolfowicz, S. J. Whiteley, and D. D. Awschalom. Electrometry by optical charge conversion of deep defects in 4h-sic. *Proceedings of the National Academy of Sciences of the United States of America*, 115(31):7879–7883, 2018.

[74] T. Iwasaki, W. Naruki, K. Tahara, T. Makino, H. Kato, M. Ogura, D. Takeuchi, S. Yamasaki, and M. Hatano. Direct Nanoscale Sensing of the Internal Electric Field in Operating Semiconductor Devices Using Single Electron Spins. *ACS Nano*, 11(2):1238–1245, 2017.

[75] M. Nonnenmacher, M. P. O'Boyle, and H. K. Wickramasinghe. Kelvin probe force microscopy. *Applied Physics Letters*, 58(25):2921–2923, 1991.

[76] J. Bylander, T. Duty, and P. Delsing. Current measurement by real-time counting of single electrons. *Nature*, 434(7031):361–364, 2005.

[77] R. J. Schoelkopf, P. Wahlgren, A. A. Kozhevnikov, P. Delsing, and D. E. Prober. The radio-frequency single-electron transistor (rf-set): A fast and ultrasensitive electrometer. *Science*, 280(5367):1238–1242, 1998.

[78] F. Dolde, M. W. Doherty, J. Michl, I. Jakobi, B. Naydenov, S. Pezzagna, J. Meijer, P. Neumann, F. Jelezko, N. B. Manson, and J. Wrachtrup. Nanoscale detection of a single fundamental charge in ambient conditions using the NV- center in diamond. *Physical Review Letters*, 112(9):097603, 2014.

[79] M. E. Trusheim and Dirk Englund. Wide-field strain imaging with preferentially aligned nitrogen-vacancy centers in polycrystalline diamond. *New Journal of Physics*, 18(12):123023, 2016.

[80] F. R. Bradbury, A. M. Tyryshkin, G. Sabouret, J. Bokor, T. Schenkel, and S. A. Lyon. Stark tuning of donor electron spins in silicon. *Physical Review Letters*, 97(17):176404, 2006.

[81] G. Wolfowicz, M. Urdampilleta, M. L. W. Thewalt, H. Riemann, N. V. Abrosimov, P. Becker, H.-J. Pohl, and J. J. L. Morton. Conditional control of donor nuclear spins in silicon using stark shifts. *Physical Review Letters*, 113(15):157601, 2014.

[82] G. Wolfowicz, C. P. Anderson, A. L. Yeats, S. J. Whiteley, J. Niklas, O. G. Poluektov, F. J. Heremans, and D. D. Awschalom. Optical charge state control of spin defects in 4H-SiC. *Nature Communications*, 8(1):1876, 2017.

[83] B. Magnusson, N. T. Son, A. Csóré, A. Gällström, T. Ohshima, A. Gali, and I. G. Ivanov. Excitation properties of the divacancy in 4H-SiC. *Physical Review B*, 98:195202, 2018.

[84] N. Aslam, G. Waldherr, P. Neumann, F. Jelezko, and J. Wrachtrup. Photo-induced ionization dynamics of the nitrogen vacancy defect in diamond investigated by single-shot charge state detection. *New Journal of Physics*, 15(1):013064, 2013.

[85] P. G. Baranov, A. P. Bundakova, A. A. Soltamova, S. B. Orlinskii, I. V. Borovykh, R. Zondervan, R. Verberk, and J. Schmidt. Silicon vacancy in SiC as a promising quantum system for single-defect and single-photon spectroscopy. *Physical Review B*, 83(12):125203, 2011.

[86] D. A. Golter and C. W. Lai. Optical switching of defect charge states in 4H-SiC. *Scientific Reports*, 7(1):13406, 2017.

[87] C. F. de las Casas, D. J Christle, J. U. Hassan, T. Ohshima, N. T. Son, and D. D Awschalom. Stark tuning and electrical charge state control of single divacancies in silicon carbide. *Applied Physics Letters*, 111(26):262403, 2017.

[88] T. Joas, A. M. Waeber, G. Braunbeck, and F. Reinhard. Quantum sensing of weak radio-frequency signals by pulsed Mollow absorption spectroscopy. *Nature Communications*, 8(1):964, 2017.

[89] C. G. Van de Walle. Stretched-exponential relaxation modeled without invoking statistical distributions. *Physical Review B*, 53(17):11292–11295, 1996.

[90] R. Chen. Apparent stretched-exponential luminescence decay in crystalline solids. *Journal of Luminescence*, 102-103(SPEC):510–518, 2003.

[91] E. H. Chen, H. A. Clevenson, K. A. Johnson, L. M. Pham, D. R. Englund, P. R. Hemmer, and D. A. Braje. High-sensitivity spin-based electrometry with an ensemble of nitrogen-vacancy centers in diamond. *Physical Review A*, 95(5):053417, 2017.

[92] I. A. Chaikovskii, G. M. Shmelev, and A. I. German. AC Conductivity of Highly Inhomogeneous Semiconductors. *Physica Status Solidi*, 129(1):393–398, 1985.

[93] S. J. Rothberg, M. S. Allen, P. Castellini, D. Di Maio, J. J. J. Dirckx, D. J. Ewins, B. J. Halkon, P. Muyshondt, N. Paone, T. Ryan, H. Steger, E. P. Tomasini, S. Vanlanduit, and J. F. Vignola. An international review of laser Doppler vibrometry: Making light work of vibration measurement. *Optics and Lasers in Engineering*, 99:11–22, 2017.

[94] S. J. Whiteley, F. J. Heremans, G. Wolfowicz, D. D. Awschalom, and M. V. Holt. Direct imaging of dynamically driven strain in quantum materials using stroboscopic scanning x-ray diffraction microscopy. *arXiv*, page 1808.04920, 2018.

[95] W. Wu and Z. L. Wang. Piezotronics and piezo-phototronics for adaptive electronics and optoelectronics. *Nature Reviews Materials*, 1(1):16031, 2016.

[96] L. Oakes, R. Carter, T. Hanken, A. P. Cohn, K. Share, B. Schmidt, and C. L. Pint. Interface strain in vertically stacked two-dimensional heterostructured carbon-mos_2 nanosheets controls electrochemical reactivity. *Nature Communications*, 7:11796, 2016.

[97] D. Sando, A. Agbelele, D. Rahmedov, J. Liu, P. Rovillain, C. Toulouse, I. C. Infante, A. P. Pyatakov, S. Fusil, E. Jacquet, C. Carrétéro, C. Deranlot, S. Lisenkov, D. Wang, J.-M. Le Breton, M. Cazayous, A. Sacuto, J. Juraszek, A. K. Zvezdin, L. Bellaiche, B. Dkhil, A. Barthélémy, and M. Bibes. Crafting the magnonic and spintronic response of $BiFeO_3$ films by epitaxial strain. *Nature Materials*, 12(7):641–646, 2013.

[98] T. D. Ladd, F. Jelezko, R. Laflamme, Y. Nakamura, C. Monroe, and J. L. O. Brien. Quantum computers. *Nature*, 464(7285):45–53, 2010.

[99] M. V. Gustafsson, T. Aref, A. F. Kockum, K. Maria, G. Johansson, and P. Delsing. Propagating phonons coupled to an artificial atom. *Science*, 346(6206):207–211, 2014.

[100] L. C. Bassett, F. J. Heremans, C. G. Yale, B. B. Buckley, and D. D. Awschalom. Electrical Tuning of Single Nitrogen-Vacancy Center Optical Transitions Enhanced by Photoinduced Fields. *Physical Review Letters*, 107(26):266403, 2011.

[101] C. F. de las Casas, D. J. Christle, J. U. Hassan, T. Ohshima, N. T. Son, and D. D. Awschalom. Stark tuning and electrical charge state control of single divacancies in silicon carbide. *Applied Physics Letters*, 111:262403, 2017.

[102] M. J. A. Schuetz, E. M. Kessler, G. Giedke, L. M. K. Vandersypen, M. D. Lukin, and J. I. Cirac. Universal Quantum Transducers Based on Surface Acoustic Waves. *Physical Review X*, 031031:1–30, 2015.

[103] S. J. Whiteley, G. Wolfowicz, C. P. Anderson, A. Bourassa, H. Ma, M. Ye, G. Koolstra, K. J. Satzinger, M. V. Holt, F. J. Heremans, A. N. Cleland, D. I. Schuster, G. Galli, and D. D. Awschalom. Spin-phonon interactions in silicon carbide addressed by gaussian acoustics. *Nature Physics*, 15:490–495, 2019.

[104] J. R. Weber, W. F. Koehl, J. B. Varley, A. Janotti, B. B. Buckley, C. G. Van de Walle, and D. D. Awschalom. Quantum computing with defects. *Proceedings of the National Academy of Sciences of the United States of America*, 107(19):8513–8518, 2010.

[105] F. J. R. Schülein, E. Zallo, P. Atkinson, O. G. Schmidt, R. Trotta, A. Rastelli, A. Wixforth, and H. J. Krenner. Fourier synthesis of radiofrequency nanomechanical pulses with different shapes. *Nature Nanotechnology*, 10:512–516, 2015.

[106] S. Hermelin, S. Takada, M. Yamamoto, S. Tarucha, A. D. Wieck, L. Saminadayar, C. Bäuerle, and T. Meunier. Electrons surfing on a sound wave as a platform for quantum optics with flying electrons. *Nature*, 477:435–438, 2011.

[107] R. W. Whatmore, P. A. Goddard, B. K. Tanner, and G. F. Clark. Direct imaging of travelling Rayleigh waves by stroboscopic X-ray topography. *Nature*, 299:44–46, 1982.

[108] E. Zolotoyabko, D. Shilo, and E. Lakin. X-ray imaging of acoustic wave interaction with dislocations. *Materials Science and Engineering: A*, 309-310:23–27, 2001.

[109] T. Reusch, F. Schülein, C. Bömer, M. Osterhoff, A. Beerlink, H. J. Krenner, A. Wixforth, and T. Salditt. Standing surface acoustic waves in $LiNbO_3$ studied by time resolved X-ray diffraction at Petra III. *AIP Advances*, 3:072127, 2013.

[110] J.-D. Nicolas, T. Reusch, M. Osterhoff, M. Sprung, F. J. R. Schülein, H. J Krenner, A. Wixforth, and T. Salditt. Time-resolved coherent X-ray diffraction imaging of surface acoustic waves. *Journal of Applied Crystallography*, 47:1596–1605, 2014.

[111] M. Holt, R. Harder, R. Winarski, and V. Rose. Nanoscale hard x-ray microscopy methods for materials studies. *Annual Review of Materials Research*, 43:183–211, 2013.

[112] G. K. Shenoy, P. J. Viccaro, and D. M. Mills. *Characteristics of the 7-GeV advanced photon source: A guide for users*. United States Department of Energy, 1988.

[113] J. N. Clark, L. Beitra, G. Xiong, A. Higginbotham, D. M. Fritz, H. T. Lemke, D. Zhu, M. Chollet, G. J. Williams, M. Messerschmidt, B. Abbey, R. J. Harder, A. M. Korsunsky, J. S. Wark, and I. K. Robinson. Ultrafast three-dimensional imaging of lattice dynamics in individual gold nanocrystals. *Science*, 341:56–59, 2013.

[114] D. O Bracher, X. Zhang, and E. L. Hu. Selective Purcell enhancement of two closely linked zero-phonon transitions of a silicon carbide color center. *Proceedings of the National Academy of Sciences of the United States of America*, 114(16):4060–4065, 2017.

[115] D. A. Golter, T. Oo, M. Amezcua, K. A. Stewart, and H. Wang. Optomechanical quantum control of a nitrogen-vacancy center in diamond. *Physical Review Letters*, 116:143602, 2016.

[116] H. Y. Chen, E. R. MacQuarrie, and G. D. Fuchs. Orbital state manipulation of a diamond nitrogen-vacancy center using a mechanical resonator. *Physical Review Letters*, 120:167401, 2018.

[117] C. Campbell. *Surface Acoustic Wave Devices and their Signal Processing Applications*. Academic Press, 1989.

[118] J. V. Comamala, A. Diaz, M. Guizar-Sicairos, A. Mantion, C. M. Kewish, A. Menzel, O. Bunk, and C. David. Characterization of high-resolution diffractive x-ray optics by ptychographic coherent diffractive imaging. *Optics Express*, 19:21333–21344, 2011.

[119] R. P. Winarski, M. V. Holt, V. Rose, P. Fuesz, D. Carbaugh, C. Benson, D. Shu, D. Kline, G. B. Stephenson, I. McNulty, and J. Maser. A hard x-ray nanoprobe beamline for nanoscale microscopy. *Journal of Synchrotron Radiation*, 19:1056–1060, 2012.

[120] M. V. Holt, S. O. Hruszkewycz, C. E. Murray, J. R. Holt, D. M. Paskiewicz, and P. H. Fuoss. Strain imaging of nanoscale semiconductor heterostructures with X-ray Bragg projection ptychography. *Physical Review Letters*, 112:165502, 2014.

[121] S. O. Hruszkewycz, M. Allain, M. V. Holt, C. E. Murray, J. R. Holt, P. H. Fuoss, and V. Chamard. High-resolution three-dimensional structural microscopy by single-angle Bragg ptychography. *Nature Materials*, 16:244–251, 2017.

[122] D. Lee, K. W. Lee, J. V. Cady, P. Ovartchaiyapong, and A. C. Bleszynski Jayich. Topical review: spins and mechanics in diamond. *Journal of Optics*, 19(3):033001, 2017.

[123] H. Seo, A. L. Falk, P. V. Klimov, K. C. Miao, G. Galli, and D. D. Awschalom. Quantum decoherence dynamics of divacancy spins in silicon carbide. *Nature Communications*, 7:12935, 2016. Article.

[124] S. Kolkowitz, A. C. Bleszynski Jayich, Q. P. Unterreithmeier, S. D. Bennett, P. Rabl, J. G. E. Harris, and M. D. Lukin. Coherent sensing of a mechanical resonator with a single-spin qubit. *Science*, 335(6076):1603–1606, 2012.

[125] S. Hong, M. S. Grinolds, P. Maletinsky, R. L. Walsworth, M. D. Lukin, and A. Yacoby. Coherent, mechanical control of a single electronic spin. *Nano Letters*, 12(8):3920–3924, 2012. PMID: 22800099.

[126] R. Manenti, A. F. Kockum, A. Patterson, T. Behrle, J. Rahamim, G. Tancredi, F. Nori, and P. J. Leek. Circuit quantum acoustodynamics with surface acoustic waves. *Nature Communications*, 8(1):975, 2017.

[127] B. A. Moores, L. R. Sletten, J. J. Viennot, and K. W. Lehnert. Cavity quantum acoustic device in the multimode strong coupling regime. *Physical Review Letters*, 120:227701, 2018.

[128] D. A. Golter, T. Oo, M. Amezcua, I. Lekavicius, K. A. Stewart, and H. Wang. Coupling a surface acoustic wave to an electron spin in diamond via a dark state. *Physical Review X*, 6:041060, 2016.

[129] A. Pateras, J. Park, Y. Ahn, J. A. Tilka, M. V. Holt, C. Reichl, W. Wegscheider, T. A. Baart, J. P. Dehollain, U. Mukhopadhyay, L. M. K. Vandersypen, and P. G. Evans. Mesoscopic elastic distortions in gaas quantum dot heterostructures. *Nano Letters*, 18(5):2780–2786, 2018. PMID: 29664645.

[130] D. M. Toyli, C. D. Weis, G. D. Fuchs, T. Schenkel, and D. D. Awschalom. Chip-scale nanofabrication of single spins and spin arrays in diamond. *Nano Letters*, 10(8):3168–3172, 2010. PMID: 20698632.

[131] P. V. Klimov, A. L. Falk, B. B. Buckley, and D. D. Awschalom. Electrically driven spin resonance in silicon carbide color centers. *Physical Review Letters*, 112:087601, 2014.

[132] K. W. Lee, D. Lee, P. Ovartchaiyapong, J. Minguzzi, J. R. Maze, and A. C. Bleszynski Jayich. Strain coupling of a mechanical resonator to a single quantum emitter in diamond. *Physical Review Applied*, 6:034005, 2016.

[133] E. R. MacQuarrie, M. Otten, S. K. Gray, and G. D. Fuchs. Cooling a mechanical resonator with nitrogen-vacancy centres using a room temperature excited state spin-strain interaction. *Nature Communications*, 8:14358, 2017. Article.

[134] M. S. J. Barson, P. Peddibhotla, P. Ovartchaiyapong, K. Ganesan, R. L. Taylor, M. Gebert, Z. Mielens, B. Koslowski, D. A. Simpson, L. P. McGuinness, J. McCallum, S. Prawer, S. Onoda, T. Ohshima, A. C. Bleszynski Jayich, F. Jelezko, N. B. Manson, and M. W. Doherty. Nanomechanical sensing using spins in diamond. *Nano Letters*, 17(3):1496–1503, 2017. PMID: 28146361.

[135] D. D. Awschalom, R. Hanson, J. Wrachtrup, and B. B. Zhou. Quantum technologies with optically interfaced solid-state spins. *Nature Photonics*, 12(9):516–527, 2018.

[136] S. D. Bennett, N. Y. Yao, J. Otterbach, P. Zoller, P. Rabl, and M. D. Lukin. Phonon-induced spin-spin interactions in diamond nanostructures: application to spin squeezing. *Physical Review Letters*, 110:156402, 2013.

[137] K. V. Kepesidis, S. D. Bennett, S. Portolan, M. D. Lukin, and P. Rabl. Phonon cooling and lasing with nitrogen-vacancy centers in diamond. *Physical Review B*, 88:064105, 2013.

[138] M. J. Rayson and P. R. Briddon. First principles method for the calculation of zero-field splitting tensors in periodic systems. *Physical Review B*, 77:035119, 2008.

[139] J. P. Perdew, K. Burke, and M. Ernzerhof. Generalized gradient approximation made simple. *Physical Review Letters*, 77:3865–3868, 1996.

[140] P. E. Blöchl. Projector augmented-wave method. *Physical Review B*, 50:17953–17979, 1994.

[141] A. Dal Corso. Pseudopotentials periodic table: From h to pu. *Computational Materials Science*, 95:337–350, 2014.

[142] V. Ivády, T. Simon, J. R. Maze, I. A. Abrikosov, and Adam Gali. Pressure and temperature dependence of the zero-field splitting in the ground state of nv centers in diamond: A first-principles study. *Physical Review B*, 90:235205, 2014.

[143] Paolo Giannozzi, Stefano Baroni, Nicola Bonini, Matteo Calandra, Roberto Car, Carlo Cavazzoni, Davide Ceresoli, Guido L Chiarotti, Matteo Cococcioni, Ismaila Dabo, Andrea Dal Corso, Stefano de Gironcoli, Stefano Fabris, Guido Fratesi, Ralph Gebauer,

Uwe Gerstmann, Christos Gougoussis, Anton Kokalj, Michele Lazzeri, Layla Martin-Samos, Nicola Marzari, Francesco Mauri, Riccardo Mazzarello, Stefano Paolini, Alfredo Pasquarello, Lorenzo Paulatto, Carlo Sbraccia, Sandro Scandolo, Gabriele Sclauzero, Ari P Seitsonen, Alexander Smogunov, Paolo Umari, and Renata M Wentzcovitch. QUANTUM ESPRESSO: a modular and open-source software project for quantum simulations of materials. *Journal of Physics: Condensed Matter*, 21(39):395502, 2009.

[144] F. Jelezko, T. Gaebel, I. Popa, A. Gruber, and J. Wrachtrup. Observation of coherent oscillations in a single electron spin. *Physical Review Letters*, 92:076401, 2004.

[145] A. P. Mirgorodsky, M. B. Smirnov, E. Abdelmounîm, T. Merle, and P. E. Quintard. Molecular approach to the modeling of elasticity and piezoelectricity of sic polytypes. *Physical Revew B*, 52:3993–4000, 1995.

[146] M. A. Stroscio, Y. M. Sirenko, S. Yu, and K. W. Kim. Acoustic phonon quantization in buried waveguides and resonators. *Journal of Physics: Condensed Matter*, 8(13):2143–2151, 1996.

[147] A. Bienfait. *Magnetic resonance with quantum microwaves*. PhD thesis, Universite Paris-Sarclay, 2016.

[148] P. S. Alexopoulos and T. C. O'Sullivan. Mechanical properties of thin films. *Annual Review of Materials Science*, 20(1):391–420, 1990.

[149] Y. Tsaturyan, A. Barg, E. S. Polzik, and A. Schliesser. Ultracoherent nanomechanical resonators via soft clamping and dissipation dilution. *Nature Nanotechnology*, 12:776, 2017.

[150] G. C. A. M. Janssen, M. M. Abdalla, F. van Keulen, B. R. Pujada, and B. van Venrooy. Celebrating the 100th anniversary of the stoney equation for film stress: Developments from polycrystalline steel strips to single crystal silicon wafers. *Thin Solid Films*, 517(6):1858 – 1867, 2009.

[151] V. V. Felmetsger, P. N. Laptev, and S. M. Tanner. Design, operation mode, and stress control capability of s-gun magnetron for ac reactive sputtering. *Surface and Coatings Technology*, 204(6):840 – 844, 2009.

[152] A. Iqbal and F. Mohd-Yasin. Reactive sputtering of aluminum nitride (002) thin films for piezoelectric applications: a review. *Sensors*, 18(6), 2018.

[153] E. Kaxiras. *Atomic and Electronic Structure of Solids*. Cambridge University Press, 2003.

[154] W. F. Koehl, B. Diler, S. J. Whiteley, A. Bourassa, N. T. Son, E. Janzén, and D. D. Awschalom. Resonant optical spectroscopy and coherent control of Cr^{4+} spin ensembles in SiC and GaN. *Physical Review B*, 95:035207, 2017.

[155] V. Heera, D. Panknin, and W. Skorupa. p-type doping of sic by high dose al implantationproblems and progress. *Applied Surface Science*, 184(1):307 – 316, 2001.